Estimation of evapotranspiration using directional thermal infrared data

Samuel Mwangi

THÈSE

En vue de l'obtention du

DOCTORAT DE L'UNIVERSITÉ DE TOULOUSE

Délivré par l'Université Toulouse 3 - Paul Sabatier

Présentée et soutenue par

Samuel MWANGI

Le 02 Février 2023

Estimation de l'évapotranspiration à l'aide des données directionnelles en infrarouge thermique

---

Ecole doctorale : **SDU2E - Sciences de l'Univers, de l'Environnement et de l'Espace**

Spécialité : **Surfaces et interfaces continentales, Hydrologie**

Unité de recherche :
CESBIO - Centre d'Etudes Spatiales de la Biosphère

Thèse dirigée par
Gilles BOULET et Albert OLIOSO

Jury

Mme. Catherine OTTLE, Rapporteur

Mme. Isabel TRIGO, Rapporteur

M. Jean-Pierre Lagouarde, Examinateur

M. Jean-Philippe Gastellu-Etchegorry, Examinateur, Président

M. Jean-Louis Roujean, Invite

M. Philippe Maisongrande, Invite

M. Gilles BOULET, Directeur de thèse

M. Albert OLIOSO, Co-directeur de thèse

Remerciement

First, I thank the Almighty God for His grace and for seeing me through to this point of my life.

This work would not have been possible without the gracious funding from the CNES and the region Occitanie, for this I am sincerely grateful.

To my supervisors, thank you for the guidance throughout the study. Many thanks Dr. Boulet. In addition to being ready to help with navigating the [many] administrative bureaucracies, your well-rounded and thorough knowledge, guidance, and input on the subject were of great inspiration. Dr. Olioso, well, you definitely do know your stuff ! Many thanks for the often critical but ever insightful discussions and the great perspectives. *Big Respec'* to the both of you. To the members of my thesis committee (Dr. Irvine, Dr. Prevot, Prof. dr. J-P G-E), your availability and guidance through this thesis period is greatly appreciated. Many thanks to Dr. Roujean, Prof. dr. Gastellu-Etchegorry and other members of the CESBIO lab who have been instrumental and helpful with various aspects of this work. Dr. J-P Lagouarde's insightful works on the subject are also acknowledged. Sincere gratitude to Dr. Ottlé, and Prof. dr. Trigo for agreeing (within short notice) to review this work,

To Dominique, Laurence and the many other members of the CESBIO team (including the Directors of the lab and school), thank you for being helpful with the smooth handling of day-to-day administrative aspects. My amazing officemates, Ludovic, Veronika, thanks ! Also greatly appreciate Vincent's accommodating demeanour. To my fellow colleagues (Pierre, Lisbeth, Juan, Luis, Kemi, Omar, Nitu, …) at the CESBIO, the discussions during the breaks were refreshing.

To me Ma, Pa (RIP) and siblings, thank you. Faith, somehow you've helped keep my sanity intact throughout this experience !

Salut.

Contents

List of Figures

List of Tables

« in the abundance of water, the fool is thirsty » - bob marley

Résumé

Abstract

Evapotranspiration (ET) is an important component of the hydrological cycle. Its estimation is required when quantifying the water use and demand over agricultural and natural surfaces. In many ET estimation methods, surface temperature - which acts as a proxy for terrestrial water status - is an essential input variable. Surface temperature is acquired in the thermal infrared (TIR) spectral domain using remote sensors (whether in-situ or space-borne) with varying view-earth-sun geometry configurations. These multi-angular view geometries can lead to varying proportions of the canopy components being sampled in the Field Of View, and thus different temperatures being observed depending on the sensor's position relative to the sun. This is termed thermal radiation directionality (TRD). It is therefore important to account for TRD to ensure consistency in flux estimation irrespective of viewing configuration. In this study, we focus on single-pixel surface energy balance (SEB) evapotranspiration models (and initial analyses on contextual SEB), and seek to analyze how thermal directionality influences such methods. For point-based SEB, we worked on extending the SPARSE (Soil Plant Atmosphere Remote Sensing of Evapotranspiration) model, wherein the original SPARSE was modified to distinguish sunlit/shaded soil/vegetation sources, and coupled with a radiative transfer model that links these four element emissions to the directional thermal radiances as observed by remote thermal infrared sensors. Initial evaluations were carried out to check the model's capability in retrieving surface fluxes over diverse environments instrumented with in-situ thermo-radiometers. This was performed using historical data that included TIR sensors at nadir (tree cover, wheat and soybean) or in two directions only, on a homogeneous cover (wheat) for which the directional effects were minimal. To compensate for the absence of measurement sites having directional surface temperature acquisitions in a sufficient range of viewing angles hence enabling the sampling of foliage and soil temperature extremes, we set up a flux station on a heterogeneous canopy in Verdu (Catalonia, Spain). The campaign was part of the HiLiaise project. Both algorithms showed no observable differences in their estimation of total fluxes when run with nadir-acquired surface temperature data. Nonetheless, by incorporating the solar direction and discriminating between sunlit and shaded elements, we observed that the partitioning of these overall fluxes between the soil and the vegetation could be improved particularly in water-stressed environments. The sensitivity

of flux and component temperature estimates to the viewing direction of the sensor was initially tested by using two - simultaneously observed - sets of thermal data (nadir and oblique) to force the models where it was shown that sensitivity to viewing direction is significantly reduced. Over the heterogeneous Vineyard site, the sensitivity of flux and component temperature estimates to the viewing direction of the sensor was also tested by using reconstructed sets of thermal data (nadir and oblique) to force the models. Here, we observed degradation in flux retrieval cross-row with better consistency along rows. Overall, it was nevertheless shown that by using the extended method, the sensitivity to viewing direction can significantly be reduced. Separately, a synthetic study was performed in a homogeneous canopy setup comparing model retrievals with those from the SCOPE model, which is able to provide 'references' of flux estimates and directional temperatures. Here, SPARSE4 is observed to improve directional consistency of the flux retrievals over wide-ranging simulation conditions, especially at higher view angles. As with directional anisotropy, different conditions were observed to influence the directional retrieval consistency, with the main driver observed to be the incoming radiation. Wind speed and vegetation fraction cover (as described by the leaf area index) also influence the directional retrievals. Nonetheless, the retrieval inconsistencies (hence weak model performance) were mostly observed to have a major influence at higher zeniths, with minimal effects on near-nadir based (as would be the case with current/recent TIR RS missions) retrievals. With respect to how directionality influences the temperature-fraction cover (T-fc) space as applied in contextual evapotranspiration modelling, initial synthetic experiments carried out utilizing the SMEX02 data and SCOPE show insignificant thermal radiation directionality (TRD) effects when the area of interest (AOI) is close to the satellite's sub-track as well as in small image scenes. This however does not necessarily apply when the AOI is located further off the sub-track (particularly in the hotspot region). Other aspects such as, how surface roughness influences directionality especially on near-bare surfaces, need to be considered for a better contextual space representation. Nonetheless, simple positioning tools (i.e. Sun path diagrams + specifications of view geometry) can qualitatively help identify this TRD exposure.

Résumé

L'évapotranspiration (ET) est une composante importante du cycle hydrologique. Son estimation est nécessaire pour quantifier l'utilisation et la demande en eau sur les surfaces agricoles et naturelles. Dans de nombreuses méthodes d'estimation de l'ET, la température de surface, qui agit comme un indicateur de l'état des eaux terrestres, est une variable d'entrée essentielle. La température de surface est acquise dans le domaine de l'infrarouge thermique (TIR) à l'aide de capteurs à distance (in situ ou spatiaux) dont les configurations géométriques de la vue, de la terre et du soleil varient. Ces géométries de vue multi-angulaires peuvent conduire à des proportions variables des composants de la canopée échantillonnés dans le champ de vision, et donc à des températures différentes observées selon la position du capteur par rapport au soleil. C'est ce qu'on appelle la directionnalité du rayonnement thermique (TRD). Il est donc important de prendre en compte le TRD pour assurer la cohérence de l'estimation du flux, quelle que soit la configuration de la vue. Dans cette étude, nous nous concentrons sur les modèles d'évapotranspiration par bilan énergétique de surface (SEB) à un seul pixel (et les analyses initiales sur le SEB contextuel) et cherchons à analyser comment la directionnalité thermique influence ces méthodes. Pour le SEB ponctuel, nous avons travaillé sur l'extension de SPARSE (Soil Plant Atmosphere Remote Sensing of Evapotranspiration), dans lequel le SPARSE original a été modifié pour distinguer les sources de sol/végétation ensoleillées/ombragées, et couplé avec un modèle de transfert radiatif qui relie ces quatre émissions d'éléments aux radiations thermiques directionnelles telles qu'observées par les capteurs infrarouges thermiques à distance. Des évaluations initiales ont été effectuées pour vérifier la capacité du modèle à récupérer les flux de surface dans divers environnements équipés de thermo-radiomètres in-situ. Ceci a été réalisé en utilisant des données historiques comprenant des capteurs TIR au nadir (couverture arborée, blé et soja) ou dans deux directions seulement, sur une couverture homogène (blé) pour laquelle les effets directionnels sont minimes. Pour pallier l'absence de sites de mesure disposant d'acquisitions directionnelles de la température de surface dans une gamme suffisante d'angles de vue et permettant donc l'échantillonnage des extrêmes de température du feuillage et du sol, nous avons mis en place une station de flux sur une canopée hétérogène à Verdu (Catalogne, Espagne). Cette campagne faisait partie du projet HiLiaise. Les deux algorithmes ne montrent aucune différence observable dans leur estimation des flux totaux lorsqu'ils sont exécutés avec des données de température de surface acquises au nadir. Néanmoins, en incorporant la direction du soleil et en distinguant les éléments éclairés par le soleil des éléments ombragés, nous observons que la partition de ces flux globaux entre le sol et la végétation peut être améliorée, en particulier dans les environnements soumis à un stress hydrique. La sensibilité des estimations de flux et de température des composants à la direction de visée du capteur a été testée en utilisant deux ensembles - observés

simultanément - de données thermiques (nadir et oblique) pour forcer les modèles où il a été montré que la sensibilité à la direction de visée est considérablement réduite. Sur le site hétérogène de Vineyard, la sensibilité des estimations du flux et de la température des composants à la direction d'observation du capteur a également été testée en utilisant des ensembles reconstruits de données thermiques (nadir et oblique) pour forcer les modèles, où nous avons observé une dégradation de la récupération du flux entre les rangées avec une meilleure cohérence le long des rangées. Dans l'ensemble, il a néanmoins été démontré qu'en utilisant le modèle à quatre composantes (SPARSE4), la sensibilité à la direction de vue peut être réduite de manière significative. Séparément, une étude synthétique a été réalisée dans une configuration de canopée homogène comparant les deux versions du modèle avec celles du modèle plus complexe SCOPE, capable de fournir des estimations de flux et de températures directionnelles pour des couverts homogènes. SCOPE est utilisé comme référence pour simuler les flux et la température de surface selon divers états de surface. Ici, on observe que SPARSE4 améliore la cohérence directionnelle des récupérations de flux dans des conditions de simulation très variées. Comme pour l'anisotropie directionnelle, différentes conditions ont été observées pour influencer la cohérence directionnelle de l'extraction, le principal facteur étant le rayonnement entrant. La vitesse du vent et la fraction de couverture végétale (décrite par l'indice de surface foliaire) influencent également les récupérations directionnelles. Néanmoins, on a observé que les incohérences d’inversion (et donc la faible performance du modèle) avaient une influence majeure aux élévations plus bas, avec des effets minimes sur les récupérations basées sur le voisinage du nadir (comme ce serait le cas avec les missions RS IRT actuelles). En ce qui concerne l'influence de la directionnalité sur l'espace température-fraction de couverture (T-fc) tel qu'il est appliqué dans la modélisation contextuelle de l'évapotranspiration, les premières expériences synthétiques réalisées à l'aide des données SMEX02 et SCOPE montrent des effets de directionnalité du rayonnement thermique (TRD) insignifiants lorsque la zone d'intérêt (AOI) est proche de la trace du satellite ainsi que dans les petites scènes d'image. Cependant, cela ne s'applique pas nécessairement lorsque l'AOI est situé plus loin de la trace (en particulier dans la région du hotspot). D'autres aspects, tels que l'influence de la rugosité de la surface sur la directionnalité, en particulier sur les surfaces presque nues, doivent être pris en compte pour une meilleure représentation spatiale contextuelle. Néanmoins, des outils de positionnement simples (c'est-à-dire des diagrammes de la trajectoire du soleil + spécifications de la géométrie de la vue) peuvent aider qualitativement à identifier cette exposition au TRD.

Chapter 1: Introduction

1.1. General introduction

Water is life. The sustenance of the world's population is very much dependent on the proper use of the Earth's water resources. The effects of climate change have however degraded these resources with harvests being threatened by extreme droughts that are becoming more frequent in many parts of the world, particularly in arid and semi-arid lands (ASAL). This has made the efficient use of water a key policy issue (i.e., how to allocate scarce water resources between essential demand points such as: agriculture / irrigation, domestic use, hydropower / electricity generation, etc.). In agricultural water usage (which usually accounts for *ca.* 70 - >80 % of water use in ASALs), it has become important to seek maximum food productivity while ensuring minimal water loss. The most productive use in this case translates to water for optimal plant growth (through transpiration - T) with as little as possible being lost via soil evaporation (E). Practically, this requires the application of hydrological methods that are able to reasonably and reliably measure or estimate evapotranspiration (ET) and its components (evaporation (E) and transpiration (T)), and thus plant-water usage, based on the available water and energy fluxes (Boulet et al., 2018; Mallick et al., 2016). Measurement of surface mass and energy fluxes (and thus ET) can be achieved with reasonable accuracy. However, in-situ flux observatories have limited spatial coverage and cannot be inexpensively and effectively applied to determine water requirements at the required scales (for example regionally). Regionalization of measurements from several experimental sites are also prone to interpolation uncertainties (Wilson et al., 2002). Alternatively, actual ET can be quantified (even predicted/forecasted) by applying models that estimate the surface water and energy budgets. For example, ET can be simulated directly through land surface modelling, where the atmospheric demand and the soil moisture that should be available to the vegetation and for soil evaporation losses are estimated, or - indirectly - by using

variables with a tight physical link to the surface water status (i.e. variables that can describe water availability/stress (Boulet et al., 2022)).

Several evapotranspiration methods have already been proposed and operationalized, whether by regional authorities or agricultural firms, to aid in irrigation planning and thus optimise agricultural water usage (e.g., SEBAL, Bastiaanssen et al., 2005). The relatively common approach is the use of surface energy balance (SEB) methods that help to partition spatially and temporally varying available energy into water and sensible fluxes. For such methods, the temperature of the surface is a key input variable. Land surface temperature (LST) has been shown to be tightly linked to land water statuses (well-watered to water-stressed surfaces). Evapotranspiration is the most effective way of dissipating incoming radiation - a wet surface will therefore have a lower temperature, with conversion to sensible heat flux (thus increase in land to air temperature difference) as the surface dries. LST can therefore be used for early detection of plant-water stress with the aim of averting permanent crop failure due to insufficient water. It can be measured either in-situ or remotely using thermoradiometers, which generally detect electromagnetic radiation signals in the thermal infrared $8-14\,\mu\mathrm{m}$ spectral sensitivity range. The use of in-situ thermal sensors can provide near real-time observations; however, they are generally at point scale and hence constrained spatially. On the other hand, space-borne thermal remote sensors acquisitions have relatively low temporal resolutions but can cover large spatial scales, which may be preferable for regional decision making. The acquisitions made by satellites vary in their spatial, spectral and radiometric resolutions depending on the selected design criteria, i.e. satellite altitude and overall orbit orientation, thermal sensor specifications, etc. The use of satellite-observed radiation must therefore be interpreted according to its spectral and directional features. For example, ensuring that tools (i.e., including those applied in thermal normalization of the radiation signal to account for directionality) used in their interpretation consider various sensor- as well as surface-specific aspects that, if not considered, may lead to an inadequate understanding of conditions at the land surface.

While efforts have mostly been directed towards addressing missing data and/or inadequate spatial and temporal resolutions (e.g. by applying gap filling methods, data fusion techniques, proposing missions with improved revisit times and spatial resolutions,

applying disaggregation techniques, among others), limited focus has been placed on how thermal radiation directionality (TRD) influences flux retrieval. TRD can be defined as the thermal anisotropy that results from the position of the sensor relative to the sun in combination with the geometry of components at the observed target (i.e., vegetation and soil components at the Earth surface). For example (Figure 1), a sensor viewing from the sun's direction (hotspot, i.e. in the syzygy Sun-satellite-Earth configuration) will generally view sunlit terrestrial elements as compared to one observing from nadir (or other directions), which see less illuminated elements. The geometry of the terrain will also affect the acquisitions since the canopy's structure and homogeneity, or lack thereof, will influence the observed thermal emission signals; e.g., in row crops, the measured emission will be influenced by whether the sensor is aligned along- or cross-row. With regard to surface temperature normalization, a general method would be to normalize to a standard direction, nadir for example, by typically considering homogeneous covers since global coverage of canopy geometries might not be readily available. This could lead to misinterpretation of temperature retrievals (hence water statuses) in heterogeneous (non-continuous) surfaces. Furthermore, the fact that the source of latent and sensible heat depends on interaction of eddies with the multiple individual elements of the canopy and thus their own skin temperatures (which are diversely observed by remote sensors), necessitates the discrimination of surface components according to their illumination or exposure to the sun. This would help achieve a better representation of the exchange dynamics and interactions at the aerodynamic level.

Directionality context and study aims

The current work is undertaken in the context of the newly proposed Thermal infRared Imaging Satellite for High resolution Natural resource Assessment (TRISHNA) mission, which is expected to be launched in the coming years. The TRISHNA mission, which was instituted by the French (CNES) and Indian (ISRO) Space Agencies, is expected to provide global LST (in addition to optical data) products with a revisit time of ~3 days with a high spatial resolution (~57m at nadir) and relatively wide field-of-view (±~34°) (Lagouarde et al., 2019) enabling multi-scale monitoring of the water and energy budgets. Further improvement of the temporal revisits is separately expected by combining acquisitions from the different missions that are flying today and scheduled in the next

future (e.g. the European Space Agency/Copernicus Land Surface Temperature Mission – LSTM (which will use two satellites), the NASA ECOSTRESS, the NASA Surface Biology and Geology mission SBG). To achieve these temporal and spatial scales, it is anticipated that the surface thermal infrared acquisitions from most of the TIR-oriented missions will be from different viewing angles (see Figure 2, where a combination of the TRISHNA, LSTM and SBG observations allow a near-total daily coverage of earth sites located at varying latitudes). Directional effects can however impact the accuracy of surface state variables inferred from such thermal data.

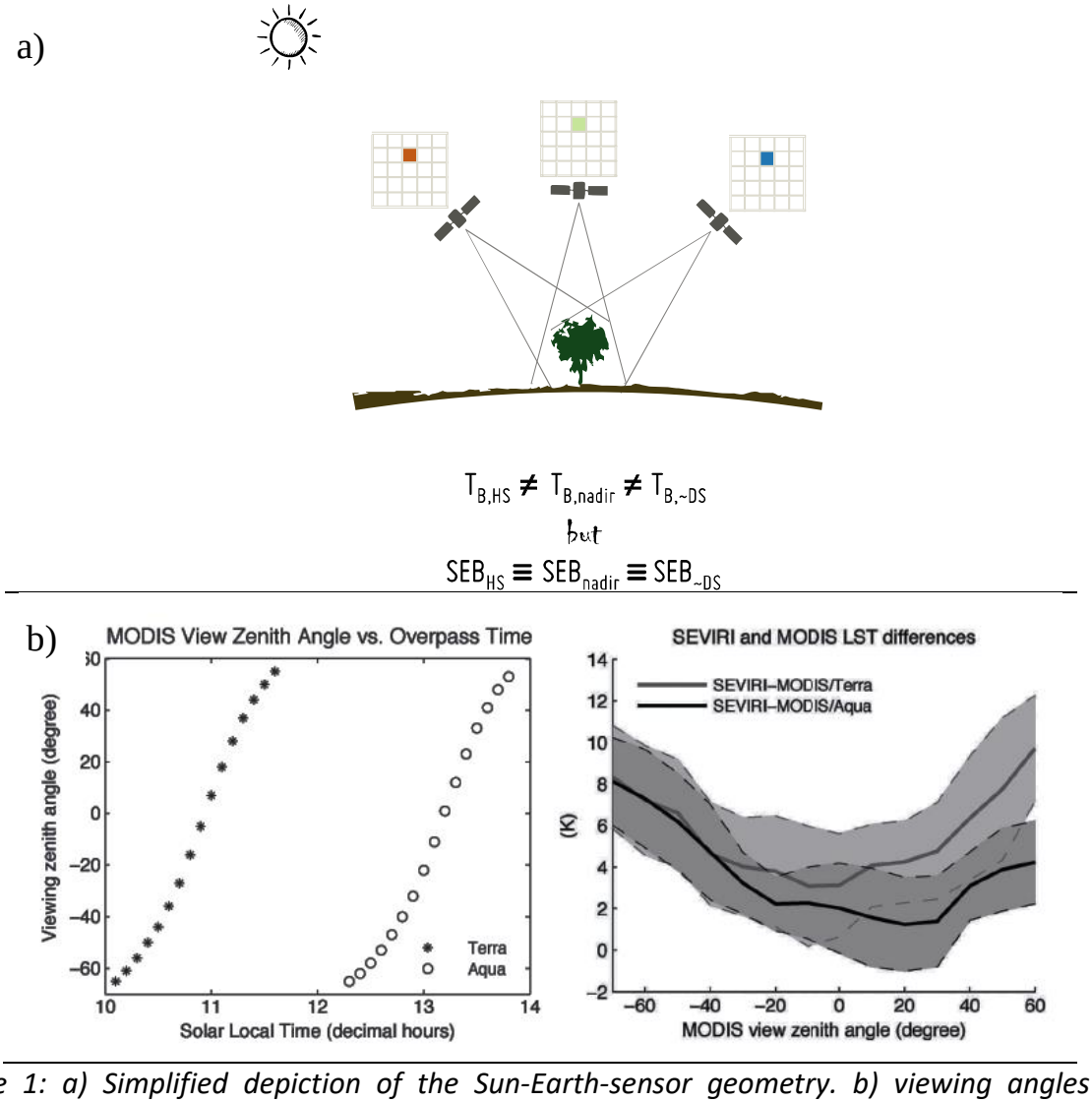

Figure 1: a) Simplified depiction of the Sun-Earth-sensor geometry. b) viewing angles and directionality influences as illustrated in thermal acquisitions by the MODIS sensors (aboard the Aqua and Terra satellites) and the SEVIRI instrument aboard the MSG over a site in Evora, Portugal (from Guillevic et al. (2013) - Figures 2 and 4).

The impact of directional anisotropy on thermal infrared observations has been demonstrated in the literature, which range from observations carried out in-situ (Kimes & Kirchner, 1983; Lagouarde & Irvine, 2008) as well as in satellite based (Guillevic et al., 2013) data. In Guillevic et al. (2013), the directionality effects on LST from the MODIS sensor (aboard the Aqua and Terra satellites) and the SEVIRI instrument on board the Meteosat Second Generation (MSG) satellite were documented. The view angle dependency of LST EO acquisitions leading to differences in MODIS versus SEVIRI LSTs was also reported in Trigo et al. (2008). Unlike the MSG geostationary satellite where the thermal acquisitions for a specific earth target are observed from the same viewing angle, the Aqua and Terra polar orbiters provide such observations from varying angles. As depicted in Guillevic et al. (2013), this generally results in variations in the proportion of illuminated and shaded elements in the sensor's field of view. As such, differences between the polar and geostationary acquisitions can reach upto 12 K (Figure 1b, Guillevic et al., 2013).

Figure 2 illustrates several simulations that were performed to check the likelihood of directionality influences of the TRISHNA, LSTM and SBG satellite orbits while overpassing three selected sites (Lonzée, Belgium - 50.552 N, 4.746 E; Grosseto, Italy - 42.82 N, 11.07 E; Wankama, Niger - 13.645 N, 2.630 E). Given the mission-specific scan angles and the achievable maximum sun angles for different locations on Earth, it is evident that the occurrence of the hotspot phenomena can only largely be expected close to the tropics. This can be seen in the sun path diagrams (Figure 2 – to ease interpretation, refer to section 3.1.4) depicting the possible view [elevation] angles in 2025 for the three sites, e.g. more likelihood of occurrence in Wankama, Niger from April to September. Note that the view zenith angles are generally uniformly distributed throughout the simulated period (see histogram in Figure 43). Nonetheless, since directional anisotropy entails more than the hotspot, directional effects may still present themselves depending on the surface characteristics coupled with the Sun-Earth-sensor geometries.

a)

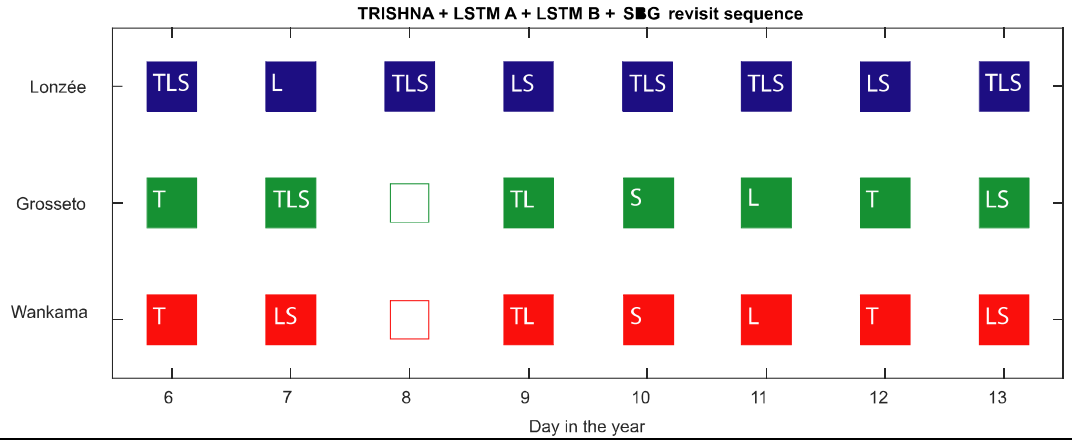

b)

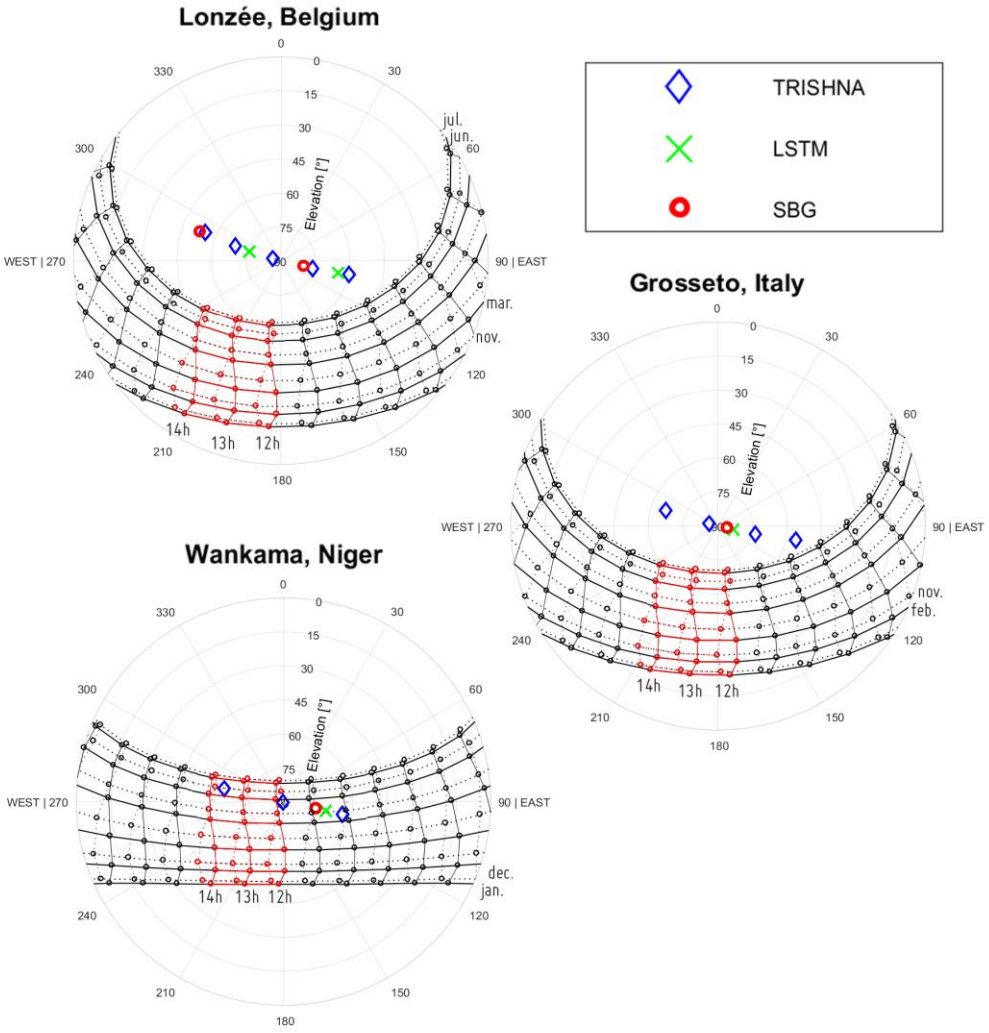

Figure 2: a) Revisits over an 8-day sequence based on a combination of three thermal infrared Earth observation missions (i.e., TRISHNA, LSTM, SBG – abbreviated T, L, S, respectively) over sites located in three latitudes (adapted from Olioso et al. (2022)). b) Sun path diagrams with the likely satellite view angles in 2025 over the three sites (date lines run from bottom-up [solid, jan-jun] and top-bottom [dotted, jul-dec]; the hour lines from right/east to left/west - see section 3.1.4)

This work seeks to investigate and understand how directional anisotropy / thermal radiation directionality influences estimation of turbulent flux. Various variables that describe the near land surface mass and energy exchanges (such as, radiation, atmospheric and canopy/surface characteristics) variously affect thermal directionality. Altogether, these variations could be expected to affect the component retrievals in energy balance methods that use directional surface temperature as the primary water status proxy. A surface energy model – the Soil Plant Atmosphere Remote Sensing of Evapotranspiration (SPARSE, Boulet et al., 2015) – is therefore extended to account for directionality issues. This is achieved by initially modifying the SEB scheme and coupling it with a directional radiative transfer model (herein the Unified François Model (Bian et al., 2018)). The methods are then tested using data from contrasting environments as well as synthetically set up datasets. The results are then interpreted in the context of surface, and thus plant water usage, i.e. through evapotranspiration. We further use synthetic datasets to preliminarily investigate and thus understand the influence of thermal directionality (considering standard orbit geometries of standardized sun-synchronous satellites) on the temperature – fraction cover feature space as used in contextual evapotranspiration modelling.

The write-up is structured as follows: the second chapter reviews the current state of the art in terms of turbulent flux modelling, i.e. hydrological models for evapotranspiration estimation - surface energy balance schemes or otherwise. In the third chapter, we describe the methods used in this study in more detail. That is, the energy balance as well as radiative transfer methods. The datasets used in assessments and the evaluations are then described in the following chapters; this includes the instruments used in the field campaigns as well as the quality of the measurements. The presentation of the results and their interpretation is done in the subsequent sections within the chapters. Any data processing and analysis methods applied on the datasets are also reported within the sections. The conclusions are finally drawn with a mention of the summarised limitations of the study as well as perspectives for future works.

1.1. Introduction générale

L'eau c'est la vie. La subsistance de la population mondiale dépend en grande partie de la bonne utilisation des ressources en eau terrestres. Les effets du changement climatique ont toutefois dégradé ces ressources, les récoltes étant menacées par des sécheresses extrêmes de plus en plus fréquentes dans de nombreuses régions du monde, notamment dans les terres arides et semi-arides (ASAL). Cette situation a fait de l'utilisation efficace de l'eau une question politique clé (c'est-à-dire comment répartir les ressources en eau rares entre les points de demande essentiels tels que l'agriculture / l'irrigation, l'utilisation domestique, la production d'énergie / électricité, etc.). En ce qui concerne l'utilisation de l'eau à des fins agricoles (qui représente généralement environ 70 - >80 % de l'utilisation de l'eau dans les ASALs), il est devenu important de rechercher une productivité alimentaire maximale tout en garantissant une perte d'eau minimale. L'utilisation la plus productive dans ce cas se traduit par l'utilisation d'eau pour une croissance optimale des plantes (par transpiration - T) avec le moins possible de pertes par évaporation du sol (E). En pratique, cela nécessite l'application de méthodes hydrologiques capables d'estimer raisonnablement l'évapotranspiration (ET) et ses composantes (l'évaporation et la transpiration), et donc l'utilisation de l'eau par les plantes, sur la base des flux d'eau et d'énergie disponibles (Boulet et al., 2018; Mallick et al., 2016). La mesure des flux d'eau et d'énergie de surface (et donc de l'ET) peut être réalisée avec une précision raisonnable. Cependant, les observatoires de flux in-situ ont une couverture spatiale limitée et ne peuvent pas être appliquées de manière efficace et peu coûteuse pour déterminer les besoins en eau aux échelles requises (par exemple, à l'échelle régionale). La régionalisation des mesures provenant de plusieurs sites expérimentaux est également sujette à de incertitudes d'interpolation. L'ET réelle peut également être quantifiée (même prédit ou prévu) en appliquant des modèles qui estiment les bilans énergétiques et hydriques de surface. Par exemple, l'ET peut être simulée directement par la modélisation de la surface terrestre, où la demande atmosphérique et l'humidité du sol qui devrait être disponible pour la végétation et pour les pertes par évaporation du sol sont estimées, ou - indirectement - en utilisant des variables étroitement liées à l'état des eaux de surface (c'est-à-dire des variables qui peuvent décrire la disponibilité/le stress hydrique).

Plusieurs méthodes d'évapotranspiration ont déjà été proposées et opérationnalisées, que ce soit par des autorités régionales ou des entreprises agricoles, pour aider à la planification de l'irrigation et ainsi optimiser l'utilisation de l'eau agricole. Parmi celles-ci, l'approche relativement courante est l'utilisation de méthodes de bilan énergétique de surface (SEB) qui aident à partitionner l'énergie disponible variant dans l'espace et dans le temps en flux d'eau et flux sensibles. Pour ces méthodes, la température de la surface est une variable d'entrée clé. Il a été démontré que la température de surface est étroitement liée à l'état des eaux terrestres (surfaces bien arrosées à stressées par l'eau). L'évapotranspiration est le moyen le plus efficace de dissiper le rayonnement entrant ; une surface humide aura donc une température plus basse, avec une conversion en flux de chaleur sensible (donc une augmentation de la différence de température entre le sol et l'air) à mesure que la surface sèche. La température de surface peut donc être utilisée pour la détection précoce du stress hydrique des plantes dans le but d'éviter une perte permanente des cultures due à un manque d'eau. Elle peut être mesurée soit in situ, soit à distance à l'aide de thermoradiomètres, qui détectent généralement les signaux de rayonnement électromagnétique dans le gamme spectrale de l'infrarouge thermique de 8 à 14 µm. L'utilisation de capteurs thermiques in situ peut fournir des observations en temps quasi réel ; néanmoins, elles sont généralement à l'échelle d'un point et donc limitées dans l'espace. D'autre part, les acquisitions de capteurs thermiques à distance spatiaux ont des résolutions temporelles relativement faibles mais peuvent couvrir de grandes échelles spatiales, ce qui peut être préférable pour la prise de décision régionale. Les acquisitions réalisées par les satellites varient dans leurs résolutions spatiales, spectrales et radiométriques en fonction des critères de conception choisis, c'est-à-dire l'altitude du satellite et l'orientation globale de l'orbite, les spécifications des capteurs thermiques, etc. L'utilisation du rayonnement observé par satellite doit donc être interprétée en fonction de ses caractéristiques spectrales et directionnelles. Par exemple, il faut s'assurer que les outils (y compris ceux appliqués à la normalisation thermique du signal de rayonnement pour tenir compte de la directionnalité) utilisés dans leur interprétation tiennent compte de divers aspects propres aux capteurs et à la surface qui, s'ils ne sont pas pris en compte, peuvent conduire à une compréhension inadéquate des conditions à la surface terrestre.

Alors que les efforts ont surtout porté sur la résolution des problèmes liés aux données manquantes et/ou aux résolutions spatiales et temporelles inadéquates (par exemple, en appliquant des méthodes pour combler les lacunes, des techniques de fusion de données, en proposant des missions avec des temps de revisite et des résolutions spatiales améliorés, en appliquant des techniques de désagrégation, etc.), on s'est peu intéressé à la façon dont la directionnalité du rayonnement thermique (TRD) influence la récupération du flux. Le TRD peut être défini comme l'anisotropie thermique qui résulte de la position du capteur par rapport au soleil en combinaison avec la géométrie des composants de la cible observée (c'est-à-dire la végétation et les composants du sol à la surface de la terre). Par exemple (Figure 1), un capteur observant depuis la direction du soleil (hotspot, c'est-à-dire dans la configuration syzygy Soleil-satellite-Terre) verra généralement des éléments terrestres éclairés par le soleil par rapport à un capteur observant depuis le nadir (ou d'autres directions), qui voient des éléments moins éclairés. La géométrie du terrain affectera également les acquisitions puisque la structure et l'homogénéité de la canopée, ou son absence, influenceront les signaux d'émission thermique observés ; par exemple, dans les cultures en rangées, l'émission mesurée sera influencée par le fait que le capteur soit aligné le long ou en travers de la rangée. En ce qui concerne la normalisation de la température de surface, une méthode générale serait de normaliser à une direction standard, le nadir par exemple, en considérant typiquement des couvertures homogènes puisque la couverture globale des géométries de la canopée pourrait ne pas être facilement disponible. Cela pourrait conduire à une mauvaise interprétation des récupérations de température (donc des états de l'eau) dans des surfaces hétérogènes (non continues). De plus, le fait que la source de chaleur latente et sensible dépende de l'interaction des tourbillons avec les multiples éléments individuels de la canopée et donc de leurs propres températures de peau (qui sont diversement observées par les capteurs à distance), nécessite la discrimination des composants de surface selon leur illumination ou leur exposition au soleil. Cela permettrait d'obtenir une meilleure représentation de la dynamique des échanges et des interactions au niveau aérodynamique.

Contexte de la directionalité et objectifs de l'étude

Les travaux actuels sont entrepris dans le cadre de la nouvelle mission TRISHNA

(Thermal infraRed Imaging Satellite for High resolution Natural resource Assessment), dont le lancement est prévu dans les prochaines années. La mission TRISHNA, qui a été instituée par les agences spatiales française (CNES) et indienne (ISRO), devrait fournir des produits LST mondiaux (en plus des données optiques) avec un temps de revisite d'environ 3 jours, avec une haute résolution spatiale (~57m au nadir) et un champ de vision relativement large (±34°) (Lagouarde et al., 2019) permettant un suivi multi-échelle des bilans hydriques et énergétiques. Une amélioration supplémentaire des révisions temporelles est attendue séparément en combinant les acquisitions des différentes missions qui volent aujourd'hui et qui sont prévus dans le futur (par exemple, la mission LSTM (Land Surface Temperature Mission) de l'Agence spatiale européenne/Copernicus (qui utilisera deux satellites), la mission ECOSTRESS de la NASA, la mission SBG (Surface Biology and Geology mission) de la NASA). Pour atteindre ces échelles temporelles et spatiales, il est prévu que les acquisitions dans l'infrarouge thermique de surface de la plupart des missions orientées TIR soient faites à partir de différents angles de vue (voir la Figure 2, où la combinaison des observations de TRISHNA, LSTM et SBG permet une couverture quotidienne quasi-totale des sites terrestres situés à différentes latitudes). Les effets directionnels peuvent cependant avoir un impact sur la précision des variables d'état de surface déduites de ces données thermiques.

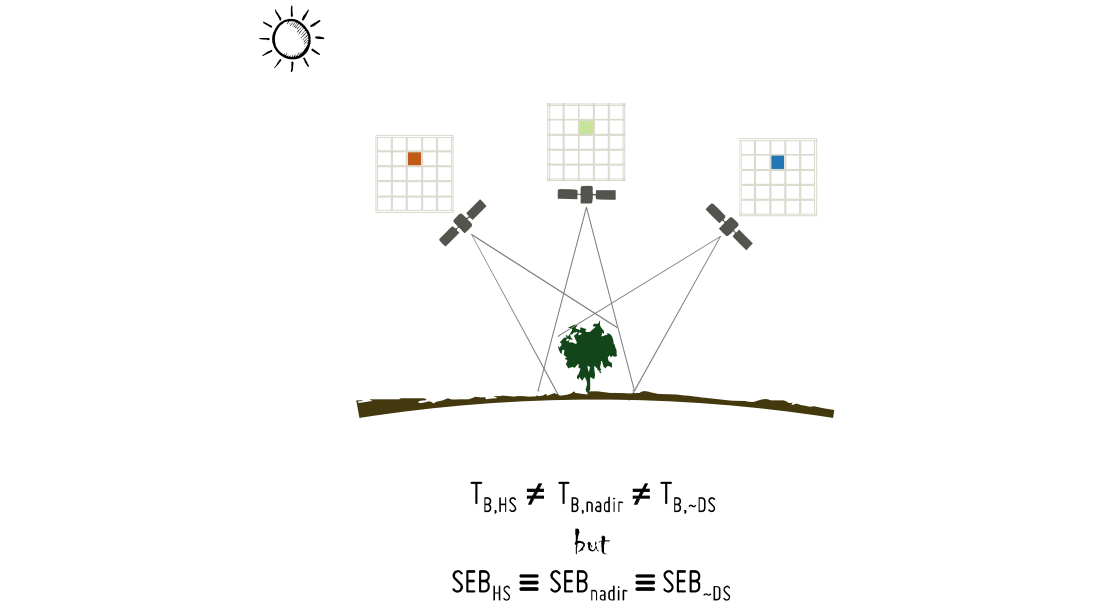

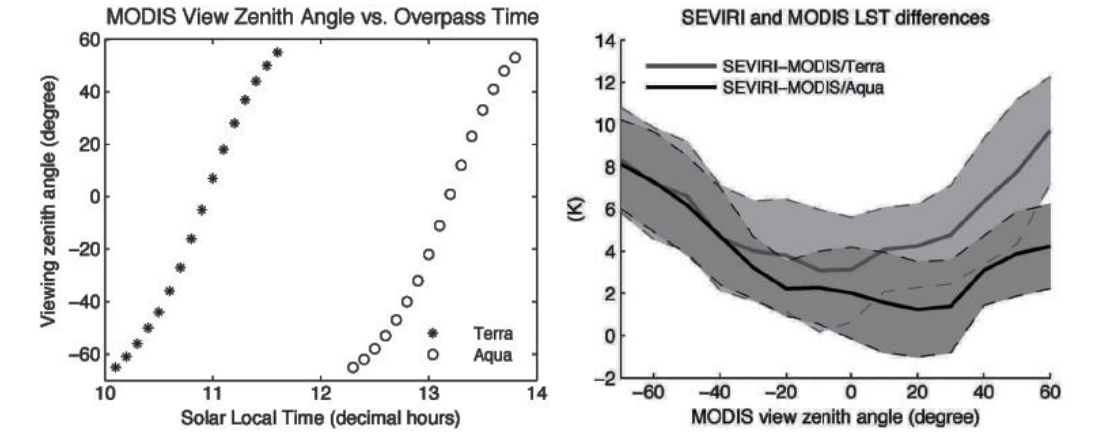

Figure 1 : La représentation simplifiée de la géométrie soleil-terre-capteur. b) les angles de vue et les influences de la directionnalité telles qu'illustrées dans les acquisitions thermiques par les capteurs MODIS (à bord des satellites Aqua et Terra) et l'instrument SEVIRI à bord du MSG sur un site à Evora, Portugal (de Guillevic et al. (2013) - Figures 2 et 4).

L'impact de l'anisotropie directionnelle sur les observations en infrarouge thermique a été démontré dans la littérature, qui va des observations réalisées in-situ (Kimes & Kirchner, 1983; Lagouarde & Irvine, 2008) aux données satellitaires (Guillevic et al., 2013). Dans Guillevic et al. (2013), les effets de directionnalité sur la LST du capteur MODIS (à bord des satellites Aqua et Terra) et de l'instrument SEVIRI à bord du satellite Meteosat Second Generation (MSG) ont été documentés. La dépendance de l'angle de vue des acquisitions LST conduisant à des différences entre les LST MODIS et SEVIRI a

également été rapportée dans Trigo et al. (2008). Contrairement au satellite géostationnaire MSG où les acquisitions thermiques pour une cible terrestre spécifique sont généralement observées à partir du même angle de vue, les orbiteurs polaires Aqua et Terra fournissent de telles observations à partir d'angles variables. Comme le montrent Guillevic et al. (2013), cela se traduit généralement par des variations de la proportion d'éléments éclairés et ombragés dans le champ de vision du capteur. Ainsi, les différences entre les acquisitions polaires et géostationnaires peuvent atteindre jusqu'à 12 K.

La Figure 2 illustre plusieurs simulations effectuées pour vérifier la probabilité d'influence de la directionnalité des orbites des satellites TRISHNA, LSTM et SBG lors du survol de trois sites sélectionnés (Lonzée, Belgique - 50,552 N, 4,746 E ; Grosseto, Italie - 42,82 N, 11,07 E ; Wankama, Niger - 13,645 N, 2,630 E). Compte tenu des angles de balayage spécifiques à la mission et des angles solaires maximaux réalisables pour différents endroits de la planète, il est évident que l'apparition des phénomènes de points chauds ne peut être attendue que près des tropiques. Cela peut être observé dans les diagrammes de la course du soleil (Figure 2 - pour faciliter l'interprétation, se référer à la section 3.1.4) décrivant les angles de vue [élévation] possibles en 2025 pour les trois sites, par exemple, une plus grande probabilité d'occurrence à Wankama, Niger d'avril à septembre. Néanmoins, étant donné que l'anisotropie de la directionnalité ne se limite pas au hotspot, les effets directionnels peuvent toujours se manifester en fonction des caractéristiques de la surface et de la géométrie des capteurs soleil-terre.

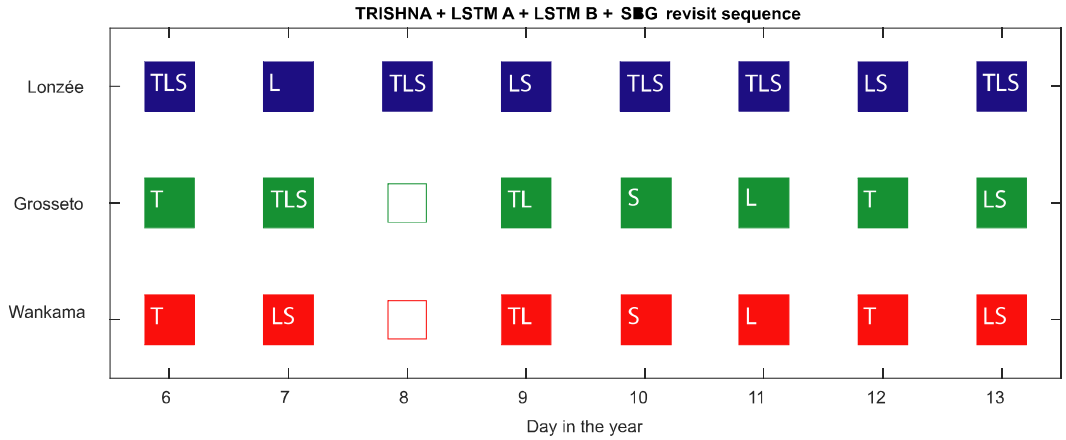

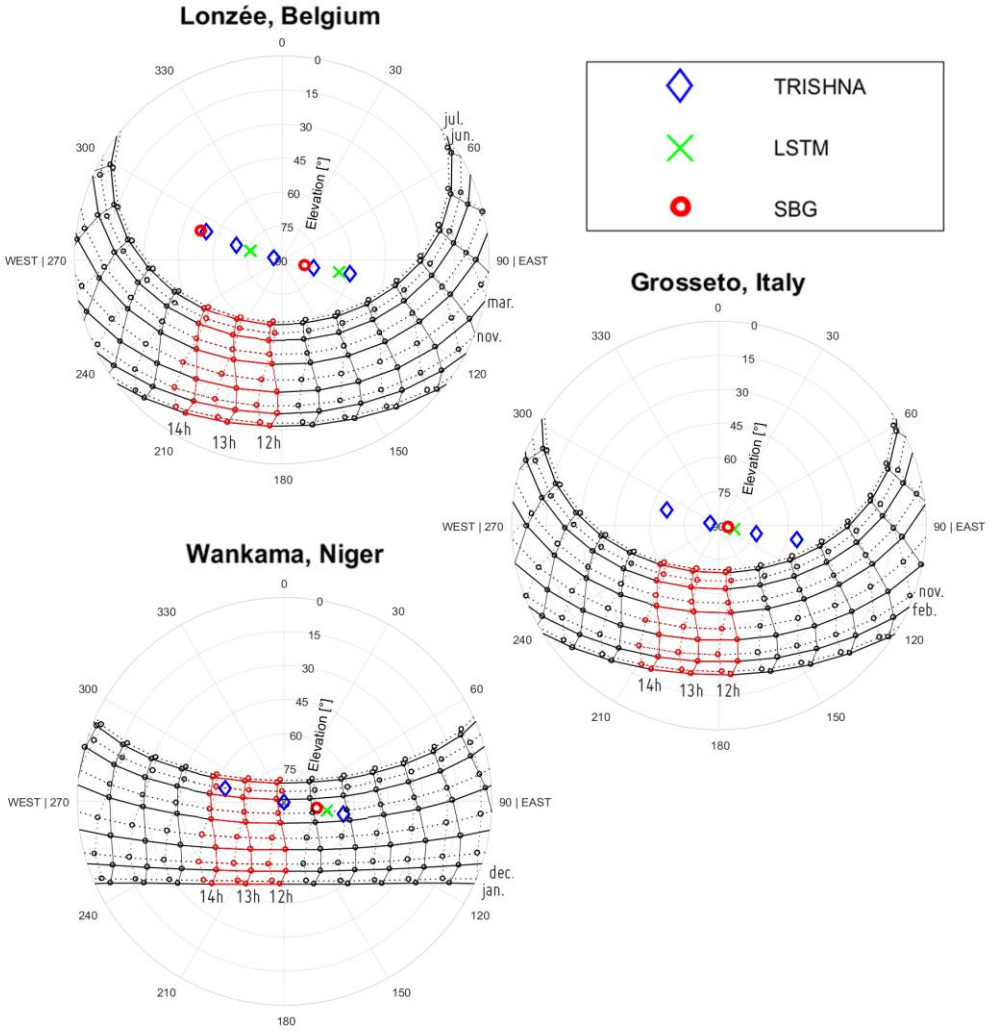

Figure 2 a) Revisites sur une séquence de 8 jours basée sur la combinaison de trois missions d'observation terrestre en infrarouge thermique (TRISHNA, LSTM, SBG - abrégé T, L, S, respectivement) sur des sites situés à trois latitudes (adapté de Olioso et al. (2022)); b) Diagrammes de la course du soleil (les lignes de date vont de bas en haut [solide, jan-juin] et de haut en bas [pointillé, juillet-déc] ; les lignes d'heure de droite/est à gauche/ouest - voir section 3.1.4) avec les angles de vue probables du satellite en 2025

Ce travail vise à étudier et à comprendre comment l'anisotropie directionnelle / la directionnalité du rayonnement thermique influence l'estimation du flux turbulent. Diverses variables qui décrivent les échanges de masse et d'énergie à proximité de la surface terrestre (telles que le rayonnement, les facteurs atmosphériques et celles de la canopée et de la surface) affectent diversement la directionnalité thermique. Dans l'ensemble, on peut s'attendre à ce que ces variations affectent la récupération des composantes dans les méthodes de bilan énergétique qui utilisent la température de surface directionnelle comme principal indicateur de l'état de l'eau. Un modèle d'énergie de surface - le Soil Plant Atmosphere Remote Sensing of Evapotranspiration (SPARSE, Boulet et al., 2015) – est donc étendu pour tenir compte des problèmes de directionnalité. Ceci est réalisé en modifiant initialement le schéma SEB et en le couplant avec un modèle de transfert radiatif directionnel (ici le Modèle François Unifié (Bian et al., 2018)). Les méthodes sont ensuite testées en utilisant des données provenant d'environnements contrastés ainsi que des ensembles de données synthétiques. Les résultats sont ensuite interprétés dans le contexte de l'utilisation de l'eau en surface, et donc par les plantes, c'est-à-dire par évapotranspiration. Nous utilisons également des ensembles de données synthétiques pour étudier et ainsi comprendre l'influence de la directionnalité thermique (en considérant les géométries d'orbite standard des satellites héliosynchrones standardisés) sur l'espace caractéristique température - fraction de couverture utilisé dans la modélisation contextuelle de l'évapotranspiration.

La rédaction est structurée comme suit : le deuxième chapitre passe en revue l'état actuel de l'art en termes de modélisation des flux turbulents, c'est-à-dire les modèles hydrologiques pour l'estimation de l'évapotranspiration - les schémas de bilan d'énergie de surface ou autres. Dans le troisième chapitre, nous décrivons plus en détail les méthodes utilisées dans cette étude. C'est-à-dire, le bilan énergétique ainsi que les méthodes de transfert radiatif. Les ensembles de données utilisés dans les évaluations et les analyses sont ensuite décrits dans les chapitres suivants ; cela inclut les instruments utilisés dans les campagnes de terrain ainsi que la qualité des mesures. La présentation des résultats et leur interprétation est faite dans les sections suivantes dans les chapitres. Toutes les méthodes de traitement et d'analyse des données appliquées aux ensembles de données sont également mentionnées dans les chapitres/sections.

Les conclusions sont enfin tirées avec une mention des limites résumées de l'étude ainsi que des perspectives pour les travaux futurs.

Chapter 2: State of the art in observation and modelling of the soil-plant-atmosphere continuum: concepts and definition of terms

In this Chapter, the theoretical and modelling framework used in the characterization of the water and energy processes in the land surface are described. That is,

- *Definition of some fundamental electromagnetic radiation concepts and how they apply to earth observation and modeling of terrestrial processes*
- *A description of the surface energy processes and a brief literature review on their physical modeling follow*
- *Concludes with a summary of the methods used to describe angular anisotropy [thermal radiation directionality]*

Ce chapitre décrit la théorie et le cadre scientifiques utilisés pour la caractérisation des processus de transfert d'eau et d'énergie à la surface de la Terre. A savoir,

- *Définition de certains concepts fondamentaux du rayonnement électromagnétique et comment ils s'appliquent à l'observation de la Terre et la modélisation des processus terrestres*
- *Suit une description des processus énergétiques de surface et une brève revue de la littérature sur leur modélisation physique*
- *Conclut par un résumé des méthodes utilisées pour décrire l'anisotropie angulaire [directionnalité du rayonnement thermique]*

Notations

α_{surf}	Surface albedo [-]
Δ	Slope of the vapor pressure-temperature curve at T_a [Pa K^{-1}]
$\tau_{atm}, \alpha_{atm}, \rho_{atm}$; ε_a	Atmosphere's transmissivity, absorptance and scattering/reflectance, respectively [-]; apparent emissivity of the atmosphere [-]
$\varepsilon_g, \varepsilon_v, \varepsilon_{sf}$	Emissivity of the soil, vegetation and entire surface, respectively [-]
Λ	Evaporative fraction [-]
γ	Psychrometric constant [Pa K^{-1}]

$\omega_{\omega,s}(\theta_v), \omega_{\omega,h}(\theta_v)$	Effective emissivity of sunlit and shaded leaves, respectively [-]
$\phi_{j=i,v}$	Solar (i) and viewing (v) azimuth angles [°]
Φ ; E_0	Relative azimuth angle between solar and viewing directions [°]; eccentricity correction factor [-]
ρC_p	Product of air density [kg m^{-3}] and the specific heat of air at constant pressure [J kg^{-1} K^{-1}]
$b(\theta_v)$	The upward directional canopy transmittance / gap frequency/fraction in viewing direction [-]
$\theta_{j=i,v}$; μ_j	Solar (i) and viewing (v) zenith angles; cosine of the zenith angle j [°]
ξ; K	Fraction of soil/ground net radiation stored in the soil, i.e., $\xi = G/R_{ng}$ [-]; soil heat conductivity in G estimation via Fourier's law [$W m^{-1}K^{-1}$]
B[.]	Blackbody radiance (Planck's law)
e_a, e_0	Air vapor pressure at the reference and aerodynamic levels [Pa].
G, H, λE	Ground, sensible and latent heat fluxes [W m^{-2}]
h, σ, λ	Planck's constant [J s], Stefan Boltzmann constant [W m^{-2} K^{-4}], wavelength [μm]
$L(\theta_v), L_a^{\downarrow}$	Out-of-canopy radiance in the viewing direction and incoming sky radiance [W m^{-2}]
LAI, σ, Ω	Leaf area index [m^2 m^{-2}], foliage projection factor [-] and clumping index [-]
r_a ; Ψ_h, Ψ_m	Aerodynamic resistance between the aerodynamic and reference levels [s m^{-1}]; stability correction functions for heat and momentum transport, respectively
$RG_{dir}, RG_{diff}, RG, C_s$	Direct, diffuse, total/global (BOA) and terrestrial (TOA, i.e., solar constant) solar irradiance [W m^{-2}]
R_n	Total (overall) net radiation [W m^{-2}]
$S^{\downarrow}, L^{\downarrow}, S^{\uparrow}, L^{\uparrow}$	Short- and long-wave irradiance and radiance, respectively
T_a, T_0, T_{xx}	Air, aerodynamic and component temperatures [K]
$Z; Z_{0h}, Z_{0m}$	Height [m], roughness lengths of heat, and momentum transfer.

2.1. Definitions: radiative and energy budget terms

Earth observation of the energy, water and carbon cycles at the near-land surface involves the monitoring of electromagnetic (EM) radiation signals (whether active or passive) of the terrestrial surface. Natural resources practitioners are therefore ideally interested in specific EM spectral ranges that are most appropriate to the study of specific earth processes. That is (list is non-exhaustive);

- Cosmic rays - for example the cosmic-ray neutron sensing technique used in the monitoring of soil moisture at intermediate spatial scale (Zreda et al., 2008)
- The optical (visible, near and short-wave infrared) spectral bands – for monitoring of vegetation (e.g. *NDVI - Normalized Difference Vegetation Index,* (Rouse et al., 1973); *NDWI - vegetation Water Index*, (Gao, 1996)), water bodies (e.g. *NDWI - open water surface,* (McFeeters, 1996)), etc.
- Thermal infrared for land and sea surface temperature monitoring (Norman & Becker, 1995)
- Active / passive microwave radiation signals that are well suited for, among others, geological mapping (e.g. volcanic unrest detection (Fernández et al., 2021)), monitoring of biomass and soil moisture & freeze-thaw (Kerr et al., 2001; Lv, et al., 2022; Njoku & Entekhabi, 1996; Rautiainen et al., 2014).

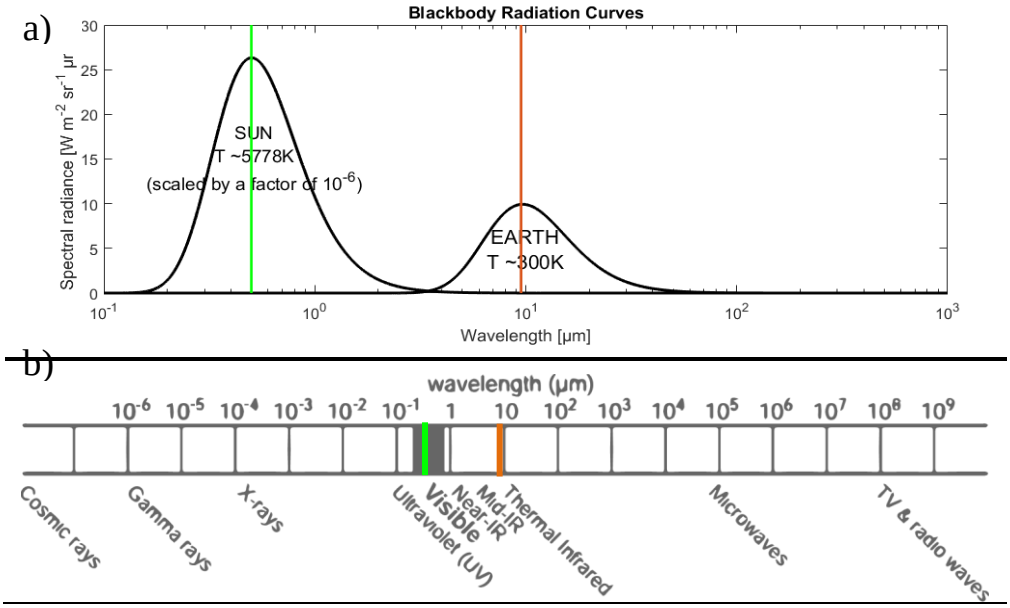

Figure 3: a) The Sun (rescaled) and Earth blackbody radiation curves and, b) the electromagnetic spectrum (EMS, adapted from Tolpekin and Stein (2012))

In the physical description of terrestrial processes, the radiation integrated over the whole EM spectrum is understood to control the energy and mass balance. As such, emissions from the Sun and by the Earth surface (Figure 3) serve as important inputs in surface energy balance (SEB) methods that model the hydrological and energy cycles.

2.1.1. Net radiation

Net radiation is the surface energy that drives terrestrial processes. It is dissipated (mainly during the day) as latent heat energy, sensible heat, soil heat conduction, among others. The overall surface net radiation is given by (see Figure 4),

$$R_n = S^{\downarrow} - S^{\uparrow} + L^{\downarrow} - L^{\uparrow} = (1 - \alpha_{surf})S^{\downarrow} - \left(\sigma T_{surf}^4 - \varepsilon_{surf} L^{\downarrow}\right) \qquad [W\ m^{-2}] \qquad (2.1)$$

$S^{\downarrow}$ and $S^{\uparrow}$ are the incoming (down welling) and outgoing (up welling) short wave radiations, respectively. Similarly, $L^{\downarrow}$ and $L^{\uparrow}$ are the incoming and outgoing long wave (thermal) radiations. α_{surf} and ε_{surf} are the Earth surface albedo and emissivity, respectively. Note that incoming and outgoing radiations are - respectively - also interchangeably termed irradiance and radiance.

A theoretical black body at a temperature T emits at all wavelengths following Planck's law, $S|L_{\lambda,T} = B_{\lambda}[T] = \frac{2hc^2}{\lambda^5\left(e^{hc/\lambda kT}-1\right)}$ $[W\ m^{-2} sr^{-1} \mu m^{-1}]$, which integrates thusly:

$$B[T] = \int_0^{\infty} B_{\lambda}[T] d\lambda \int \cos\theta\, d\Omega = \sigma T^4 \qquad [W\ m^{-2}] \qquad (2.2)$$

where $B_{\lambda}[.]$ is the wavelength-dependent blackbody function (Planck's); the function can be integrated throughout the spectral range and over the field or hemisphere of emission as $B[.]$, which is the Stefan Boltzmann (SB) law, σ is the SB constant. The integration over the hemisphere of emission is written $\int \cos\theta\, d\Omega = \int_0^{2\pi} d\varphi \int_0^{\pi/2} \cos\theta \sin\theta\, d\theta = 2\pi \cdot 1/2$; $\cos\theta$ here transforms the normal-plane radiant flux density (assumed to be isotropic) to the beam's direction according to Lambert's cosine law. θ, φ are the zenith and azimuth angles of the hemisphere. T is the [surface] radiative temperature.

Ideally, all terms in Equation (2.1) can be expressed using Equation (2.2) while taking into consideration the emissivity of the respective surface/body. For the radiation emitted from a real terrestrial body (Earth surface objects such as vegetation, soil, snow, etc.), the emissivity (which is derived according to Kirchhoff's energy conservation law, and realistically less than 1) is required in Equation (2.2); e.g., as used in Equation (2.1). Due to directional anisotropy of radiation fluxes, the directional radiation within points in the

hemisphere of emission will differ. As detailed in Norman and Becker (1995), where the thermal infrared spectral domain is mostly addressed, these anisotropy effects can be described by the Sun-Earth-sensor geometry and surface characteristics (i.e. surface roughness, canopy structure and water stress conditions).

Short- and long-wave irradiance and radiance

The ***incoming radiation*** components are the main energy sources that drive flux processes at the atmospheric boundary layer. These irradiances (***incoming shortwave and longwave*** radiations) are drawn from the Sun and the atmosphere, respectively. The dominant spectral wavelengths (wavelength of maximum radiation, $\lambda_{\max}$) of the irradiances, as well as that of the longwave radiance, are described by the Sun's surface, and Earth's atmosphere and surface temperatures (T) and can thus be inferred from Wien's displacement law,

$$\lambda_{\max}\,[\mu\mathrm{m}] = \frac{2898\,[\mu\mathrm{m}\cdot\mathrm{K}]}{\mathrm{T}\,[\mathrm{K}]} \qquad (2.3)$$

i.e. using average temperatures of the Sun's and Earth's surfaces, Wien's law yields the visible / optical $(2898 \div \sim 5778\,[\mu\mathrm{m}])$ and thermal infra-red $(2898 \div \sim 300\,[\mu\mathrm{m}])$ spectral ranges for the short- ($\mathrm{S}^{\downarrow}$) and long-wave ($\mathrm{L}^{\uparrow}$) radiation, respectively (Figure 1). Wien's radiation law, however, tends to fail at extremely low frequency experiments (Jammer, 1989).

Simply, the ***solar (or shortwave) irradiance*** at bottom of atmosphere (BOA) can be defined as the product of the extra-terrestrial irradiance at the top of atmosphere (TOA) and the atmosphere's transmissivity. The irradiance at TOA is described by the solar constant (i.e., $\mathrm{C_s} \approx 1361\,[\mathrm{W}\cdot\mathrm{m}^{-2}]$ or the electromagnetic radiation flux emitted by the Sun's surface as projected over Earth's TOA). $\mathrm{C_s}$ was first reasonably measured by *Claude Pouillet* (Dufresne, 2008), with recent more accurate measurements made using satellites orbiting above the Earth's atmosphere. Using this constant (and with the knowledge of the Sun's radius and its distance to Earth), the Sun's surface temperature as required when deriving the dominant solar radiation wavelength (Wien's displacement Eqn. (2.3)) could thus be estimated (i.e., through Equation (2.2)). The terrestrial solar irradiance (while considering Lambert's cosine law) can be written as:

$$S^{\downarrow} = C_s \mu_s E_0 \cdot \tau_{atm} \qquad [W\ m^{-2}] \tag{2.4}$$

where μ_s is the cosine of the solar zenith angle (θ_s); $E_0 = (r_0/r)^2 \approx f(da)$ is the eccentricity correction factor, which is the squared ratio of the mean Earth-Sun distance, r_0, to the distance at any instance of the year, r (Annear & Wells, 2007); this correction factor can be expressed as a function of the day angle (da), i.e. $E_0 = 1.00011 + 0.034221\cos(da) + 0.00128\sin(da) + 0.000719\cos(2da) + 0.000077\sin(2da)$; $da = 2 \cdot \pi \cdot (d_n - 1)/365$; d_n is the day number of the year. $\tau_{atm} = 1 - \alpha_{atm} - \rho_{atm}$ is the atmosphere's transmissivity, defined as the complement after accounting for any absorption (α_{atm}) and scattering/reflection (ρ_{atm}) by atmospheric compositions (e.g. gasses, water vapour, etc.). Simple parameterizations for the atmosphere's transmissivity have been proposed, e.g. $\tau_{atm} = 0.75 + 2 \cdot 10^{-5}(Z)$ as described in Allen et al. (1998) for clear-sky conditions; Z [m] being the elevation.

In equilibrium, absorptance and emittance at each wavelength are equal (Kirchhoff's law of thermal radiation (Tolpekin & Stein, 2012)). Part of the solar radiation and Earth emission is absorbed by and stored in the atmosphere; this is later emitted for the ***down-welling sky (longwave) radiation*** ($L^{\downarrow}$) while some is lost into space. In remote (space borne in particular) Earth observation, this lost atmospheric emission as well as any scattering in the observer direction need to be accounted for to achieve accurate surface emission (hence surface temperature) retrievals.

The ***upwelling radiation*** is essentially made of the ***reflected short-wave*** radiation ($S^{\uparrow} = \alpha_{surf} S^{\downarrow}$) and the ***reflected*** as well as the ***emitted long-wave*** radiation ($L^{\uparrow} = \varepsilon_{surf}\sigma T_{surf}^4 + \rho_{surf} L^{\downarrow} = \varepsilon_{surf}\sigma T_{surf}^4 + (1 - \varepsilon_{surf})L^{\downarrow}$). Considering the Earth surface to be opaque and ensuring energy conservation, some of the down-welling radiation is scattered or reflected back into the atmosphere. These reflected fluxes (integrated throughout the hemisphere of reflection – equivalent to hemisphere of emission term as defined in Equation (2.2)) are dependent on the surface characteristics; specifically, surface albedo (optical range) and reflectance (thermal range, assuming that Earth surface is an isothermal surface). Depending on the isotropy/anisotropy of the incident radiation and/or the surface roughness (Lambertian or non-Lambertian), the reflected radiation will either be specular or diffuse in nature, hence introducing directionality aspects (Norman &

Becker, 1995; Schaepman-Strub et al., 2006).

2.1.2. Energy conservation: available energy and turbulent fluxes

All the radiant energy that is available at the surface (Equation (2.1)) is dissipated in some form. In most natural Earth surfaces, some of the radiation flux is conducted in the soil. The remaining available energy is then used to drive other processes (i.e., as latent and sensible heat with some used for chemical and other processes). In vegetated surfaces, turbulent heat (latent and sensible) transfers are the dominant components, with chemical and other energy uses deemed negligible. It is also important to note that surface fluxes (sensible and soil heat transport) can contribute to the available energy - at night and sometimes during the day (e.g., advection of heat over wet surfaces).

For energy conservation, the available energy (AE) is thus expressed as:

$$AE = \mathrm{R_n} - \mathrm{G} = \mathrm{H} + \lambda\mathrm{E} \qquad [\mathrm{W\ m^{-2}}] \tag{2.5}$$

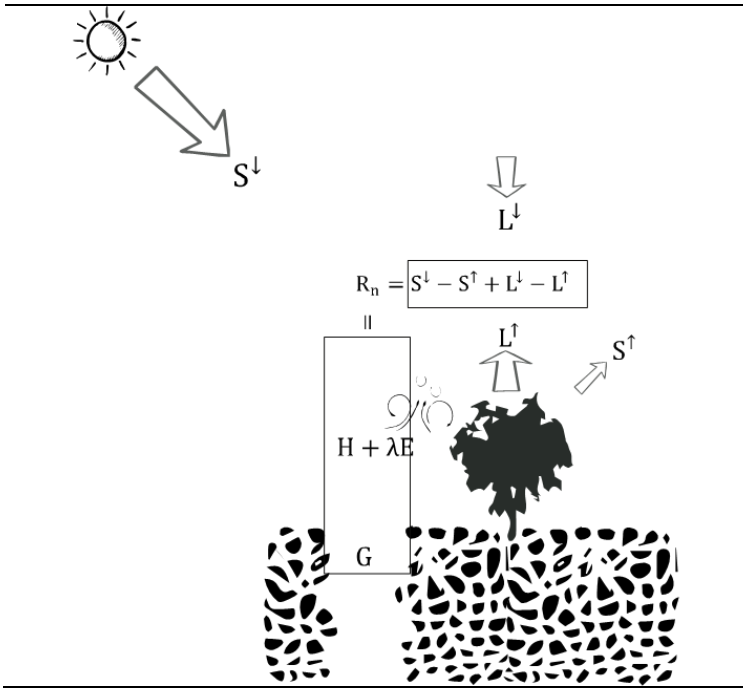

Figure 4: simple illustration of the radiative and energy balance of a natural terrestrial landscape

where:

$\mathbf{G}\ [\mathbf{W\ m^{-2}}]$ is the soil/ground heat flux. This is the heat flow in the land soil substrate. It results from energy transport in the soils, mainly through conduction and in some cases (e.g. very shallow soils) through radiation and convection (Sauer & Horton, 2015). Soil

heat flow, considered analogous to heat flow in solids, can theoretically be estimated through Fourier's law as $\mathrm{G} = -K\frac{\partial \mathrm{T}}{\partial \mathrm{Z}}$. Since it is described by the temperature gradient over the soil depth profile ($\frac{\partial \mathrm{T}}{\partial \mathrm{Z}}$), it is generally considered as positive during the day (energy is stored in the soil column) and negative at night (as energy lost from the soil). Other soil characteristics, including water content, influence soil heat storage through their contribution to the effective soil thermal conductivity term ($K\ [\mathrm{W\,m^{-1}K^{-1}}]$), i.e. the average of the thermal conductivities of the individual soil constituents, weighted by their respective volume fractions (also the series model). Models for K can however take different forms ranging from (Dong, McCartney, & Lu, 2015): *i)* mixing models (series, parallel, geometric, …), *ii)* empirical models that interpolate or scale the thermal conductivity depending on saturation states, porosity or soil type, and *iii)* mathematical models (e.g. de Vries (1963)) that are analogous to other predictive models and are based on phase volume fractions. Compared to the calorimetric estimation method (described in section 2.2.2.1 further below, which describes soil heat storage by modelling thermal transfer in terms of the soil characteristics/properties and temperature changes), the gradient method is more consistent with soil heating and cooling but is however very sensitive to the thermal conductivity term, K (Colaizzi, Evett, Agam, Schwartz, & Kustas, 2016). They, like other authors, therefore advocated for preference of the calorimetric method as it exhibits little sensitivity to input data. When modelling $\mathbf{G}$, both methods are nevertheless relevant and consequently applied as they describe the heat transfer in space and its variation in time.

In surface energy balance theory, it is however typical to express the soil storage term, $\mathbf{G}$**,** as a fraction of the radiation absorbed by the surface (i.e., fraction of the net radiation available to the soil or weighting between the soil and vegetation based on their respective cover fractions). For improved realism, the diurnal variations of this fraction are often considered (for example using Santanello and Friedl (2003) method - further described in section 3.2.2). The difficulty of estimating the infinitesimal temporal change in soil temperature required when modelling the soil heat transport when using sun-synchronous satellites gives further credence to the use of such a diurnal $\mathbf{G}$ to soil net radiation ratio.

$\mathbf{H}$ $[\mathbf{W\ m^{-2}}]$ is the sensible heat flux at the near-land surface. Heat transport between two surface levels results from free convection by temperature gradients and forced convection as driven by the horizontal wind profile (Parodi, 2000). Accordingly, sensible heat flux is primarily driven by the temperature status (of the surface and atmosphere) coupled with the turbulent mixing at the atmospheric boundary layer. H can be estimated by combining the aerodynamic surface and air temperatures and a resistance derived using the log-profile theory of heat and momentum transport. For instance, bulk equations based on the Monin-Obukhov Similarity Theory (MOST, Foken, 2006) have often been used to describe the turbulent transfer between the ground surface and the atmosphere (Zheng, Van Der Velde, Su, Booij, & Hoekstra, 2014):

$$\mathrm{H} = \rho \mathrm{C_p} \mathrm{C_h} \mathrm{u} (\mathrm{T_s} - \mathrm{T_a}) \qquad [\mathrm{W\ m^{-2}}] \tag{2.6}$$

where ρ is the air density, $\mathrm{C_p}$ the specific heat of air,

$\mathrm{C_h} = \frac{k^2}{\left(\ln\left(\frac{\mathrm{Z}-\mathrm{d_0}}{\mathrm{Z_{0m}}}\right) - \Psi_\mathrm{m}\left(\frac{\mathrm{Z}-\mathrm{d_0}}{\mathrm{L}}\right) + \Psi_\mathrm{m}\left(\frac{\mathrm{Z_{0m}}}{\mathrm{L}}\right)\right)\left(\ln\left(\frac{\mathrm{Z}-\mathrm{d_0}}{\mathrm{Z_{0h}}}\right) - \Psi_\mathrm{h}\left(\frac{\mathrm{Z}-\mathrm{d_0}}{\mathrm{L}}\right) + \Psi_\mathrm{h}\left(\frac{\mathrm{Z_{0h}}}{\mathrm{L}}\right)\right)}$ is the surface exchange coefficient for heat transfer and $\mathrm{u} = \frac{\mathrm{u_*}}{k}\left(\ln\left(\frac{\mathrm{Z}-\mathrm{d_0}}{\mathrm{Z_{0m}}}\right) - \Psi_\mathrm{m}\left(\frac{\mathrm{Z}-\mathrm{d_0}}{\mathrm{L}}\right) + \Psi_\mathrm{m}\left(\frac{\mathrm{Z_{0m}}}{\mathrm{L}}\right)\right)$ is the wind speed measured at Z described as a function of the u_* according to the MOST. u_* is the eddy or friction velocity defined as the square root of the ratio of surface stress to air density, k is the von Kármán constant, which according to different authors, can range from 0.35 to 0.43 (Foken, 2006) but often set to 0.41. Z is the observation height, $\mathrm{d_0}$ the zero-plane displacement height, $\mathrm{Z_{0m}}$ the roughness length of momentum transfer and $\mathrm{Z_{0h}}$ is the roughness length of heat transfer. Ψ_m and Ψ_h are the stability correction functions for momentum and heat transfer, respectively. Some examples of proposed stability functions for stable and unstable conditions in the atmospheric surface layer are described in Businger et al. (1971), Brutsaert (1999) and Su (2005). $\mathrm{L} = -\frac{\rho \mathrm{C_p} \mathrm{u_*^3} \mathrm{T_a}}{k \mathrm{g H}}$ is the Obukhov length, g the gravity acceleration.

To avoid the iterative solution in the MOST scheme above, the SPARSE SEB model (used in this study and described in Chapter 3) applies the Richardson number method.

$\boldsymbol{\lambda \mathbf{E}}$ $[\mathbf{W\ m^{-2}}]$ is the latent heat flux use/loss from evaporation of water, here a product of

the specific latent heat of vaporization of water ($\lambda \approx 2.26 \cdot 10^6$ [J Kg^{-1}]) and the evaporated water per unit time (E [Kg m^{-2} s^{-1}][mm s^{-1}]). It is constrained by the available radiation energy, the amount of water available at the surface as well as the prevailing meteorological conditions and atmospheric moisture demand (i.e., the vapour pressure deficit). By assuming all the other terms of the energy balance are known, the latent heat flux can be determined as the residual of the energy budget Equation (2.5).

Other terms (for example, energy used up in chemical and photosynthesis processes, heat input from precipitation and other sources/sinks) are usually neglected in the energy balance equation of the biosphere, especially in analyses involving the observed energy balance closure as well as in surface energy balance modelling. These are usually disregarded as they generally constitute low energy amounts (Lagouarde & Boulet, 2016).

Daily evapotranspiration, evaporative fraction and partitioning

In water resources management, temporally aggregated values of evapotranspiration (e.g. daily evapotranspiration) are more useful/relevant. The mass balance ET equivalent is thus,

$$\mathrm{ET} = \int_{t=0}^{t=86400} \mathrm{E}\,\mathrm{dt} \qquad [\mathrm{mm\ d^{-1}}] \tag{2.7}$$

t is time in [s]. Equation (2.7) integrates a time series of instantaneous values of λE [W m^{-2}] and cannot therefore be applied when only a few (often one in remote sensing of evapotranspiration) estimates are available. In such cases, the evaporative fraction has been applied. Evaporative fraction is the fraction of available energy ($\mathrm{R_n} - \mathrm{G}$) that is used for evaporation/transpiration;

$$\Lambda = {\lambda \mathrm{E}}/{(\mathrm{R_n} - \mathrm{G})} \qquad [-] \tag{2.8}$$

this ratio has often been assumed to remain constant throughout the day, especially around solar noon (i.e. $\Lambda_{\mathrm{instantaneous}} = \Lambda_{\mathrm{day}} = {\lambda \mathrm{E}_{day}}/{(\mathrm{R_{n,day}} - 0)}$; it is common to assume G aggregates to 0 throughout the day / night). It has nonetheless been observed that the evaporative fraction is generally not constant throughout the day (i.e. the Λ preservation

is mostly valid under dry conditions (Hoedjes et al., 2008)) leading to the proposal of more realistic aggregation techniques that are also dependent on atmospheric forcing and surface characteristics (Delogu et al., 2012). The latent heat to incoming solar radiation ratio has also been applied to scale evapotranspiration from instantaneous to daily values, e.g. as applied in the Sentinel for Evapotranspiration programme (SenET, Nieto et al., 2020).

In the biosphere, the total λE can be discriminated or partitioned between the soil evaporation losses and transpiration. The latter is water that is used up for adequate plant functioning and productivity. In agro-hydrology, optimal plant productivity signifies maximizing carbon gain while minimizing water loss, i.e., minimizing the temporally integrated sum of $T - \lambda A$ (Medlyn et al., 2011); T is the transpiration, λ here is the marginal water use efficiency defined as the marginal water cost per carbon gain and A the net carbon assimilation rate.

The components of the surface energy balance described above can be measured in-situ (through dedicated experimental sites), through Earth observation techniques or estimated using energy balance models. Techniques used in flux and ancillary data measurement are described in section 2.2 with modelling methods summarised further below.

2.2. Measurement theory and techniques

2.2.1. Meteorological variables and surface temperature

The interactions within the soil-vegetation-atmosphere continuum largely comprise of mass and energy exchanges (for example, the hydrological cycle). Estimating the water and energy transfer at the land surface therefore requires knowledge of the status of the atmosphere and vice versa. The status of the atmosphere is described by meteorological conditions, which include precipitation, air temperature and relative humidity, wind speed and direction, and incoming (solar, atmospheric) radiation. As mentioned earlier, surface/air temperatures and wind speed control the near-land surface heat and momentum transport through free and forced convection, respectively. Radiation controls the available energy while air humidity and precipitation (and other water inputs) control

atmospheric moisture demand and available water. These meteorological variables are, in most cases, observed continuously and simultaneously using dedicated weather stations instrumented with pluviometers, hygrometers, anemometers, etc. While the measurements are commonly done in-situ, atmospheric conditions can also be characterized over large spatial scales using ensemble estimates from global circulation models (e.g. meteorological data use for sentinel for evapotranspiration (SenET, Nieto et al., 2020) estimates).

2.2.2. Radiative, mass and energy transfer terms and surface temperature

In addition to the meteorological conditions, radiative energy at the land surface (i.e. upwelling and down-welling radiation) need to be observed, in-situ or otherwise, as they form the source of energy that drives land surface processes.

2.2.2.1. Available, turbulent energy and the energy balance closure problem

Ideally, radiation retained in the system less any storages should be available for partitioning into turbulent fluxes. In the energy balance of terrestrial surfaces, this is given by Equation (2.5), i.e., $\mathrm{R_n} - \mathrm{G} = \lambda\mathrm{E} + \mathrm{H}$.

Observing the available energy entails quantifying (directly or indirectly) the various prevailing radiation components (hence the net radiation) and the ground heat flux.

Net radiation is basically calculated by applying Equation (2.1) with the four stream short-wave and long-wave radiation components as input. The up- and down-welling short wave radiation components can be measured in-situ by use of pyranometers (spectral response: 350 to 2800 nm). To discriminate between direct and diffuse components, pyrheliometers and [shaded] pyranometers are used. Pyrgeometers with a spectral response of ~5000 to 50000 nm are utilized for the long wave radiation. Net radiometers typically integrate both the optical and thermal range instruments so as to observe all four fluxes simultaneously. Conversely, remotely sensed products generally employ a combination of methods to approximate the net radiation at the surface. For example, well-documented equations (such as Equation (2.4)) are used for the solar irradiance at BOA (also Downward Surface Shortwave Flux – DSSF), which when combined with a remotely observed radiances (for the surface albedo) yield the net solar radiation. For

instance, the DSSF from the Land Surface Analysis Satellite Application Facility (LSA SAF) applies a similar algorithm with the atmospheric transmittance estimated depending on the pixel's cloud cover status; the output is produced at the spatial resolution of the SEVIRI instrument aboard the geostationary Meteosat Second Generation (MSG) satellite (Carrer et al., 2008; Geiger et al., 2008). The net long wave radiation can then be estimated with knowledge of the land surface temperature (from thermal sensors) and air temperature, which can be obtained from reanalysis data/models.

Ground heat flux measurements are usually carried out by using heat conduction plates placed at a depth (e.g. 5cm for a vegetated surface (Sauer & Horton, 2015)) below the soil surface. The installation depth should be below the drying front to avoid biases due to additional [latent] energy sinks (Colaizzi et al., 2016; Sauer & Horton, 2015). Soil heat flux plates generally use an enclosed thermopile sensor and have to be placed horizontally in the soil to allow the measurement of the temperature gradient; the thermopile then generates a voltage output that is proportional to the heat flux density (Sauer & Horton, 2015). The sensing plate only measures the soil heat flux at the installation depth ($\mathrm{G}_{0-\delta\mathrm{Z}}$ in Figure 5 and Equation (2.9)). It is therefore important to account for any heat storage at the soil layer just above the plate. This can be achieved by applying the calorimetric method (Equation (2.9)), where the unaccounted storage term is added to the measurement. This however requires knowledge of soil properties as well as the temperature profile of the near-surface layer.

$$\mathrm{G}_0 = \mathrm{G}_{0-\delta\mathrm{Z}} + \mathrm{C}(\partial\mathrm{T}/\partial\mathrm{t})\delta\mathrm{Z} \qquad [\mathrm{W\,m^{-2}}] \tag{2.9}$$

where $\mathrm{G}_{0-\delta\mathrm{Z}}$ is the ground heat flux observed at a depth $\delta\mathrm{Z}$ below the ground surface, $\mathrm{C}\,[\mathrm{J\,m^{-3}\,K^{-1}}]$ is the volumetric heat capacity of the soil layer, which is calculated by weighting the heat capacities of the various soil components by volume (Colaizzi et al., 2016; Sauer & Horton, 2015). $\partial\mathrm{T}/\partial\mathrm{t}\ [\mathrm{K\,s^{-1}}]$ is the change in soil temperature (T) over time (t) and $\delta\mathrm{Z}\,[\mathrm{m}]$ is the thickness of the soil layer. In the absence of any heat plate measurements, the calorimetric method can be applied throughout the soil column by extending the calculations to deeper soil profile layers (e.g. up to 1 metre). However, this requires that soil moisture and soil temperature probes are available at deeper layers.

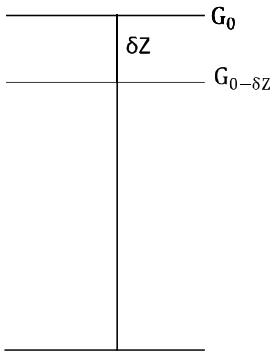

Figure 5: illustration of the soil column / profile as used in the calorimetric soil heat flux calculation method

Regarding the surface turbulent fluxes, measurement techniques can vary in complexity:

Water fluxes at the near-land surface can be quantified in terms of latent heat energy exchanges or in terms of mass flux. Accordingly, such flux observations (in terms of mass or energy) can be achieved through: *i)* Lysimetric techniques where the evaporation from the soil is quantified, *ii)* Sap flow techniques where the rate of transpiration within a plant system can be estimated, and *iii)* eddy-covariance systems. Separately, the Bowen ratio method (see below – Equation (2.11)) has variously been applied. While lysimetric and sap flow methods can help separate the water fluxes between the soil and vegetation sources, they can be cumbersome to perform/install. Processing of the raw output (especially from sap flow measurements) can also be somewhat complicated leading to misinterpretations if not carefully carried out. Another partitioning method, the Flux Variance Similarity Partitioning (FVSP), has separately been proposed (Scanlon & Kustas, 2010; Scanlon & Sahu, 2008). It applies similarity theory on water vapour and carbon dioxide eddy covariance measurements, i.e. transpiration and evaporation are – respectively - directly correlated and inversely correlated to the CO_2 fluxes.

Eddy covariance systems are capable of directly measuring the overall surface water (and sensible) fluxes. Other - relatively inexpensive - turbulence estimation techniques, such as surface renewal (which entails estimation of sensible heat flux using high frequency air temperature measurements (McElrone et al., 2013; Rosa & Tanny, 2015)) and flux variance, allow indirect measurement of evapotranspiration by applying the residual or Bowen methods (McElrone et al., 2013; Zhao et al., 2010). I.e., the residual

method is simply a rearrangement of Equation (2.5),

$$\lambda E = R_n - G_0 - H \qquad [W\ m^{-2}] \tag{2.10}$$

and the Bowen ratio (β) conservation approach (Bowen, 1926; Cellier & Olioso, 1993),

$$\beta = H/\lambda E = \left(C_p/\lambda\right)(\partial T/\partial r) \approx \left(C_p/\lambda\right)(\Delta T/\Delta r) \qquad [-] \tag{2.11}$$

as defined previously, C_p is the air specific heat at constant pressure, λ is the latent heat of vaporization; T here is the air potential temperature and r the mixing ratio for humidity gradients. Consequently, $\lambda E = (R_n - G_0)/(1 + \beta)$ and $H = \beta\,(R_n - G_0)/(1 + \beta)$

Energy imbalance*:* In-situ measurement terms of the available energy and turbulent flux (measured directly using eddy covariance systems) rarely balance out due to biases resulting from scaling and instrumentation errors leading to the well-known energy balance closure problem. As discussed in Foken (2008), the available energy has often been characterized to be larger than turbulent fluxes in most experiments. The energy balance closure issue, commonly addressed by applying the residual or Bowen (sensible to latent heat flux) ratio correction methods, can be traced to either the estimation of the available energy (e.g., errors in measurement of the net radiation and/or the ground heat flux) or the right hand side with respect to the turbulent fluxes. Sources of energy balance non-closure can be categorized into (Wohlfahrt & Widmoser, 2013): *i)* footprint mismatch, *ii)* measurements and calculation errors, *iii)* advective flux divergence, and *iv)* inadequate sampling of low frequency turbulent motions. Working with experimental data collected from 22 sites spread throughout a 50 year period, Wilson et al. (2002) also discussed circumstantial evidence pointing to a link between non-closure of the energy balance with CO_2 fluxes. Foken (2008) nonetheless mostly attributed the imbalance problem to scale issues. For example, the footprint of the eddy covariance system (turbulent fluxes) will typically be larger than that of the net radiometer (radiation fluxes), in part due to differences in measuring heights. Typical component error values are 5 - 20% for latent, sensible and net radiation and 20 - 50% for the ground heat flux (Foken, 2008). The larger errors in the soil conduction flux are often as a result of insufficient or missing calculations in the storage term. It is nonetheless worth remembering that a large majority of the imbalance consists of $Rn - G > LE + H$. As such, the scale issue argument may not hold, as that should ideally mean (or result in) $AE <> LE + H$ being equilibrated. Observably,

the footprint issue that is mostly not well corrected for is the soil heat storage since many tend to place heat flux plates close (and often below) the vegetation, thus disregarding grounds under direct solar illumination.

2.2.2.2. Land surface temperature

Thermo-radiometers meant for the measurement of surface temperature ideally observe the earth surface emission within a specific spectral range (8 – 14 μm). This applies to both in-situ and space-borne radiometers. From the thermal acquisitions, the black body function (e.g. Equation (2.2)) can be inverted for the brightness temperature (i.e., T_B - the temperature that would be estimated through the Planck's function if a body were a blackbody). Decomposing T_B eventually yields the surface radiative temperature. This emissivity correction is necessary especially when inverting surface temperature using surface energy balance models. This nonetheless depends on whether (or not) the SEB model being applied has the emissivity correction/accounting in-built; thus requiring as input the surface brightness or radiative temperatures, respectively.

In-situ installed radiometers provide acquisitions at point scale while satellites can achieve a much larger scale but at a reduced spatial resolution. Recent advances in thermal remote sensing have however allowed retrievals at medium spatial resolution. Higher resolution acquisitions can also be obtained by using unmanned aerial vehicles. Note that, thermal infrared acquisitions (just like optical remote sensing) are also susceptible to cloud coverage, thus reducing their utility under such overcast conditions.

Evapotranspiration estimates are generally useful at field to regional scale leading users towards downscaled LST products. Different LST disaggregation or sharpening methods have therefore been proposed in the literature. They range from (Chen et al., 2014): *i)* Bayesian techniques, where multi-resolution remotely sensed data are integrated to allow statistical inference of LST at a finer resolution; *ii)* Tobler's first law of geography, which assumes spatial autocorrelation to downscale coarse LST; and *iii)* surface energy balance methods that consider conservation of energy both at coarse and finer scale. The Sentinel for Evapotranspiration (*SenET, now ET4FAO*, Nieto et al., 2020) programme, for example, employs sharpened LST to provide operational ET estimates.

2.3. Review of surface energy balance and directionality modelling methods

2.3.1. Surface energy fluxes: evapotranspiration estimation

2.3.1.1. Radiative balance and net radiation

In surface energy balance (SEB) modelling of the soil-vegetation-atmosphere continuum, the overall radiative balance follows energy conservation laws as already presented in section 2.1.1. That is, the energy available for land exchange processes is equal to irradiances (incoming/down welling) less radiances (outgoing/ up welling); in both the dominant optical and thermal spectral domains. Therefore, the short wave net radiation is controlled by the incident solar radiation and the surface albedo while the long-wave net radiation is aggregated from the sky irradiance (depending chiefly on air temperature and humidity) and the surface emission (function of LST).

For single-source methods (see below), the net radiation is the result of the general/overall equation while for multi-source, partitioning of the net radiation between sources is necessary. Since all radiation terms are defined at bottom of atmosphere (BOA), the atmosphere's transmittance is required if only top of atmosphere (TOA) data (e.g. space-borne earth observation data) is available. In addition to the different methods proposed in the literature (e.g. see Allen's expression mentioned in 2.1.1), a common and simple approach used to derive the atmospheric transmittance is regressing BOA or surface albedos (i.e., reflectances integrated over the hemisphere) against planetary (or TOA) albedos at pixels with in-situ measurements (see Roerink, Su, and Menenti (2000)). The resulting regression helps to define the albedos for other pixels.

2.3.1.2. Energy balance for turbulent fluxes

Evapotranspiration models solve the energy balance as given by Equation (2.5) while variously retrieving the ET estimate. I.e., point- and contextual-based surface energy balance methods (Lagouarde & Boulet, 2016).

Table 1: Some of the surface energy balance (SEB) schemes in the literature

SEB schemes: category		*Literature*
Point-based SEB [one- and two-source]	*0-D*	*Surface Energy Balance System* (***SEBS***, Su, 2002) *Two Source Energy Balance* (***TSEB***, Norman et al., 1995) *Soil Plant Atmosphere Remote Sensing of Evapotranspiration* (***SPARSE***, Boulet et al., 2015) *Surface Temperature Initiated Closure* (***STIC***, Mallick et al., 2014)
	1-D	*Soil Canopy Observation Photochemistry and Energy fluxes* (***SCOPE***, van der Tol, Verhoef, Timmermans, Verhoef, & Su, 2009)
	3-D	MAESPA (***MAESPA***, Duursma & Medlyn, 2012)
Contextual SEB models [one- and two-source]		*Moran Vegetation Index - Temperature trapezoidal method* (***VIT***, Moran et al., 1994) *Simplified Surface Energy Balance Index* (***S-SEBI***, Roerink et al., 2000) *Surface Energy Balance Algorithm for Land* (***SEBAL***, Bastiaanssen et al., 1998) *Mapping Evapotranspiration at high Resolution with Internalized Calibration* (***METRIC***, Allen et al., 2007) *Two-source Trapezoid Model for Evapotranspiration* (***TTME***, Long & Singh, 2012) *Enhanced Two-source Evapotranspiration Model for Lland* (***ETEML***, Yang et al., 2015)

Further description of some of the schemes tabulated in Table 1 follows:

2.3.1.2.1. Point-based SEB.

Evapotranspiration is essentially treated as the residual in the energy balance equation. Here, assimilation of thermal infrared or other remotely sensed data in sequential or smoothing schemes is possible. While this is also possible with contextual SEB, the spatial contribution of all state variables and wet- and dry-edge derivation needs to be considered making it more cumbersome. The aim of point-based surface energy balance modelling is the minimization of the observed-simulated state variable differences and optimising model parameters that are relatively difficult to estimate.

Point SEB evapotranspiration models can also vary in their dimensional complexities ranging from: the 0-D models that lump soil and vegetation into one or two (in) dependent

components; 1-D, where the vegetation source is discretized into several vertical elements; to 3-D models that consider the energy budget partitioning in both vertical and horizontal domains. Note that, while we differentiate between 0- and 1-D herein, they may be viewed as somewhat equivalent since they essentially solve the transfer equations on the vertical.

0-D

The energy budget, and thus the water budget, is solved by considering lumped sources, i.e., in single source models, the energy balance is computed for soil-vegetation evapotranspiration while in dual-source, coupling is done between soil evaporation (E) and vegetation transpiration (T), which allows for separation of the two. A brief presentation of models under this category follows (not exhaustive as it only details several well-known surface energy balance methods used in the broader ET community).

Surface Energy Balance System (SEBS)

The SEBS model (Su, 2002) is a single-source algorithm that estimates terrestrial evapotranspiration by lumping the soil and vegetation surface components together. Again, the radiative balance used in SEBS is as presented in previous sections (Equation (2.1)). The energy balance Equation (2.5) (EBE) applies. The algorithm (originally validated against cotton, shrub and grass data) has been applied in numerous evapotranspiration studies. It is applicable with remote sensing data that will, in many instances, have mixed pixels with varying vegetation coverage. The algorithm retrieves actual evapotranspiration through a bounded or relative evaporative fraction (Λ_r) limited by the wet and dry fluxes extremes (i.e., $\Lambda_r = \frac{\lambda E}{\lambda E_{wet}} = 1 - \frac{H - H_{wet}}{H_{dry} - H_{wet}}$). λE_{wet} is derived using a Penman Monteith approximation. The actual sensible heat - H - is estimated using Monin Obukhov Similarity Theory using an expression equivalent to Equation (2.6), section 2.1.2. Sensible heat in dry conditions ($H_{dry} = R_n - G$) is described by the energy balance equation under the dry limit (where latent heat tends to zero due to the limitation of soil moisture), while H_{wet} is retrieved by rearranging the EB equation under wet conditions. The main evaporative fraction (Λ or EF) expression from which the actual latent heat is estimated is as follows:

$$\Lambda = \frac{\lambda E}{R_n - G} = \frac{\Lambda_r \lambda E_{wet}}{R_n - G} \qquad [-] \tag{2.12}$$

The ground heat flux ($G = [\Gamma_C + (1 - f_c)(\Gamma_S - \Gamma_C)]R_n$) is parameterized by the flux-to-net radiation ratios of bare soil ($\Gamma_S = 0.315$) and full vegetation cover ($\Gamma_C = 0.05$). f_C is the fraction of the pixel covered by vegetation canopy. Further details in Su (2002).

In single source models, the non-equivalence of the roughness lengths for momentum (Z_{0m}) and heat (Z_{0h}) transport is usually addressed by incorporating a difficult-to-define excess resistance term (defined as the product of the von Kármán constant and the inverse Stanton number, $kB^{-1} = \ln(Z_{0m}/Z_{0h})$). It is termed radiometric kB^{-1} where the radiometric instead of the aerodynamic temperature is used, and aerodynamic kB^{-1}, when Z_{0m} is used instead of Z_{0h} (Boulet et al., 2012; Matsushima, 2005). This empirical scaling limitation can be minimized by conceptualizing the surface exchanges into a two-source (vegetation and soil) system, which helps overcome the radiometric representation of the surface (Carlson et al., 1995; Friedl, 2002).

Two-Source Energy Balance (TSEB)

Proposed by Norman et al. (1995), the TSEB model allows a two-source description of the soil-vegetation-atmosphere flux interactions where the soil and vegetation components are either coupled in a “parallel” or “series” mode. In the “parallel” resistance mode, soil and vegetation are positioned side by side whereas the “series” network assumes the vegetation completely covers the ground hence preventing the soil from directly interacting with air above the vegetation canopy. The method thus allows separating the turbulent fluxes between the soil and the vegetation, e.g. separation of transpiration from evaporation in the overall latent fluxes. TSEB was formulated after discussions in *La Londe les Maures, France* (Carlson et al., 1995) where it was observed that there was a need for a better representation of the resistance and temperature at the aerodynamic level in SEB modelling, in addition to incorporating source-weighting in thermal signals. Unlike methods that apply two nearly simultaneous observations of T_B from sensors observing at oblique (off-nadir) angles (e.g. from the Along Track Scanning Radiometer (ATSR)) to allow derivation of component temperatures, TSEB allows inversion of only one directional temperature for the two sources.

TSEB incorporates handling of surface brightness temperature (T_B) observed at a space-borne radiometer as $T_B(\theta) = \left[\varepsilon(\theta)\left(T_{RAD}(\theta)\right)^4 + \left(1-\varepsilon(\theta)\right)(T_{SKY})^4\right]^{0.25}$; $\varepsilon(\theta)$ is the directional thermal emissivity (in the original TSEB version, a canopy emissivity is applied for the combined soil and vegetation surface). T_{SKY} is the hemispherical temperature of the sky. The directional radiometric temperature ($T_{RAD}(\theta)$) is then given by;

$$T_{RAD}(\theta) = \left[f(\theta)T_V^4 + \left(1-f(\theta)\right)T_S^4\right]^{0.25} \qquad [K] \qquad (2.13)$$

where T_V and T_S are the canopy and soil component temperatures, respectively. $f(\theta)$ is the fraction of radiometer's field of view that is occupied by the canopy, which is a function of view zenith angle (θ) and fraction of vegetation cover ($f_C = 1 - e^{-0.5LAI}$; LAI is the leaf area index), i.e., $f(\theta) = 1 - e^{-0.5LAI/\cos(\theta)}$; 0.5 is the foliage projection factor of a spherical leaf distribution (see Figure 10). As will be presented in the following chapter, a similar formulation is used in the SPARSE surface energy balance model.

Briefly: TSEB assumes, as a reasonable first guess, that the vegetation will have access to enough water in the root-zone to allow transpiration at the potential rate. A Priestley-Taylor approximation of the transpiration is used. The sensible heat of the canopy can thus be derived (as the residual of the canopy energy budget). The initial T_v is then obtained and used to derive T_S. These derived canopy and soil temperatures may however fail to satisfy the energy balance. I.e. when the energy balance of the soil is simulated, the resulting sensible heat of the soil (H_S) may yield a negative residual soil latent heat energy (λE_S, evaporation). In such a case, the soil latent heat flux is set to zero and a new sensible heat for the soil is calculated for closure of soil's energy budget. With the resulting new T_S, a new T_v is obtained (through Equation (2.13)) for a more reasonable canopy sensible heat flux (and consequently a new vegetation latent energy from the canopy energy balance equation). This procedure allows the transpiration to be less than potential. If the newly computed $H_v > R_{n,v}$, which means λE_v is negative, then the transpiration is set to zero and $H_C = R_{n,C}$ is forced. The overall latent heat is zero ($\lambda E_S + \lambda E_C = 0$). Again, T_v and T_S are recalculated for a new H_S. The soil's energy balance is then recomputed for a new G. These iterations are carried out until canopy and soil temperatures that ensure closure of the soil-vegetation-atmosphere energy balance are

obtained.

1-D and 3-D SVAT methods

One- and three-dimensional SVATs discretize the spatial domain into several elements, i.e., either in the vertical dimension (z) or both vertically and horizontally (x, y, z). This makes such methods more complex as they require estimation of the mass and heat balance per element (with interaction between the discretized cells also an important consideration for a tightly coupled system). A brief overview of some 1-D and 3-D evapotranspiration methods follows:

1-D: SCOPE

The Soil Canopy Observation, Photochemistry and Energy fluxes (SCOPE, van der Tol et al., 2009) is a comprehensive soil vegetation atmosphere transfer model developed to allow monitoring of energy and photosynthesis (and fluorescence) processes of vegetated surfaces. As a vertical (1-D) integrated model, the surface is made of a soil layer with the vegetation canopy discretized into several layers. SCOPE combines several models allowing a more realistic representation of the canopy system. I.e.: the SAIL (Verhoef, 1984) and 4SAIL (Verhoef, Jia, Xiao, & Su, 2007) models for the optical and thermal radiative transfers, respectively; PROSPECT leaf reflectance/transmittance (Jacquemoud & Baret, 1990) and Ball-Berry conductance (Collatz, Ball, Grivet, & Berry, 1991) methods for better estimation of the leaf biochemistry and photosynthesis; several methods for the ground heat storage, including a force restore method; among others. Recently (Yang et al., 2021), modifications have been made to the model with updates aiming at reducing the computational demand of the energy and radiative balance modules. Being a realistic representation of the vegetated terrestrial surface, SCOPE can serve as a source of reference data for evaluating other remote sensing based methods (Bian et al., 2020; Duffour et al., 2016; Jiang et al., 2022). A brief evaluation of the SCOPE versions is presented in section 6.1.3.1.

3-D energy budget methods

While for homogeneous canopies (e.g. herbaceous vegetation) where the turbid medium holds and 0D and 1D models are therefore well-suited, 3D representation might be

required for heterogeneous canopies or complex landscapes. Due to the complexity of simulating water, heat and momentum transport and interactions in the atmospheric boundary layer, models that model such interactions in the three-dimensional (3D) space are nonetheless limited, with those that are available mostly allowing a loose coupling between the discretized 3D grids/components through 0D or 1D turbulent flux parameterizations instead of Large Eddy Simulation. For example, Bian et al. (2017), coupled the TRGM radiosity model (a 3D radiative transfer method) with an energy balance process scheme inspired by the SCOPE 1D model. Current work is also ongoing to couple the 3D DART radiative scheme with the SCOPE scheme. Some processes, such as horizontal heat advection, need to be well represented in such schemes to allow better realism of the spatial distribution of simulated fluxes. Another scheme, the MAESPA model (Duursma & Medlyn, 2012; Vezy et al., 2018) allows for a 3D representation of surface exchanges at the tree and stand levels.

2.3.1.2.2. Contextual SEB methods

Contextual models have been very helpful in estimating latent fluxes over large spatial extents without requiring lots of ground based input variables. These methods are also insensitive to net radiation, atmospheric correction and initial surface and atmospheric conditions (Carlson, 2007). Contextual evapotranspiration approaches are based on the surface temperature – vegetation index (T_{surf} - VI) triangle/trapezoidal method introduced for ET estimation by Price (1990). The method was first proposed by Goward et al. (1985) who found that latent heat exchange from plants (“greenness”) was a key factor controlling surface temperature. An overview of the T_{surf} – VI is given in Carlson (2007). A somewhat different approach relates the surface temperature to surface albedo (Menenti et al., 1989). Contextual models therefore seek to exploit the physically meaningful relationship that exists between the evaporative fraction (EF) and remotely detectable surface characteristics, e.g., normalized difference vegetation index (NDVI), land surface temperature, soil moisture (Gallego-Elvira et al., 2013; Tang, Li, & Tang, 2010). Also note that some of contextual models exploit more complex parameterizations that use aerodynamic equations (e.g., SEBAL (Bastiaanssen et al., 1998), METRIC (Allen et al., 2007)). The key difference between contextual and single-point SEB methods can therefore mainly be ascribed to the capability of by-passing the use of most

meteorological data.

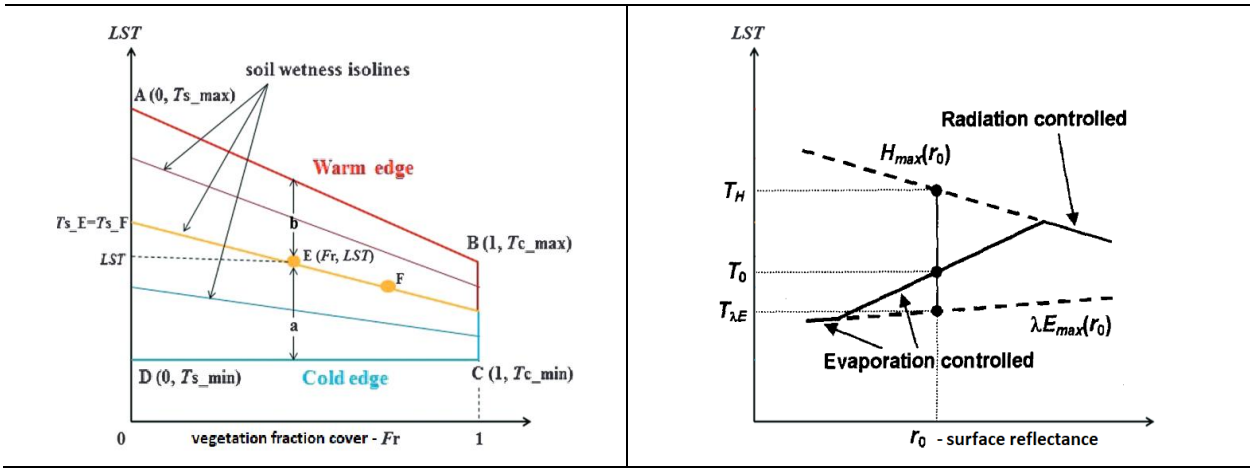

Figure 6: Trapezoidal space as applied in contextual evapotranspiration modelling; left) LST versus vegetation fraction cover, and right) LST versus surface reflectance as used in S-SEBI. Depictions according to Yuting Yang and Shang (2013) and Roerink et al. (2000), respectively

Below, a summary of the theoretical basis of a selected few of these methods is given:

One source

Moran VIT trapezoidal method

Moran et al. (1994) introduced a contextual trapezoid method that is based on the vegetation index – temperature (VIT) physical relation that had been observed in earlier works by Goward et al. (1985) and Price (1990). The VIT method entails constructing the vegetation index versus temperature feature space that integrates a wide-range of surface characteristics (i.e., fully vegetated and well-watered to bare soil and water depleted surfaces). They therefore defined a water deficit index (WDI) based on observed temperatures relative to the extremes in the cold and dry edges as described by the VIT contextual space;

$$\mathrm{WDI} = 1 - \frac{\lambda \mathrm{E}}{\lambda \mathrm{E}_{\mathrm{pot}}} = \frac{\mathrm{T}_{\mathrm{CE}} - \mathrm{T}_{\mathrm{surf}}}{\mathrm{T}_{\mathrm{CE}} - \mathrm{T}_{\mathrm{DE}}} \qquad [-] \tag{2.14}$$

where $\lambda \mathrm{E}$ and $\lambda \mathrm{E}_{\mathrm{pot}}$ are the respective prevailing (measured) and potential latent heat fluxes. T is the temperature with subscripts $\mathrm{CE}, \mathrm{DE}, \mathrm{surf}$ referring to the cold edge, dry edge and prevailing surface temperatures, respectively.

Simplified Surface Energy Balance Index (S-SEBI)

In S-SEBI (Roerink et al., 2000), the surface temperature versus albedo relationship is described as either “evaporation controlled” (wet / cold edge) or “radiation controlled” (dry / warm edge). In the former, the decrease of evapotranspiration is as a result of less soil moisture availability. Here, the surface temperature will increase with increasing reflectance (decreasing net radiation) since the increase in sensible heat exceeds the decrease in net radiation. In the latter, the soil moisture has been depleted (available energy is only used for heating the surface, i.e. as sensible heat), and the surface temperature thus decreases with increase in reflectance. This is because the available energy (thus sensible heat) reduces as a result of decrease in net radiation occasioned by the reflectance increase.

Where the “evaporation” and “radiation” controlled temperature-reflectance relationships can be derived, S-SEBI expresses the evaporative fraction for each pixel as;

$$\Lambda = \frac{\mathrm{T_H} - \mathrm{T_{surf}}}{\mathrm{T_H} - \mathrm{T_{\lambda E}}} \qquad [-] \tag{2.15}$$

where $\mathrm{T_{surf}}$ is the surface temperature; T_H and $T_{\lambda E}$ are the extreme temperatures derived from the ‘radiation controlled’ and ‘evaporation controlled’ relationships, respectively. In S-SEBI, it is assumed that these extremes can be derived from the remotely observed image. This assumption only holds when dry and wet areas can be identified in the image and the prevailing atmospheric conditions are constant.

A feature space of the surface temperature versus surface albedo (ρ) is utilized to fit the $T_H - \rho$ and $T_{\lambda E} - \rho$ (linear) regressions where;

$$\mathrm{T_H} = \mathrm{a_H} + \mathrm{b_H}\rho \;;\; \mathrm{T_{\lambda E}} = \mathrm{a_{\lambda E}} + \mathrm{b_{\lambda E}}\rho \qquad [\mathrm{K}] \tag{2.16}$$

These relationships are site and time specific. Combining Equation (2.15) and Equation (2.16) yields $\Lambda = \frac{\mathrm{a_H} + \mathrm{b_H}\rho - \mathrm{T_{surf}}}{\mathrm{a_H} - \mathrm{a_{\lambda E}} + (\mathrm{b_H} - \mathrm{b_{\lambda E}})\rho}$. Given a pixel’s surface temperature and reflectance, the sensible and latent heat fluxes are consequently calculated from the standard evaporative fraction expression as $\mathrm{H} = (1 - \Lambda)(\mathrm{R_n} - \mathrm{G})$ and $\lambda\mathrm{E} = \Lambda(\mathrm{R_n} - \mathrm{G})$, respectively.

In instances where pixel-wise surface temperatures utilized in fitting the $\mathrm{T_H}$ vs ρ and/or

$T_{\lambda E}$ vs ρ are influenced by directional anisotropy as described by the sun-land-sensor geometry (Luquet et al., 2004; Mattar et al., 2014), errors may arise in the estimation of the evaporative fraction and consequently the latent heat flux.

Surface Energy Balance Algorithm for Land (SEBAL)

The SEBAL model, formulated in Bastiaanssen et al. (1998), has been used in practical applications to estimate evapotranspiration using remotely sensed data (Bastiaanssen et al. 2005). It is relatively more complex but still relies on exploiting the extremes in wet ($H_{min} = 0;\ \lambda E_{max} = R_n - G$) and dry ($H_{max} = R_n - G;\ \lambda E_{min} = 0$) pixels to approximate the sensible heat (H) for other pixels. The instantaneous latent heat flux, calculated as the residual, is estimated and used to derive the evaporative fraction for every pixel, i.e., $\Lambda = \frac{R_n - G - H}{R_n - G}$. With this, the evapotranspiration, aggregated over the daily timescale, is estimated as;

$$ET_{24} = {8.64 * 10^7 * \Lambda * R_{n24}}/{\lambda \rho_w} \qquad [mm\ d^{-1}] \qquad (2.17)$$

where $R_{n24} = S_{n24} + L_{n24} \approx (1 - \alpha_{24})\tau_{24} S_{exo,24} - 110\tau_{24}$ is the net daily radiation, $S_{exo,24}$ is the extra-terrestrial radiation, α_{24} and τ_{24} are the surface albedo and atmospheric transmittance, respectively; λ the latent heat of vaporization and ρ_w is the density of water.

Estimation of the evaporative fraction, Λ, hinges on a reasonable estimate of the prevailing sensible heat flux. The pixel-based sensible heat is therefore written in its most simple form as $H = \rho_a C_p u_* T_*$, which is theoretically and physically equivalent to the MOST formulation as presented in section 2.1.2. ρ_a is the moist air density, C_p is the specific heat at constant pressure. u_* the friction velocity and $T_* = {\delta T}/{[\ln(z_2/z_1) - \Psi_h(z_2, L) + \Psi_h(z_1, L)]} = {a + bT_{surf}}/{\sim}$ is the temperature scale. δT is the vertical air temperature difference between heights z_1 and z_2, which are fixed at 0.1 m and 2.0 m, respectively in SEBAL to avoid problems emanating from the heat roughness length - z_{0h}. Ψ_h is the stability correction for heat transport. L is the Monin-Obukhov length. Using the sensible heat extremes at the wet and dry pixels, the δT at these limits can thus be derived. These extreme differences are correlated to the surface temperatures for the

image specific relationship $\delta T(T_s) = a + bT_s$. To enable this, the T_* for the extreme pixels are first calculated, i.e for the cold pixel, $\delta T = 0$, $T_* = 0$ and thus $H = 0$ while for the dry pixel T_* is given by $T_* = {H_{max}}/{\rho_a C_p u_*} = {R_n - G}/{\rho_a C_p u_*}$. This allows 'anchoring' the sensible flux hence ensuring outliers of *H* estimates are avoided (Bastiaanssen et al., 1998, 2005).

Estimates of T_* and T_s for the dry and cold pixels are then used in the T_* equation to establish values for a and b (linear regression coefficients valid for one particular moment and landscape). These are subsequently utilized to derive T_* for other image pixels. The pixel-based sensible heat estimates can thus be derived for eventual estimation of the evaporative fraction and the daily evapotranspiration through Equation (2.17).

Two source

Besides the single source methods, a number of authors (Long & Singh, 2012; Yongmin Yang et al., 2015; Yuting Yang & Shang, 2013) have devised contextual models that partition the overall latent fluxes between the soil and the vegetation. This is quite important when investigating the biosphere as it helps decision makers apportion scarce water resources for optimal [biomass] production. In these methods, the available energy in the terrestrial system is apportioned between the soil and vegetation components through a Beer Lamberts approximation (similar to the two-source point SEB methods). The land surface temperature as used to plot the cloud of points in the trapezoid space is thus decomposed into the soil and canopy temperatures. I.e., the extremes in the land surface temperature – fraction cover (LST-f_c) feature space can be described – cold edge temperatures (at minimum and maximum fraction cover) represent minimum soil and canopy temperatures, respectively and warm edge temperatures (at minimum and maximum fraction cover) are taken as the maximum soil and vegetation temperatures, respectively.

In the enhanced two-source evapotranspiration model for land (ETEML, Yang et al., 2015), for example, these extreme characteristics are used to derive the slopes of the warm and cold edges for any point in the space as well as the slope for the isoline that passes through that point. Isolines describe the soil/surface wetness within the LST-F_c space (Yuting Yang & Shang, 2013). In addition to the LST-T_a difference and fraction

cover, the isoline's slope helps to arrive at an estimate of soil/canopy temperatures (hence component deficit indices) for the point/pixel and thus an estimate of the component turbulent fluxes.

2.3.2. Directionality (angular anisotropy)

Scientific work on angular anisotropy of remotely sensed data is broadly ordered according to the spectral domain: optical and thermal. Angular anisotropy can be described as the variability in radiation signals depending on the direction of view, with most literature defining directional anisotropy as the difference between oblique and nadir signals (Cao et al., 2019; Lagouarde & Irvine, 2008; Lagouarde et al., 2014). This anisotropy arises primarily from the Sun-Earth-sensor geometry, with surface characteristics also playing an important part. The largest directionality effect is usually observed in the solar direction (the hotspot). Kuusk (1991) describes the hotspot effect (in optical remote sensing) as the sharp maximum of diffuse scattering/reflectance of radiation in the backward direction; in meteorology and astronomy, this phenomenon is known as heiligenschein and opposition effect, respectively. Unlike in the optical domain where the hotspot arises from the maximum backscattering, in thermal remote sensing the hotspot results from the sunlit elements in the Sun's direction, which are inherently warmer/hotter.

Kuusk anisotropy model

Kuusk's (1985) model is one of the earliest directional reflectance methods that has also been used to describe the hotspot effect in the optical radiation spectrum. The definition of the joint probability of achieving the line of sight r' for the incident solar radiation and subsequently achieving an outward sight r without being intercepted is written,

$$\mathrm{Q} = \exp\left[-\left(\mathrm{m_h} + \mathrm{m'_h} - \sqrt{\frac{\mathrm{G}}{\mu}\frac{\mathrm{G'}}{\mu'}}\int_0^h u(t) r_{\xi',\xi}\left(l_{i,j}\right)dt\right)\right] \qquad [-] \qquad (2.18)$$

where $\mathrm{m}_h = \int_0^h \frac{\mathrm{G}}{\mu} u(t)dt$ is the mean number of intersections of r within the canopy layer (from level 0 to h); G is the leaf projection factor and μ is the cosine. u is the leaf volume

density – hence $\int_0^h u(t)dt = LAI$. $r_{\xi',\xi}(l_{i,j})$ is a normalized autocorrelation or cross-correlation function with $l_{i,j}$ being the distance in the x, y plane *(see Figure 1 and the expressions – e.g., Equation (7) - in Kuusk (1985) for more details)*. The Kuusk's (1985) model makes a number of assumptions, among others: multi-scattering is disregarded; polarization, interference and diffraction effects are ignored

The Yan et al. (2012) bidirectional reflectance distribution function (BRDF) model, which is detailed further below (section 3.1.1), describes the Sun-Earth-sensor geometry in heterogeneous [row] canopies by applying a modified version of the Kuusk's (1985) method (e.g. by considering leaf clumping (Nilson, 1971) and multi-scattering (Hapke, 1981)).

Duffour-Roujean-Lagouarde parametric model

The Roujean-Lagouarde (R-L, Duffour, Lagouarde, & Roujean, 2016), which is a simple two parameter angular anisotropy method adapted from Roujean's (2000) reflectance model, can translate the remotely sensed directional temperatures ($\mathrm{T}(\theta_\mathrm{i}, \theta_\mathrm{v}, \varphi)$) into a standard (nadir, $\mathrm{T_N}$) direction. The transformation is written as,

$$\mathrm{T_N} = \mathrm{T}(\theta_\mathrm{i}, \theta_\mathrm{v}, \varphi) - \Delta\mathrm{T_{HS}} \left\{ \frac{\mathrm{e}^{-\mathrm{k}\delta} - \mathrm{e}^{-\mathrm{k}\delta_\mathrm{N}}}{\mathrm{e}^{-\mathrm{k}\delta_\mathrm{HS}} - \mathrm{e}^{-\mathrm{k}\delta_\mathrm{N}}} \right\} \qquad [\mathrm{K}] \qquad (2.19)$$

subscripts $\mathrm{i, v, N, HS}$ denote solar/illumination, viewing, nadir and hotspot directions, respectively. $\delta = \sqrt{(1/\mu_\mathrm{i}{}^2 + 1/\mu_\mathrm{v}{}^2 - 2\cos(\xi)/\mu_\mathrm{i}\mu_\mathrm{v})}$; ξ is the phase/scattering angle between solar and viewing directions derived using the spherical cosine rule as $\xi = \cos^{-1}(\mu_\mathrm{i}\mu_\mathrm{v} + \sin(\theta_\mathrm{i})\sin(\theta_\mathrm{v})\cos(\varphi))$; φ is the relative azimuth angle between solar and viewing directions. $\Delta\mathrm{T_{HS}} = (\mathrm{T_{HS}} - \mathrm{T_N})$ and k are the R-L parameters that depend on meteorological forcing and canopy structure, respectively (Duffour et al., 2016). With proper calibration of the two condition-dependent parameters, the parametric model has potential to be applied in operational settings by allowing the appropriate correction of directional anisotropy in remote acquisitions.

Vinnokov kernel-based method

This is a kernel based (isotropic, emissivity and solar kernels) angular anisotropy method,

which converts directionally observed land surface temperatures to directional-independent temperatures (Vinnikov et al., 2012). In the three-Kernel approach, the isotropic kernel is corrected by the 'emissivity' ($\varphi(\gamma)$ – for surface temperature dependence on viewing angle) and 'solar' ($\psi(\gamma, \xi, \beta)$ – for the effects from spatial and directional inhomogeneity of surface heating and shadowing) kernels. The directional temperature viewed at zenith γ, given Sun zenith ξ and a relative Sun-satellite azimuth, β is thus written as: $T(\gamma, \xi, \beta) = T_0\big(1 - A\varphi(\gamma) + D\psi(\gamma, \xi, \beta)\big)$. $T_0 = T(\gamma = 0, \xi)$ is the land surface temperature in the nadir direction $(\gamma = 0)$. A and D are coefficients that should be estimated from the observations (Vinnikov et al., 2012).

FR97, TFR97 and UFR97

Francois, Ottle and Prevot (1997) proposed an analytical radiative transfer method for the out of canopy thermal radiances, FR97. Being physically-based, the FR97 model (which considers two surface sources, i.e. soil and vegetation), can serve as a reliable tool for inversion of angular temperatures for a better understanding of surface processes. Bian et al. (2016) introduced sunlit and shaded soil elements for the 'three-component FR97 (TFR97)' and afterwards incorporated Yan et al.'s (2012) method (among others) for the four-component Unified Francois model (UFR97, Bian et al., 2018). The UFR97 is described further in the next chapter.

SAIL 4SAIL

While aiming at improving the angular responses of Suits's (1971) uniform canopy reflectance method, the scattering of arbitrarily inclined leaves (SAIL, Verhoef, 1984) was proposed. SAIL is an analytical radiative transfer model for simulating optical radiative components of canopies. The four-stream radiative fluxes as applied in the Suits, SAIL models include: the solar incident/irradiance flux, downward and upward diffuse fluxes, and the observed radiance. To consider the four-stream radiation components in the thermal infrared spectral domain, the SAIL model was extended (4SAIL, Verhoef et al., 2007). Both SAIL and 4SAIL are used within the SCOPE soil vegetation atmosphere transfer modelling tool (described in section 2.3.1) to describe the radiative transfer in the optical and thermal spectrums, respectively.

DART

DART (discrete anisotropic radiative transfer) is a comprehensive 3-D radiative transfer scheme that models leaf specular and polarization mechanisms as well as topography and hotspot (Gastellu-Etchegorry et al., 1996), and can therefore be used to simulate Satellite / airborne / in-situ imaging spectro-radiometer and LiDAR 'observations'. Classically, it applies the deterministic ray tracing and discrete ordinate methods (DART-FT, Flux tracking) to realistically model radiation transfer in a variety of heterogeneous scenes/domains (i.e., *inter alia*, the atmosphere, vegetated terrestrial surfaces, urban areas) with the DART-RC (DART-Ray Carlo, which combines both the stochastic and deterministic, forward Monte Carlo and Flux Tracking methods) applied for the LiDAR simulations. The recent iteration of the model (DART-Lux, Wang et al., 2022) applies bi-directional Monte-Carlo techniques to simulate the propagation of radiation for user-defined (or sensor-specific) settings hence significantly reducing the computation time while still maintaining the high precision levels attained through flux tracking. Evidently, given its holistic nature, DART is able to simulate angular/directional anisotropy in both the optical and thermal spectral domains.

Concluding remarks

This chapter recalls some of the fundamental scientific theories that have enabled the estimation (whether through instrumentation or modelling) of exchange processes in the near-land surface. The radiation from the sun serves as the main energy source. This radiation (less any radiances and net long-wave emission losses), in combination with the water availability at the surface and the water holding capacity of the atmosphere will then drive the prevailing heat and water (or evapotranspiration) fluxes. An important variable that infers the terrestrial mass and energy statuses is the land surface temperature, which is generally susceptible to directional anisotropy effects that arise due to the sun-target-sensor geometry coupled with surface characteristics (e.g. canopy structure and water status). Theories that describe this phenomenon are thus summarised.

Main points from this chapter:

- The radiative balance is described by short-wave and long-wave irradiances less the respective radiances. At the land-surface, the radiation energy is used to drive terrestrial processes, which are mainly – heat storage (mainly in the soil), sensible heat flux and latent heat energy. The radiative and energy budget can be measured in-situ, remotely or estimated using physically based simulation methods.
- Measurement of energy balance turbulence components can be done directly (e.g. using Eddy-Covariance systems) or indirect (e.g. surface renewal, flux variance). The observed energy balance closure is an important consideration especially in direct methods that do not ensure the energy budget closure.
- Estimation methods that estimate the surface energy balance can use the land surface temperature as a proxy for the prevailing water status. These methods can broadly be categorized into: point-based or contextual; single-source or multi source methods.
- Land surface temperature is susceptible to thermal radiation directionality. Several theories have been proposed in the literature, which allow modelling of the angular anisotropy phenomenon (in the optical domain, and extended to the thermal spectrum). They range from parametric, kernel-based to analytical models.

In the following chapter, we present an extension of the two-source Soil Plant Atmosphere Remote Sensing of Evapotranspiration model wherein the extended SPARSE surface energy balance (SEB) scheme is coupled with a radiative transfer method that discriminates the sources into their sunlit and shaded components. The suitability of SPARSE is based on it being a dual source scheme that has been evaluated and shown to provide reasonable estimates [and partitioning] of evapotranspiration. In the chapter, the original Soil Plant Atmosphere Remote Sensing of Evapotranspiration (SPARSE, Boulet et al., 2015) is therefore introduced and the extended scheme (SPARSE4, Mwangi, Boulet, & Olioso, 2022) described. In Chapters 4, 5 and 6, the model is evaluated. The chapters and subsections therein are organized in manuscript form. Chapter 4 and 5 evaluate the method using data collected over diverse canopies (homogeneous

and heterogeneous landscapes). Chapter 6 and subsequent sections then describe synthetic experiments, which detail analyses related to: 6.1) point-based SEB, and 6.2) initial evaluations on thermal radiation directionality effects on contextual SEB.

Chapter 3: Description of methods: extended SPARSE model theoretical framework

In this Chapter, a detailed description of the methods implemented and applied in the current study is given. That is,

- *The original dual source SPARSE model is first summarized*
- *The unified* François *model, a radiative transfer method that discriminates illuminated from shaded elements, is detailed*
- *Other essential methods (e.g., TIR scaling to the narrow spectral range of sensors, …) are also presented*
- *A description of the extended SPARSE surface energy balance scheme follows*
- *Finally, the coupling and implementation framework is summarized*

Dans ce chapitre, une description détaillée des méthodes mises en œuvre et appliquées dans l'étude actuelle est donnée. A savoir,

- Le modèle original SPARSE à deux sources est d'abord résumé
- *Le modèle unifié de François, une méthode de transfert radiatif qui distingue les éléments éclairés des éléments ombragés, est détaillé*
- *D'autres méthodes essentielles (par exemple, la mise à l'échelle TIR pour la gamme spectrale étroite des capteurs, …) sont également présentées*
- *Une description du schéma étendu de bilan énergétique de surface SPARSE suit*
- *Enfin, le cadre de couplage et de mise en œuvre est résumé*

Notations

α	Cavity effect factor [-]
α_g, α_v	Soil/ground (g) and vegetation (v) albedos [-]
β_s, β_v	Soil evaporation and vegetation transpiration efficiencies [-]
Δ	Slope of the vapor pressure-temperature curve at T_a [Pa K^{-1}]
$\varepsilon_a = F\varepsilon_a^{cs}$	Apparent emissivity of the atmosphere [-]. F – parameterization factor for conditions other than cs: clear-sky [-]
$\varepsilon_g, \varepsilon_v, \varepsilon_{sf}$	Emissivity of the soil, vegetation and entire surface, respectively [-]

$L^{\uparrow}_{TIRxx=vs,vh,gs,gh}$	Emitted radiation forcing terms in the net radiation scheme; for sunlit (s) and shaded (h) soil (g) and vegetation (v) [W m^{-2}]
γ	Psychrometric constant [Pa K^{-1}]
$\omega_{\omega,s}(\theta_v), \omega_{\omega,h}(\theta_v)$	Effective emissivity of sunlit and shaded leaves, respectively [-]
$\phi_{j=i,v}$	Solar (i) and viewing (v) azimuth angles [°]
φ	Relative azimuth angle between solar and viewing directions [°]
ρC_p	Product of air density [kg m^{-3}] and the specific heat of air at constant pressure [J kg^{-1} K^{-1}]
σ	Stefan Boltzmann constant [W m^{-2} K^{-4}]
$\tau_\omega \mid b(\theta_v)$	The upward directional canopy transmittance / gap frequency/fraction in viewing direction [-]
$\theta_{j=i,v};\ \mu_j$	Solar (i) and viewing (v) zenith angles; cosine of an angle j [°]
ξ	Fraction of soil/ground net radiation stored in the soil, i.e., $\xi = G/R_{ng}$ [-]
C_c, C_t	Contribution of sunlit and shaded leaves, respectively, to the emitted leaves radiation reflected by the soil (also apply for leaf emission reflected by other leaves) [-]
e_a, e_0	Air vapor pressure at the reference and aerodynamic levels, respectively [Pa].
G, H, λE	Ground, sensible and latent heat fluxes [W m^{-2}]
h, d	Vegetation height and leaf width [m]
K_g, K_z	Fractions/contribution of sunlit and shaded visible soil [-]
K_c, K_t	Contribution of sunlit and shaded vegetation to out-of-canopy radiation [-]
$K_T; fd$	Clearness index [-] and fraction of diffuse radiation [-], respectively
$L(\theta_v), L^{\downarrow}_a$	Out-of-canopy radiance in the viewing direction and incoming sky radiation [W m^{-2}]
LAI, ɑ, Ω	Leaf area index [m^2 m^{-2}], foliage projection factor [-] and clumping index [-]
M	Hemispherical average gap frequency [-]
r_a	Aerodynamic resistance between the aerodynamic level and the reference level [s m^{-1}]
r_{as}/r_{av}	Aerodynamic resistance between the soil/vegetation and the aerodynamic level [s m^{-1}]
r_{vv}	Surface resistance between the aerodynamic and the reference levels [s m^{-1}]
$RG_{dir}, RG_{diff}, RG, C_s$	Direct, diffuse, total/global (BOA) and terrestrial (TOA) solar radiations, respectively [W m^{-2}]
R_n	Total (overall) net radiation [W m^{-2}]
$R_{ng,s};\ R_{ng,h}$	Net radiation over the sunlit (s) and shaded (h) soil [W m^{-2}]
$R_{nv,s};\ R_{nv,h}$	Net radiation over the sunlit and shaded vegetation [W m^{-2}]
T_a, T_0, T_{xx}	Air, aerodynamic and component temperatures [K]

Introduction

Theoretically, one of the methods used to estimate evapotranspiration involves solving the surface energy budget equation (Equation (2.5)) for a surface temperature that results from the aggregation of the various temperature sources within the soil-canopy system and observed by remote sensors. As mentioned in section 2.3.1, the surface energy partitioning can either be: single-source - if one single temperature is used to compute all fluxes - or dual-source - if the surface is represented by two bulk temperature sources (one for the soil component considered as a homogeneous isothermal surface and another for the vegetation component seen as a big transpiring leaf, also isothermal). In addition to allowing the partitioning between evaporation and transpiration, the development of dual source models was also meant to realistically address the contribution of varying soil and vegetation skin temperatures to the aerodynamic temperature, which influences the sensible heat flux (Boulet et al., 2012). While remotely-observed radiometric temperature can be defined as the soil and vegetation temperatures weighted by their relative cover fraction in the viewing direction, the link of these component temperatures to the aerodynamic temperature is described according to turbulence resistance between the aerodynamic level and the soil and the vegetation (Norman et al., 1995). Since source temperatures (i.e., sunlit and shaded elements of the soil or vegetation) may exhibit large differences depending on their exposure to the Sun, it is necessary to incorporate the source temperature variations to enable a more accurate representation of conditions at the aerodynamic level.

To drive such surface energy balance models, measurements from in-situ stations have primarily been used as forcing input. The advent of remote sensing (RS), which provides observations of Earth surface characteristics e.g. surface brightness temperature, soil moisture, vegetation indices, albedo, etc., has made estimation of land surface fluxes at various spatial and temporal scales more practical. Of the terrestrial state variables retrievable from space, land surface temperature (LST) is tightly linked to the surface turbulent fluxes and plant water stress hence its ubiquitous use in evapotranspiration estimation methods. While in-situ thermal infra-red (TIR) sensors can provide point measurements from a fixed direction (generally from nadir or close to nadir), space-borne

sensors, which provide observations at larger spatial scales, often view pixels on Earth from varying directions each observation instance. For example, the Moderate Resolution Imaging Spectroradiometer (MODIS) sensor aboard the Terra and Aqua satellites provides, among other products, global LST at a spatial resolution of ~1 km every few days and over a broad-range of viewing angles (≤ 65°, see Chapter 1, Figure 1). As detailed in the first chapter, the recently proposed TRISHNA mission is expected to provide global LST products with relatively high temporal and spatial resolutions (Lagouarde et al., 2019). Due to the multi-angular nature of the acquisitions, directional effects are likely to manifest in the thermal EO acquisitions impacting the retrieval accuracy of subsequent inferences of surface state estimates.

The need to incorporate directional aspects has necessitated the use of simple radiative methods that link the observed brightness temperature with the prevailing component temperatures, particularly in dual-source models. These, however, do not account for the solar-Earth-viewing geometry, which can lead to significant thermal radiation directionality (TRD) effects (also referred to as TIR directional anisotropy); an extreme case of TRD is the hotspot effect that results from the syzygy Sun-satellite-Earth configuration, where the sensor mostly observes sunlit elements. According to Kimes and Kirchner (1983), Lagouarde et al. (2014), and Duffour et al. (2016), oblique-nadir temperature differences (i.e., thermal radiation directionality) can reach 15 °C. Since LST uncertainties of 1-3 °C may in-turn result in flux errors in the order of ~100 Wm^{-2} (Kustas & Norman, 1996), accounting for anisotropy in evapotranspiration models has the potential of significantly improving the derived estimates. Formulations that address thermal radiation directionality, and thus the hotspot phenomenon, are fundamentally extensions of the optical domain’s reflectance theory. As detailed in Cao et al.'s (2019) review and summarised in Chapter 2 (section 2.3.2), they range from geometric, parametric, hybrid to 3-D radiative transfer models.

For dual-source evapotranspiration models, it is more suitable to invert component temperatures using radiative transfer or hybrid methods. Bian et al. (2018) recently developed the physically-based unified four-component (UFR97) model. Their radiative scheme is an extension of the two-component Francois et al.'s (1997) model and incorporates bi-directional aspects from Yan et al. (2012), which is in-turn based on

Kuusk's (1985) hotspot method. They tested the model on homogeneous, row-crop and forest covers (assuming a spherical foliage projection) where they showed that it could satisfactorily retrieve directional temperatures with component sunlit/shaded soil/vegetation temperatures used as input. The relatively easy to implement UFR97 method can thus be used for direct assimilation of directional TIR data and thereby help to address directional anisotropic issues in surface energy balance inversion schemes.

In this Chapter, the coupling of the classical dual source SPARSE model with the UFR97 radiative method is detailed. The chapter begins with a brief description of the two-source Soil Plant Atmosphere Remote Sensing of Evapotranspiration (SPARSE, Boulet et al., 2015), which is then followed by the detailed description of the various theoretical components in the extended SPARSE (hereafter also termed SPARSE4).

I. Soil Plant Atmosphere Remote Sensing of Evapotranspiration - SPARSE

The SPARSE model is a dual-source soil vegetation atmosphere transfer (SVAT) model proposed in Boulet et al. (2015). It is based on the two-source energy balance – TSEB – rationale (described in section 2.3.1). However, unlike in the original TSEB, where the potential canopy latent flux is estimated through the Priestley-Taylor method, SPARSE utilizes a Penman-Monteith approximation. It is argued that the Priestley-Taylor coefficient (~1.3) may not be reasonable for natural vegetation and regions with strong vapour pressure deficit (Agam et al., 2010; Boulet et al., 2015; Colaizzi et al., 2012). Priestley-Taylor formulations have been shown to consistently underestimate transpiration partitioning of total ET, this is especially the case in semi-arid lands (Agam et al., 2010).

In SPARSE, the out-of-canopy thermal radiation as observed by a remote sensor is equivalent to Equation (2.13), which weights the emission from the soil and vegetation sources according to the fraction in the field of view of the sensor. For the net radiation, the incoming radiation and irradiances are partitioned according to Equation (3.39), but only considering two-sources with the terms in the energy balance (i.e. latent and sensible heat fluxes) written as in Equations (3.50), (3.51), (3.52) and (3.53) (again, for the soil

and vegetation components only, i.e., without discriminating shaded and sunlit elements). The model is thus implemented to solve the energy and radiative balances while taking into account the water status boundary condition as described by the observed thermal emission or brightness temperature.

To account for the turbulent mixing at the atmospheric boundary layer, SPARSE applies the Shuttleworth-Wallace resistance scheme as formulated in Shuttleworth and Gurney (1990),

$$r_a = \frac{\ln\left(\frac{z-d}{z_{om}}\right)^2}{k^2 u_a (1+R_i)^m} \tag{3.0.a}$$

$$r_{as} = \frac{z_v e^{n_{sw}} \ln\left(\frac{z-d}{z_{om}}\right)\left(e^{\frac{-n_{sw} z_{om,s}}{z_v}} - e^{\frac{-n_{sw}(d+z_{om})}{z_v}}\right)}{n_{sw} k^2 u_a (z_v - d)} \tag{3.0.b}$$

$$r_{av} = \left(\frac{w}{u_a} \frac{\ln\left(\frac{z-d}{z_{om}}\right)}{\ln\left(\frac{z_v-d}{z_{om}}\right)}\right)^{0.5} \frac{n_{sw}}{4\alpha_0 LAI(1-e^{-0.5 n_{sw}})} \tag{3.0.c}$$

$$r_{vv} = r_{av} + \frac{r_{stmin} \prod f}{LAI_g} \tag{3.0.d}$$

where the vegetation has a height z_v and w leaf width, u_a is the wind speed measured at height z, $d = 0.66 z_v$ the displacement height, $z_{om} = 0.13 z_v$ is the roughness length for momentum exchange, $z_{om,s} = 0.005\ \mathrm{m}$ is the roughness length for momentum exchange over bare soil, $k = 0.41$ is the von Karman constant, $n_{sw} = 2.5$, $\alpha_0 = 0.005$, r_{stmin} is the minimum stomatal resistance. $R_i = \frac{5g(z-d)(T_0-T_a)}{T_a u_a^2}$ is the Richardson number used for the stability corrections; g is the acceleration of gravity, $m = 0.75$ in unstable conditions and $m = 2$ in stable conditions. LAI_g is the green (photosynthetically active) LAI. $\prod f$ is the product of weighting stress functions related to environmental factors influencing stomatal resistance, i.e., temperature, solar radiation and vapour pressure deficit. These are taken from Braud et al. (1995).

II. Extended SPARSE

3.1. Radiative transfer and net radiation terms

3.1.1. UFR97 four-component scheme

The unified Francois UFR97 four-component model (Bian et al., 2018) extends the three-component TFR97 (Bian et al., 2016) model, which is based on the FR97 model (Francois et al., 1997), by incorporating aspects of Yan et al.'s (2012) bi-directional reflectance distribution function (BRDF) model.

The out-of-canopy radiance in the viewing direction, θ_v, is derived as;

$$L(\theta_v) = K_g\tau_\omega(\theta_v)\varepsilon_g \cdot B(T_{gs}) + K_z\tau_\omega(\theta_v)\varepsilon_g \cdot B(T_{gh}) + \omega_{\omega,s}(\theta_v) \cdot B(T_{vs}) + \omega_{\omega,h}(\theta_v) \cdot B(T_{vh}) + [1 - \varepsilon_c(\theta_v)]L_a^{\downarrow} \quad (3.1)$$

where $K_g\tau_\omega(\theta_v)\varepsilon_g$, $K_z\tau_\omega(\theta_v)\varepsilon_g$, $\omega_{\omega,s}(\theta_v)$ and $\omega_{\omega,h}(\theta_v)$ are the effective emissivity of sunlit and shaded soil, sunlit and shaded leaves, respectively. $B(.)$ is the blackbody function as described by Equation (2.2). Equation (3.1) differs from a two-source formulation (used in the classic SPARSE, i.e. Equation (2.13)), which lumps the sunlit and shaded elements for each source (soil and vegetation).

3.1.1.1. Sunlit and Shaded Leaves

For the sunlit vegetation, the fraction is computed by partitioning the volume into two layers: *1.* Upper layer where all observed leaves are assumed to be sunlit and *2.* Lower layer where sunlit fraction of visible leaves is calculated using Yan et al.'s (2012) model. Contribution of sunlit leaves to out-of-canopy radiance thus becomes;

$$K_c = \frac{[1 - b_1(\theta_v) + K_{g1} * K_{c2}]}{[1 - b(\theta_v)]} \quad (3.2)$$

where $1 - b_1(\theta_v)$ is assumed to be the proportion of sunlit visible leaves in the upper layer. $b_1(\theta_v)$ is the gap fraction of the upper layer given by;

$$b_1(\theta_v) = e^{-\frac{G\Omega_v LAI_1}{\mu_v}} \quad (3.3)$$

G is the foliage projection factor (0.5, $\left(\frac{2}{\pi}\right)\sin\theta_j$ and $\cos\theta_j$ for a spherical/random, vertical and horizontal foliage, respectively (Nilson, 1971; Roujean, 1996; 2000)); further described below (Equations (3.25) and (3.26)); μ is the cosine of an angle (viewing angle here). LAI_1 is the leaf area index of the upper layer given by;

$\mathrm{LAI}_1 = \mathrm{u} * \mathrm{h}_1 . \mathrm{u}\,(\text{leaf volume density function}) = \frac{\mathrm{LAI}}{\mathrm{h}}$, h is the canopy height, $\mathrm{h}_1 = \sqrt{\mathrm{h}_{1,\mathrm{i}}\mathrm{h}_{1,\mathrm{v}}}$;

$\mathrm{h}_{1,\mathrm{j}} = \frac{-\ln\left[1-\beta\left(1-e^{-G\Omega_j \mathrm{LAI}/\mu_j}\right)\right]\mu_j}{G\Omega_j \mathrm{u}}$: $\mathrm{j} = \mathrm{i}, \mathrm{v}$; i and v being the solar and viewing directions, respectively. β is a coefficient in Bian et al. (2018) set to 0.58 over homogeneous scenes.

$\Omega_j = \frac{-\ln(b(\theta_j))\mu_j}{\mathrm{LAI}*G}$ is the clumping index derived by inverting the gap frequency exponential formula given in Nilson (1971).

$$K_{g1} = \exp\left[-\left(\Omega_i \frac{G_i}{\mu_i} + \Omega_v \frac{G_v}{\mu_v} - w\sqrt{\Omega_i\Omega_v \frac{G_i}{\mu_i}\frac{G_v}{\mu_v}}\right)\mathrm{LAI}_1\right] \tag{3.4}$$

represents the sunlit visible background of the upper layer.

$$K_{c2} = 1 - \exp\left[-w\sqrt{\Omega_i\Omega_v \frac{G_i}{\mu_i}\frac{G_v}{\mu_v}}\,\mathrm{LAI}_2\right] \tag{3.5}$$

is the proportion of sunlit visible leaves in the lower layer.

where the hotspot parameter/function is expressed as;

$$w = \frac{d}{h\delta}\left(1 - e^{-h\delta/d}\right) \tag{3.6}$$

d here is the leaf width, h as previously defined (i.e. canopy height) and $\delta = \sqrt{\frac{1}{{\mu_i}^2} + \frac{1}{{\mu_v}^2} - \frac{2\cos(\xi)}{\mu_i\mu_v}}$ while ξ is the phase/scattering angle between solar and viewing directions derived using the spherical cosine rule as $\xi = \cos^{-1}(\mu_i\mu_v + \sin(\theta_i)\sin(\theta_v)\cos(\varphi))$; φ is the relative azimuth angle between solar and viewing directions. At exactly the hotspot position (i.e. $\theta_v = \theta_i$ and $\varphi = 0$), w is undefined in its current form. In this case, it can be approximated through a Taylor expansion ($w \approx$

$\frac{d}{h\delta}\left(1-\left\{1+\left(\frac{-h\delta}{d}\right)+\frac{1}{2!}\left(\frac{-h\delta}{d}\right)^2+\cdots\right\}\right)\approx 1-\frac{h\delta}{2d}=1$). In Figure 7, $\frac{d}{h}$ ratio is observed to have a significant influence on the hotspot parameter especially for very short vegetation. Overall, high w values are concentrated very close to the hotspot region (in the solar principal plane) and nadir (orthogonal/cross plane), which would translate to the higher contribution of sunlit elements in the viewing direction - K_c and K_g.

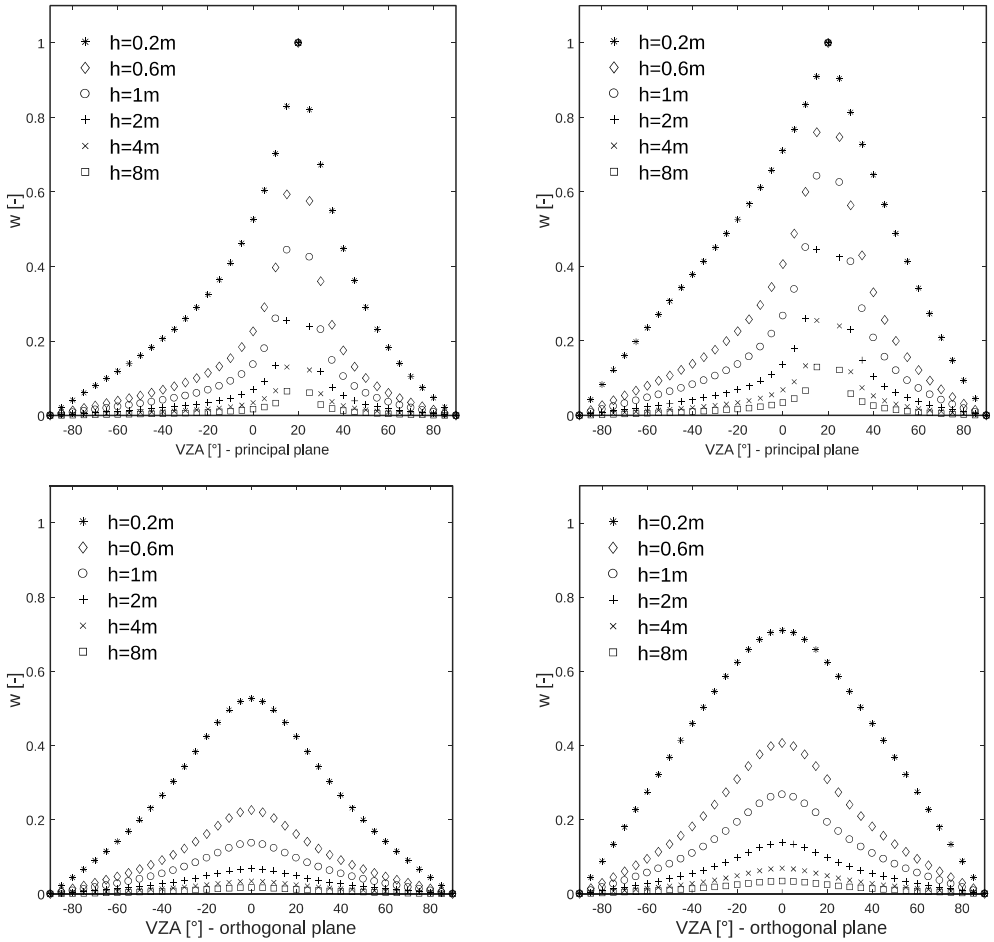

Figure 7: Hotspot parameter (w) over the solar principal plane (top) and orthogonal / cross plane (bottom) for left: 5 cm leaf and right:10 cm leaf. ($SZA = 20°$, $SAA = 90°$). h is the canopy height

Contribution of the shaded leaves is hence;

$$K_t = 1 - K_c \tag{3.7}$$

The effective emissivity expressions of the sunlit ($\omega_{\omega,s}(\theta_v)$) and shaded ($\omega_{\omega,h}(\theta_v)$) leaves finally become;

$$\omega_{\omega,s}(\theta_v) = [1 - b(\theta_v)]\varepsilon_v K_c + (1 - M)b(\theta_v)(1 - \varepsilon_g)\varepsilon_v C_c + (1 - \alpha)[1 - b(\theta_v)M][1 - b(\theta_v)](1 - \varepsilon_v)\varepsilon_v C_c \quad (3.8)$$

$$\omega_{\omega,h}(\theta_v) = [1 - b(\theta_v)]\varepsilon_v K_t + (1 - M)b(\theta_v)(1 - \varepsilon_g)\varepsilon_v C_t + (1 - \alpha)[1 - b(\theta_v)M][1 - b(\theta_v)](1 - \varepsilon_v)\varepsilon_v C_t \quad (3.9)$$

where ε_v and ε_g are the leaf and soil emissivities respectively; α is the cavity effect factor (François, 2002; Francois et al., 1997) that defines part of the incident radiation that is reflected by the leaves and finally absorbed by the canopy. Fitting the α vs θ_v data provided in François (2002) yields $\alpha = 0.3168 + 0.0029\exp(0.0605 \cdot \theta_v)$; an alternative option, i.e. a regression based on the α vs θ_v data of the canopy-emissivity model (C-EP, Cao et al., 2018), can also be applied as it is more suitable for low viewing elevations. Accordingly, the fitted C-EP regression is written: $\alpha = 0.2625 + 0.0021\exp(0.0536 \cdot \theta_v)$ *(AFM anonymous Reviewer, Personal Communication, December 2021)*, The cavity effect expressions show a similar trend for low zenith angles with higher deviations being observed at low elevations (Figure 8). Within viewing (and scan angles, i.e. $0 \leq \theta \leq 60$) that are likely to feature in space-borne observations, the differences on resulting canopy emissivity (~0.002) can be considered acceptable (Cao et al., 2018). Nonetheless, the C-EP method should be preferred for higher zeniths since the differences can become large especially for surfaces with higher canopy coverage.

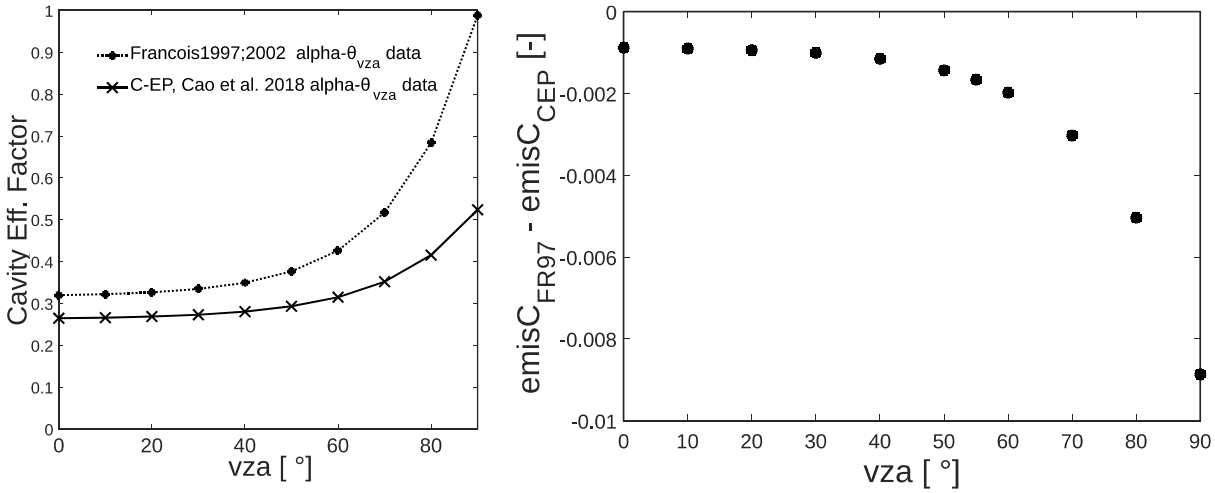

Figure 8: Left: the cavity effect factors as calculated using expressions derived from Francois et al. (1997) and Cao et al. (2018) α vs θ_v data; Right: differences of the resulting canopy emissivities over the entire viewing range

M is the hemispherical average gap frequency, which is expressed as (Francois et al.,

1997);

$$M = \frac{1}{\pi}\int_{-\frac{\pi}{2}}^{\frac{\pi}{2}} b(\theta)d\theta = \frac{1}{\pi}\int_{-\frac{\pi}{2}}^{\frac{\pi}{2}} e^{-G\cdot\frac{LAI}{\mu}}d\theta \quad (3.10)$$

C_c and C_t are - respectively - the contributions of sunlit and shaded leaves inside the canopy to the radiation emitted from leaves and reflected by the soil. The same apply for the radiance emitted from the leaves and reflected by other leaves. These proportions are given by;

$$C_c = \frac{[1 - b(\theta_i)]\mu_i}{G_i \cdot LAI} \quad (3.11)$$

$$C_t = 1 - C_c \quad (3.12)$$

Note that the separation coefficients K_c, K_t, C_c and C_t are normalized (as above) before deriving the effective emissivities of the sunlit and shaded leaves, such that $\omega_{\omega,s}(\theta_v)$ and $\omega_{\omega,s}(\theta_v)$ (in Equations (3.8), (3.9), respectively) equivalently sum up to $\omega_\omega(\theta_v)$ as provided in Francois et al. (1997).

3.1.1.2. Sunlit and Shaded Soil

τ_ω in the effective emissivity of sunlit $(K_g\tau_\omega(\theta_v)\varepsilon_g)$ and shaded $(K_z\tau_\omega(\theta_v)\varepsilon_g)$ soil represents the upward directional canopy transmittance. The sunlit (K_g) fraction of visible soil is calculated thusly (refer to Equation (2.18));

$$K_g = \frac{\exp\left[-\left(\Omega_i\frac{G_i}{\mu_i} + \Omega_v\frac{G_v}{\mu_v} - w\sqrt{\Omega_i\Omega_v\frac{G_i}{\mu_i}\frac{G_v}{\mu_v}}\right)LAI\right]}{b(\theta_v)} \quad (3.13)$$

Similarly, the complement is the shaded fraction of visible soil (K_z);

$$K_z = 1 - K_g \quad (3.14)$$

3.1.1.3. Gap fraction cases and leaf projection function G

3.1.1.3.1. Homogeneous, Row and Forest canopies

For homogeneous canopies, the angular gap fraction is retrieved from Nilson's (1971) exponential formula with the effective LAI (LAIe) (and average total foliage clumping index ($\widetilde{\Omega}$)) derived as in Chen et al. (2005) and Chen (1996):

$$\mathrm{LAIe} = -2\int_0^{\frac{\pi}{2}} \ln[\mathrm{b}(\theta)]\cos(\theta)\sin(\theta)\,\mathrm{d}\theta = -2\int_0^{\frac{\pi}{2}} \ln\left[\mathrm{e}^{-G\cdot\frac{\mathrm{LAI}}{\mu}}\right]\cos(\theta)\sin(\theta)\,\mathrm{d}\theta \qquad (3.15)$$

$$\mathrm{b}(\theta_j) = \mathrm{e}^{-\frac{G\widetilde{\Omega}\mathrm{LAI}}{\mu_j}} \text{ and } \widetilde{\Omega} = \frac{\mathrm{LAIe}}{\mathrm{LAI}} \qquad (3.16)$$

For forest covers, the gap fraction is formulated to account for the large gaps among the tree crowns and small gaps within the crowns (Bian et al., 2018; Li et al., 2017):

$$\mathrm{b}(\theta_j) = \mathrm{e}^{-\frac{\lambda\pi r^2}{\mu_j'}} + \left(1 - \mathrm{e}^{-\frac{\lambda\pi r^2}{\mu_j'}}\right)\cdot \mathrm{e}^{-G\cdot\frac{\mathrm{sLAI}}{\mu_j'}} \qquad (3.17)$$

λ is the crown count density, which can be estimated using the effective leaf area index, the single tree LAI (sLAI) and the horizontal crown radius (r) as $\lambda = \mathrm{LAI}/(\mathrm{sLAI}\cdot\pi r^2)$. $\mu_j' = \cos(\theta_j')$ is the cosine of the transformed angle $\theta_j' = \tan^{-1}\left[\frac{t}{r}\cdot\tan(\theta_j)\right]$. *t* is the vertical crown radius.

3.1.1.3.2. Row crop average gap fraction (Yan et al., 2012):

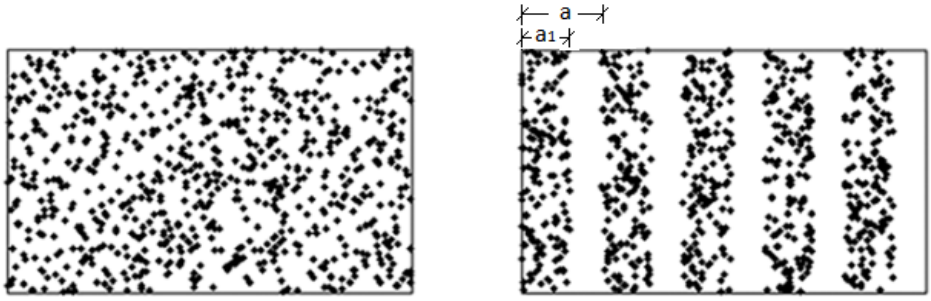

Figure 9: Left: homogenous, and right: row vegetation canopies as depicted in Yan et al. (2012)

For row crops with ***a₁*** row width and ***a*** row spacing, the directional gap frequency is retrieved according to the theory by Yan et al. (2012). The general expression is written:

$$\mathrm{b}(\theta_j,\varphi) = \frac{1}{\mathrm{A}}\left[\left(\mathrm{A}_1 - \mathrm{htan}(\theta_j) - 2\frac{\sin(\theta_j)}{\mathrm{Gu}}\right)\cdot \mathrm{e}^{-\frac{G\mathrm{uh}}{\mu_j}} + \left(\mathrm{A}_2 - \mathrm{htan}(\theta_j) + 2\frac{\sin(\theta_j)}{\mathrm{Gu}}\right)\right] \qquad (3.18)$$

where $\mathrm{b}(\theta,\varphi)$ is the angular gap frequency when $A_1<A_2$, $\varphi \neq 0$ and $0 \leq \mathrm{htan}(\theta_j) \leq \mathrm{A}_1$; $\mathrm{A}_1 = \mathrm{a}_1/\sin(\varphi)$, $\mathrm{A} = \mathrm{a}/\sin(\varphi)$, are the effective row width and spacing, respectively. $\mathrm{a}_2 = \mathrm{a} - \mathrm{a}_1$ and φ is the relative azimuth between viewing and cross-row directions. Here, $\mathrm{u} = \mathrm{a}/\mathrm{a}_1\cdot\mathrm{LAI}/\mathrm{h}$.

For other conditions, the number of rows penetrated by the radiation beam before reaching the ground surface (or number of rows penetrated by the radiation in the viewing direction, subscript v) is first defined as:

$$n = \text{INTEGER}\left[\frac{\text{htan}(\theta_{j=i,v})}{A}\right] \tag{3.19}$$

If the beam is not along-row, i.e. $\varphi \neq 0$, then:

If $\mathbf{A_1 \leq A_2}$

If $nA \leq \text{htan}(\theta_j) \leq nA + A_1$

$$b(\theta_j, \varphi) = \frac{1}{A}\left\{\left(nA + A_1 - \text{htan}(\theta_j) - 2\frac{\sin(\theta_j)}{G_u}\right)\cdot e^{-\frac{G_u(h - nA_2\cot(\theta_j))}{\mu_j}} + \left(nA + A_2 - \text{htan}(\theta_j) + 2\frac{\sin(\theta_j)}{G_u}\right)\cdot e^{-\frac{nG_uA_1\cot(\theta_j)}{\mu_j}}\right\} \tag{3.20}$$

If $nA + A_1 \leq \text{htan}(\theta_j) \leq nA + A_2$

$$b(\theta_j, \varphi) = \frac{1}{A}\left\{\left(\text{htan}(\theta_j) - nA - A_1 - 2\frac{\sin(\theta_j)}{G_u}\right)\cdot e^{-\frac{G_u(n+1)A_1\cot(\theta_j)}{\mu_j}} + \left(nA + A_2 - \text{htan}(\theta_j) + 2\frac{\sin(\theta_j)}{G_u}\right)\cdot e^{-\frac{nG_uA_1\cot(\theta_j)}{\mu_j}}\right\} \tag{3.21}$$

If $nA + A_2 \leq \text{htan}(\theta_j) \leq (n+1)A$

$$b(\theta_j, \varphi) = \frac{1}{A}\left\{\left(\text{htan}(\theta_j) - nA - A_1 - 2\frac{\sin(\theta_j)}{G_u}\right)\cdot e^{-\frac{G_u(n+1)A_1\cot(\theta_j)}{\mu_j}} + \left(\text{htan}(\theta_j) - nA - A_2 + 2\frac{\sin(\theta_j)}{G_u}\right)\cdot e^{-\frac{G_u[h - (n+1)A_2\cot(\theta_j)]}{\mu_j}}\right\} \tag{3.22}$$

If $\mathbf{A_1 > A_2}$

If $nA \leq \text{htan}(\theta_j) \leq nA + A_2$

Same as Equation (3.20)

If $nA + A_2 \leq h\tan(\theta_j) \leq nA + A_1$

$$b(\theta_j, \varphi) = \frac{1}{A}\left\{\left(h\tan(\theta_j) - nA - A_2 + 2\frac{\sin(\theta_j)}{G u}\right) \cdot e^{-\frac{G u[h-(n+1)A_2 \cot(\theta_j)]}{\mu_j}} + \left(nA + A_1 - h\tan(\theta_j) - 2\frac{\sin(\theta_j)}{G u}\right) \cdot e^{-\frac{G u[h-nA_2 \cot(\theta_j)]}{\mu_j}}\right\} \quad (3.23)$$

If $nA + A_1 \leq h\tan(\theta_j) \leq (n+1)A$

Same as Equation (3.22)

If the beam is along-row, i.e. $\varphi = 0$, then:

$$b(\theta_j, \varphi) = \frac{1}{A}\left(A_1 \cdot e^{-\frac{G uh}{\mu_j}} + A_2\right) \quad (3.24)$$

since $A = a/\sin(\varphi)$, $A_1 = a_1/\sin(\varphi)$ and $A_2 = a_2/\sin(\varphi)$, Equation (3.24) can be re-written as, $b(\theta_j, \varphi) = \frac{1}{a}\left(a_1 \cdot e^{-\frac{G uh}{\mu_j}} + a_2\right)$, i.e., weighting between a_1, whose gap fraction is a function of uh (or the hedgerow leaf area), and a_2, which is bare (gap fraction = 1).

Ideally, these row gap probability formulations ensure that the fraction of vegetation cover remains relatively the same (from nadir to oblique) for along row views while increasing cross-row. In addition to the whorl structure, branch and shoot geometry, the clumping of vegetation/foliage elements can occur at tree spacing (Chen, 1996). The clumping index required to derive the effective leaf area index (as used in the continuous formulation) may not be well known, with the uncertainties in resulting gap estimates being exacerbated if vegetation spacing is also unaccounted for. The row gap expressions can therefore help to address the canopy clumping (arising from spacing geometries) that are not well addressed when using the generic homogeneous cover scheme.

Foliage projection factor – G function

The leaf projection factors in the direction $\theta = \cos^{-1}(\mu)$ for different leaf inclinations, assuming a uniform azimuth orientation, are given by (Nilson, 1971; Roujean, 1996; 2000):

i. Spherical/isotropic, horizontal and vertical leaf distributions:

$$G = \begin{cases} \frac{1}{2}, & \text{spherical/random distribution} \\ |\mu| = |\cos(\theta_v)|, & \text{horizontal/planophile foliage} \\ \frac{2}{\pi}\sin(\theta_v), & \text{vertical/erectophile foliage} \end{cases} \quad (3.25)$$

ii. Foliage inclined at $\theta' = \cos^{-1}(\mu')$ from the horizontal (or the zenith angle of the leaf normal):

$$G = \begin{cases} \mu\mu', & \theta_v + \theta' \leq {}^{\pi}/_{2} \\ \frac{2}{\pi}\left\{\mu\mu'\sin^{-1}\left(\cot(\theta_v)\cot(\theta')\right) + (1-\mu^2-\mu'^2)^{0.5}\right\}, & \theta_v + \theta' > {}^{\pi}/_{2} \end{cases} \quad (3.26)$$

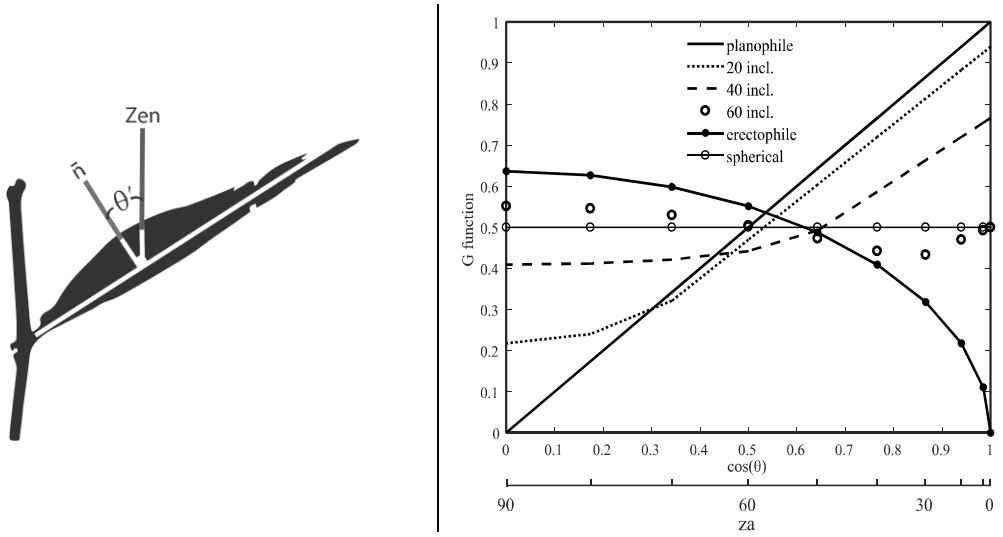

Figure 10: Left: description of leaf inclination angle geometry; Right: projection factors, G, as calculated using expressions from Nilson (1971), i.e., Equations (3.25), (3.26)*. A uniform azimuth orientation of the leaves is assumed.*

The projection factors as estimated using the Equations (3.25) and (3.26) are illustrated in Figure 10. The closer the average leaf inclination angle is to 57.5 ° (well documented random foliage inclination (Chen & Black, 1991)), the more spherical or random the local alignment of the leaves. These expressions should however be applied with care since limitations do exist; for example, applying the generic gap probability equation ($b = e^{-G\Omega LAI}$), a fully erectophile leaf canopy will (by definition) result in a gap fraction of 1 irrespective of leaf area, which may not be realistic.

3.1.1.4. Reflected atmospheric radiation

Most surfaces (e.g. the Earth) are not blackbodies and will therefore have different emittances (reflectances) depending on the material. As such, some of the atmospheric radiation emitted, $L_a^{\downarrow}$, in the earth's direction is reflected. In the viewing direction this reflected radiation is written $[1-\varepsilon_{sf}(\theta_v)]L_a^{\downarrow}$.

For natural surfaces, composed mainly of vegetation and soil sources, the emissivity of the entire canopy ($\varepsilon_c(\theta_v)$) is given by (Francois et al., 1997);

$$\varepsilon_{sf}(\theta_v) = 1 - b(\theta_v)M\left(1-\varepsilon_g\right) - \alpha[1-b(\theta_v)M](1-\varepsilon_v) \tag{3.27}$$

As elsewhere, the vegetation and the soil sources are respectively subscripted v and g.

3.1.2. Long-wave radiation in the narrow $8-14\ \mu m$ spectral band of the observing thermal sensor

Field thermo-radiometers usually provide measurement in the $8-14\ \mu m$ thermal infrared spectral sensitivity range. It is also common to have satellite radiometers observing in the $10.5-12.5\ \mu m$ thermal band. Olioso (1995) noted that significant errors could arise if the measuring spectral window of the sensor is not taken into account. The [spectrally-scaled] measured thermal radiation is therefore given by (Olioso, 1995):

$$f_\lambda(T_B)\sigma T_B^4 = \varepsilon_{surf,\lambda} f_\lambda(T_{rad})\sigma T_{rad}^4 + \left(1-\varepsilon_{surf,\lambda}\right)L_\lambda^{\downarrow} \tag{3.28}$$

where σ is the Stefan Boltzmann constant, T_B is the measured brightness temperature, T_{rad} the radiative surface temperature and $L_\lambda^{\downarrow}$ is the down-welling atmospheric radiation in the narrow observation band. By assuming $f_\lambda(T_B) \approx f_\lambda(T_{rad})$, the unknown T_{rad} can be solved for. $f_\lambda(T)$ and $L_\lambda^{\downarrow}$ for the two narrow bands [$\lambda = 8-14\ \mu m$ and $10.5-12.5\ \mu m$] are expressed as:

$$f_\lambda(T) = \begin{cases} -0.6732 + 0.6240\cdot 10^{-2}T - 0.9140\cdot 10^{-5}T^2, & \lambda_{8-14\ \mu m} \\ -0.2338 + 0.2288\cdot 10^{-2}T - 0.3617\cdot 10^{-5}T^2, & \lambda_{10.5-12.5\ \mu m} \end{cases} \tag{3.29}$$

$$L_{\lambda:8-14}^{\downarrow} = \varepsilon_{a,\lambda} f_\lambda(T_a)\sigma T_a^4 \tag{3.30}$$

T_a is the air temperature. Likewise, the atmospheric apparent emissivity $\varepsilon_{a,\lambda}$ in the $8-14\ \mu m$ and $10.5-12.5\ \mu m$ window are given by (Idso, 1981):

$$\varepsilon_{a,\lambda} = \begin{cases} 0.15 + 5.03 \cdot 10^{-6} e_a \exp(2450/T_a), & \lambda_{8-14\ \mu m} \\ 5.91 \cdot 10^{-6} e_a \exp(2450/T_a), & \lambda_{10.5-12.5\ \mu m} \end{cases} \quad (3.31)$$

All temperatures are in [K] and the atmospheric vapour pressure e_a in [hPa]. Further details can be found in Idso (1981) and Olioso (1995).

3.1.3. Global solar radiation partitioning

Fraction of incoming diffuse radiation (fd) is estimated following the sky clearness index (K_T) method proposed in Erbs et al. (1982). Where the atmosphere's optical depth data is available, a modified function according to Carrer et al. (2013) is applied for $K_T > 0.80$:

$$fd = \begin{cases} 1 - 0.09K_T, & K_T \leq 0.22 \\ 0.9511 - 0.1604K_T + 4.388K_T^2 - 16.638K_T^3 + 12.336K_T^4, & 0.22 < K_T \leq 0.80 \\ 0.165 \mid (1 - \exp(-\tau_{opt}))/(1 - (1 - \mu_s)\exp(-\tau_{opt})), & K_T > 0.80 \end{cases} \quad (3.32)$$

where $K_T = RG/(C_s \mu_s)$ is the clearness index, $RG = S\downarrow$ is the global solar irradiance at bottom of atmosphere, $C_s = 1368\ W\ m^{-2}$ the terrestrial solar radiation constant, μ_s is the cosine of the solar zenith angle), and τ_{opt} is the aerosol optical thickness. Consequently, $RG = RG_{dir} + RG_{diff} = RG_{dir} + fd \cdot RG$.

Figure 11 illustrates the estimated compared to observed fraction of diffuse (fd) radiation. The sample data used for the diagram was collected at the Bensalem site in Tunisia. The global incoming radiation was measured using a pyranometer with a hemispherical view while the direct radiation was observed using a narrow-view pyrheliometer. Generally, the trend is well reproduced with a relatively large observation band being observed.

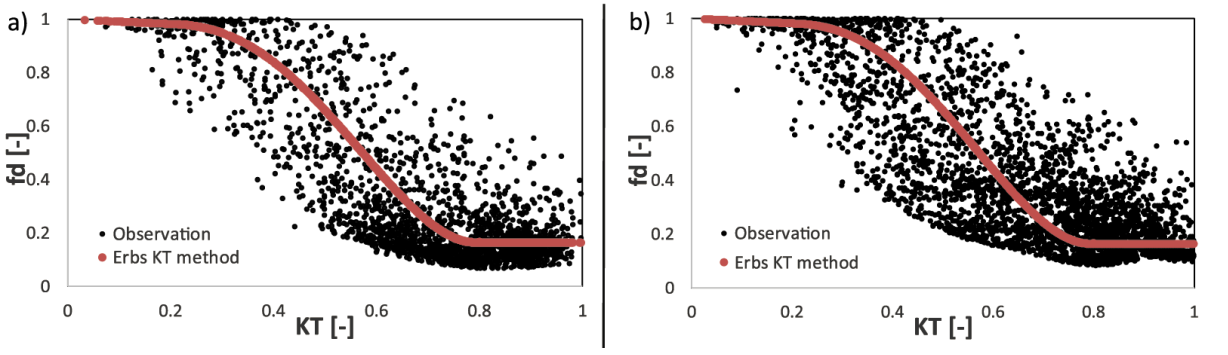

Figure 11: fd (fraction of incoming diffuse radiation) plots using Erbs et al.'s (1982) clearness index (K_T) method on BenSalem dataset for years a) 2014 and b) 2016

3.1.4. Sun angles

In addition to the nadir direction, solar as well as viewing (an algorithm for the polar orbiter's view angles is presented in section 6.2.2) directions are important in radiative and surface energy balance partitioning as they help to respectively describe the solar irradiance and thermal radiance observed by a remote sensor.

Sun angles: zenith and azimuth (SZA, θ_i and SAA, ϕ_i)

Many algorithms applied to estimate the incident solar radiation at any location on the globe at any time require such solar information together with details related to the optical depth of the atmosphere (e.g. Equation (2.4)). Sun angles algorithms can be used to accurately calculate the position of the Sun for any location at any given time (Campbell & Norman, 1998a; Iqbal, 1983).

The solar zenith angle ($\theta_i = \cos^{-1}\mu_i = \pi - \beta_i$)is derived from:

$$\mu_i = \sin\beta_i = \sin\phi\sin\delta + \cos\varphi\cos\delta\cos ha \tag{3.33}$$

where β_i is the solar elevation/altitude, φ is the latitude; $ha = 15(t - t_0)$ is the hour angle; t is time and t_0 is the time of solar noon, δ is the solar declination (i.e., the angle between line joining the centers of the Sun and the Earth to the Equatorial plane), which can be calculated as (series from Fourier analysis (Spencer, 1971)):

$$\begin{aligned}\delta = {} & 0.006918 - 0.399912\cos da + 0.070257\sin da - 0.006758\cos[2\cdot da] \\ & + 0.000907\sin[2\cdot da] - 0.002697\cos[3\cdot da] \\ & + 0.00148\sin[3\cdot da]\end{aligned} \tag{3.34}$$

$da = 2\cdot\pi\cdot(d_n - 1)/365$ is the day angle, d_n being the day number of the year. While 365 days/year is assumed and used as the denominator here, the days in a particular year according to the Gregorian calendar may be applied (i.e., for leap years).

The solar azimuth angle (ϕ_i) is then derived from:

$$\cos(\pi - \phi_i) = -\frac{\sin\varphi\sin\beta_i - \sin\delta}{\cos\varphi\cos\beta_i} \tag{3.35}$$

Sun path diagram

For any point on Earth, it is possible to locate the Sun's position at any time by using solar algorithms as described above. A Sun path diagram acts as a visual aid that can help to easily position the Sun throughout the year. It plots the path of the Sun at any local geographical coordinate (normally longitude-independent) on any particular day from sunrise to sunset (*date lines*). Within these *date lines*, *hour lines (Analemmas)* can be deciphered that provide the hourly position of the Sun throughout a given year. Typical sun path diagrams for three latitudes are illustrated below.

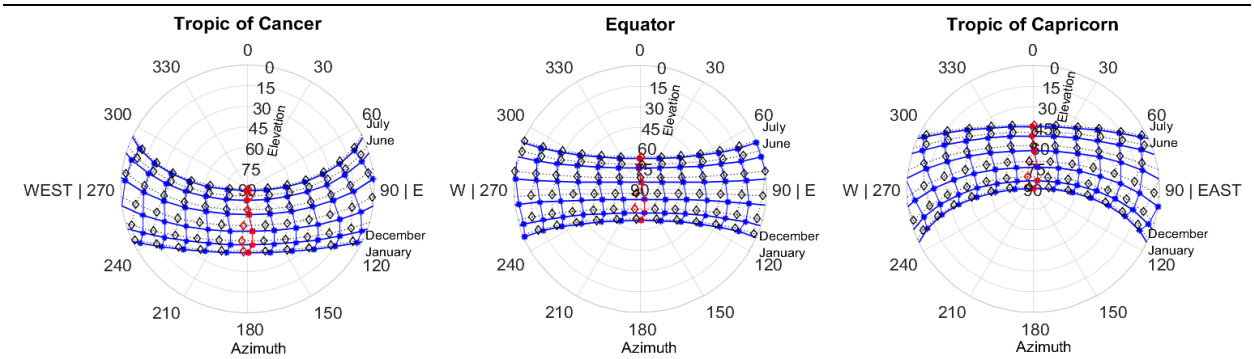

Figure 12: Sun path diagrams summarizing sun angles for (from left to right): the Northern Tropic, Equator and Southern Tropic. Typical solar noon analemmas in red with morning and afternoon hour lines to the right and left, respectively. January to June datelines (solid) and July to December datelines (dotted)

Since earth observing satellites have laid-down design criteria/specifications (for example, satellite altitude, orbit orientation, scan angle, local overpass time, etc.), it is possible to combine Sun path diagrams with view geometry information for easy visualization of the Sun-Earth-sensor geometry (see depictions in Figure 2, Figure 46).

3.1.5. Incoming longwave radiation (overcast and clear–sky days)

Generally, remotely sensed data applied in surface energy balance modelling is mostly usable during clear-sky days. This is because information from overcast/cloudy days can be contaminated due to atmospheric absorption in the sensing spectral ranges (in particular the ozone absorption range around the 10 um wavelength). Additionally, when deriving the incoming longwave radiation (part of the radiative balance), the calculation of atmospheric emission needs to account for any clouds (since the apparent emissivity

of cloudy skies is higher than that of clear-sky conditions).

To identify clear days, we first apply the $\mathrm{Meeus99}$ scheme detailed in Annear and Wells (2007).

Meeus99 (clear and cloudy days)

In Meeus99 method (as described in Annear and Wells (2007)), the clear-sky solar radiation is computed as a function of the parameterized ground surface reflectivity, atmospheric albedo, direct and scattered radiation. Clear-sky (and overcast) conditions are identified by comparing the observed solar radiation at the bottom of the atmosphere with the estimated clear-sky radiation:

$$\mathrm{R_{gcs}} = \frac{\varphi_\mathrm{d} + \varphi_\mathrm{i}}{1 - \mathrm{r_g} \cdot \mathrm{r_s}} \tag{3.36}$$

where φ_d and φ_i are the direct and scattered radiances in clear-sky conditions. $\mathrm{r_g}$ is the reflectivity of the ground surface, i.e. the fraction of the incident radiation reflected back into the atmosphere (it is dependent on the surface material and the angle of the sun), $\mathrm{r_s}$ the atmospheric albedo. The direct and scattered solar radiations are estimated according to Bird and Hulstrom (1981). Equation (3.36) should be equivalent to Equation (2.4) with a clear atmosphere's transmissivity.

Incident sky radiance

The incoming longwave radiation is one of the four components of the radiative budget (see Equation (2.1)). As a consequence, it also contributes to the outgoing thermal radiation (i.e., the reflected thermal radiation, which is scaled in the direction of the TIR sensor using the method described in section 3.1.2). Here, the incoming sky radiance is estimated according to Brutsaert's (1975) analytical method, i.e., $\mathrm{RA} = \varepsilon_\mathrm{a}^\mathrm{cs}\sigma\mathrm{T_a^4}$. The apparent emissivity of the atmosphere (clear-sky) is written as,

$$\varepsilon_\mathrm{a}^\mathrm{cs} = 1.24(\mathrm{e_a}/\mathrm{T_a})^{\frac{1}{7}} \tag{3.37}$$

where $\mathrm{e_a}$ and $\mathrm{T_a}$ are the air vapor pressure and temperature, respectively. This method, however, only applies to clear skies and it is therefore necessary to have corrections for overcast days.

While Brutsaert's (1975) method is kept for the clear sky days, it is modified according to Brutsaert (1982) - as detailed in Herrero and Polo (2012) - for the apparent emissivity in cloudy conditions. The method introduces a parameterized factor (F) that scales the clear-sky emissivity to cloudy conditions. The apparent emissivity is thus defined as,

$$\varepsilon_a = F\varepsilon_a^{cs} = (1 + CN^2)\varepsilon_a^{cs} \quad (3.38)$$

C is a cloud dependent coefficient (originally set to 0.22 in Brutsaert (1982) but herein tuned using the incoming longwave measurements) and N, also an atmosphere-dependent coefficient, is parameterized as a function of clearness (K_T) and relative humidity (rh) following Herrero and Polo (2012), i.e., $N = 1 - 0.45K_T - 3.5 \cdot rh \cdot K_T + 4 \cdot rh^2 \cdot K_T$, with its limits set at [0 1], 0 for clear skies and 1 for total overcast skies. ε_a^{cs} is the clear-sky emission as defined in Equation (3.37). Since the C and N parameters (in cloudy conditions) will generally be higher than 0, the apparent emissivity in cloudy skies is estimated to be [realistically] higher than that in clear-sky conditions.

3.2. Available energy and turbulent fluxes: the energy budget

3.2.1. Net radiation

The incoming solar and sky radiations serve as initial inputs for the net radiation terms. The sunlit and shaded contribution functions detailed for the solar domain in Yan et al. (2012) and also applied (with some modifications) in the thermal spectrum by Bian et al. (2018) are used to partition the incoming short- and long-wave radiations between the sunfleck/shaded components. Presently, the turbid canopy radiative method by Taconet et al. (1986), which is in use in the standard SPARSE model, has been extended to incorporate the sunlit/shaded components (Equations (3.41) - (3.48)). The net short-wave ($\mathrm{RG_{xx}}$) and absorbed sky emission ($\mathrm{RA_{xx}}$) terms are separated from the unknown surface thermal emissions ($\mathrm{L^{\uparrow}_{TIRxx}} = \mathrm{f(T_{xx})}$) for the net radiation terms:

$$\mathrm{R_{n,xx}} = \mathrm{RG_{xx}} + \mathrm{RA_{xx}} + \mathrm{L^{\uparrow}_{TIRxx}} \quad (3.39)$$

$\mathrm{xx} = \mathrm{v, g}$ and $\mathrm{xx} = \mathrm{vs, vh, gs, gh}$ for SPARSE and SPARSE4, respectively; “v” and “g” denote the vegetation and the soil/ground surface sources, which can either be sunlit (“s”) or shaded (“h”) in the extended formulation. Like in the original SPARSE, the surface

emission terms ($L^{\uparrow}_{TIRxx}$) are defined around air temperature. The grey-body thermal emissions are defined around air temperature and estimated through a Taylor expansion:

$$\sigma T^4_{x=vs,vh,gs,gh} = \sigma(T_a + T_x - T_a)^4 \approx \boldsymbol{\sigma T_a^4} + \rho C_p \frac{\boldsymbol{4\sigma T_a^3}}{\rho C_p}(T_x - T_a) \approx \boldsymbol{X_{\varepsilon 1}} + \rho C_p \frac{\boldsymbol{X_{\varepsilon 2}}}{\rho C_p}(T_x - T_a) \quad (3.40)$$

Component emissions are written thusly:

$$\begin{aligned} L^{\uparrow}_{TIRvs} &\approx \frac{f_{vs}\left[(\varepsilon_v + \rho_v f_{vh})\left(\rho_g(1-f_{vh})f_{vs}\varepsilon_v + \varepsilon_g\right) + \varepsilon_v(\rho_v f_{vh} f_{vs}\varepsilon_v + f_{vh}\varepsilon_v - 2)\right]}{1 - f\rho_v\rho_g} X_{\varepsilon 1} \\ &+ \frac{X_{\varepsilon 2} f_{vs}}{\left(1 - f\rho_v\rho_g\right)}\{\varepsilon_v\left[(\varepsilon_v + \rho_v f_{vh})\rho_g(1-f_{vh})f_{vs} + \rho_v f_{vh} f_{vs}\varepsilon_v - 2\right](T_{vs} - T_a) \\ &+ f_{vh}\varepsilon_v^2(T_{vh} - T_a) \\ &+ (\varepsilon_v + \rho_v f_{vh})\left[(1-f_{sol})\varepsilon_g\left(T_{gs} - T_a\right) + f_{sol}\varepsilon_g\left(T_{gh} - T_a\right)\right]\} \end{aligned} \quad (3.41)$$

$$\begin{aligned} L^{\uparrow}_{TIRvh} &\approx \frac{f_{vh}\varepsilon_v\left[\left(\left(\rho_v f_{vs} + \rho_g\right)f_{vh} + f_{vs}\right)\varepsilon_v + \varepsilon_g - 2\right]}{1 - f\rho_v\rho_g} X_{\varepsilon 1} \\ &+ \frac{X_{\varepsilon 2} f_{vh}\varepsilon_v}{\left(1 - f\rho_v\rho_g\right)}\{f_{vs}\varepsilon_v(T_{vs} - T_a) \\ &+ \left[\left(\rho_v f_{vs} + \rho_g\right)f_{vh}\varepsilon_v - 2\right](T_{vh} - T_a) + (1-f_{sol})\varepsilon_g\left(T_{gs} - T_a\right) \\ &+ f_{sol}\varepsilon_g\left(T_{gh} - T_a\right)\} \end{aligned} \quad (3.42)$$

$$\begin{aligned} L^{\uparrow}_{TIRgs} &\approx \frac{(1-f_{sol})\varepsilon_g\left[(f - f_{vh}f_{vs})\varepsilon_v + \rho_v f_{vh}\varepsilon_g - 1\right]}{1 - f\rho_v\rho_g} X_{\varepsilon 1} \\ &+ \frac{X_{\varepsilon 2}(1-f_{sol})\varepsilon_g}{\left(1 - f\rho_v\rho_g\right)}\{(1-f_{vh})f_{vs}\varepsilon_v(T_{vs} - T_a) \\ &+ f_{vh}\varepsilon_v(T_{vh} - T_a) + \left[(1-f_{sol})\rho_v f_{vh}\varepsilon_g - 1\right]\left(T_{gs} - T_a\right) \\ &+ \rho_v f_{vh} f_{sol}\varepsilon_g\left(T_{gh} - T_a\right)\} \end{aligned} \quad (3.43)$$

$$L^{\uparrow}_{TIRgh} \approx \frac{f_{sol}\varepsilon_g\left[(f - f_{vh}f_{vs})\varepsilon_v + \rho_v f_{vh}\varepsilon_g - 1\right]}{1 - f\rho_v\rho_g} X_{\varepsilon 1}$$
$$+ \frac{X_{\varepsilon 2} f_{sol}\varepsilon_g}{\left(1 - f\rho_v\rho_g\right)}\left\{(1 - f_{vh})f_{vs}\varepsilon_v(T_{vs} - T_a) + f_{vh}\varepsilon_v(T_{vh} - T_a)\right. \quad (3.44)$$
$$\left. + \rho_v f_{vh}(1 - f_{sol})\varepsilon_g\left(T_{gs} - T_a\right) + \left(f_{sol}\rho_v f_{vh}\varepsilon_g - 1\right)\left(T_{gh} - T_a\right)\right\}$$

where $f = f_{vs} + f_{vh}$ (cover fraction) and $1 - f = f_{gs} + f_{gh}$ (gap fraction equivalent to the transmissivity to the background soil) are defined at nadir ($\cos(\text{vza}) = \cos(0^0) = 1$); $f_{sol} = f(\theta_s) = 1 - e^{-G \cdot LAI/\mu_s}$. $f_{vs} = K_c f$; $f_{vh} = K_t f$; $f_{gs} = K_g(1 - f)$ and $f_{gh} = K_z(1 - f)$. K_c, K_t, K_g and K_z are sunlit/shaded contribution terms as previously defined. α_v and α_g are the vegetation and soil albedos (reflectance in the optical domain) while $\rho_v = 1 - \varepsilon_v$ and $\rho_g = 1 - \varepsilon_g$ are the thermal reflectance for the vegetation and soil, respectively. While the exponential Beer's law (i.e. $1 - f = e^{-G \cdot LAI}$ for a homogeneous cover) is generally used to describe the transmission of radiation beams (e.g. Boulet et al., 2015; Braud et al., 1995; Taconet et al., 1986), attenuation of diffuse light occurs in all directions. An alternative option is thus made available. By assuming non-black leaves, an absorptivity term ($a = 0.5$ for total solar radiation) is introduced in the integrated transmission: $2\int_0^{\pi/2} e^{-\sqrt{a} \cdot G \cdot LAI/\mu} \sin(\theta)\cos(\theta)\, d\theta$ (Campbell & Norman, 1998b). Similarly, such transmission can be assumed for the direct solar radiation scattered from a Lambertian surface that resembles the conceptual Case 3 reflection (directional-hemispherical, Nicodemus et al., 1977; Schaepman-Strub et al., 2006).

The incoming solar and sky emission terms are partitioned as:

$$
\begin{aligned}
&RG_{vs} + RA_{vs} \\
&= RG_{dir}\left[f_{sol}(1-\alpha_v) + \frac{f_{vs}\alpha_g(1-f_{sol})[(1-\alpha_v)+\alpha_v f_{vh}]}{1-f\alpha_v\alpha_g}\right] \\
&+ f_{vs}RG_{diff}\left[(1-\alpha_v) + \frac{(1-\alpha_v)\left[\alpha_v f_{vh}(1-f_{vs}) + \alpha_g(1-f)\right] + \alpha_v f_{vh}\alpha_g(1-f)}{1-f\alpha_v\alpha_g}\right] \\
&+ f_{vs}RA\left[\varepsilon_v \right. \\
&\left. + \frac{\varepsilon_v\left[\rho_v f_{vh}(1-f_{vs}) + \rho_g(1-f)\right] + \rho_v f_{vh}\rho_g(1-f)}{1-f\rho_v\rho_g}\right]
\end{aligned} \tag{3.45}
$$

$$
\begin{aligned}
&RG_{vh} + RA_{vh} \\
&= RG_{dir}\left[\frac{f_{vh}\alpha_g(1-f_{sol})(1-\alpha_v)}{1-f\alpha_v\alpha_g}\right] + f_{vh}RG_{diff}\left[\frac{(1-\alpha_v)\left[1+\alpha_g(1-f)\right]+\alpha_v f_{vs}}{1-f\alpha_v\alpha_g}\right] \\
&+ f_{vh}RA\left[\frac{\varepsilon_v\left[1+\rho_g(1-f)\right]+\rho_v f_{vs}}{1-f\rho_v\rho_g}\right]
\end{aligned} \tag{3.46}
$$

$$
\begin{aligned}
&RG_{gs} + RA_{gs} \\
&= \frac{(1-\alpha_g)\left\{(1-f_{sol})\left[RG_{dir}\left(1+\alpha_v f_{vh}\alpha_g(1-f_{sol})\right) + \alpha_v f_{vh}\alpha_g(1-f)RG_{diff}\right] + f_{gs}RG_{diff}\right\}}{1-f\alpha_v\alpha_g} \\
&+ \frac{\varepsilon_g RA\left[f_{gs} + (1-f_{sol})\rho_v f_{vh}\rho_g(1-f)\right]}{1-f\rho_v\rho_g}
\end{aligned} \tag{3.47}
$$

$$
\begin{aligned}
RG_{gh} + RA_{gh} = &\frac{(1-\alpha_g)\left\{f_{gh}RG_{diff} + f_{sol}\alpha_v f_{vh}\alpha_g[(1-f_{sol})RG_{dir} + (1-f)RG_{diff}]\right\}}{1-f\alpha_v\alpha_g} \\
&+ \frac{\varepsilon_g RA\left[f_{gh} + f_{sol}\rho_v f_{vh}\rho_g(1-f)\right]}{1-f\rho_v\rho_g}
\end{aligned} \tag{3.48}
$$

3.2.2. Energy balance scheme

Recalling from above, the SPARSE surface energy balance model (Boulet et al., 2015) is based on the two-source TSEB (Norman et al., 1995) rationale. In SPARSE, however, the potential canopy latent flux is estimated through a Penman-Monteith approximation, differing from the classic TSEB which utilizes the Priestley-Taylor method. SPARSE also employs bounding similar to SEBS (Su, 2002) where theoretical potential and fully

stressed flux limits for the soil and vegetation are derived.

The net radiation ($R_{n,xx}$) terms according to Equation (3.39) are partitioned for retrieval of the soil (G), sensible (H) and latent (λE) heat fluxes. The available energy is thus written as:

$$R_{n,xx} - G = R_{n,xx}(1- \xi) = \lambda E_{xx} + H_{xx} \tag{3.49}$$

ξ is the fraction of soil/ground net radiation stored in the soil, i.e., $\xi = G/R_{ng}$. Therefore, $\xi = 0$ for the vegetation layers. For diurnal variations of the ground heat storage, the sinusoidal function by Santanello and Friedl (2003) is also included, i.e., $\xi = \xi_{max} \cdot \cos[2\pi(t + 10800)/B]$; t [s] is the time relative to solar noon, B [s] is a deviation minimization factor while 10800 [s] accounts for the three-hour lag between the maximum incoming radiation and maximum fraction (ξ_{max}).

Soil and vegetation component latent fluxes are treated as representative averages for the surface (here $gx = g \text{ and } vx = v$ for SPARSE; and $gx = gs, gh \text{ and } vx = vs, vh$ for SPARSE4):

$$\lambda E_g = \sum_{gx} \frac{\rho C_p}{\gamma} \beta_s \frac{e_{sat}(T_{gx}) - e_0}{r_{as}} \tag{3.50}$$

$$\lambda E_v = \sum_{vx} \frac{\rho C_p}{\gamma} \beta_v \frac{e_{sat}(T_{vx}) - e_0}{r_{vv}} \tag{3.51}$$

likewise, the component sensible heat fluxes are defined as:

$$H_g = \sum_{gx} \rho C_p \frac{T_{gx} - T_0}{r_{as}} \tag{3.52}$$

$$H_v = \sum_{vx} \rho C_p \frac{T_{vx} - T_0}{r_{av}} \tag{3.53}$$

where ρC_p denotes the volumetric heat capacity of air, γ the psychrometric constant, $e_{sat}(T_{xx}) = e_{sat}(T_a) + \Delta(T_{xx} - T_a)$ is the saturated vapour pressure at temperature T_{xx}, Δ the slope of the vapour pressure-temperature curve at T_a. e_0 is the partial vapor pressure at the aerodynamic level; r_{as} is the soil to aerodynamic level resistance, and $r_{vv} = r_{av} + r_{sto}$ the minimum total resistance for latent heat exchange between the vegetation and

the aerodynamic level; r_{av} is the vegetation-to-aerodynamic level resistance; r_{sto} is the canopy stomatal resistance (defined below). β_s, β_v are the respective evaporation and transpiration efficiencies, defined as the ratio between actual and unstressed latent heat fluxes in actual surface conditions, functionally equivalent to soil and vegetation surface conductances, respectively. For the dependence of aerodynamic resistance to stability correction, the aerodynamic temperature (T_0), component temperatures (T_{xx}), energy fluxes and e_0 are solved and updated iteratively (Richardson number) until convergence. Similar to SPARSE, aerodynamic resistances are expressed according to Shuttleworth and Gurney (1990). Surface components very often alternate between sun and shade and we therefore assume no clear distinction between sunlit/shaded elements. Thus, only the soil and vegetation sources are distinguished with similar (evaporation/transpiration) efficiencies applying to both sunlit/shaded sources.

Canopy stomatal conductance

While Chen and Liu (2020) observe that shortcomings resulting from theoretical and practical issues are more serious in big-leaf photosynthesis than in big-leaf evapotranspiration models, they recommend theoretical consistency in conductance formulation and aggregation. Owing to the inter-dependence between stomatal conductance and assimilation rate in Ball-Berry schemes (e.g., Collatz et al., 1991; Medlyn et al., 2011), and the necessity to have a method that is theoretically consistent with the physics of the original model, we prefer and consequently retain a conductance scheme that considers the product of several relevant environmental factors as used in SPARSE (Boulet et al., 2015; Braud et al., 1995; Noilhan & Planton, 1989; Olioso et al., 1995). We follow the method by Sinclair et al. (1976) who implemented an irradiance-dependent conductance method for sunfleck/shaded leaves, which is more compatible with SPARSE's model structure. Of critical importance is the proper scaling from leaf to canopy stomatal conductance using the respective sunlit/shaded leaf area indices (LAI_{vx}). The stomatal resistance (r_{sto}) to be aggregated for the minimum resistance to latent heat ($r_{vv} = r_{av} + r_{sto}$) as used in Equation (3.51) is thus written as:

$$r_{sto} = \frac{r_{stmin} \prod f}{LAI_{vx}} \qquad (3.54)$$

where r_{stmin} is the minimum stomatal resistance; $\prod f = f_{Rg} f_{ea}$ is the product of environmental factors - f_{Rg} is the radiation factor, which measures the influence of photosynthetically active radiation and f_{ea} is the vapor pressure deficit factor, which represents the effects of vapor pressure deficit of the atmosphere on the surface resistance (Braud et al., 1995; Noilhan & Planton, 1989; Olioso et al., 1996). Note that, as r_{sto} is currently formulated, the impacts of temperature and soil moisture are not considered and are thus accounted through the vegetation efficiency (β_v).

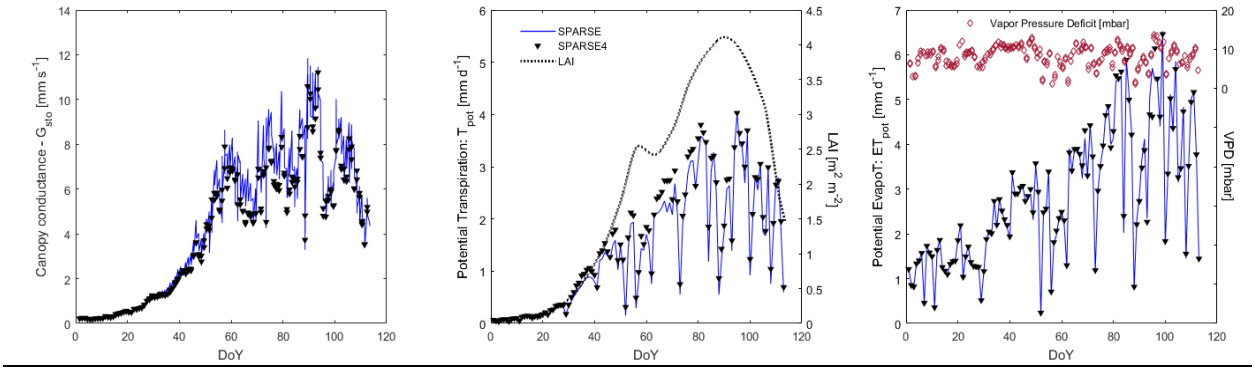

Figure 13: Calculated canopy conductance, potential transpiration and potential evapotranspiration - computed using data from the R3 wheat site

Figure 13 illustrates the canopy conductance from SPARSE compared to SPARSE4 (modified and rescaled according to Equation (3.54)) at the R3 site (see data description in Section 2.2.2). Also shown are the daily potential transpiration and evapotranspiration rates over the wheat growing cycle. In conditions where water is not limiting (potential), the extended scheme should ideally simulate latent fluxes equivalent to SPARSE since the saturation demand due to the atmospheric vapor deficit is the same in both cases. The modified and rescaled canopy conductance reduces the deviations - from the SPARSE reference - of the potential latent energy estimates. This improvement, which is mostly apparent when the surface is relatively well vegetated, allows a better and physically consistent representation of the near land-surface conditions.

In SPARSE (and hence SPARSE4), the stomatal conductance ($g_{sto} = 1/r_{sto}$) is coupled with the vegetation efficiency (β_v), a term that is related to the plant-water stress, to derive the latent fluxes. The efficiency can be viewed here as a separate conductance term that represents the impact of water stress (related to soil moisture in the root zone) on the vegetation. Coupling the two conductance terms allows the derivation of flux estimates in

potential as well as in prevailing/actual conditions.

3.3. Implementation

SPARSE ($xx = v, g$) separately solves the radiative and energy budgets for the soil (g) and vegetation (v) sources. The two continuity equations (Equations (3.55.b) and (3.55.c)) and two energy balance equations, together with the link between the component temperatures and the out-of-canopy radiance (Equation (2.13)) are thus solved for the 6 unknowns, i.e., $T_{xx=g,v}$, T_0, e_0, β_v & β_s. For the new version SPARSE4, there are four components ($xx = vs, vh, gs, gh$) since each source - soil (g) or vegetation (v) - is split into a sunlit (s) and a shaded (h) component. This leads to four energy budget and two continuity equations, which together with the out-of-canopy thermal link (Equation (3.1)) are to be solved to retrieve the 8 unknowns: $T_{xx=vs,vh,gs,gh}$, T_0, e_0, β_v & β_s. Therefore, for both SPARSE and SPARSE4, the system of equations is underdetermined and one unknown must be fixed a priori. The energy budget and continuity equations are written as:

$$\begin{cases} (R_n - G) - (H + \lambda E) = \sum_{xx} R_{n,xx}(1- \xi) - (H_{xx} + \lambda E_{xx}) = 0 & (3.55.a) \\ \rho C_p \dfrac{T_0 - T_a}{r_a} = H = \sum_{xx} H_{xx} & (3.55.b) \\ \dfrac{\rho C_p}{\gamma} \dfrac{e_0 - e_a}{r_a} = \lambda E = \sum_{xx} \lambda E_{xx} & (3.55.c) \end{cases}$$

where r_a is the aerodynamic-to-reference level resistance; and as noted earlier in the section, ξ only applies to the soil and is set to zero for vegetation elements. Other terms are as defined above.

SPARSE can be run in either ‘retrieval’ (‘inverse’) or ‘prescribed’ (‘forward’) modes. Similar to TSEB, both modes assume the soil surface layer dries first while the vegetation transpires at potential rate ($\beta_v = 1$). In the ‘prescribed’ mode, the soil evaporation and vegetation transpiration efficiencies are known and the SPARSE4 model uses a 4-by-4 (2-by-2 for SPARSE) energy budget matrix system to solve for the fluxes and temperatures directly. For consistency, the ‘prescribed’ mode is used herein as it allows

a more straightforward separation of the interacting terms and thus get rid of the system's under-determination. The transpiration efficiency is therefore prescribed by initially setting it to ($\beta_v = 1$) and the system of equations solved iteratively by decreasing β_s incrementally from ($\beta_s = 1$) till a value that minimizes the difference between the observed and simulated T_{rad}. If a minimum difference is not reached and the soil is dry (β_s, thus evaporation, close to 0), then one assumes that the vegetation is undergoing stress. β_s is then at its minimum (e.g., $\beta_s \approx 0$) and, similarly, β_v is decreased incrementally until the difference between the observed and simulated radiative temperatures is minimal (i.e. simulated T_{rad} ≈ observed T_{rad}).

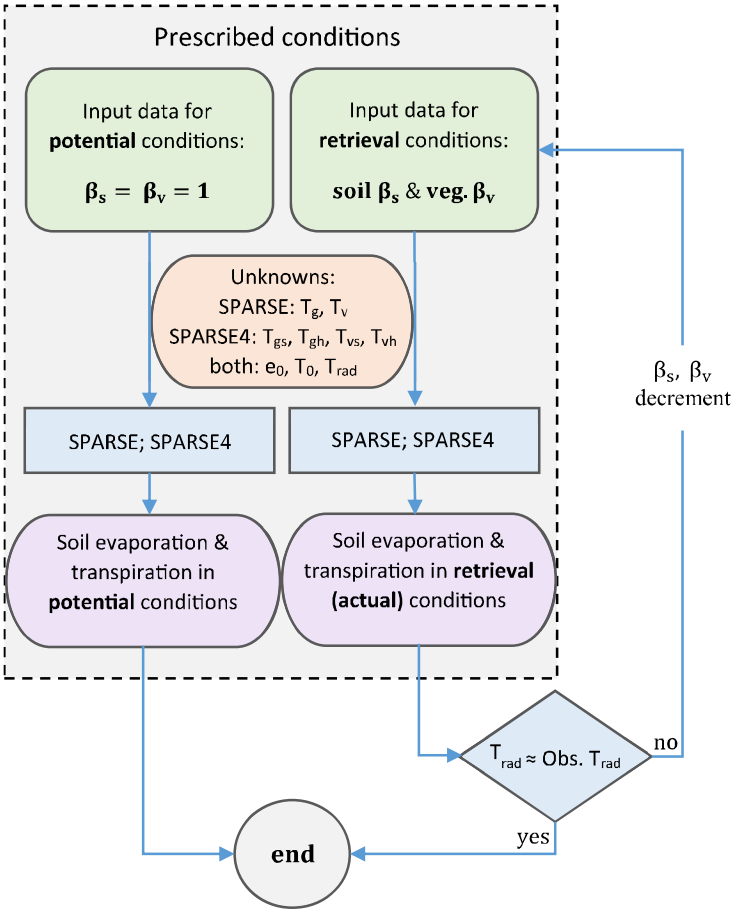

Figure 14: The model flow diagram (adapted from Boulet et al. (2015))

The simultaneous retrieval procedure of the fluxes and temperatures from the energy and radiative set of equations is illustrated by Figure 14 and summarized by Equations (3.55.a), (3.55.b) and (3.55.c). That is: the incoming short- and longwave radiation fluxes

are partitioned between the components; a first guess of the aerodynamic temperature then provides a solution for the component emissions (thus temperatures) for onward derivation of the initial component fluxes; the temperature and partial vapor pressure at the aerodynamic level are then iteratively computed for stability convergence (Richardson number – see Chapter 3, section I). By modulating the evaporation/transpiration efficiencies, i.e. applying a linear decrement of the efficiencies, the procedure can be repeated until the surface temperature boundary condition is met (i.e. simulated ≈ observed surface temperature).

Model formulation: SPARSE4

A matrix with the linearized set of energy balance equations (Equations (3.55.a), (3.55.b) and (3.55.c)) is implemented and solved simultaneously. The left-hand side (LHS) contains the forcing coefficients and the set of temperature unknowns ($T_{xx} - T_a$; $xx: vs, vh, gs, gh$) with the knowns in the right-hand side (RHS). The augmented matrix to be solved is written thusly:

$$\left(\begin{array}{cccc|c} a_{11} & a_{12} & a_{13} & a_{14} & b_1 \\ a_{21} & a_{22} & a_{23} & a_{24} & b_2 \\ a_{31} & a_{32} & a_{33} & a_{34} & b_3 \\ a_{41} & a_{42} & a_{43} & a_{44} & b_4 \end{array}\right) \tag{3.56}$$

where the LHS forcing coefficient terms (a_{ij}) are:

$$\begin{pmatrix} \frac{\rho C_p}{r_{av}} + \frac{\rho C_p \Delta\beta_v}{\Upsilon r_{vv}} & -L^{\uparrow}_{TIRvs(3)} & -L^{\uparrow}_{TIRvs(4)} & -L^{\uparrow}_{TIRvs(5)} \\ -L^{\uparrow}_{TIRvs(2)} & & & \\ -L^{\uparrow}_{TIRvh(2)} & \frac{\rho C_p}{r_{av}} + \frac{\rho C_p \Delta\beta_v}{\Upsilon r_{vv}} & -L^{\uparrow}_{TIRvh(4)} & -L^{\uparrow}_{TIRvh(5)} \\ & -L^{\uparrow}_{TIRvh(3)} & & \\ -L^{\uparrow}_{TIRgs(2)} x_g^c & -L^{\uparrow}_{TIRgs(3)} x_g^c & \frac{\rho C_p}{r_{as}} + \frac{\rho C_p \Delta\beta_s}{\Upsilon r_{as}} & -L^{\uparrow}_{TIRgs(5)} x_g^c \\ & & -L^{\uparrow}_{TIRgs(4)} x_g^c & \\ -L^{\uparrow}_{TIRgh(2)} x_g^c & -L^{\uparrow}_{TIRgh(3)} x_g^c & -L^{\uparrow}_{TIRgh(4)} x_g^c & \frac{\rho C_p}{r_{as}} + \frac{\rho C_p \Delta\beta_s}{\Upsilon r_{as}} \\ & & & -L^{\uparrow}_{TIRgh(5)} x_g^c \end{pmatrix} \tag{3.56.lhs}$$

and the RHS (b_i):

$$\begin{pmatrix} \mathrm{RG_{vs}} + \mathrm{RA_{vs}} + \mathrm{L^{\uparrow}_{TIRvs(1)}} - \left(\frac{\rho \mathrm{C_p} \beta_v}{\Upsilon \mathrm{r_{vv}}} [\mathrm{e_{sat}}(\mathrm{T_a}) - \mathrm{e_0}] - \frac{\rho \mathrm{C_p}}{\mathrm{r_{av}}} (\mathrm{T_0} - \mathrm{T_a})\right) \\ \mathrm{RG_{vh}} + \mathrm{RA_{vh}} + \mathrm{L^{\uparrow}_{TIRvh(1)}} - \left(\frac{\rho \mathrm{C_p} \beta_v}{\Upsilon \mathrm{r_{vv}}} [\mathrm{e_{sat}}(\mathrm{T_a}) - \mathrm{e_0}] - \frac{\rho \mathrm{C_p}}{\mathrm{r_{av}}} (\mathrm{T_0} - \mathrm{T_a})\right) \\ \left(\mathrm{RG_{gs}} + \mathrm{RA_{gs}} + \mathrm{L^{\uparrow}_{TIRgs(1)}}\right) \mathrm{x_g^c} - \left(\frac{\rho \mathrm{C_p} \beta_s}{\Upsilon \mathrm{r_{as}}} [\mathrm{e_{sat}}(\mathrm{T_a}) - \mathrm{e_0}] - \frac{\rho \mathrm{C_p}}{\mathrm{r_{as}}} (\mathrm{T_0} - \mathrm{T_a})\right) \\ \left(\mathrm{RG_{gh}} + \mathrm{RA_{gh}} + \mathrm{L^{\uparrow}_{TIRgh(1)}}\right) \mathrm{x_g^c} - \left(\frac{\rho \mathrm{C_p} \beta_s}{\Upsilon \mathrm{r_{as}}} [\mathrm{e_{sat}}(\mathrm{T_a}) - \mathrm{e_0}] - \frac{\rho \mathrm{C_p}}{\mathrm{r_{as}}} (\mathrm{T_0} - \mathrm{T_a})\right) \end{pmatrix} \quad (3.56.\mathrm{rhs})$$

$\mathrm{x_g^c} = 1 - \mathrm{x_g}$ is the complement. Each of the four thermal emission functions ($\varepsilon_{\mathrm{TIRxx}}$) is split into five terms, i.e., $\mathrm{L^{\uparrow}_{TIRxx}} = \mathrm{f}\left(\mathrm{X_{\varepsilon 1}}, \mathrm{X_{\varepsilon 2}}(\mathrm{T_{vs}} - \mathrm{T_a}), \mathrm{X_{\varepsilon 2}}(\mathrm{T_{vh}} - \mathrm{T_a}), \mathrm{X_{\varepsilon 2}}\left(\mathrm{T_{gs}} - \mathrm{T_a}\right), \mathrm{X_{\varepsilon 2}}\left(\mathrm{T_{gh}} - \mathrm{T_a}\right)\right) = \mathrm{L^{\uparrow}_{TIRvs(1)}} + \mathrm{L^{\uparrow}_{TIRxx(2)}}(\mathrm{T_{vs}} - \mathrm{T_a}) + \mathrm{L^{\uparrow}_{TIRxx(3)}}(\mathrm{T_{vh}} - \mathrm{T_a}) + \mathrm{L^{\uparrow}_{TIRxx(4)}}\left(\mathrm{T_{gs}} - \mathrm{T_a}\right) + \mathrm{L^{\uparrow}_{TIRxx(5)}}\left(\mathrm{T_{gh}} - \mathrm{T_a}\right)$. $\mathrm{X_{\varepsilon 1}}$ and $\mathrm{X_{\varepsilon 2}}$ are the grey-body emission terms as previously defined. While solving the augmented matrix, the soil evaporation efficiency (β_s) is initially reduced while keeping the transpiration efficiency at potential ($\beta_v = 1$). If the minimum soil evaporation efficiency, β_s is reached before convergence, the β_v is then tuned. This iterative procedure continues until the simulated directional temperature converges to the input observation.

Concluding remarks

In this chapter, the various radiative and energy balance theories as used and implemented in the current work are detailed. The soil plant atmosphere remote sensing of evapotranspiration (SPARSE) is extended to account for the Sun-Earth-sensor geometry (SPARSE4). Briefly, SPARSE is a dual source surface energy balance scheme that characterizes land processes (radiation and turbulent fluxes) by inverting the temperature of the surface, which acts as a proxy for the prevailing water status. It is composed of a set of aerodynamic and linearized energy budget equations of the two (soil and vegetation) sources, and the link of the component emissions to the out-of-canopy thermal signal as observed by a remote sensor. Here, the sunlit and shaded

elements of the classic two source SPARSE model are thus discriminated. In addition to nadir (or zenith) direction, the solar and viewing directions are important in the description of prevailing surface fluxes using directional surface temperatures. Accordingly, Erbs et al.'s (1982) method that partitions the incoming solar radiation into its diffuse and direct components is first incorporated. A radiative model (the unified Francois model, UFR97) that is capable of describing the solar-surface-observer geometry is then coupled with the extended energy balance scheme, SPARSE4. In addition to homogenous canopies, the UFR97 model also considers heterogeneous scenes, for example for row canopies. Other methods, such as the brightness temperature scaling method (to account for the sensing range of most thermal infrared radiometers), are also incorporated.

In the following, the methods presented herein are analysed and evaluated. In particular, the original and extended schemes are used to simulate exchanges at the near land surface and subsequently evaluated using data (both from real observations and synthetic).

Chapters 4, 5, 6: Characterization of the land surface: analyses and evaluations of the extended SPARSE using observations and complex models

In the following Chapters, the assessments and analyses of previously presented methods are summarized. That is,

- *A description of the experimental sites and datasets used in the evaluations*
- *Modeling of surface components and their subsequent evaluations over the various vegetated canopies*
- *Evaluation of the synthetic experiments: directionality consistency*
- *Finally, preliminary results from contextual evapotranspiration modeling exercises are presented*

Ces chapitres, les évaluations et les analyses des méthodes présentées précédemment sont résumées. A savoir,

- *Une description des sites expérimentaux et des ensembles de données utilisés dans les évaluations*
- *Modélisation des composantes de surface et leurs évaluations ultérieures sur les différents couverts végétaux*
- *Évaluation des expériences synthétiques : cohérence de la directionnalité*
- *Enfin, les résultats des exercices de modélisation de l'évapotranspiration contextuelle sont présentés*

The chapters present evaluations using datasets (collected over several flux sites and synthetic). The datasets as used to drive and assess the surface energy balance models are contained and described within the next sections, which are organized in manuscript format. In the first part (Chapter 4), the surface energy balance methods (SPARSE and SPARSE4) are evaluated using datasets over diverse canopies. Chapter 5 then describes further evaluations carried out using data collected from a vineyard field campaign. The last part describes synthetic experiments, which separately relate to: 6.1*)* point-based SEB, and 6.2*)* initial analyses carried out on contextual SEB.

Chapter 4: Analyses and evaluations of the extended SPARSE - Assessments over diverse canopies

This section is based on methods described in Chapter 3 (as reported in Mwangi et al. (2022))

Summary

The spatial distribution of evapotranspiration is often obtained from dual source energy balance models forced by surface temperature data. The use of multi-angular remotely-sensed thermal data in such methods makes them susceptible to directional-anisotropy/thermal-radiation directionality effects that may result from the satellite's position, relative to the Sun, at overpass time. It is therefore important to have these effects accounted for to ensure realistic flux retrievals irrespective of sensor viewing position. At present, dual source models generally interpret surface temperature according to two sources, representing the soil surface and the vegetation. This may be insufficient to adequately represent the limiting temperature conditions that not only depend on the source type but also their exposure to the Sun. Here, we present a modified version of the SPARSE (Soil Plant Atmosphere Remote Sensing Evapotranspiration) model, wherein the original SPARSE is modified to incorporate sunlit/shaded soil/vegetation elements and coupled with a radiative transfer model that links these four component emissions to out-of-canopy directional radiances as observed by remote sensors. An initial evaluation is carried out to check the model's capability in retrieving surface fluxes over diverse environments instrumented with in-situ thermo-radiometers. When run with nadir-acquired thermal data, both algorithms show no observable difference in their retrieval of total fluxes. We nonetheless show that by incorporating the solar direction and discriminating between sunlit and shaded elements, the partitioning of these overall fluxes between the soil and vegetation can be improved especially in water-stressed environments. We also test the sensitivity of flux and component temperature estimates to the viewing direction of the thermal sensor by using two sets of TIR data (nadir and oblique) acquired simultaneously to force the models and show that sensitivity to viewing direction is significantly reduced. This is an important aspect particularly when using high resolution spatial and temporal data from Earth observation missions that inherently have to consider a wide-range of viewing angles in their design.

Keywords: Evapotranspiration, thermal infrared radiation (TIR), Soil Vegetation Atmosphere Transfer (SVAT), temperature inversion.

Résumé

La distribution spatiale de l'évapotranspiration est souvent obtenue à partir de modèles de bilan énergétique à double source forcés par des données de température de surface. L'utilisation de données thermiques télédétectées multiangulaires dans ces méthodes les rend sensibles aux effets de directionnalité de l'anisotropie et du rayonnement thermique qui peuvent résulter de la position du satellite par rapport au Soleil au moment du passage. Il est donc important de tenir compte de ces effets pour garantir des récupérations de flux réalistes, quelle que soit la position de visée du capteur. Actuellement, les modèles à double source interprètent généralement la température de surface selon deux sources, représentant la surface du sol et la végétation. Cela peut s'avérer insuffisant pour représenter adéquatement les conditions de température limites qui dépendent non seulement du type de source mais aussi de leur exposition au soleil. Nous présentons ici une version modifiée du modèle SPARSE (Soil Plant Atmosphere Remote Sensing Evapotranspiration), dans laquelle le modèle SPARSE original est modifié pour incorporer des éléments de sol et de végétation éclairés par le soleil et ombragés, et couplé à un modèle de transfert radiatif qui relie ces quatre composantes d'émissions aux radiances directionnelles hors canopée telles qu'observées par les capteurs à distance. Une évaluation initiale est effectuée pour vérifier la capacité du modèle à récupérer les flux de surface sur divers environnements instrumentés avec des thermo-radiomètres in-situ. Lorsqu'ils sont exécutés avec des données thermiques acquises au nadir, les deux algorithmes ne montrent aucune différence observable dans leur récupération des flux totaux. Nous montrons néanmoins qu'en incorporant la direction du soleil et en discriminant les éléments éclairés et ombragés, la partition de ces flux globaux entre le sol et la végétation peut être améliorée, en particulier dans les environnements soumis à un stress hydrique. Nous testons également la sensibilité des estimations de flux et de température des composants à la direction de visée du capteur thermique en utilisant deux ensembles de données TIR (nadir et oblique) acquises simultanément pour forcer les modèles et montrer que la sensibilité à la direction de visée est considérablement réduite. Il s'agit d'un aspect important, en particulier lors de l'utilisation de données spatiales et temporelles à haute résolution provenant de missions d'observation de la Terre qui, par nature, doivent tenir compte d'une large gamme d'angles de vue dans leur conception.

Mots clés : Evapotranspiration, rayonnement infrarouge thermique (TIR), transfert sol-végétation-atmosphère (SVAT), inversion de température.

4.1. Introduction

Here we present an evaluation of the extended SPARSE scheme. Most of the literature

on the theory has been described and presented in the earlier sections (particularly Chapter 3). The following sub-sections therefore build on the framework presented in Chapter 3, which details the coupled SPARSE-UFR97 model (hereafter SPARSE4) meant for inverting directionally anisotropic thermal data for evapotranspiration and water stress estimation were described. By coupling SPARSE with the UFR97 radiative method, the original scheme was extended from a two- (soil/vegetation) to a four-component (sunlit/shaded soil/vegetation) formulation. The dual-source SPARSE model, which inverts surface temperature for source emissions and separate retrieval of soil evaporation and vegetation transpiration fluxes, has already been extensively assessed and shown to be capable of reasonably estimating and partitioning turbulent fluxes. The theoretical and implementation aspects behind the original and extended SPARSE models have been introduced in the previous chapter. In the following, these formulations are evaluated and their performance analyzed using field measurements collected from diverse environments, which include two olive Orchards and two other experimental sites (cultivated with soybean and wheat). Finally, conclusions are drawn and outlooks on continuing and future works with respect to thermal radiation directionality assessments are presented.

4.2. Data over diverse canopies

The datasets used to initialize / run the models and for performance evaluations are drawn from four contrasting sites. Two Olive Orchards located in: Nasrallah, Tunisia (Latitude, Longitude: 35.30° N, 9.92° E: 2014) and Agdal, Morocco (31.60° N, 7.98° W: 2003) with vegetation cover fractions of ~7% (Chebbi et al., 2018) and ~60% (Er-Raki et al., 2009), respectively. Experimental datasets for the other two sites were collected during the growing periods of Soybean: 1990 (Avignon: 43.90° N, 4.80° E, France; Olioso et al., 1996) and flood-irrigated wheat: 2004 (R3: 31.67° N, 7.59° W, Morocco; Duchemin et al., 2006), hence varying vegetation cover fractions.

Table 2: Model data requirement

Data	Source	Range
	Characteristics (both model formulations)	
Surface albedo [-]	*Field: i.e. $S\uparrow/S\downarrow$*	varying
Vegetation albedo; soil and vegetation emissivity [-]	*Literature*	~0.15-0.25; 0.96, 0.98
Bio-physical parameters: leaf area index (LAI – [$m^2 m^{-2}$]), leaf inclination distribution function (LIDF - spherical foliage assumed herein: i.e., σ = 0.5 [-]), vegetation height [m], minimum stomatal resistance (r_{stmin} - [$s\ m^{-1}$]),	*Field* Agdal: Avignon: Nasrallah: R3:	LAI; height; r_{stmin} * ~1.8; ~6; 200*[a] ~0.4 – 4.0; ~0.2 – 0.8; 80*[b] ~0.21; ~5.8; 200*[a] ~0 – 4.2; ~0.1 – 0.8; 100*[c]
	Forcing and fluxes (both formulations)	
Meteorological data: Incoming solar radiation ($S\downarrow$ - [$W\ m^{-2}$]), air & surface temperature [°C], relative humidity [-], wind speed [$m\ s^{-1}$]	*Field*	varying
Fluxes [$W\ m^{-2}$]: radiation; latent, sensible and ground heat	*Field*	varying
	Other data	
Viewing direction: Zenith *(SPARSE and SPARSE4)* and Azimuth *(SPARSE4)*	*Field*	nadir (all sites) and oblique (R3)
Solar direction [°]: Zenith and Azimuth *(SPARSE4)*	*From local time & geo. co-ord.*	as per solar algorithm: ~0 – 90; ~0 – 360

[a] Delogu et al. (2018); [b] Wigneron et al. (1999); [c] Olioso et al. (2002)

Unlike contextual surface energy balance methods, which can be applied with limited inputs, point-based SEB methods require meteorological variables as input to allow the description of turbulence at the near-land surface. Table 2 provides a summary of the input data collected from the sites. These can broadly be categorized into: data used for

model runs – meteorological, biophysical information; and evaluation data – flux measurements from the installed radiometers and eddy covariance systems.

Meteorological and surface biophysical input variables

Forcing data collected from the meteorological stations at the four locations include air temperature, relative humidity, wind speed and direction. These are recorded at heights of 9.2, 3, 9.8 and 2 m for Agdal, Avignon, Nasrallah and R3 sites, respectively. Surface temperature, which is needed to force the surface energy balance, is also measured on-site using Apogee Infra-red radiometers (Apogee Instruments Inc., UT, USA) observing from zenith. The R3 study site is also equipped with an oblique-viewing radiometer (at 45° elevation). Surface temperature in Avignon is measured using a Heimann kT17 thermal radiometer. Additionally, incoming solar and sky radiation data from the installed pyranometers and pyrgeometers were available. See Table 3 for a summary of the instruments. Except for Avignon, where recordings were made at hourly intervals, measurements at the other sites were collected on half-hourly basis.

Other than angular data (i.e., viewing azimuth, solar zenith and azimuth angles), no additional information is required to run the extended model for a homogeneous canopy that assumes a spherical foliage. The solar zenith and azimuth angles are calculated from the local time and geographic coordinates of an area of interest; the Sun angles and daylength algorithm (Campbell & Norman, 1998a; Iqbal, 1983) as described in section 3.1.4 is used herein.

Observations for evaluation (fluxes and temperatures)

In all sites but Avignon, sensible and latent energy fluxes were measured using eddy covariance (EC) systems, which consisted of temperature probes, hygrometers, and 3D sonic anemometers that measured the fluctuations of air temperature, water vapor and wind velocity components. The raw EC data at the Agdal site was processed using the ‘ECpack’ processing tool developed by the Meteorology and Air Quality Group, Wageningen University (Hoedjes et al., 2007). Nasrallah’s EC system data was analysed using the ‘eddy pro’ software developed and maintained by LI-COR Biosciences and the ‘ReddyProc’ tool used for gap-filling (Chebbi et al., 2018). For R3, processing of the raw

data was done using the 'EdiRe' software package from the University of Edinburgh (Duchemin et al., 2006). The ground heat flux was measured using soil heat plates installed within a few centimeters depth (a correction was applied to account for the heat storage between the sensor and the soil surface). Net radiation was calculated as a residual from the incoming and outgoing short- and long-wave radiation observations from 4 component net radiometers; at Avignon, direct measurements of Rn were performed using 2 component net radiometers. In Avignon sensible heat flux was measured using 1D sonic anemometers and latent heat flux was computed as the residual of the energy balance equation. Latent heat flux was also measured using a Bowen ratio system providing results consistent with the residual method (Cellier & Olioso, 1993). Correction of latent heat fluxes at the R3 wheat field was similarly achieved by ensuring Bowen conservation (Boulet et al., 2015). There was a good daily energy budget closure at the Nasrallah Olive site, which was characterized by a regression slope of $98\ \%$ (Chebbi et al., 2018). An absolute energy closure of $90\ \%$ has also been reported for the Agdal Olive site (Er-Raki et al., 2009).

While overall fluxes are important, separating them between the soil and vegetation components is key particularly to users in water deficit regions who are faced with the need to allocate the scarce resource to the plant for optimal agricultural production. Transpiration data were however only available at the Nasrallah and Agdal orchard sites. To allow adequate representation of the olive trees at the Nasrallah site, rescaling of sap-flow observations was necessary. The rescaled measurements were calculated using parameters (i.e., trunk diameter, total stem section) taken from old and young olive trees (Chebbi et al., 2018). For Agdal, data filling was done using a linear regression for the site proposed in Er-Raki et al. (2009), i.e. $0.44\mathrm{ET}_0 + 0.49$; where $\mathrm{ET}_0\ [\mathrm{mm\ d^{-1}}]$ is the daily reference evapotranspiration (estimated in their work using the FAO-56 Penman-Monteith equation).

For Nasrallah, performance reporting primarily focuses on the dataset collected over the year 2014 whereas some other evaluation variables are drawn from years 2013 and 2015. This is because continuous meteorological, EC and sap-flow data that had minimal errors were readily available for year 2014 while other data were collected in the other years. For instance, measurement of shaded soil temperatures only began in year 2015;

however, the turbulent flux as well as sap flow measurements collected during that year had a lot of intermittent but frequent instrument-related errors. In this isolated tree agro-system, positioning an infrared thermometer in the shade or over the sunlit soil was technically straightforward, while the sunlit and shaded leaf elements were more homogeneously distributed and could not fall within the field-of-view (FOV) of a single instrument. We therefore interpreted the difference between a nadir-looking narrow-FOV TIR radiometer and the hemispherical radiometer to retrieve both elementary temperatures. The sunlit vegetation temperature was therefore recomputed from the outgoing longwave radiation (from the hemispherical radiometer), shaded vegetation temperature and sunlit/shaded soil temperatures (from the narrow-FOV TIR radiometers looking at the central canopy gap and bare soil, respectively). That is, the outgoing longwave radiation was assumed to be a function of the bare soil and vegetation (weighted by the gap fraction and foliage cover fraction, respectively) and a small contribution from the reflected sky emittance. From the calculated average foliage temperature, the sunlit vegetation temperature was indirectly solved for by weighting the sunlit/shaded vegetation elements using their respective contribution coefficients from UFR97.

Evaporation proxy

Surface soil moisture can act as a proxy for estimating the evaporation efficiency and hence the amount of water lost through the soil. The soil evaporation efficiency is defined as the ratio between actual and potential/maximum evaporation. The 'reference' soil evaporation efficiency (also 'relative humidity at the ground surface' according to Noilhan and Planton (1989)) is given by a sinusoidal function described in Merlin et al. (2011) as:

$$\beta_s = \begin{cases} \left[0.5 - 0.5\cos\left(\pi \frac{\theta_{0-5\mathrm{cm}}}{\theta_{\max}}\right)\right]^{\mathrm{p}}, & \theta_{0-5\mathrm{cm}} < \theta_{\max} \\ 1, & \theta_{0-5\mathrm{cm}} \geq \theta_{\max} \end{cases} \quad (4.1)$$

where $\theta_{0-5\mathrm{cm}}$ and $\theta_{\max}$ are the observed and saturation soil water contents at the surface layer (here volumetric $[\mathrm{m}^3\mathrm{m}^{-3}]$ soil moisture at 5 cm depth is used); p [-] is a shape parameter related to soil texture. Such a function can also act as an observation operator when assimilating satellite acquisitions of surface soil moisture in soil-vegetation-

atmosphere transfer algorithms.

Table 3:Instrumentation (including name of manufacturer and model) at the Agdal, Avignon, Nasrallah and R3 sites

Instrument; Manufacturer; Model	**Agdal** *(Hoedjes et al., 2007; Williams et al., 2004)*	**Avignon** (Cellier & Olioso, 1993; Albert Olioso et al., 1996)	**Nasrallah** *(Chebbi et al., 2018)*	**R3** (Boulet et al., 2015; Duchemin et al., 2006)
Radiation	Net radiometer; Kipp & Zonen; CNR1	Net rad. differential pyrradiometer; Crouzet, FR Rg; Kipp & Zonen; CM5	Net radiometer; Husekflux, Delft, NL; NR01 :- SR01, IR01	Net radiometer; Kipp & Zonen; CNR1
Turbulent fluxes	Eddy Covariance (EC) system; Campbell Sci. Ltd., USA; 3D sonic anemometer CSAT3; Hygrometers - CS7500, KH20	1D sonic anemometer - *H*; Campbell Sci., UK; CA27. Residual and Bowen ratio methods – *LE (home built based on a HMP35A Vaisala (Helsinki, Finland) humidity sensor, a differential air pumping system and type T thermocouples; cf.* Cellier and Olioso (1993)	EC system; Campbell, USA; 3D sonic anemometer CSAT3; Hygrometers - LI-COR7200, LI-COR7500	EC system; Campbell, USA; CSAT sonic anemometers; Krypton fast-response hygrometers
Wind speed	Wind vane/anemometer; R.M. Young Co.; WP200	CIMEL (Paris, France) cup anemometer	Anemometer; R.M. Young, USA	Anemometer; R.M. Young, USA; A100R
Relative humidity	Humidity probe; Vaisala, FI; HMP45C	Humidity probe; *HMP35A Vaisala (Helsinki, Finland)*	Humidity probe; Vaisala; HMP155/45	Humidity probe; Vaisala; HMP45C
Air temperature	Temperature probe; Vaisala, FI; HMP45C	Homemade temperature copper probe	Temperature probe; Vaisala; HMP155/45	Temperature probe; Vaisala; HMP45C
Ground heat flux	Heat flux plates; Hukseflux, Delft, NL;	Calorimetric method: i.e., from temperature profiles (type T thermocouples) down to 1 m and soil heat capacity calculated from soil moisture and soil density profiles	Heat flux plates; Hukseflux, Delft, NL; HFP01	Heat flux plates; REBS Inc., USA; HFP3
Surface temperature	Thermo-radiometer; Apogee Inc., UT, USA IRTS-Ps	Heiman kT17 thermo-radiometer, Wiesbaden, Germany	Thermo-radiometer; Apogee Inc., UT, USA IR120	Thermo-radiometers; Apogee Inc.; IRTP1541, IRTP1383

4.3. Sunlit and shaded contributions

The Unified Francois (UFR97) model, as detailed earlier, estimates contributions of sunlit and shaded elements depending on the solar and viewing directions. Here we only present a simulated example of the Morocco R3 site as it is the only one with oblique thermal measurements. The site is instrumented with two Apogee Infrared radiometers viewing from nadir and oblique (at 45° inclination). Figure 15 highlights the simulated contributions of the sunlit and shaded soil and vegetation elements. The daily variations are more differentiable in the nadir case where contribution of sunlit elements is highest around solar noon (peaks/troughs in sunlit/shaded element envelopes in Figure 15). With the solar azimuths ranging from 110° - 250° (10 AM - 3 PM), the south-facing off-nadir thermal sensor is simulated to observe varying sunlit/shaded soil elements while mostly viewing the shaded vegetation over the experiment period. This observation is as expected for a site that is located in the Northern Subtropics.

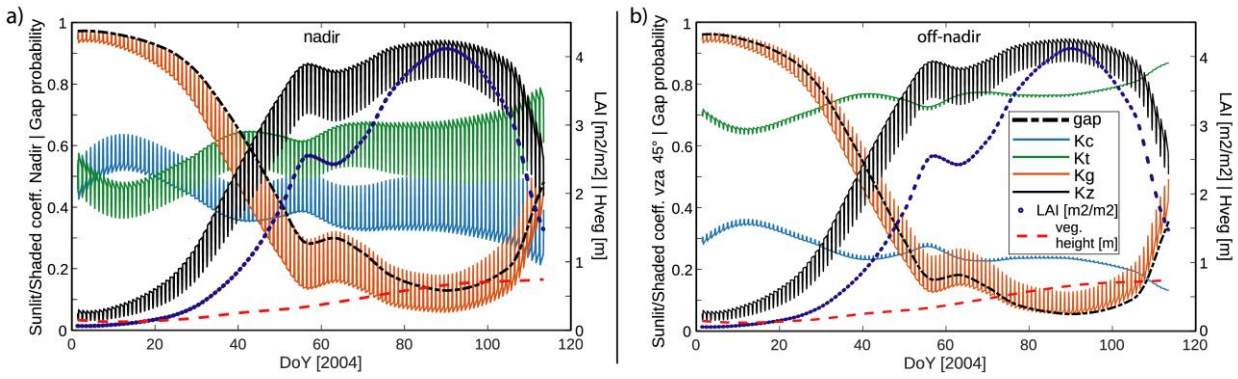

Figure 15: Contributions of sunlit/shaded soil (K_g/K_z) and sunlit/shaded vegetation (K_c/K_t) components and gap fraction (probability) at the R3 wheat site (10 AM - 3 PM) as simulated by the UFR97 method for a) Nadir-, and b) off-nadir/oblique-facing radiometer. Solar noon depicted by peaks in sunlit elements and troughs in shaded elements.

4.4. Global fluxes and partitioning

In this and subsequent sections, the 'prescribed' model runs were forced with surface temperature measurements acquired at nadir, except for the R3 site which also had oblique TIR observations. Performance in estimating total fluxes is analyzed first, then

we look at how those fluxes were partitioned between the vegetation and soil sources, and finally on the estimated evaporation efficiency. For an initial overview of how the models perform under different atmospheric conditions, outputs from clear skies were distinguished from cloudy days following the method detailed in section 3.1.5. However, throughout the rest of this study focus is mainly on outcomes from the combined clear-sky and overcast datasets. Further reporting on the nadir- and oblique-derived estimates at the R3 site is discussed in section 4.5.2. The objective functions used for assessing the performance of the models include: the root mean square error/difference (RMSE [variable's units]), correlation coefficient (*R* [-]) and bias [variable's units].

4.4.1. Overall (global) fluxes

Daily RMSEs and correlation coefficients for the overall fluxes over the four sites are compared in Table 4 with the columns denoted 'All data' reporting on the combined clear-sky and overcast output. Similarly, Figure 16 illustrates comparisons of the combined data. From inspection of the tabulated metrics, it can be observed that even by applying relatively simple sky radiation scaling methods, clear-sky performances can be replicated, i.e., the respective model performances between cloudless and combined outcomes are comparable in all test sites. This highlights the utility of models meant to be used with all-weather remotely sensed data. While this may be desirable temporal-wise, their usage in cloudy conditions would require the use of thermal data that is less influenced by the atmosphere's visibility conditions (e.g. in-situ/field-collected data or unmanned aerial vehicles – UAV imagery), which typically have limited spatial coverage.

Some site-specific characteristics could also be observed to influence the overall results. In Nasrallah, for example, the prevailing dry conditions coupled with the fact that only around 7% of the surface is vegetated lead to the flux simulations being mostly attributed to the soil, and more so to the sensible heat flux. With much less available energy being assigned to latent fluxes, relatively low RMSEs could be achieved for the site. However, the latent flux goodness-of-fit for the site as described by the correlation coefficient was not as good although a small improvement could be observed with SPARSE4. Contrarily, at the Agdal orchard - which has a higher vegetation cover fraction and is frequently irrigated - the turbulent fluxes RMSEs are relatively higher but with much better

correlation. The hourly performances are displayed in Figure 16 where both models demonstrate nocturnal equivalence with some differences being observed during the day. The relatively large early-morning biases of latent fluxes at the Nasrallah site, which are somewhat reduced in the new model formulation, can also be seen to be averaged out by the reduced nighttime biases.

Table 4: SPARSE and SPARSE4 global fluxes performance: RMSEs [W m^{-2}], correlation coefficients - R [-] and bias [W m^{-2}] for the four sites

		SPARSE		SPARSE4	
		RMSE/correlation/bias		RMSE/correlation/bias	
		Clear skies	All data	Clear skies	All data
Agdal	Rn	29/0.99/-19	34/0.99/-24	21/0.99/-4	23/0.99/-5
	LE	64/0.83/11	63/0.82/8	61/0.83/9	57/0.83/6
	H	75/0.87/-29	74/0.86/-28	63/0.88/-12	61/0.88/-11
	G	27/0.88/15	25/0.88/14	27/0.84/2	26/0.84/2
Avignon	Rn	43/0.98/-12	42/0.98/-11	36/0.98/7	38/0.98/7
	LE	44/0.95/-12	43/0.95/-12	48/0.94/2	47/0.94/-1
	H	41/0.90/-13	40/0.89/-14	42/0.78/-4	44/0.77/-3
	G	39/0.89/16	38/0.86/16	39/0.82/11	38/0.80/11
Nasrallah	Rn	35/0.98/-3	34/0.98/4	32/0.98/3	33/0.98/4
	LE	38/0.59/6	39/0.56/7	35/0.62/2	36/0.60/3
	H	48/0.93/-29	47/0.92/-26	44/0.94/-20	44/0.93/-19
	G	42/0.94/13	41/0.93/14	43/0.93/9	41/0.93/12

TIR-view →		***nadir***	***oblique***	***nadir***	***oblique***	***nadir***	***oblique***	***nadir***	***oblique***
R3	Rn	35/0.98/6	36/0.99/7	39/0.98/1	38/0.98/1	41/0.99/13	41/0.99/12	42/0.98/12	43/0.98/11
	LE	48/0.84/-3	46/0.89/5	48/0.83/-6	48/0.87/-1	36/0.94/4	37/0.93/4	40/0.93/5	41/0.91/4
	H	59/0.82/-19	54/0.81/-27	59/0.83/-23	56/0.82/-28	49/0.84/-8	52/0.83/-8	49/0.85/-11	52/0.84/-10
	G	30/0.83/15	32/0.83/16	29/0.82/11	29/0.81/12	37/0.71/6	37/0.70/6	36/0.66/3	36/0.65/3

The net radiation, which is the main source of energy for the system, is observed to be increased with SPARSE4. This tends to reduce the bias (in absolute terms) and the RMSE except in R3. Changes are mostly significant in diurnal periods as shown in Figure

16 and also at night for Nasrallah. In Agdal, the reduced net radiation biases (lower negative biases according to Table 4) also appear to be partly contributed by the relatively higher net radiation for the vegetation (Figure 20). The turbulent fluxes RMSEs at Avignon are fairly higher for the new model. The differences, which can possibly be attributed to the added model complexities, are nonetheless counterbalanced by improved biases. In terms of mean errors, both formulations appear to consistently overestimate the ground heat flux while generally underestimating the sensible heat fluxes. These biases can mainly be attributed to the estimates at nighttime when the ground (sensible) heat fluxes are generally overestimated (underestimated). Night soil temperatures estimated by both models generally appear to be underestimated (Figure 18) thus explaining the biases since the low temperatures suggest less soil emissions and therefore more soil net radiation, which is then available for the soil energy fluxes and therefore partly explaining the overestimation of the soil heat flux. The inverse effect of the increased net radiation on sensible heat flux is likely as a result of the inherent/theoretical direct relation between sensible heat flux and temperature and the fact that latent fluxes are capped. The biases are nevertheless somewhat suppressed in SPARSE4 for all fluxes across all sites.

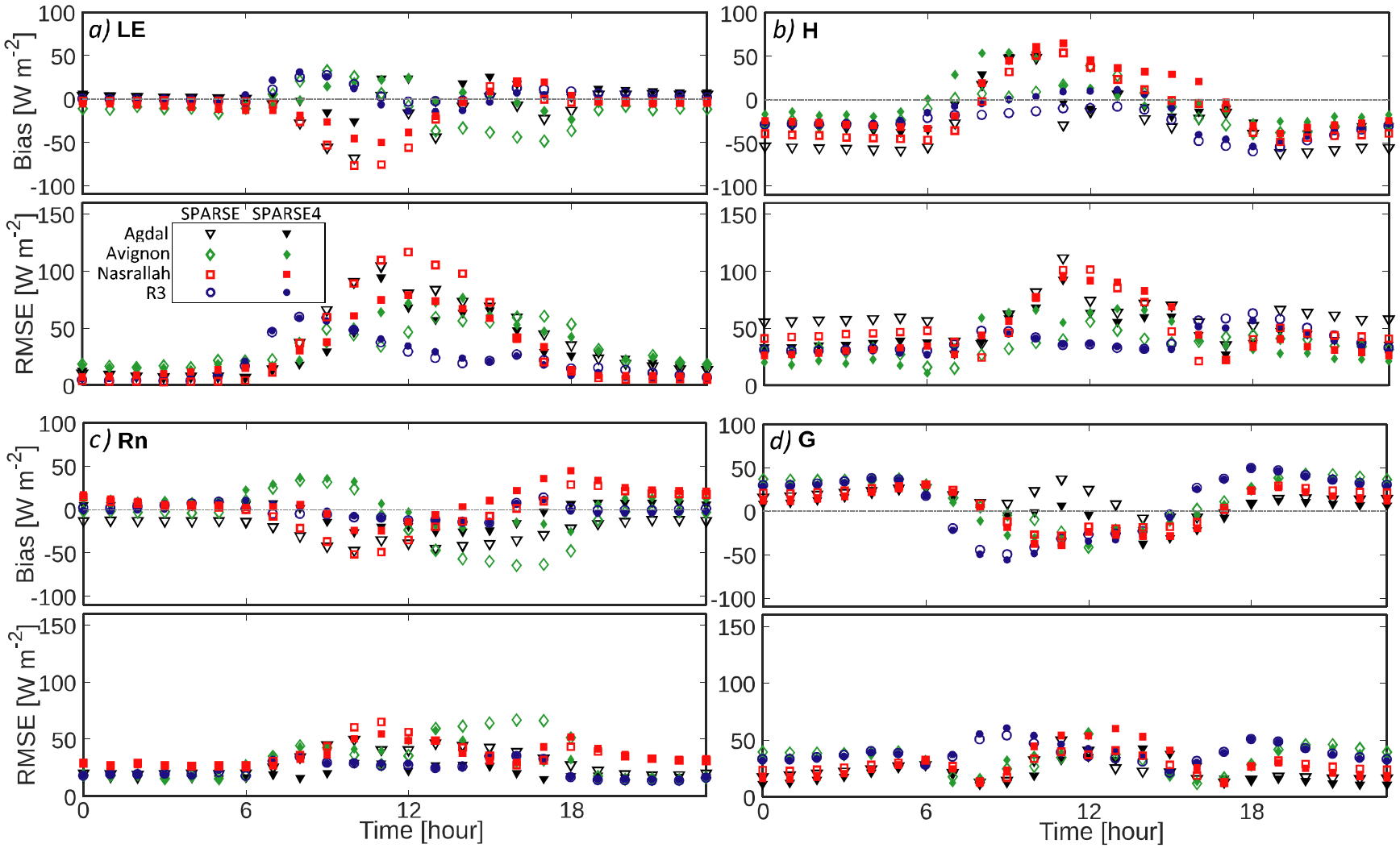

Figure 16: Nocturnal/diurnal trends of bias and RMSEs; for a) latent heat flux, b) sensible heat flux, c) net radiation, and d) ground heat flux. Hollow and solid shapes represent SPARSE and SPARSE4, respectively; shape/color (site): triangle/black (Agdal), lozenge/green (Avignon), square/red (Nasrallah), and circle/blue (R3)

4.4.2. Flux partitioning and temperatures

This sub-section reports on the partitioning of the total fluxes starting with the decomposition of evapotranspiration between the soil and vegetation at the Nasrallah and Agdal orchard sites. As previously noted, availability of sap-flow data is limited to these two sites. The daily transpiration rates simulated during the study periods are illustrated in Figure 17. For Nasrallah, the respective root mean square errors [mm/day], correlation [-] and bias [mm/day] for SPARSE were: $0.15, 0.91, -0.12$; and for SPARSE4: $0.09, 0.90, -0.02$. The models' RMSEs, correlations and bias for Agdal were $0.40, 0.96, -0.35$ and $0.23, 0.96, -0.04$, respectively. The overall reduction of the bias - by at least 40 % - translated to the transpiration in the new formulation being higher than in the standard SPARSE hence allowing the estimates to closely follow the reference observations particularly during the summer.

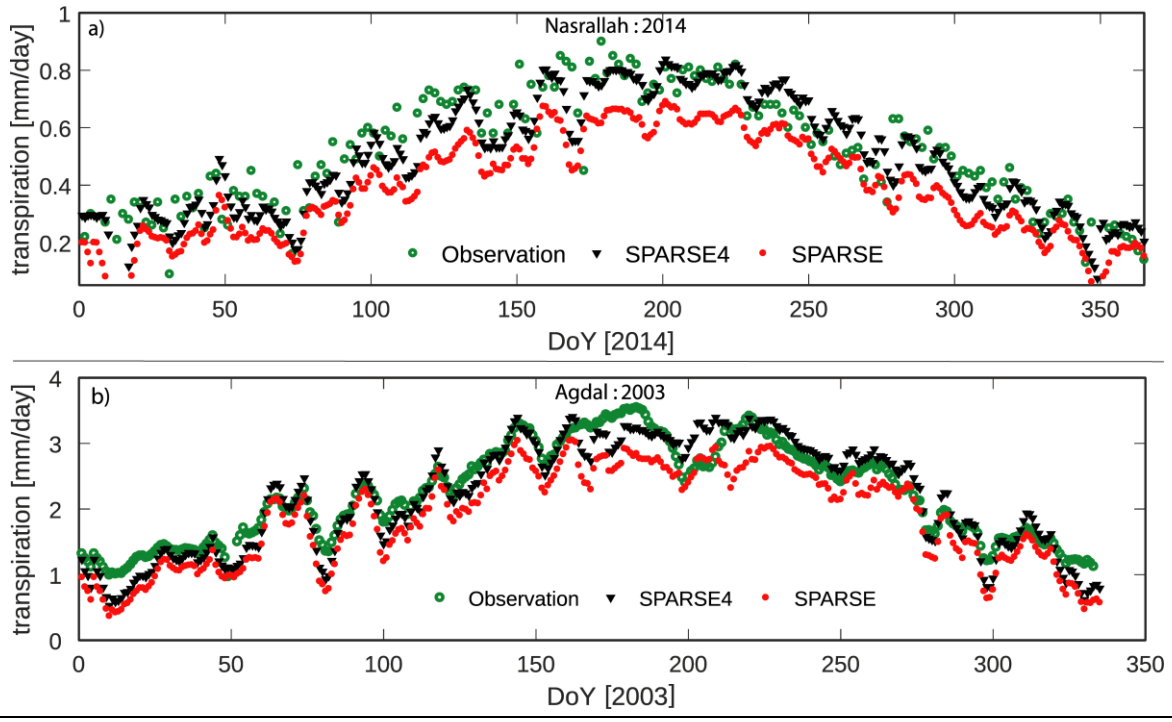

Figure 17: Observed (green ⭘) and simulated (SPARSE: red ●, SPARSE4: black ▼) transpiration –time series' for a) Nasrallah and b) Agdal sites.

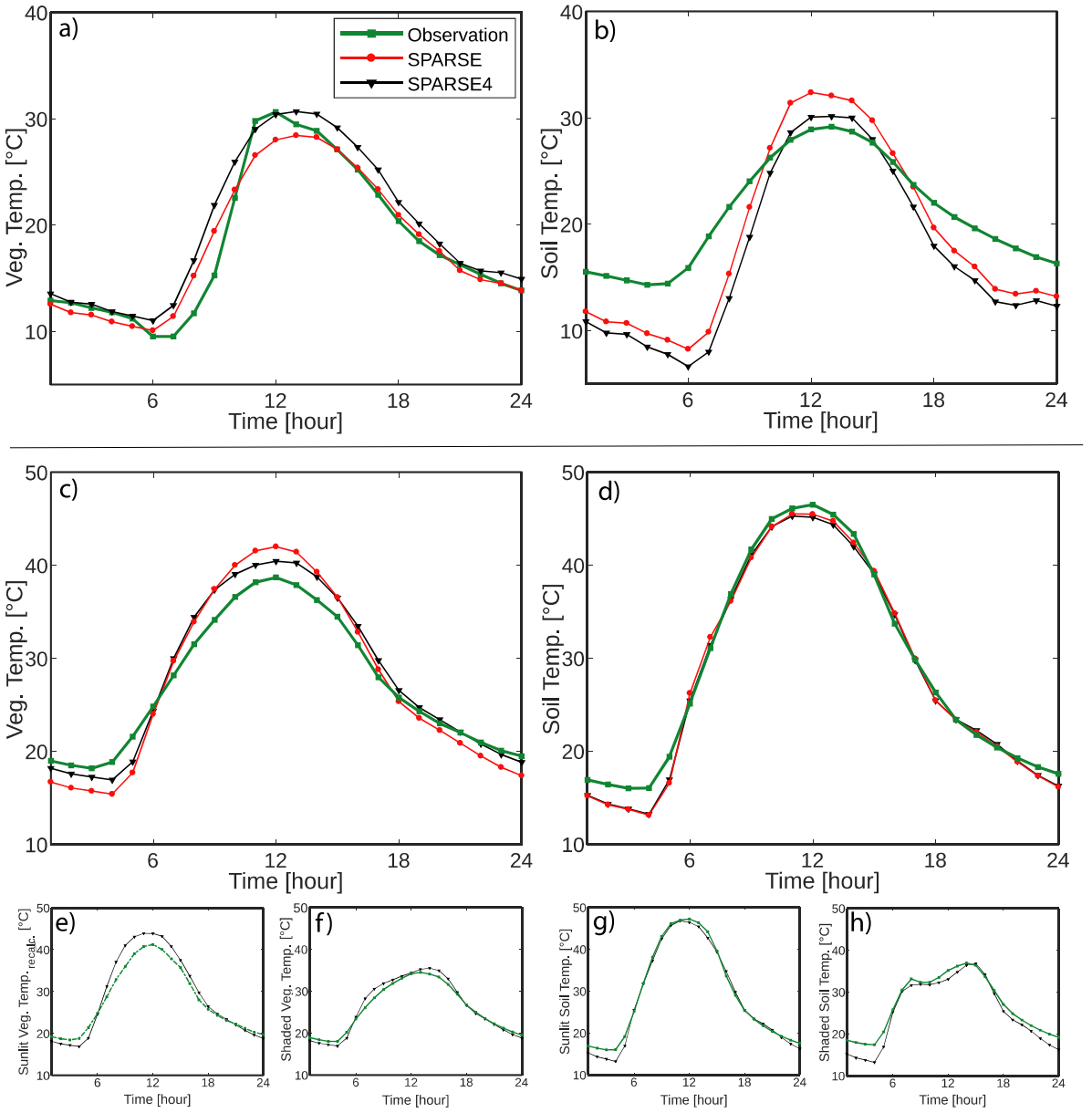

Figure 18: Vegetation and soil temperatures (estimated and observed) over the simulation period in Agdal (a, b) and Nasrallah (c, d); and e, f) sunlit and shaded vegetation elements; g, h) sunlit and shaded soil at the Nasrallah site (key applies to all figures)

The simulated temperatures for the Agdal and Nasrallah (2015) sites are shown in Figure 18. For Agdal, the measurements were taken as the soil/vegetation averages. For Nasrallah, however, the sunlit soil, shaded soil and shaded vegetation temperatures were available but only from year 2015. As detailed in section 4.2, the sunlit vegetation temperature was re-calculated from the long-wave radiation observations and the measured sunlit/shaded soil and shaded vegetation temperatures. Estimates by SPARSE4, which outputs both shaded and sunlit temperatures, are compared to the observations in Figure 18. The nocturnal soil temperature estimates are generally underestimated resulting in the already noted

biases on the soil energy fluxes. The TIR Apogee sensor that provides the shaded soil temperatures (installed under a tree) records slightly higher night temperatures when compared to the sensor in the open field (in the Sun during the day). This phenomenon is however not replicated by the model since the entire soil is considered shaded at night.

4.4.3. Soil evaporation efficiency

Unavailability of sap flow data due to complexities involved in collecting accurate measurements can make the assessment of evapotranspiration partitioning impractical for some sites. Nonetheless, how well a model estimates vegetation (latent heat) fluxes can be deduced from overall evapotranspiration and soil evaporation. This can practically be obtained as the difference between total evapotranspiration from eddy covariance measurements and soil evaporation inferred from surface soil moisture. Here, we compare the soil efficiencies retrieved by SPARSE to the proxy soil evaporation efficiency given by Equation (4.1) (Merlin et al., 2011). The modeled soil efficiencies are illustrated and compared to the proxy in Figure 19.

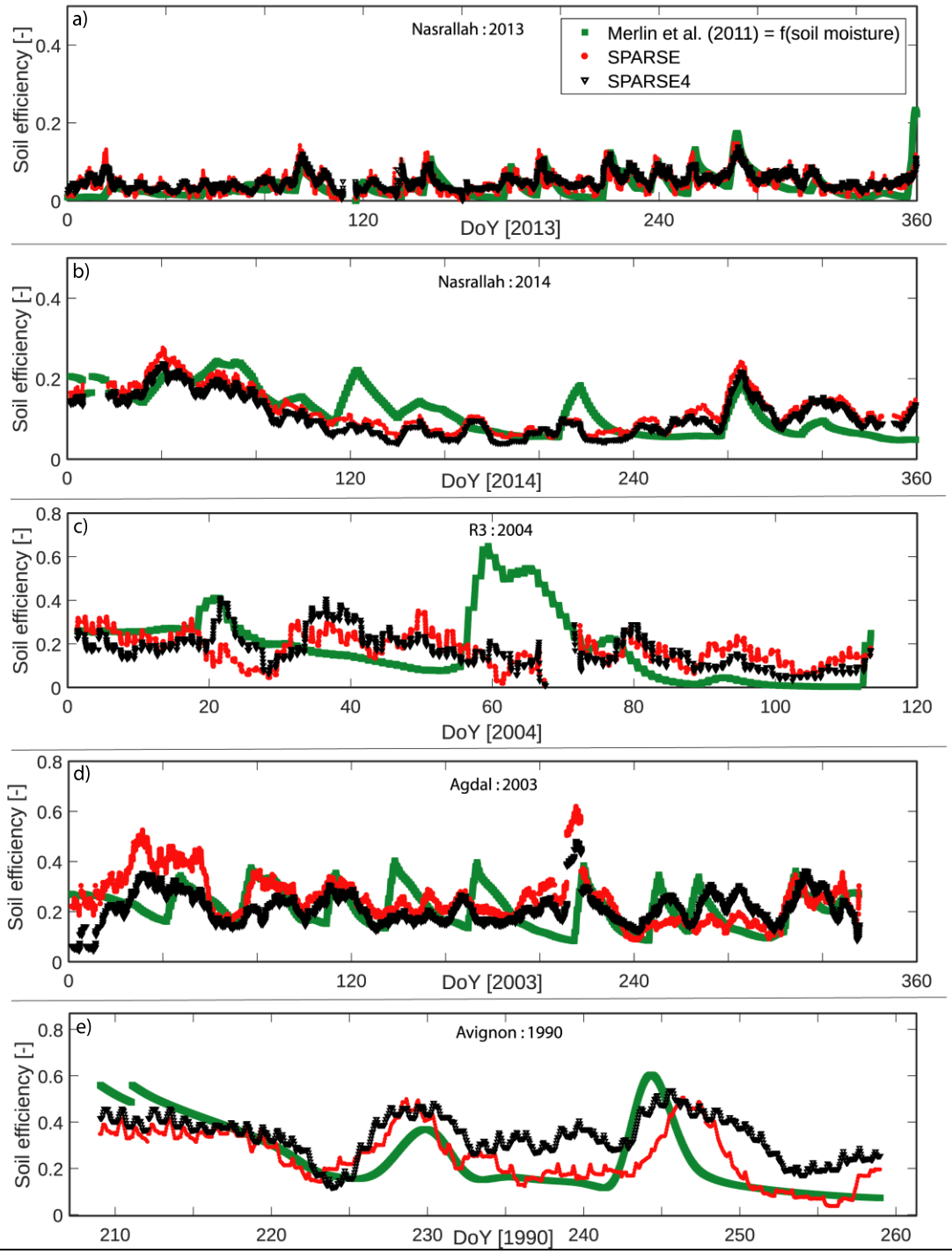

Figure 19: Time series' of soil evaporation efficiencies (SPARSE: red and SPARSE4: black) with Merlin et al.'s (2011) method as the proxy (in green) a, b) Nasrallah - 2013 and 2014, c) R3, d) Agdal, and e) Avignon

In Nasrallah, where the soil is greatly stressed, the models' soil efficiency simulations are able to reproduce the 'observation' with both models generally showing a better fit with variations of the soil moisture inferences. The new scheme appears to capture most peaks in R3 and Agdal, especially around the first soil water inputs, with slightly better timing. Otherwise, the soil efficiency estimations by the two models were almost

similar in the four experiments. In addition to the peak in R3 at maximum vegetation development (from DoY ~55 to ~70 excluding missing simulations arising from a surface temperature data gap), some peaks in the evaporation efficiencies at the Agdal site corresponding to irrigation episodes are not well captured.

4.5. Discussion

4.5.1. Overall performance and the influence of direction on partitioning

The SPARSE and SPARSE4 energy balance schemes were evaluated over two orchards and two crop experimental sites. Overall, it was apparent that both models could satisfactorily estimate the global fluxes. While there was a general reduction of flux biases with SPARSE4, performance between the models was almost similar when using the nadir-retrieved temperature inputs since such measurements are generally not influenced by TRD effects. These results are expected as all the four sites are situated in relatively high latitudes where directionality effects on the nadir measurements are negligible due to the medium/low Sun angles throughout the simulation periods. R3, which was the only site with an oblique-viewing radiometer, also provided measurements that were simulated to originate from mostly shaded elements as illustrated in Figure 15*.b*. Consequently, the nadir- and oblique-derived total flux estimates were retrieved with reasonable accuracy by both schemes (Table 4). In order to derive differentiated and possibly improved total flux retrievals from the new model formulation, surface temperature differences arising from thermal radiation directionality effects should be present. As reported earlier, directionality effects can be quite large especially when viewing in the solar direction warranting the use of a directionality model to simulate out-of-canopy radiances. These thermal directionality effects could however not be tested at present due to limitations related to unavailability of directional thermal measurements. SPARSE has also been shown to exhibit equifinality (Boulet et al., 2015; Boulet et al., 2018) where consistent/similar total fluxes can be estimated with different stress-level combinations of the individual sources. We acknowledge and expect that this aspect is also present in the new formulation.

Figure 20 illustrates the component net radiations as simulated by the two models. Also shown are the vegetation cover fractions in the solar as well as nadir directions. Consideration of the solar direction, i.e. where direct radiation is partitioned with

respect to the solar elevation, ensures more radiation is apportioned to the vegetation in the new formulation. The rationale is twofold: 1) the diffuse fraction (fd) as defined by Erbs et al. (1982) decreases with increase in the sky clearness index, therefore high global solar radiation will generally result in high direct radiation in the solar direction; and 2) gap fraction – complement to vegetation cover fraction as illustrated in Figure 20 - diminishes (hence canopy fraction increases) from nadir to the Sun's zenith (which is often oblique especially in the subtropics and temperate regions); this additional radiation received by the vegetation can then be partitioned between the turbulent fluxes. Indeed, this leads to the higher vegetation available energy in the Agdal site, which is then apportioned for the higher canopy turbulent fluxes thus the slightly higher transpiration. However, if one assumes minimal errors in the diffuse radiation measurements, then it should be acknowledged that the use of Erbs et al.'s (1982) method introduces additional partitioning uncertainties as depicted by the observed diffuse fraction band in Figure 11. With relatively more radiation reaching the soil, the classical SPARSE model attains a better simulation of the ground heat flux in terms of RMSE and correlation although this appears to in-turn lead to relatively higher positive biases. While the discrimination between shaded and sunlit elements likely results in better partitioning of vegetation's available energy between sensible (H_v) and latent (LE_v) heat fluxes, the expected impact of vegetation temperatures on the absolute H_v values is not apparent - especially for densely vegetated scenes and unstressed vegetation. When the vegetation is unstressed, the new formulation will generally apportion the relatively higher vegetation available energy as unstressed H_v since LE_{vpot}/Rn_{vpot} is inherently similar to that simulated by SPARSE.

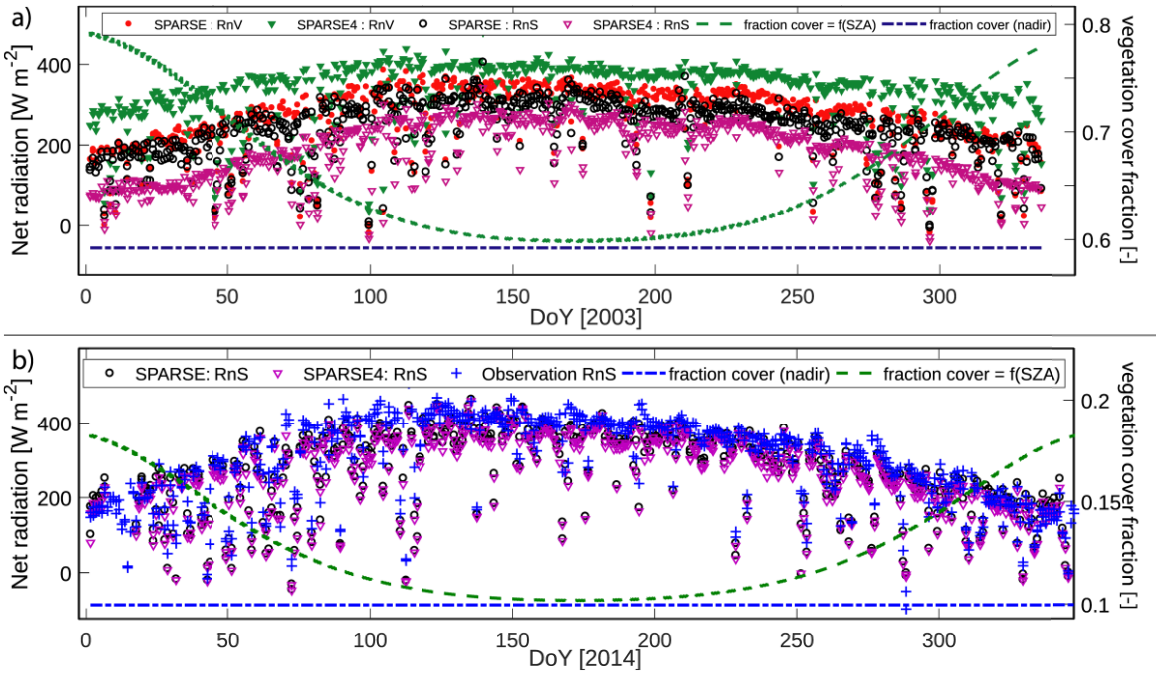

Figure 20: a) Vegetation/soil net radiation (noon) at the Agdal site and b) Nasrallah soil net radiation. Right axis: nadir vegetation cover fraction (only dependent on LAI and LIDF) and vegetation cover fraction in the Sun direction (dependent on LAI, LIDF and solar elevation).

While the UFR97 method provides gap frequencies treatment for homogeneous/continuous covers, row (Yan et al., 2012) and forest (Bian et al., 2018; Li et al., 2017), this study applies the homogeneous method across all sites since it ensured consistency with the observations. When compared to the continuous cover method, Li et al.'s (2017) method has been shown to provide significantly larger gap fractions especially at nadir (Bian et al., 2018). We also observe its underestimation of vegetation cover fraction when compared to the observations at the orchards. The radiative model could nonetheless be improved by using the discontinuous versions, which we expect can further improve the results. The method's suitability in surface energy balance partitioning however requires careful analysis before it can be properly applied. With respect to applying different cavity effect formulations (FR97 and C-EP), we observe that the differences in the resulting fluxes are very small (results not shown). This is because the orders of magnitude of both cavity effect formulations are quite close for nadir views with the differences in the resulting canopy emissivity being marginally higher for larger viewing zeniths.

4.5.2. Sensitivity of estimates to nadir vs off-nadir viewing

It is important to test the sensitivity of evapotranspiration derivation methods to the

sensor direction of view because prevailing surface condition retrievals (temperatures, radiation and turbulent fluxes) should essentially be similar whatever the geometry of data acquisition. This is a key consideration aspect since space-borne sensors, which presently act as essential sources of input data for Earth observation methods, generally observe terrestrial pixels from off-nadir directions, with the viewing orientations changing often depending on the satellite's location in its orbit. While the Sun-synchronous concept used in some missions (e.g., MISTIGRI, Lagouarde et al., 2013) minimizes the impact of thermal radiation directionality by allowing same viewing geometry for a given location, it cannot entirely eliminate effects resulting from solar position variations (Duffour et al., 2016; Duffour et al., 2015). For instance, future high resolution satellite missions in the TIR domain (e.g., TRISHNA, Lagouarde et al., 2019) will observe a given location with very different observation angles from one overpass to the other. This will allow frequent revisit capacities, which are indeed necessary for reasonable temporal upscaling of evapotranspiration estimates (Delogu et al., 2021). While the retrieval parameters (e.g. overpass time) can be duly chosen such that the hotspot is rarely observed, these specifications mean that it is likely for the sensors to acquire remote sensing data close to the hotspot particularly over the tropics and subtropics (see for example Duffour et al. (2016)). Additionally, directionality is also an issue for current missions including MODIS, and is usually ignored (except for the amount of vegetation in the sensor's field of view). SPARSE 4 was designed to account for such differences in viewing direction and changes in Sun position, and it is important to evaluate potential improvements in this sense comparatively to SPARSE. We therefore test the models' output sensitivity to observation angle for the R3 site when forced with surface temperature observations acquired simultaneously either at nadir or from a 45° (south-facing) elevation angle.

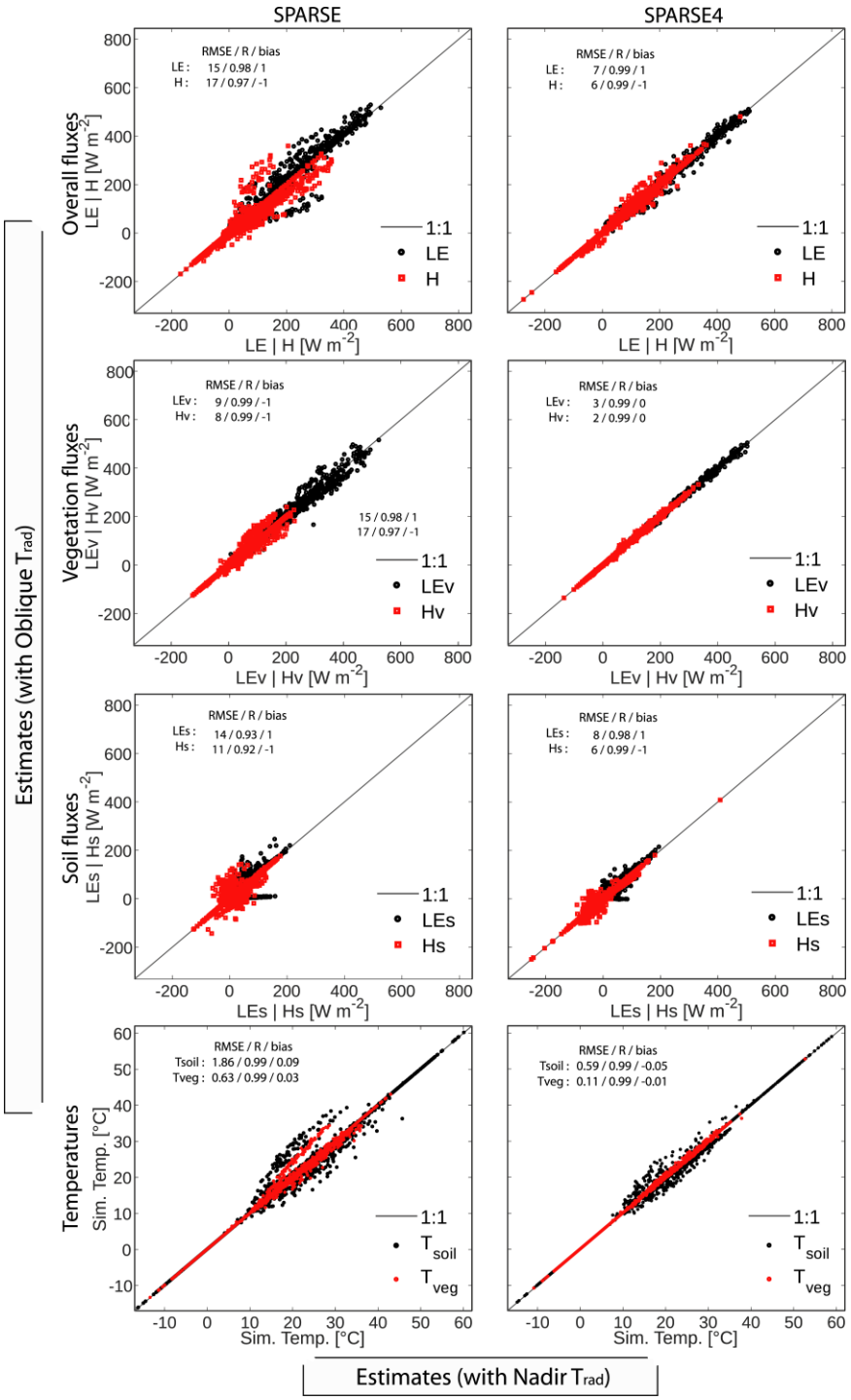

Figure 21: Sensitivity of estimates to angular thermal data. I.e.: estimates using oblique-observed T_{rad} (ordinate) vs estimates from nadir-observed surface temperature (T_{rad}) input (abscissa). Inset: RMSE, R and bias of oblique-based estimates versus nadir-based estimates.

Figure 21 plots the oblique- against nadir-retrieved model estimates for the two SPARSE formulations and the performance evaluation of the respective nadir and oblique simulation sets are tabulated in Table 4. The small differences between the temperatures observed from the two directions (within ~3°C) allow the overall fluxes

to be satisfactorily reproduced by both models. Reproduced retrievals of vegetation fluxes by SPARSE4 however appear better and it can also be observed that angular surface temperature inputs have slightly more impact on SPARSE's retrieval of soil temperatures. This can in part be explained by the fact that the gap fraction reduces from nadir to off-nadir and the underlying physical assumption of the soil being stressed prior to vegetation. This lower oblique gap means that the fraction of soil (and hence its contribution to the signal) in the field of view of the sensor is reduced leading to variations in the simulated soil stress efficiency and thus the soil temperatures. Additionally, the coupling of the soil and vegetation in the net radiation scheme means any deviations in soil emissions ultimately influence the vegetation's radiative and energy budgets. The influence on soil fluxes in extended model can be interpreted the same way although its consideration of the shaded soil (which reduces the average temperature variations) appears to diminish the overall effect. There is consequently a tendency to simulate similar, albeit potential *(subscript $_{pot}$)* or unstressed, vegetation fluxes in both SPARSE4 scenarios.

The inversion capabilities of the coupled model are quite promising since it is apparent that, even with thermal data measured from different directions, the prevailing component temperatures and fluxes (radiative and energy) at the land surface can satisfactorily be retrieved and reproduced with SPARSE4 estimates being more consistent when compared to SPARSE's retrievals. Nevertheless, the method's inversion and turbulent flux reproduction capabilities over the entire Sun-observer polar grid requires further verification. Since we also see no observable improvement in overall flux retrievals especially when thermal radiation directionality effects (oblique-nadir temperature differences) are negligible, a study that will encompass a wide-ranging combination of Sun-Earth-sensor geometries (including the hotspot region) is necessary.

4.6. Conclusions

In this study, we have presented an extended formulation of the Soil Plant Atmosphere Remote Sensing Evapotranspiration (SPARSE) model where sunlit and shaded elements have been distinguished in the energy and radiative balance schemes. A clearness index method was hence adopted to partition the incoming global solar radiation into its direct and diffuse components. Since remote thermal infra-red sensors usually observe within a narrow spectral window, a method that accounts for

this important aspect has also been incorporated. For thermal radiation directionality effect accounting, coupling was done with the Unified Francois (UFR97) radiative transfer model that links the sunlit/shaded soil/vegetation surface emissions with out-of-canopy radiance in the viewing direction. A preliminary evaluation of the extended method was then carried out to assess its capability in estimating and partitioning overall fluxes on two orchards and over growing cycles of soybean and wheat.

We observed that the partitioning of total fluxes does improve when sunlit and shaded elements are distinguished leading to better transpiration estimates especially in water stressed regions. By weighting between shaded/sunlit elements, the tendency by the original SPARSE model to simulate higher vegetation temperatures was also largely reduced. Since remotely sensed data are often acquired from oblique directions, models that invert the measured surface temperatures should be insensitive to any angular effects. It was thus observed that the extended formulation, coupled with an anisotropy model, resulted in better reproduction of flux and component temperature estimates from directional thermal data. This is particularly important when using data whose signal could be influenced by the Sun-Earth-sensor geometry particularly in the hotspot direction. Satellite missions whose objectives include ecosystem functioning and stress monitoring (e.g. TRISHNA, LSTM) can / will be able to provide thermal observations at relatively high spatial and temporal resolutions by proposing a wide range of viewing repeat-cycle angles. While we contend that the new formulation is not meant to replace the standard SPARSE algorithm especially when inverting thermal data less influenced by TRD, its consideration of directionality aspects/effects (which are not only limited to the hotspot region) as well as its demonstrated capabilities of flux partitioning in water-deficit terrains are worth further investigation. These should form part of a future study whose main focus will be thermal radiation directionality effects on turbulent flux estimation. Such analyses should also potentially be able to inform the selection of algorithms that normalize directionality-influenced remote sensing products to a particular standard direction.

Chapter 5: Observation and modelling of surface components over a heterogeneous (row) canopy

This section is basis of an article (in preparation/soumis)

Summary

The viability of agricultural production is largely dependent on the efficient use of water resources. With evapotranspiration (ET) accounting for nearly all the water lost from croplands and wooded areas, accurate ET estimation methods are needed for a better understanding of irrigation demands. While surface temperature can help to detect water deficiencies in such environments, it can also be susceptible to directionality influences leading to an incorrect interpretation of observed surface emission signals. In this section, we perform model assessments and check the influence of thermal radiation directionality using flux data over a vineyard located in Verdu (Cataluña, Spain) collected in the context of the HiLiaise project. The non-continuous row site is oriented ~E-W and is drip irrigated. Instrumentation at the site included: net radiometers, an eddy covariance system for turbulent fluxes monitoring, as well as thermal cameras that provided elemental soil and vegetation temperatures. To derive the overall directional surface temperatures (nadir and off-nadir), the measurements were aggregated by weighting the elemental values with their respective cover fractions in the viewing direction (derived using the Unified Francois model or DART). The aggregated temperatures from the turbid model were compared to those from a 3-D radiative transfer [DART] model (which utilized a more realistic vine mock-up) where correspondence was demonstrated. The reconstructed surface temperatures were then used in surface energy balance (SEB) modelling schemes. Here, the soil plant atmosphere remote sensing of evapotranspiration (SPARSE) dual source model together with an extended version which discriminates shaded/unshaded elements (SPARSE4), were used to estimate the energy fluxes. Similar to observations made in evaluations in the earlier section (on crops and orchards), we observed that both model formulations are able to retrieve overall fluxes satisfactorily. The sensitivity of flux and component temperature estimates to the viewing direction of the sensor was tested by using reconstructed sets of thermal data (nadir and oblique) to force the models, where we observed degradation in flux retrieval cross-row with better consistency along rows. Overall, it is nevertheless shown that by using the extended method, the sensitivity to viewing direction can significantly be reduced further off-nadir. Additionally, evaluation of output from the two-source energy balance (pyTSEB formulations) – applied as part of the SenET programme over the broader Lleida

region – show that the evapotranspiration products follow the general trend of in-situ observations. This can be explained by the relatively good agreement between the reanalysis input data and the field measurements. Conversely, driving SPARSE with the reanalysis and other SenET input data also yields similar results to the products. To exploit strengths inherent in a variety of methods, the use of an ensemble of models in the dissemination of ET products should thus be considered.

Keywords: vineyard, evapotranspiration, surface energy balance, thermal radiation directionality, temperature inversion

Résumé

La viabilité de la production agricole dépend largement de l'utilisation efficace des ressources en eau. L'évapotranspiration (ET) représentant la quasi-totalité de l'eau perdue par les terres cultivées et les zones boisées, des méthodes d'estimation précises de l'ET sont nécessaires pour mieux comprendre les demandes d'irrigation. Si la température de surface peut aider à détecter les déficits hydriques dans de tels environnements, elle peut également être sujette à des influences de directionnalité conduisant à une interprétation incorrecte des signaux d'émission de surface observés. Dans cette étude, nous effectuons des évaluations de modèles et vérifions l'influence de la directionnalité du rayonnement thermique en utilisant des données de flux sur un vignoble situé à Verdu (Catalogne, Espagne) recueillies dans le cadre du projet HiLiaise. Le site à rangs non-continus est orienté E-W et est irrigué au goutte-à-goutte. Les instruments utilisés sur le site comprennent : des radiomètres nets, un système de covariance de tourbillon pour la surveillance des flux turbulents, ainsi que des caméras thermiques qui fournissent les températures élémentaires du sol et de la végétation. Pour dériver les températures de surface directionnelles globales (nadir et off-nadir), les mesures ont été agrégées en pondérant les valeurs élémentaires avec leurs fractions de couverture respectives dans la direction d'observation (dérivées en utilisant le modèle unifié de François ou DART). Les températures agrégées du modèle turbide ont été comparées à celles d'un modèle de transfert radiatif 3-D [DART] (qui utilisait une maquette de vigne plus réaliste) où la correspondance a été démontrée. Les températures de surface reconstruites ont ensuite été utilisées dans des schémas de modélisation du bilan énergétique de surface (SEB). Ici, le modèle à double source SPARSE (soil plant atmosphere remote sensing of evapotranspiration) ainsi qu'une version étendue qui discrimine les éléments ombragés/non ombragés (SPARSE4), ont été utilisés pour estimer les flux d'énergie. Comme dans une étude précédente (sur les cultures et les vergers), nous avons observé que les deux formulations du modèle sont capables de retrouver les flux globaux de manière satisfaisante. La sensibilité des estimations de flux et de température des composants à la direction de visée du capteur a été testée en utilisant des ensembles reconstruits de données thermiques (nadir et oblique) pour forcer les modèles, où nous avons observé une dégradation de la récupération des flux entre les rangs avec une meilleure cohérence le long des rangs. Dans l'ensemble, il est néanmoins démontré qu'en

utilisant la méthode étendue, la sensibilité à la direction de visée peut être réduite de manière significative au-delà du nadir. De plus, l'évaluation des résultats du bilan énergétique à deux sources (formulations pyTSEB) - appliqué dans le cadre du programme SenET sur la région élargie de Lleida - montre que les produits d'évapotranspiration suivent la tendance générale des observations in-situ. Cela peut s'expliquer par l'accord relativement bon entre les données d'entrée de la réanalyse et les mesures de terrain. Inversement, le pilotage de SPARSE avec les données d'entrée de la réanalyse et d'autres SenET donne également des résultats similaires aux produits. Pour exploiter les forces inhérentes à une variété de méthodes, l'utilisation d'un ensemble de modèles dans la diffusion des produits ET devrait donc être envisagée.

Mots clés : vignoble, évapotranspiration, bilan énergétique de surface, directionnalité du rayonnement thermique, inversion de température

5.1. Introduction

This part builds on the analyses in the previous chapter where homogeneity of the canopy was generally assumed. Here, we evaluate the surface energy balance methods using data collected over a heterogeneous (row) landscape.

The economic livelihood of many in semi-arid regions largely depends on fruit production. Vineyards, for example, are commonplace in the relatively dry regions of Spain. With evapotranspiration (ET) accounting for nearly all the water lost from such areas, accurate ET methods are necessary for better irrigation demand estimation. This can be achieved by solving the soil water balance [up to the rootzone] with the aim of quantifying soil water deficits that indicate the need for irrigation. Methods that directly estimate states in the vadose zone however require difficult-to-estimate input variables whose uncertainties may lead to poor estimates of water requirements. Alternatively, indirect methods that use proxies to water-status can be used. Several such methods have been proposed in the literature with some already operationized, among them are physically-based surface energy balance (SEB) methods (e.g. SEBS, Su, 2002; SEBAL, Bastiaanssen et al., 1998; TSEB, Norman et al., 1995). Typically, terrestrial variables related to water availability are required to drive these models, i.e. used to set boundary conditions for near land surface interactions. For instance, remote sensing based methods use the temperature of the surface as a proxy for the water status when inverting the surface energy budget for ET. Land surface temperature (LST) is typically derived from the emission signals observed by radiometers sensing in the thermal infrared domain.

Unlike in-situ thermal measurements, remotely sensed surface temperatures allow the monitoring of water fluxes over larger spatial scales. However, several issues confront users when using thermal emission data retrieved from space: missing data (for example, due to overcast conditions), inadequate spatial and temporal resolutions and thermal radiation directionality issues. Efforts have mostly been directed towards addressing the first two (e.g. by applying gap filling methods, data fusion techniques, proposing missions with improved revisit times and spatial resolutions, applying disaggregation techniques, among others) with limited focus on how thermal directionality influences flux retrieval. Granted, Olioso et al. (2022) has postulated that the contribution of surface temperature uncertainties to errors in the estimation of the energy balance ranks lower relative to uncertainty in other variables required in SEB schemes, e.g., uncertainty in the roughness lengths for turbulent exchanges. Nonetheless, uncertainties due to thermal directionality, which can lead to large nadir-off nadir differences; for instance, upto 15 K over vineyards (Lagouarde et al., 2014), can lead to inaccuracies in retrieved turbulent fluxes. Additionally, since the relation between the roughness lengths of heat and momentum are indirectly related to the temperature - where they help to distinguish between aerodynamic and radiant temperatures (Carlson et al., 1995; Friedl, 2002), any errors arising from an insufficient roughness length parameterization can, by extension, be attributed to uncertainties in temperature. In all, this necessitates the use of more realistic surface temperatures when estimating the energy balance.

Heterogeneous canopies such as vineyards are complex remote sensing targets that can contribute to considerable directional variability of observed surface signals depending on a sensor's view direction (Kimes & Kirchner, 1983; Luquet et al., 2003). For instance, cross-row, the gap (or soil) fraction (and thus the observed soil emissions) will vary considerably with viewing zenith/elevation since the further from nadir a measurement is made, the larger the fraction of vegetation viewed. This is however not the case when observing along the row where the gap fraction will exhibit little variation with viewing elevation. Additionally, depending on the row orientation, the proportion of the viewed gap that is illuminated or shaded will change depending on the time or the position of the sun. The direction of the sun (relative to the row geometry, whether along- or cross row) will also influence the radiation intercepted and consequently retained by the various surface components.

A field campaign within the framework of the HiLiaise and ESA WineEO projects was conducted during the spring and summer periods of 2021 in a Tempranillo vineyard located in Lleida province, north-eastern Spain. In addition to meteorological and elemental temperature measurements, various components of the radiation and surface energy balance were monitored. After performing initial corrections aimed at enhancing the observed surface energy balance, the data were applied in model evaluations. Land surface temperature is required as an input to infer the prevailing terrestrial water status. This proxy variable was reconstructed from the elemental thermal measurements, consequently allowing the evaluation/comparison of retrievals from relatively simple radiative transfer methods with those simulated by the more realistic and comprehensive 3-D model. Regarding the near-land surface processes, the Soil Plant Atmosphere Remote Sensing of Evapotranspiration model simulated the energy exchanges during the period. Data from the Sentinel for evapotranspiration (SenET, Nieto et al., 2020) programme were also separately used for inter-comparisons. That is, the SenET evapotranspiration [extracted for our AOI] are compared with the in-situ data and, separately, the reanalysis and sharpened land surface temperature (Sentinel 3 LST data disaggregated to match the resolution of Sentinel 2 optical information) data are used to drive the SPARSE formulations. In the following, the site along with the collected and processed data are described, the results from the model assessments are then presented. Finally, conclusions are drawn.

5.2. Row canopy: Verdu vineyard site

5.2.1. *Experimental site description and instrumentation*

The study area is located in Verdu, Lleida province, north-east of Spain (latitude: 41.596° N; longitude: 1.126° W). The vineyard at the site is privately owned and managed. Lleida has a temperate semi-arid climate (class BSk, Koppen climate classification) characterized by cold winters and hot dry summers, with the annual potential evapotranspiration often exceeding the precipitation. The cultivar is Tempranillo. The tree spacing is ~1.1 m and the row spacing ~4.1 m with the vineyard's rows oriented roughly East-West (~110° from north). The row scene schematic is shown in Figure 22. The land use of the immediate environs is predominantly viticultural. According to results of a soil analysis of the site, the sand,

loam, clay compositions are 26.32%, 28.36%, 45.32%, respectively. The soil's relatively stony nature, especially at the topmost layer, helps to control and thus reduce evaporation losses allowing more effective irrigation water usage.

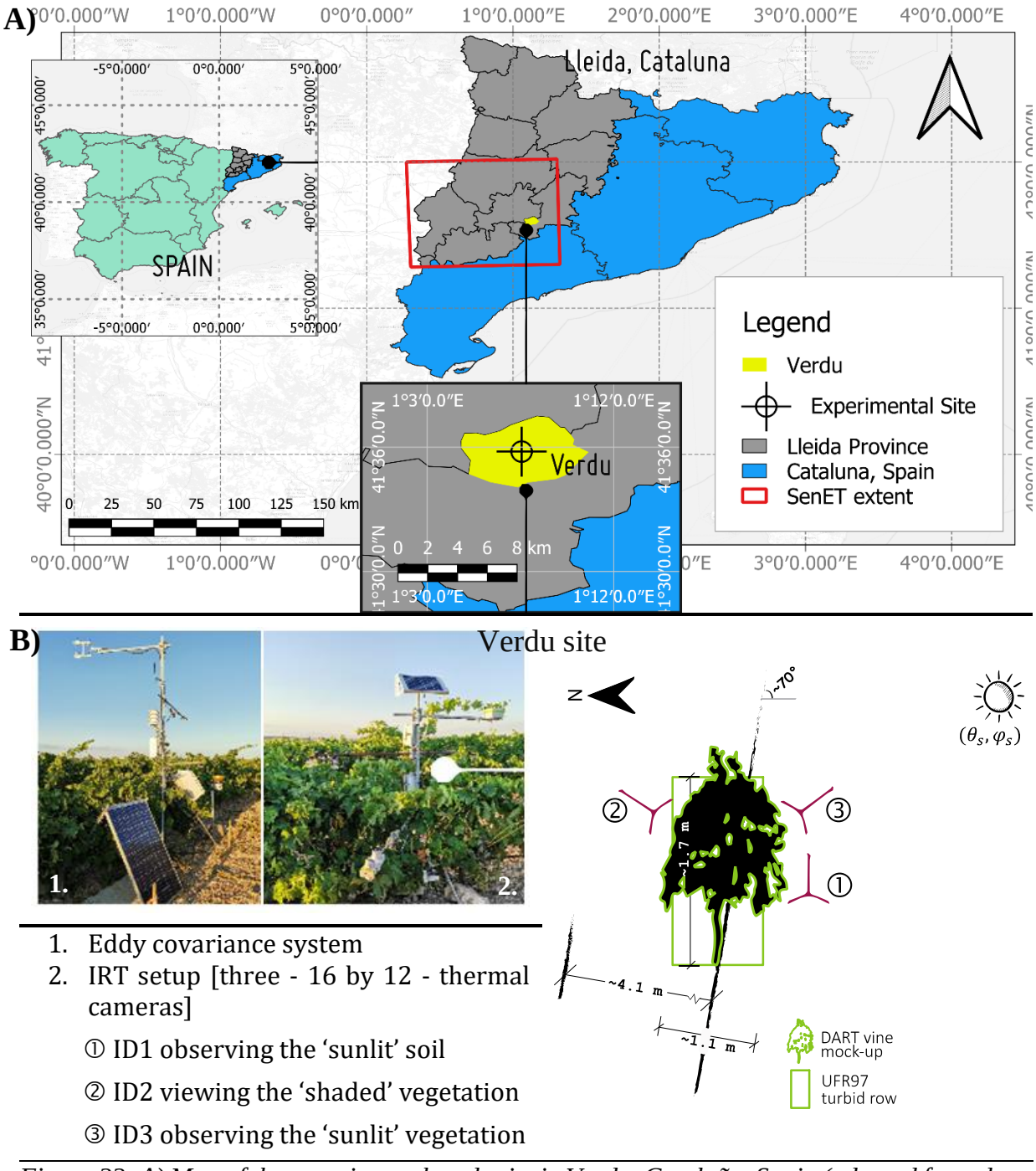

1. Eddy covariance system
2. IRT setup [three - 16 by 12 - thermal cameras]
   - ① ID1 observing the 'sunlit' soil
   - ② ID2 viewing the 'shaded' vegetation
   - ③ ID3 observing the 'sunlit' vegetation

Figure 22: A) Map of the experimental study site in Verdu, Cataluña, Spain (adapted from data retrieved from gadm.org); including the Sentinel for Evapotranspiration (SenET) spatial extent; B) the eddy covariance system and thermal camera installations at the vineyard; and a depiction of the scene & setup details.

5.2.2. *Data*

Instrumentation

The data collection campaign took place from April to September 2021 as part of the ESA WineEO and HiLiaise projects. The experimental installations at the study site included:

- SN 500-SS four-component net radiometer (Apogee Instruments) for observing down- and up-welling shortwave (model SP-510 and model SP-610, respectively) and longwave (model SL-510 and SL-610, respectively) radiation fluxes. Due to logistical constraints, the instrument was installed atop the row/canopy hence mostly viewing the vegetation elements.
- An eddy covariance system (IRGASON instrument, Campbell Scientific) for the monitoring of turbulent flux exchanges installed 3 m above the ground surface. It consisted of an open-path gas analyzer with a 3D sonic anemometer.
- Hygrovue5 temperature and humidity sensor (Campbell Scientific) for measuring the air temperature and relative humidity above the canopy at ~3 [m].
- Three HFP01 soil conduction plates placed at 5 cm depth below the surface for sensing the ground heat flux. Two of the plates were placed under the canopy and one between the row. Subsequent correction to include the heat storage at the top layer was done using the calorimetric method.
- Thetaprobes (ML2x) for soil moisture and soil temperature measurements. Three probes were installed under the canopy sensing at varying depths (5, 15, 30 cm) and one installed between the rows at 5 cm depth.
- Three SKR 1840 NDVImetre sensors (SKYE Instruments) for observing the irradiance and radiances in the red and near infrared spectral domains. That is, one NDVI (Normalized Difference Vegetation Index) instrument observed the respective narrow-band irradiances while the other two were placed such that they could observe the radiances atop the canopy and bare soil, respectively.
- Three thermal cameras (ID1, ID2, ID3) for measurement of the component surface temperatures. The TIR cameras have 16x12 pixels. These were

installed to view the bare soil, and the vegetation from two directions (i.e., in the sun's direction and in the shade) and sampling every 15 minutes. To be consistent with most of the other observed variables (with 30-minute acquisition intervals), only the half hourly temperatures were used. See Figure 22 for the installation set-up.

Selected radiation and meteorological variables are displayed in Figure 23. The European Centre for Medium-Range Weather Forecasts (ECMWF) reanalysis (ERA5) data used in retrieval of the Sentinel for Evapotranspiration (SenET, Nieto et al., 2020) estimates are observed to be relatively accurate – when compared to the in-situ measurements. The variations in the incoming solar radiation at overpass time (which are likely due to clouds) are not replicated in the reanalysis data. In the SenET framework, these overcast datasets are excluded as a consequence of cloud filtering of land surface temperature acquisitions. The daily aggregates of the short wave radiation - used within the SenET programme to scale from instantaneous to daily ET values - are nonetheless somewhat similar.

Biophysical data and data processing procedures

The leaf area index (LAI) was measured using a destructive approach. Since the canopy cover is expected to vary during vine development, it was necessary to scale the LAI so as to ensure a temporal trend. An exponential regression (following the NDVImetre documentation, e.g. $LAI = a \cdot e^{(b\mathrm{NDVI})}$ (Street et al., 2007)) was hence fitted. To this end, the red and near infrared (NIR) radiation signals measured by the NDVImetre sensors were used to compute the normalized difference vegetation index as: $\mathrm{NDVI} = \frac{\rho_{NIR}-\rho_{RED}}{\rho_{NIR}+\rho_{RED}}$; $\rho = \mathrm{radiance/irradiance}$ is the reflectance in the near infrared (NIR) and RED spectral domains. The derived NDVI (from signals acquired above the canopy, Figure 23) were subsequently used to scale the clump LAI to mimic the vegetative growth throughout the period. The temporally varying canopy cover obtained from this procedure was applied in other parts of this study, i.e., for the energy balance closure corrections and in the modelling exercises.

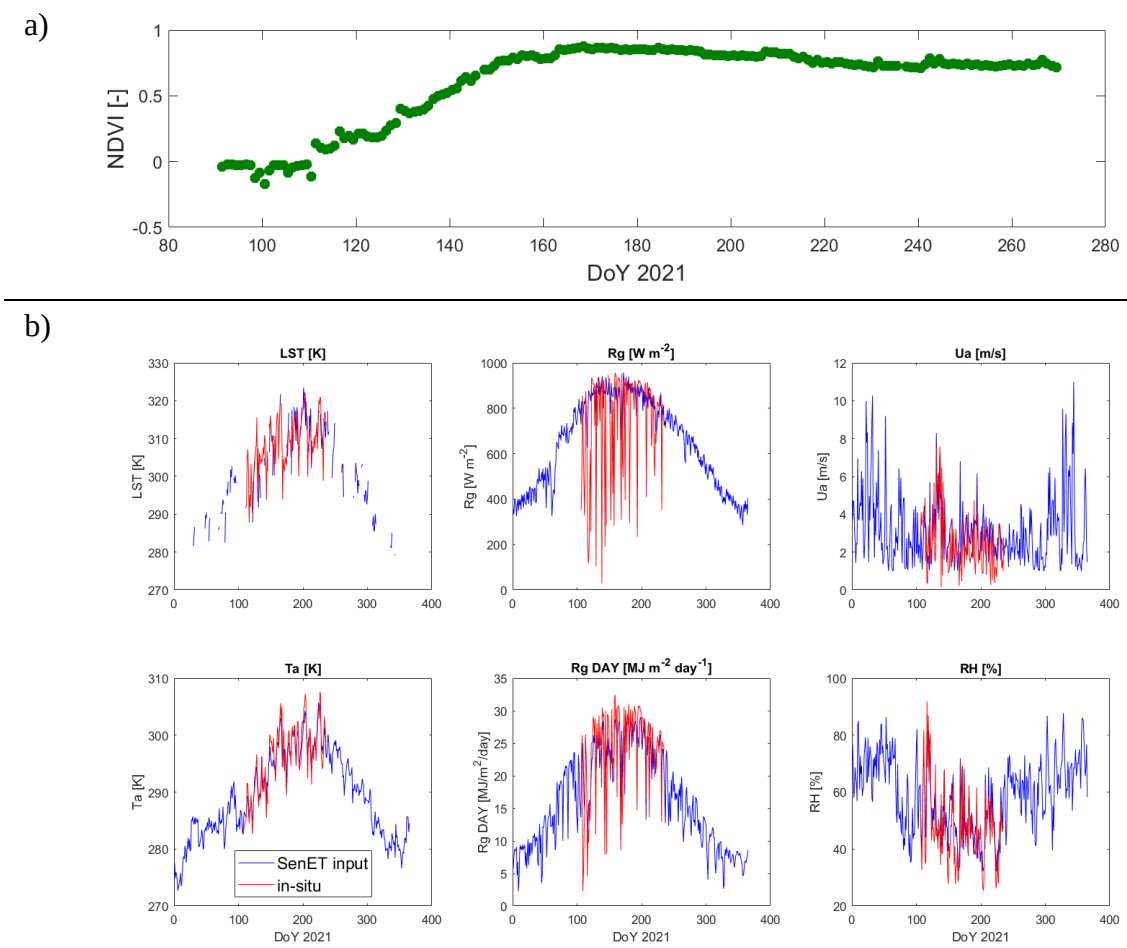

Figure 23: a) The NDVI computed using the near infrared and red signals measured above the canopy. b) Meteorological and other variables – in-situ (red), sentinel for evapotranspiration (SenET) reanalysis ensemble input (blue) at the Verdu experimental site.

Processing and correction of the raw eddy covariance data was carried out using the *EasyFlux DL* (Campbell Scientific) program. A simple gap-filling method (linear interpolation - based on the instantaneous to daily flux ratio from the immediate observed past) was then applied to address any missing data in the processed turbulent fluxes. The wind speed (u_a) was recomputed from the horizontal wind speed vector components from the sonic anemometer, i.e., $u_a = (u^2 + v^2)^{0.5}$.

Available energy, turbulent fluxes and the energy balance closure

The total available energy at the surface ($R_n - G_0$) is used up for the turbulent energy fluxes (sensible and latent heat fluxes). This yields the surface energy balance (SEB) equation, which is recalled here from section 2.1.2 (Equation (2.5)) as;

$$R_n - G_0 = \lambda E + H \tag{5.1}$$

R_n [W m^{-2}] is the net radiation equivalent to total (solar and thermal) irradiances less

total radiances, G_0 [W m^{-2}] is the ground heat flux, λE [W m^{-2}] and H [W m^{-2}] are the latent heat and sensible heat fluxes, respectively.

Unlike other methods (e.g. flux variance, surface renewal) that can only measure surface turbulent fluxes indirectly, eddy covariance systems allow direct measurement of latent and sensible fluxes (McElrone et al., 2013; Rosa & Tanny, 2015; Zhao et al., 2010). As such, the ideal energy budget closure, where the observed available energy is equivalent to the measured turbulent fluxes, is rarely realized in EC. The observed available energy has, in majority of the cases, been found to be larger than the observed turbulent fluxes (Foken, 2008). This is the well documented energy balance closure problem, which has been investigated and shown to be a recurring issue in multitudes of flux experimental sites (Foken, 2008; Wilson et al., 2002). Wilson et al. (2002) discussed circumstantial evidence pointing to a link between the non-closure of the energy balance with CO_2 fluxes while Foken (2008) mostly attributed the imbalances to miscalculations and scale issues, either in the available energy (net radiation or ground heat) or in the resulting turbulence measurements. Energy imbalance can also arise from advective fluxes and/or an inadequate sampling of low frequency turbulent motions (Wohlfahrt & Widmoser, 2013). Here, attempt is only made at correcting the terms in Equation (5.1). We nonetheless recognize the likely existence of other error sources to the SEB non-closure.

Corrections of the energy imbalance at the site

Errors in the soil heat flux often result from insufficient or missing calculations in the storage term, i.e. the heat stored in the soil above the heat plate (Foken, 2008). In Verdu, excluding this term contributed to the energy imbalance as it resulted in relatively large discrepancies in the estimated storage and thus an incorrect available energy. The calorimetric method (Sauer & Horton, 2015) was therefore applied to account for the additional storage. The calorimetric approach is preferred in majority of storage corrections since it has been documented as not being very sensitive to input data (Colaizzi et al., 2016; Liebethal et al., 2005). Accordingly, the corrected heat storage is written as Equation (2.9). The soil water content and soil temperature measurements were used in these calculations. Missing soil temperatures to be used in the corrections were reconstructed using a sinusoidal method that related existing surface soil temperature with available [5 cm] soil temperatures. A Savitzky-Golay filter (Savitzky & Golay, 1964) was applied to smooth out any sharp variations. Temperature

has the greatest influence on G_0 estimates (Liebethal et al., 2005) deeming these transformations for missing soil temperatures necessary. It is however acknowledged the reconstructions may have further contributed to the energy balance uncertainties.

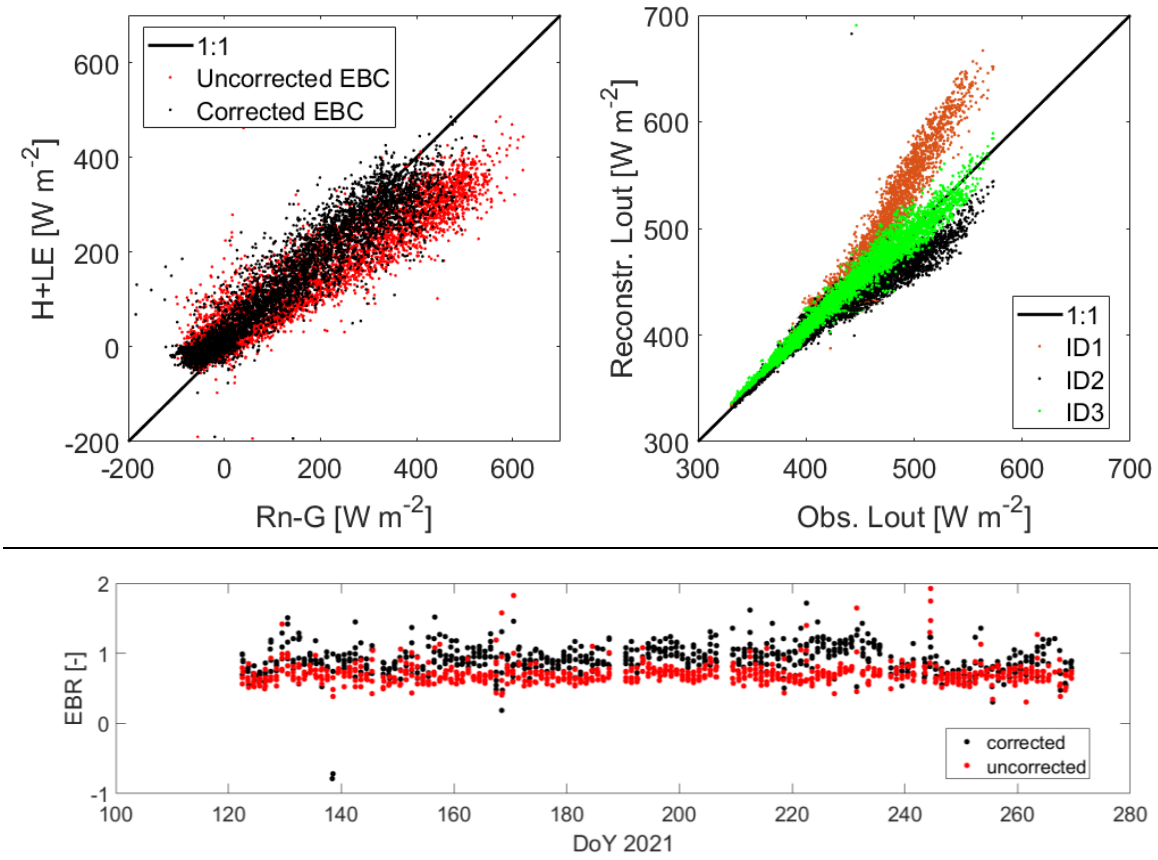

Figure 24: The energy balance closure in terms of the available energy and turbulent fluxes at the Verdu site. The measured upwelling thermal emission compared to emissions calculated using the different component temperature measurementss. The uncorrected and corrected mid-day energy balance ratios over the period.

The radiance measurements from the net radiometer were also subjected to some corrections. This was to reduce any scale biases emanating from the fact that the four-stream instrument was located just above the vegetation canopy. An initial comparison of the outgoing longwave radiation to the surface emission as calculated from the component temperatures (from the thermal sensors) showed that the measured longwave radiation was mostly coming from the exposed vegetation elements (ID3 in Figure 24). Following similar logic, the same issue could also be expected to influence the short wave radiance observations. Rescaling the radiations based on the relative fraction covers of the soil and vegetation resulted in a net radiation estimate that helped reduce the energy imbalance.

Figure 24 plots the observed energy balance, both with and without flux corrections. The energy closure error from the observed data was quite apparent, with only ~69% of the available energy being accounted for by the eddy-covariance measurements. The source of the imbalance was observed to mainly originate from the insufficient soil heat flux and the radiances measured by the net radiometer. The corrections made to the soil heat flux, i.e. by including the soil storage term of the top layer (using the calorimetric method), resulted in an improvement of the energy balance closure slope by ~1000 basis points to ~77 %. The shape – as described by the correlation coefficient – remained more or less the same, i.e., 0.95, 0.94 for the corrected and uncorrected cycles, respectively. The corrections on the ground heat flux mostly affected the daytime closures, where failure to include the top 5 cm soil layer led to significant underestimation of the storage term. This highlights the need for proper flux processing workflows to avoid inadvertently missed terms in the observed energy balance. To further refine the closure, the net radiation was reconstructed to address the potential scale issues arising from the proximal positioning of the net radiometer to the vegetation (see the outgoing longwave emission comparisons in Figure 24 where radiation measurements generally tally with the exposed vegetation emissions). A further enhancement of the closure was henceforth achieved, with the regression slope improving to ~87.5%.

The averaged day energy balance ratio (EBR, i.e., fraction of the daytime turbulent fluxes to the available energy), saw an improvement to 0.93 from 0.61, showing a similar enhancement as the EBC slope. The mid-day EBR of the corrected energy balance terms (Figure 24b) is also closer to the 1-to-1 equivalence throughout the experimental period. The corrected fluxes were applied in the further evaluations of the surface energy balance modelling below.

Temperature

The thermal cameras were installed to monitor the thermal infrared emission of the surface components throughout the experimental period. The field setup - with the relative positioning of the thermal sensors - is shown in Figure 22. That is, two cameras (ID1 and ID3) observing the sunlit soil and vegetation elements and the ID2 camera observing the shaded vegetation. Retrieval of emissions by source calls for emissivity correction of the observed brightness temperatures. Accordingly, we used the [manufacturer] recommended simple correction method (i.e., inversion of the radiation

equation) to obtain the component (or target) radiative temperatures (T_{xx}) from the thermal sensor observations,

$$T_{xx} = \left(\frac{T_{sensor}^4 - (1-\varepsilon)\varepsilon_{background} T_{background}^4}{\varepsilon} \right)^{0.25} \quad (5.2)$$

The air temperature served as the background temperature in these corrections. The emissivities of the soil and vegetation targets were taken as 0.96 and 0.98, respectively while the atmosphere's apparent emissivity (emissivity of the background) was estimated using Brutsaert's (1975, 1982) method; i.e., $\varepsilon_{background} = \varepsilon_a = F\varepsilon_a^{cs}$; where $\varepsilon_a^{cs} = 1.24(e_a/T_a)^{1/7}$ is the clear sky apparent emissivity. e_a and T_a are the air vapor pressure and temperature, respectively. F is a parameterized factor that scales the clear-sky emissivity to cloudy conditions (Brutsaert, 1982; Herrero & Polo, 2012). Further correction for the sensing wave-band was done using expressions from Idso (1981) and Olioso (1995) as described in section 3.1.2.

The directional surface temperature used to drive the models was subsequently reconstructed from the elemental temperatures weighted by their respective cover fractions in the view direction (both nadir and off-nadir). Due to the likelihood of mixed pixels, the sunlit elements were taken as the ~75th percentile of the observations from the cameras in the sun, while the shaded vegetation temperature was taken as the ~25th percentile of the pixels in the IRT camera inclined to view the shaded vegetation elements. The Chebyshev's inequality theorem, which is more general and can thus be applied to any probability distribution, yields $P(|T-\mu| \geq \sqrt{2}\sigma) \leq 50\%$ for the foremost realistic bound, $\mu \pm \sqrt{2}\sigma$; μ is the mean and σ the standard deviation. Accordingly, respective values at ~μ-$\sqrt{2}\sigma$ and ~μ+$\sqrt{2}\sigma$ were selected to represent the shaded and sunlit elements in place of the respective mean (μ) values.

The weighting expression for the surface temperature is written thusly (e.g. Lagouarde et al. (2014));

$$T_{surf} = \left[\sum_{xx=vs,vh,gs,gh} K_{xx}(\theta_v, \varphi_v) T_{xx}^4 \right]^{0.25} \quad (5.3)$$

where $K_{xx=vs,vh,gs,gh}(\theta_v, \varphi_v)$ are the fractions of the individual surface components. Subscripts xx denote the sunlit (s) and shaded (h) soil (g) and vegetation (v) elements. The fractions or weights were herein estimated using the Unified Francois model (Bian

et al., 2018; Francois et al., 1997), which incorporates aspects of the row canopy BRDF method proposed by Yan et al. (2012). T_{xx} are the elemental or component temperatures of the shaded/sunlit soil/vegetation.

5.3. Methods

We utilize the Soil Plant Atmosphere Remote Sensing of Evapotranspiration (SPARSE, Boulet et al., 2015) model to simulate the land surface energy exchanges. SPARSE, like the two source energy balance model (TSEB, Norman et al., 1995), is a surface energy balance (SEB) method that simulates soil-vegetation-atmosphere interactions and consequently retrieves actual/prevailing surface (soil and vegetation) fluxes by inverting the surface temperature. The scheme has recently been extended to discriminate the soil and vegetation sources into their respective sunlit/shaded components (SPARSE4, Mwangi et al., 2022) where an extended energy balance scheme was coupled with the Unified Francois radiative model (Bian et al., 2018; Yan et al., 2012). The algorithms are described in detail in section 3.1.1.

Input and methodology

Here, the variables required to drive the surface energy balance schemes (SPARSE/SPARSE4) include: meteorological conditions (wind speed, air temperature and humidity) and the surface biophysical characteristics (leaf area index, vegetation height, etc.). Boundary conditions (in terms of water availability) are described by the surface temperature input as well as the potential and stress limits mentioned above. The minimum stomatal resistance of the vineyard was taken as ~100 s/m (Teixeira et al., 2007).

The processed temperature data (i.e. the emissivity corrected thermal measurements) were first used as input in radiative transfer schemes to perform an inter-comparison exercise. Three clear-sky days (DoYs: 128, 183, 211) were selected to perform these experiments. Consequently, directional surface temperatures simulated by the Unified Francois (UFR97 - see Equation (3.1) further above) and the thermal-based four-stream Scattering by Arbitrarily Inclined Leaves (4SAIL, Verhoef, Jia, Xiao, & Su, 2007) radiative models were evaluated against those simulated by the 3D DART (discrete anisotropic radiative transfer) radiative scheme, which was taken as the ‘reference’. The 3D vine objects/mock-ups used in DART were built using the

blender.org software and pictures of the vines. The reconstructions of directional temperatures as applied in the experiments are described in sections 5.2.2 and 5.4.1. The surface energy balance methods (SPARSE and SPARSE4) were then driven using the reconstructed surface temperatures. In the first part, the surface temperatures of the entire campaign period were used and the models evaluated using the EB EC observations (section 5.4.2). Separately, the radiation and meteorological data from the ERA5 ensemble estimates as used in SenET products were used to drive the SEB methods and this allow an intercomparison with the SenET product. The second part involved the evaluation of the SEB schemes in terms of directionality. Section 5.4.3 therefore reports an evaluation of the SPARSE and SPARSE4 models (in directional consistency experiments) using the reconstructed directional surface temperatures - separately based on: i) reconstructions by UFR97 over the whole period, and ii) reconstructions from DART over the selected clear sky days.

5.4. Results and Discussion

5.4.1. *Surface temperature reconstruction: comparison with the DART model*

In this section, we propose to evaluate the UFR97 RTM (presented earlier in section 3.1.1) by comparing it with a reference 3D radiative transfer scheme, DART, as well as a 1D model that does not account for canopy heterogeneity, 4SAIL. Accordingly, we compare the surface temperatures simulated using the DART model to the temperature simulated by the different RTMs (i.e., UFR97 and 4SAIL). The UFR97 radiative transfer method has already been evaluated against the thermal radiosity-graphics combined model, a 3D radiative transfer method, where its retrieval capabilities were demonstrated over continuous as well as heterogeneous canopies (Bian et al., 2018). Those evaluations are thus complemented here by utilizing the 3-D DART model. As described previously (section 2.3.2), DART is a comprehensive 3-D radiative transfer scheme that models leaf specular and polarization mechanisms as well as topography and hotspot (Gastellu-Etchegorry et al., 1996) and can therefore be used to simulate thermal infrared remote sensing ‘observations’ in a variety of heterogeneous scenes.

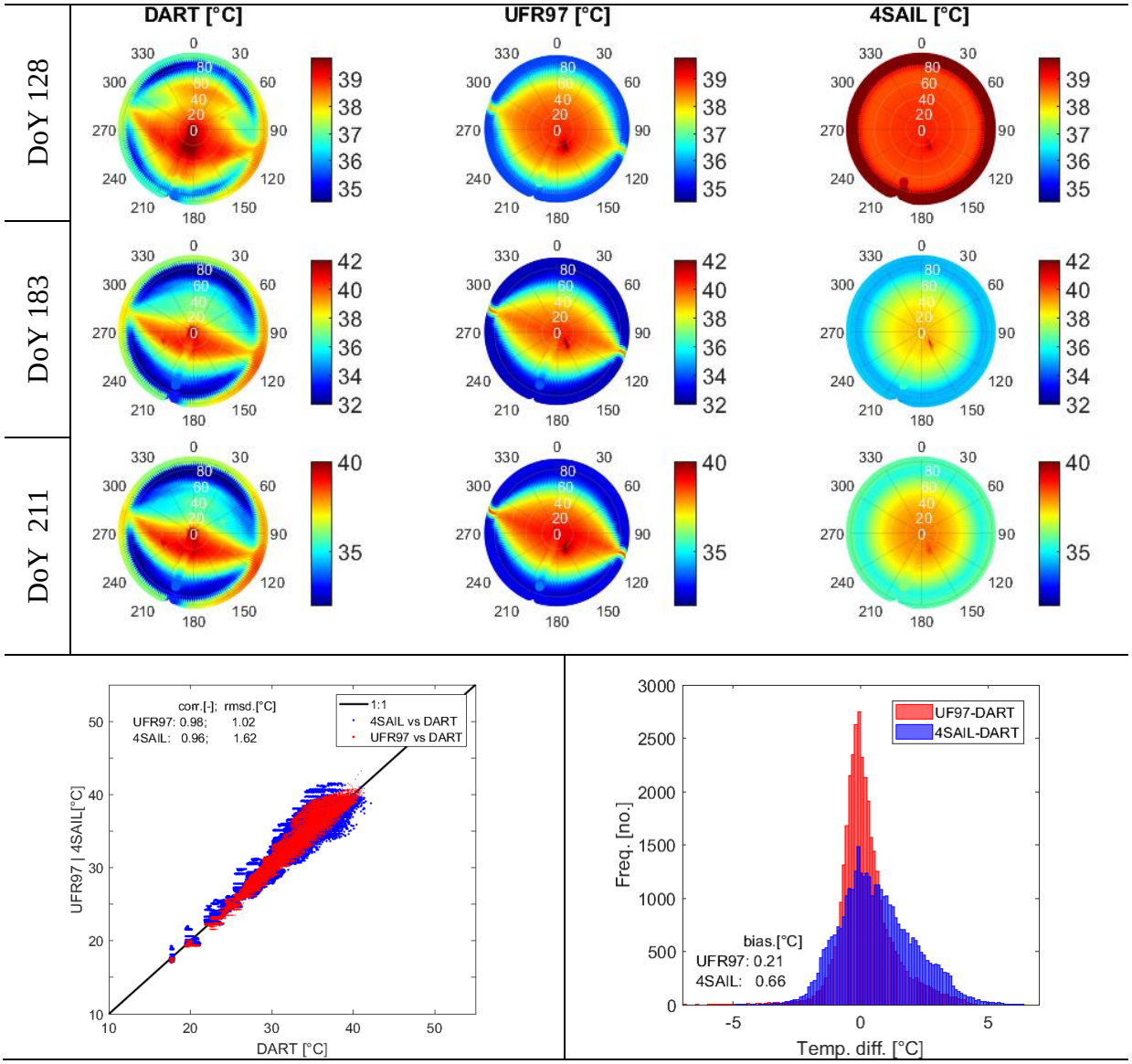

Figure 25: Inter-comparison of the UFR97 (and 4SAIL) temperatures to those simulated by the DART 3-D model. a) noon polar plots depicting the simulated angular temperatures; presented separately for the 3 selected periods b) scatterplot and metrics of day-time UFR97 and 4SAIL-retrieved surface temperatures versus those simulated by the 3-D DART model, and c) the corresponding histograms of temperature differences. b) and c) combine all daytime data.

The data used for this exercise has been described in section 5.2. In UFR97, a turbid vine model, thus considering a discontinuous row canopy, is assumed while the vine mock-up in DART was more realistic (depiction in Figure 22). Sunlit and shaded temperatures were then used as inputs of the UFR97 model, using the reconstruction expression (Equation (3.1), (5.3)). In DART, the average soil and vegetation temperatures [$T_{ave}=(T_{sun}+T_{shd})/2$] were needed as input and a [$\Delta=(T_{sun}-T_{shd})/2$] used to assign illuminated [$T_{ill}=T_{ave}+\Delta$] and shaded [$T_{shd}=T_{ave}-\Delta$] mock-up element temperatures for the directional temperature simulations.

Considering that the DART simulations utilized realistic vine mock-ups (see Figure

22), the UFR97 model (which employs a turbid geometrical model) performs quite well when retrieving the directional signals, and generally outperforms the 4SAIL radiative method that is based on a homogeneous canopy. Accordingly, the consideration of the row geometry in UFR97 ensures that the distribution of temperatures over the angular viewing space (i.e., shape of polar plots, particularly along the row) is better replicated. The distribution of differences (Figure 25) also shows that the UFR97-estimated temperatures were generally close to those simulated by DART, yielding a mean error of 0.21 °C versus 0.69 °C achieved by the 4SAIL radiative transfer. Nonetheless, use of a turbid model means that the unified Francois model could not model some specific phenomena. For example, the column used to represent the row (where the canopy leaf area is uniformly grouped vertically) may not be very realistic given that the vine generally consists of the lower part (trunk) and the upper whorl structure (see the vine mock-up illustration in Figure 22). At relatively low sun altitudes, this canopy structure usually makes it possible to observe more shadows (or vice versa) especially when viewing from low elevation angles. The symmetry of the UFR97 simulations where they tend to disperse uniformly across the row arises from the fundamental description of the method, i.e., it is essentially a product of the gap probability (based on the row geometry (Yan et al., 2012)) and the anisotropy variations of Kuusk's (1985) illuminated / shaded probabilities that are based on a homogeneous scene.

5.4.2. *Model estimates*

Evaluation with in-situ data

To simulate the energy budget components, the SPARSE energy balance modelling schemes were first forced using the reconstructed nadir surface temperatures (in addition to other meteorological inputs). Figure 26 scatters the estimated turbulent fluxes against the observations. As exhibited by the daylong performance metrics, the models satisfactorily (and similarly) retrieved the overall fluxes. There was however a tendency for the models to overestimate the daytime sensible heat flux while somewhat underestimating the respective nighttime flux at the site leading to relatively small biases (overall biases were -5.32 W m^{-2} and -3.36 W m^{-2} for SPARSE and SPARSE4, respectively). In addition to inherent model-induced errors, this could also, in part be attributed to measurement errors as given by the observed energy imbalance, i.e., lower observed turbulent fluxes relative to the measured available

energy. While the representation of the surface as a row-scene could possibly help in the realistic characterization of flux partitioning (not tested here since such data was not available), this does not necessarily translate into a significant improvement in overall performance. Provided the correct effective canopy area together with surface temperatures with little thermal directionality influences are used in surface energy modelling, reasonable flux retrievals can seemingly be achieved.

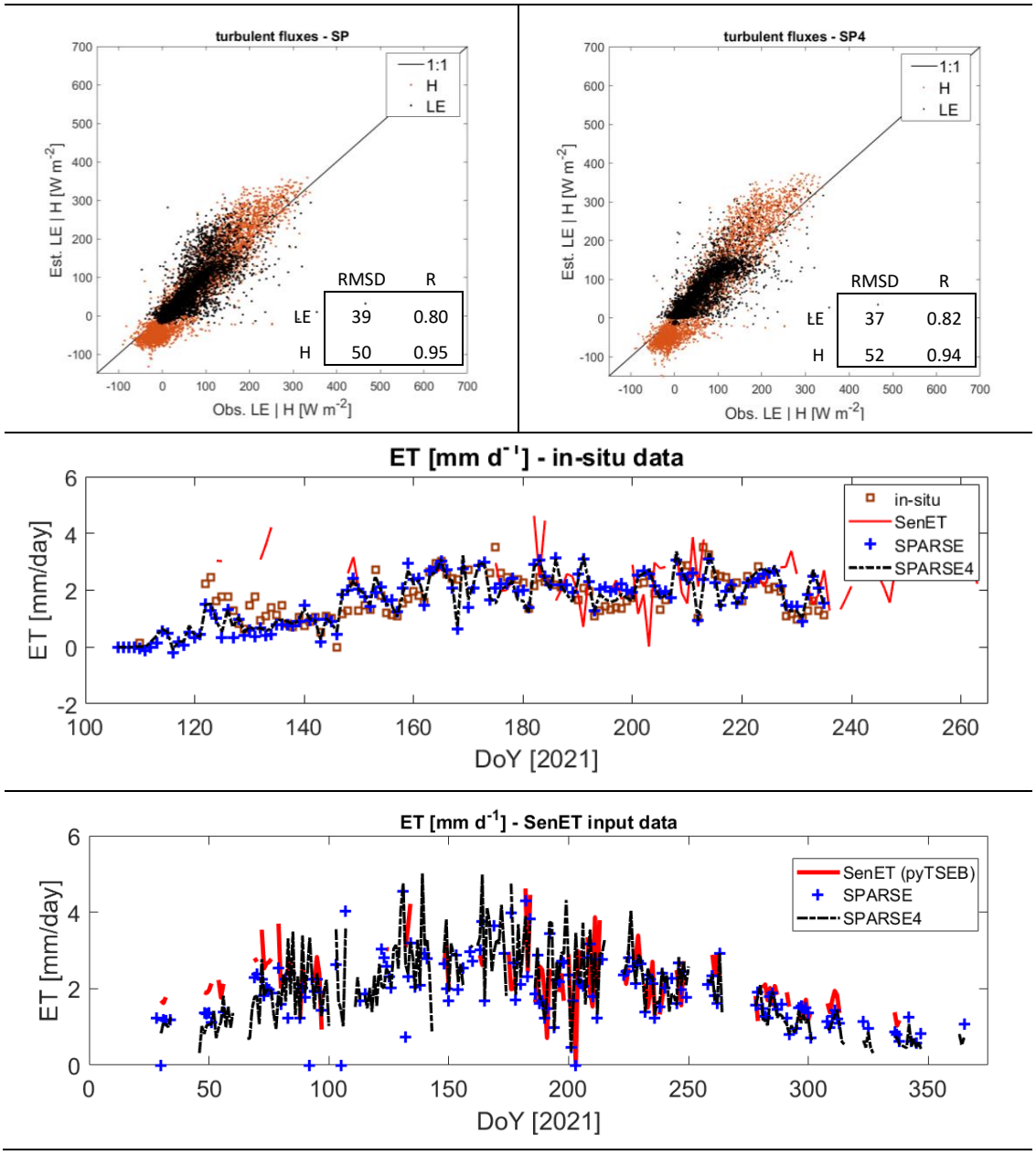

Figure 26: a) scatter plots of simulated versus observed turbulent fluxes at the Verdu site; left, SPARSE and right, SPARSE4; b) modelled (using in-situ meteorological and ancillary data) and in-situ daily evapotranspiration time-series'; c) time-series' of ET simulated by the various modelling schemes using the SenET data (reanalysis and Sentinel Verdu extracts) as input.

Table 5: performance metrics of the overall fluxes and recalculated average component temperatures*

	SPARSE			*SPARSE4*		
	RMSD	*r*	*bias*	*RMSD*	*r*	*bias*
LE	39	0.80	3	37	0.82	2
H	50	0.95	-5	52	0.94	-3
G	49	0.78	17	49	0.77	11
Rn	32	0.99	14	33	0.99	15
T_v^*	3.14	0.95	-0.49	1.65	0.98	-0.77
T_g^*	3.65	0.95	-0.58	3.15	0.96	-1.13

Separately, the surface energy balance models also simulated source temperatures, which could hence be compared with the observations. The UFR97 coefficients were used in weighting of the elemental temperatures for the average component temperatures used in the performance metrics calculations in Table 5. Overall, the estimated component temperatures were realistically reproduced. Qualitatively, this is illustrated in the time series' in Figure 27 - i.e. the thermal camera measurements (labelled ID1, ID2, ID3 in Figure 22) and the modelled temperature. Quantitatively, these modeled temperatures were satisfactory (Table 5).

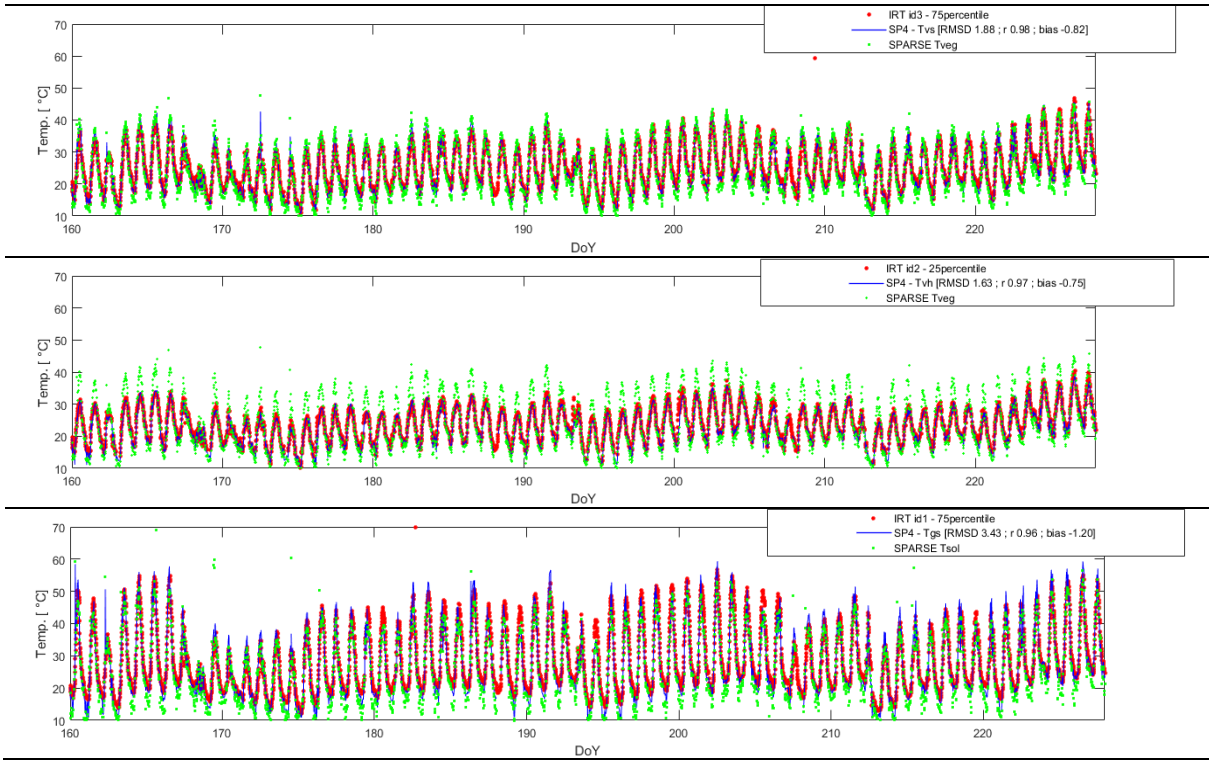

Figure 27: Observed and simulated component temperatures over the period. Top to bottom – 'sunlit' and 'shaded' vegetation and 'sunlit' soil, respectively.

•

5.4.3. *Directional consistency analyses*

Ideally, the estimated overall surface fluxes should exhibit consistency, irrespective of the viewing direction of the thermal signal input. They should not be affected by the sensing direction/geometry of a remote sensor. To check this retrieval consistency, the directional surface temperatures were reconstructed using Equation (5.3) as detailed in section 5.2.2 above. These were then used to rerun the models for comparison of the oblique-retrieved fluxes versus the nadir-retrieved ones. The polar plots of the resulting metrics are illustrated in Figure 28.

Retrieval consistency is generally degraded cross-row with a much better consistency between nadir and oblique retrievals along the vine row. Along row, the gap fraction tends to remain relatively constant from nadir to higher zenith angles. This is however not the case cross-row where the observed vegetation fraction cover will increase with decrease in elevation. Early on in the growth period, when the surface is mostly bare, thermal directionality effects are mainly observed to influence flux retrievals in the hotspot region (Figure 28 a). For such periods, the influences are nonetheless of low magnitudes. Even for periods with relatively full row development, the hotspot region somewhat adds to the nadir versus oblique flux retrieval inconsistencies. The row geometry's contribution to the retrieval directionality influences also becomes apparent during such stages (especially at larger zenith angles).

		SPARSE		SPARSE4	
		rRMSD [-]	MAE [W m^{-2}]	rRMSD [-]	MAE [W m^{-2}]
		midday / ~1200 hrs			
Per1 (low FVC)	LE	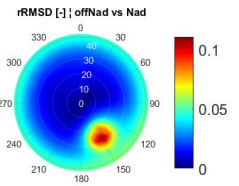	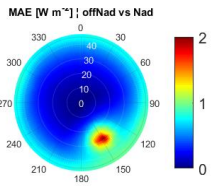	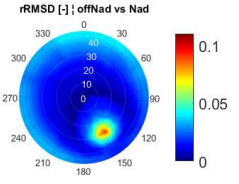	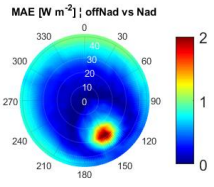
	H	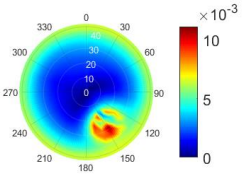	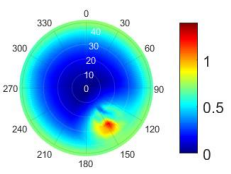	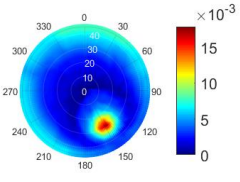	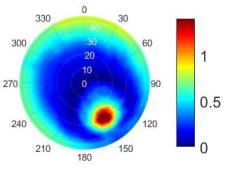
Per2 (fully	LE				

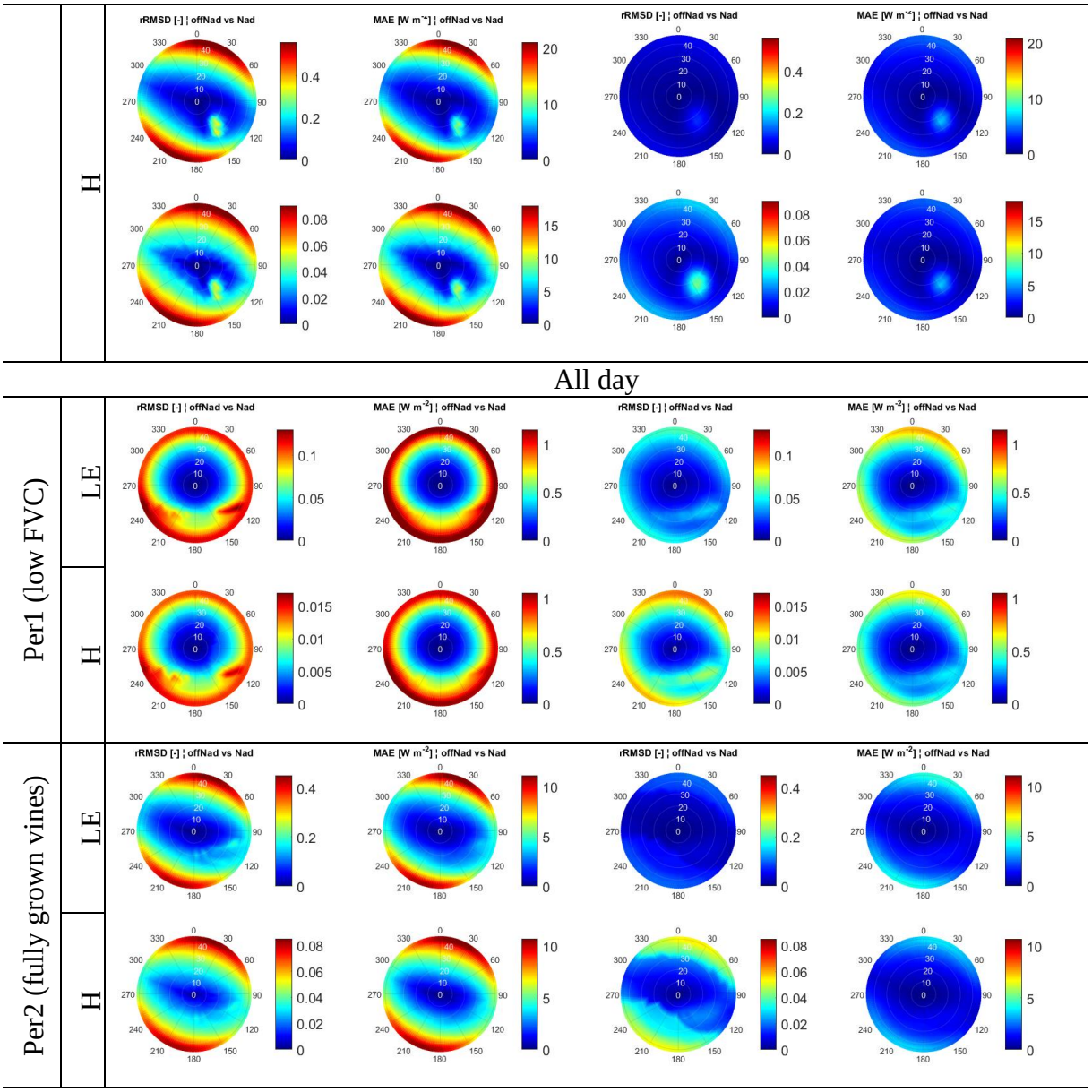

Figure 28: LE and H polar plots of oblique-vs-nadir rRMSD and MAE for the growth period [noon and all-day]

In addition to the full period dataset, which contained the directional temperatures reconstructed using the UFR97 model (as described above), the sample dataset used for the DART comparisons was also applied to the models. This data was limited to only three clear-sky days. The directional temperature reconstructions as compared to those simulated by the 3D DART model are presented in Figure 25. Figure 29 below shows the directional inconsistencies observed when the DART temperatures are used in the inversion of the surface energy balance (latent and sensible energy fluxes) in SPARSE and SPARSE4.

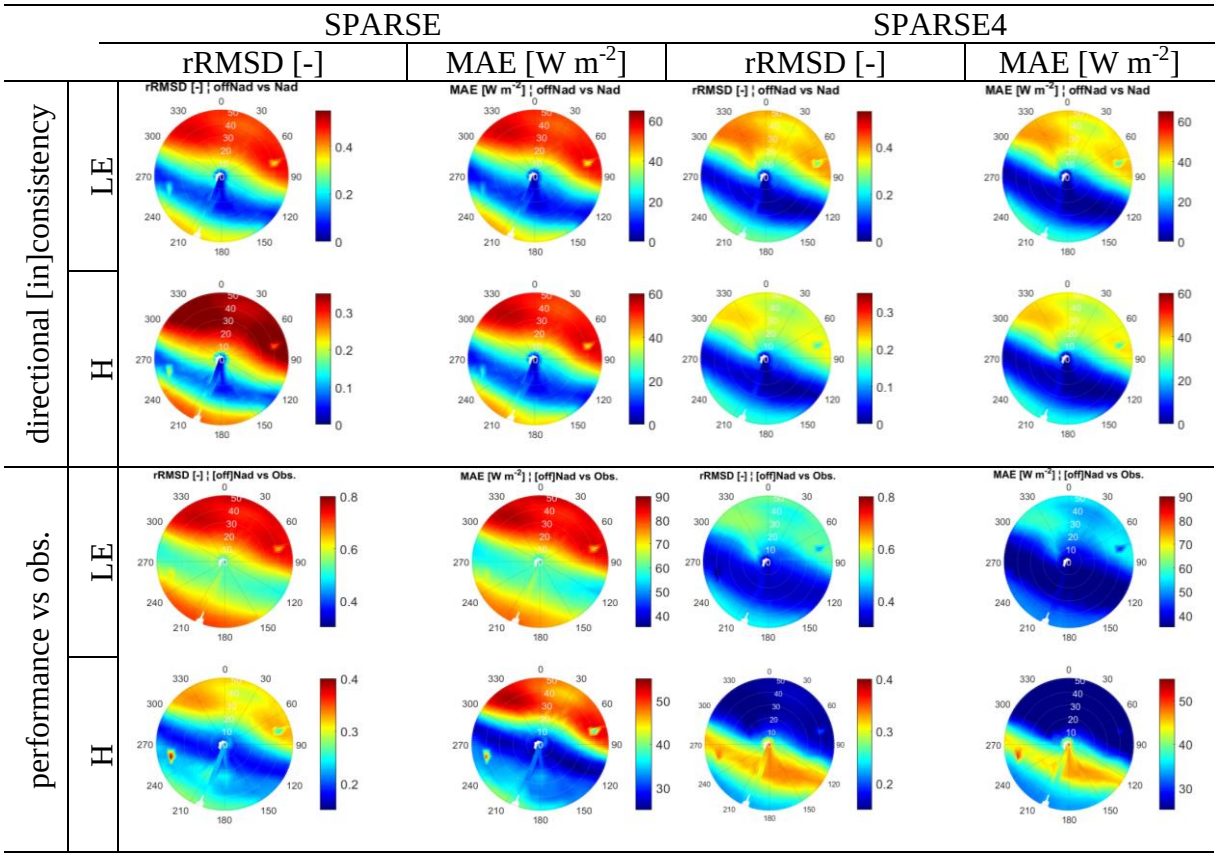

Figure 29: directional inconsistency (nadir- versus oblique-based estimates) for the two SPARSE surface energy balance methods; b) comparison of the directional retrievals as compared to the eddy covariance observations. Polar plot illustrations use the around noon data over the three selected clear-sky days

The symmetry (in the simple turbid models: here the heterogeneous UFR97, and homogeneous Nilson's (1971)/Beer Lambert's schemes) versus the dissymmetry (in DART with the more realistically modelled vine mock-up) in the simulated directional temperatures described earlier (section 5.4.1) does indeed influence the retrieval consistency between different TIR input directions. Along the row (i.e., at view angles close to the row direction), DART simulates relatively contrasting temperatures in the directions in and away from the Sun's direction. While the symmetry simulated by the UFR97 model in the Sun's direction is able to reproduce the temperature distributions in DART, the lower temperatures close to the row - in the direction away from the sun - are not well replicated. As pointed out in section 5.4.1 (Figure 25), this can be perhaps be ascribed to the radiative method applied, which is a product of row gap frequency according to Yan et al. (2012) and the illumination/shade anisotropy variations or probabilities of Kuusk's (1985) that are based on a homogeneous scene. Applying such disparately lower temperatures when inverting the surface energy balance tends to infer a lower surface water-stress. Henceforth, the lower

temperatures in the Sun's opposite direction are inconsistently manifested in form of higher [lower] latent [sensible] heat fluxes.

Better directional consistency does not necessarily imply an overall better model performance. Whereas the oblique-based (close to zenith) model estimates can be seen to be consistent with the nadir-based estimates (with degraded consistency further off-nadir), the performance relative to the real observations may indicate and thus be interpreted otherwise. Unless the inconsistencies manifest in large magnitudes (as would be the case in scenes with large vegetation fraction covers), then standardizing directional thermal data to a specific direction (e.g. nadir) should not be assumed to result in better flux estimations. As shown in Figure 29 (i.e., sensible heat flux estimated using SPARSE4), the performance further off-nadir can sometimes be better than the more consistent near-nadir estimates. Nonetheless, more robust algorithms that ensure directional consistency are necessary as that would give users confidence in obtaining appropriate direction-independent outputs.

5.5. Conclusions

An experimental field study was carried out in the framework of the HiLiaise project aiming at monitoring surface components of a Vineyard in Verdu, Cataluña, Spain. The processed and corrected (for the observed energy imbalance) fluxes are presented. The energy balance closure was improved considerably after correcting the available energy (net radiation less soil heat flux) terms. That is, by including the top layer storage term for the overall soil heat flux and separately enhancing the radiances measured by the net radiometer to account for scale (or proximity) issues. These measurements were then applied for onward assessment of methods used to estimate the surface energy balance, where an inter-comparison with the Sentinel for Evapotranspiration variables was also done (also see appendix for additional SenET analyses). For the surface energy balance modelling, the directional surface temperature was initially reconstructed from the measured elemental temperatures, whereupon we demonstrated the applicability of the relatively simple Unified Francois model over the heterogeneous row canopy. While homogeneity of the surface is often assumed in methods used for characterizing land surface processes, it is necessary to consider realistic canopy geometries for better modelling of angular anisotropy dynamics. A preliminary comparison between the UFR97 model, 4SAIL and the 'reference' DART simulations was thus performed, where it was shown that the UFR97

simulations were more consistent with the DART ‘truths’ particularly in terms of temperature distribution over the polar space.

When run using the nadir-reconstructed surface temperatures, the surface energy balance SPARSE schemes yielded reasonable surface turbulent flux estimates, which as expected were relatively similar since both methods are based on a similar model structure (model assumptions, physics, among others). A realistic retrieval of component thermal emissions was also achieved where the overall trends and magnitudes of the various surface elements were replicated. As for the inter-comparison with the sentinel for evapotranspiration extracts, the equivalence of input variables (e.g. meteorological variables from ERA5 versus those observed at the site) meant that the evapotranspiration extracts of the AOI were generally of similar magnitude with those attained in-situ. To check the angular retrieval consistency, the reconstructed temperatures (directional, i.e. nadir and off-nadir) were used to re-run the SPARSE and SPARSE4 energy balance schemes. Both methods ensured flux consistency along-row with degraded performance being observed cross-row. This was more pronounced in the SPARSE estimates.

The study has demonstrated the necessity of incorporating more realistic canopy representations if directional retrieval consistency is to be maintained. While the use of a homogeneous radiative scheme may be sufficient when using near-nadir thermal measurements, better modeling of the canopy should allow better flux consistency especially for higher view angles. However, the realism of simple radiative schemes used for heterogeneous surfaces needs to be improved to mimic naturally occurring asymmetries (as modeled by more complex 3D models) and thus reduce directionality effects.

Chapter 6: Influence of thermal radiation directionality (TRD) on surface flux retrieval

6.1. Point-scale surface energy balance experiments

This section is basis of an article (in preparation)

Summary

The susceptibility of surface energy balance modelling to thermal radiation directionality is tested. Here, we apply the SPARSE dual source and the extended surface energy balance schemes for flux estimation and directionality analyses using 'truths or references' in a continuous canopy experimental setup. To this end, we use the soil canopy observation of photosynthesis and energy fluxes (SCOPE, SCOPE-lite) model to provide the 'reference' observations for a variety of homogeneous surface conditions, which range from a sparsely vegetated and water stressed surface to a sufficiently watered and fully vegetated canopy. The surface exchange components simulated by SCOPE were then used to invert and assess the aforementioned surface energy balance methods. First, a comparison of the 'references' with the SPARSE simulations obtained using the standard nadir brightness was undertaken. Generally, both SEB schemes are observed to retrieve the overall fluxes with reasonable accuracy. The agreement between the reference and the SEB estimates is however somewhat degraded at lower stomatal resistance and with increasing wind speed. This is most likely due to the differences in model structures between the compared SPARSE/SPARSE4 and reference SCOPE methods. Since nadir- versus oblique-based simulated components should ideally be equal, analyses to check the angular retrieval consistency were carried out. Within sparsely (as well as densely) vegetated surfaces, where the directional anisotropy is usually low due to uniformity and thus negligible surface roughness, little retrieval inconsistencies between nadir and oblique-based estimates were observed over the polar grid. Relatively larger inconsistencies were however observed at intermediate canopy leaf areas. With regard to other characteristics, the incoming radiation (particularly around noon) appeared to be the main driver of the observed inconsistencies with wind speed and vegetation water status also contributing to some of the mismatches. Conversely, influence emanating from the soil water status was mostly only observed when the surface was sparsely vegetated. This is because soil emission signals contribute relatively little to the out-of-canopy radiation when there is dense vegetation. The extended SPARSE is nonetheless observed to reduce the

retrieval inconsistencies in most of the simulated scenarios (especially with increasing canopy cover fraction). We also analyse the possibility of such influences on thermal remotes sensing through polar orbiters. It is thus shown that such effects tend to be minimal since polar orbiters are inherently designed to provide acquisitions within a narrow viewing range, with more enhanced temporal resolutions (hence reduced view zeniths) diminishing the effects further.

Keywords: thermal infrared, thermal radiation directionality, surface energy balance, evapotranspiration

Résumé

La susceptibilité de la modélisation du bilan énergétique de surface à la directionnalité du rayonnement thermique est testée. Ici, nous appliquons la source double SPARSE et les schémas étendus de bilan énergétique de surface pour l'estimation des flux et les analyses de directionnalité en utilisant des " vérités ou des références " dans une configuration expérimentale de canopée continue. À cette fin, nous utilisons le modèle SCOPE (soil canopy observation of photosynthesis and energy fluxes, SCOPE-lite) pour fournir des observations de "référence" pour une variété de conditions de surface homogènes, qui vont d'une surface peu végétalisée et soumise à un stress hydrique à une canopée suffisamment arrosée et entièrement végétalisée. Les composantes d'échange de surface simulées par SCOPE ont ensuite été utilisées pour inverser et évaluer les méthodes de bilan énergétique de surface mentionnées ci-dessus. Tout d'abord, une comparaison des "références" avec les simulations SPARSE obtenues en utilisant la luminosité standard du nadir a été entreprise. En général, on observe que les deux schémas SEB récupèrent les flux globaux avec une précision raisonnable. La concordance entre la référence et les estimations SEB est cependant quelque peu dégradée lorsque la résistance stomatique est faible et que la vitesse du vent augmente. Ceci est très probablement dû aux différences de structures de modèles entre les méthodes comparées SPARSE/SPARSE4 et SCOPE de référence. Puisque les composantes simulées basées sur le nadir et celles basées sur l'oblique devraient idéalement être égales, des analyses visant à vérifier la cohérence de la récupération angulaire ont été effectuées. Sur les surfaces à végétation éparse (ou dense), où l'anisotropie directionnelle est généralement faible en raison de l'uniformité et donc d'une rugosité de surface négligeable, on a observé peu d'incohérences entre les estimations basées sur le nadir et celles basées sur l'oblique sur la grille polaire. Des incohérences relativement plus importantes ont toutefois été observées pour les surfaces foliaires intermédiaires de la canopée. En ce qui concerne les autres caractéristiques, le rayonnement entrant (en particulier vers midi) semble être le principal facteur des incohérences observées, la vitesse du vent et l'état hydrique de la végétation contribuant également à certaines des incohérences. Inversement, l'influence émanant de l'état hydrique du sol n'a été observée que lorsque la surface était peu végétalisée. Cela s'explique par le fait que les signaux d'émission du sol contribuent relativement peu au rayonnement hors canopée en présence d'une végétation dense. On observe néanmoins

que l'extension de SPARSE réduit les incohérences d'extraction dans la plupart des scénarios simulés (en particulier lorsque la fraction de couverture de la canopée augmente). Nous analysons également la possibilité de telles influences sur la télédétection thermique par des orbiteurs polaires. Il est ainsi démontré que de tels effets ont tendance à être minimes puisque les orbiteurs polaires sont intrinsèquement conçus pour fournir des acquisitions dans un champ de vision étroit, avec des résolutions temporelles plus élevées (donc des zéniths de vue réduits) diminuant encore les effets.

Mots clés : infrarouge thermique, directionnalité du rayonnement thermique, bilan énergétique de surface, évapotranspiration

6.1.1. Introduction

The water or mass balance at the near land surface consists of several processes; *inter alia*, runoff, recharge, evaporation and transpiration. Over natural land, evapotranspiration (ET) has been found to account for over 60% of water fluxes (accounting for nearly 90% of the precipitation in arid and semi-arid lands (Huxman et al., 2005)), making it a key component of the hydrological cycle. ET estimation is usually achieved by applying models that simulate the soil water content (i.e., water available to the vegetation and for soil evaporation losses) or – indirectly - by using variables with a tight link to the surface water status. Surface energy balance (SEB) methods driven by the Land Surface Temperature (LST) are common examples of the latter. These physically based surface energy balance modelling schemes have been detailed earlier in section 2.3.1, and can broadly be classified as either point- or contextual-based. In point-based methods (as applied in the study presented in this section), atmospheric demand as described by meteorological conditions define the [potential] water-holding capacity with the radiation [both incoming and outgoing] and surface water availability describing the actual/prevailing conditions. Accordingly, LST can be utilized in point SEB modelling to arrive at the prevailing available energy and thus actual water status.

Surface temperature signals from field radiometers installed in-situ will generally be observed from a standard fixed direction (for example nadir). Conversely, drones/UAVs (unmanned aerial vehicles) and space-borne sensors provide thermal infrared acquisitions with varying degrees of temporal and spatial resolutions, and from several directions. Due to angular anisotropy of the radiant signals, the observed surface brightness temperature usually varies depending on the direction of view, which generally changes from one overpass to the next (Guillevic et al., 2013; Olioso

et al., 2022). Indeed, most space-borne satellites with moderate to high revisit times observe the same location on earth from a wide range of directions, for example, up to ~60° zenith [~scan] for MODIS, ~34/37° in the soon-to-be launched TRISHNA. The observed variation in surface thermal emission is mainly due to different proportions of sunlit and shaded surface elements being observed in the sensor's field of view (as described by the sun-earth-sensor geometry). This can lead to directional anisotropies (off-nadir to nadir temperature differences) of up to 15 °C (Kimes & Kirchner, 1983; Lagouarde et al., 2014). Notwithstanding the differences in the simultaneously measured directional-dependent surface temperatures (at a particular instant), source temperatures and thus the overall surface fluxes remain the same. It is therefore important to account for such directionality in surface energy balance methods that rely on surface temperature to detect water stress since such TRD in remotely sensed thermal signals can significantly influence the estimation of heat fluxes and thus the evapotranspiration. Assessing (both quantitatively and qualitatively) this influence is therefore important. Previously, Duffour et al. (2016) looked at the influence of various surface characteristics on the resulting directional thermal signals. They observed that, in addition to meteorological conditions (such as wind speed, incoming radiation, etc.), vegetation characteristics (e.g. leaf or vegetation area) and surface water stress also play a role in thermal directional anisotropy.

Carrying out intensive measurement experiments of directional thermal data that comprise a wide range of surface characteristics is difficult. For instance, measurement of simultaneous directional temperatures would require a complex setup composed of multiple, but likely insufficient, thermo-radiometers and goniometers. Such difficulty could therefore warrant the use of reference models to provide state 'truths' through synthetic experiments. This is because models are able to provide outputs for broad input scenarios that would otherwise be unfeasible in real field setups/experiments. By using comprehensive models that consider canopy processes (energy and mass fluxes, photosynthesis, etc.) as well as depicting the canopy structure in great detail, the resulting surface processes as prevailing in the 'real world' can be characterised with appropriate realism and accuracy. As such, synthetic experiments can help simulate, in a physically realistic manner, the distribution of radiation signals in specific configurations that may be of interest to earth observation objectives. Such data can,for example,be used in evaluating relatively

simple methods used in the modelling of the surface energy balance. However, care should be taken when selecting models that can be used as the source of 'reference' or 'observation' data of land processes. They should be well tested, validated and proved as being able to provide accurate data that properly describe various terrestrial processes. The SCOPE (soil canopy observation of photochemistry and energy fluxes, Van Der Tol et al., 2009; Yang et al., 2021) model has, for instance, been evaluated in numerous studies and has shown to provide accurate estimates of vegetated surface processes (Duffour et al., 2015; Verrelst et al., 2015). With respect to directional anisotropy, SCOPE integrates the analytical scattering of arbitrarily inclined leaves (SAIL. Verheof, 1984) and 4SAIL (Verhoef et al., 2007) radiative transfer methods, which have been proven to appropriately describe the four-stream directional-dependent signals in the optical and thermal spectral domains, respectively.

In the current work, we performed synthetic experiments where the SCOPE / SCOPE lite model was used to simulate 'observation truths' of surface components (fluxes and directional temperatures) for a range of surface vegetation cover and water stress conditions. That is, fully stressed to well-watered surfaces of sparsely to fully vegetated canopies, among others. These were then applied on the relatively simple surface energy balance (SPARSE / SPARSE4) modelling schemes for performance evaluations as well as to assess the influence of thermal directionality on the retrievals. In the following sections, we describe the data and methods used; starting with a brief description of the surface energy balance methods, then summarizing the experimental data generation setup, that is, selection of simulation characteristics for further analyses. We then present and interpret the output from the experimental analyses. Finally, conclusions are drawn and perspective on future work is postulated.

6.1.2. Materials and Methods

6.1.2.1. Methods

Soil Plant Atmosphere Remote Sensing of Evapotranspiration (SPARSE)

Here we apply the SPARSE model (Boulet et al., 2015), a dual source surface energy balance method that estimates evapotranspiration and surface water stress by inverting the land surface temperature. The scheme's recent extension (Mwangi et al., 2022) detailed in sections 3.1, 3.2, 3.3 (SPARSE4), which discriminates the

sunlit/shaded elements, was also used.

6.1.2.2. Experimental setup: methodology and data

Summary of approach

The SCOPE tool acted as the source of 'observation' data that was then used in the analysis of the SPARSE / SPARSE4 surface energy balance methods. The assumption of treating SCOPE as the 'reference' - while rather bold since no model can perfectly represent reality - is well founded because the model has been shown in the literature to realistically characterize processes and interactions at the near land surface (e.g., Duffour et al., 2015; Verrelst et al., 2015). Accordingly, the directional brightness temperature simulations from SCOPE (see further description below) were used to force the SPARSE/SPARSE4 energy budgets. To this end, SCOPE was run to give fluxes and other outputs that are independent of viewing direction. This was done for a wide-range of fraction of vegetation cover, and soil and vegetation water stress conditions whilst varying some meteorological variables. The elemental temperatures were concurrently simulated and used within SCOPE (through the integrated extended 4SAIL) to retrieve the directional (both nadir and off-nadir) surface canopy temperatures. To reduce the computation time required, these simulations were limited to 55 ° viewing zeniths (e.g., MODIS scan angles). The simulations were then run at 5 ° intervals of the zenith and azimuth angles within the polar space. A comparison of the SCOPE and SCOPE lite versions is thus first presented. The directional surface temperatures were subsequently used (together with the meteorological and ancillary data) to drive the surface energy balance methods and consequently retrieve the prevailing fluxes. The aim was to check how directional temperatures could be used to consistently simulate the energy budget with SCOPE acting as the reference point. Initial assessments were between simulations obtained using nadir brightness temperatures, where we evaluate SPARSE and SPARSE4 from nadir brightness temperatures all over the day for each simualation case. Further analyses focus on the estimates retrieved by applying directional off-nadir temperatures (second part of the results section where we evaluate SPARSE and SPARSE4 as a function of the geometry of the measurements (i.e., inversion in each direction)). More details on these data generation experiments follow below, i.e., a brief description of the 'reference' model used (and thus a comparison of the SCOPE and SCOPE lite modelling schemes – version 2.0, which has since been refined in

v2.1), the input data used to perform the experiments and how the ‘reference’ output were prepared. This is then followed by a presentation of the aforementioned surface energy balance and directionality analyses. That is: *i)* evaluation of SPARSE and SPARSE4 from nadir brightness temperatures (over the three clear sky days with varying sun positions throughout the days), and *ii)* evaluation of SPARSE and SPARSE4 as a function of the geometry of the 'directional thermal measurements’ (SEB inversion in each viewing direction).

Energy balance in the soil-vegetation-atmosphere continuum

Soil Canopy Observation of Photosynthesis and Energy fluxes (SCOPE)

SCOPE (van der Tol et al., 2009) is a comprehensive soil vegetation atmosphere transfer (SVAT) model that combines several physically-based methods that describe the radiative, turbulent and biochemistry processes within 1-D vegetation canopies. In the thermal domain, SCOPE employs a variation of the four-stream SAIL radiative model (4SAIL, Verhoef et al., 2007), an extension of the Scattering of Arbitrarily Inclined Leaves (Verhoef, 1984) that is applicable in the optical radiation spectrum. The model has previously been evaluated extensively on various aspects that describe terrestrial processes and exchanges (Duffour et al., 2015; Verrelst et al., 2015) where it has been found to perform with reasonable accuracy and can therefore serve as a reference source.

In the following sections, both versions of the SCOPE model (SCOPE “full” and SCOPE “lite”) are therefore used to provide the ‘references’ where it is run in direct mode (with the data tabulated in Table 6) for retrieval energy fluxes as well as directional (nadir and off-nadir) surface brightness temperatures. The version used in majority of the analyses below is SCOPE version 2.0, which has since been updated to version 2.1.

Directional surface temperature and surface fluxes: synthetic truths

We utilized the SCOPE model (version 2.0) to simulate surface variables that were treated as the ‘observations’ to either be used as input for further modeling exercises, or against which the surface energy balance methods were assessed. A key SCOPE output used in this study is the directional out- or top-of-canopy (nadir and off-nadir) brightness temperatures, i.e., the temperature of the surface as would be observed by a remote thermal infrared sensor. SCOPE applies the integrated (modified) four

stream 4-SAIL radiative transfer method to simulate these directional thermal emissions. Note that atmospheric correction was not necessary since the model provides bottom of atmosphere (BOA) top of canopy (TOC) radiation signals.

The directional surface temperatures simulated by SCOPE were then used as input in the SPARSE methods for retrieval of fluxes in the defined (according to Table 6) conditions. Other variables, such as surface albedo, were also obtained from the SCOPE outputs.

Biophysical parameters and water status

Several canopy conditions were selected to perform these experiments and aid in further analysis. These characteristics were chosen such that they represented conditions that are likely to occur naturally, i.e., from sparsely to densely vegetated surfaces (low to high leaf area indices (LAIs), respectively), a broad range of water statuses for the canopy/vegetation layer and the soil substrate. A homogeneous canopy was applied in this study following the continuous canopy assumption inherent in SCOPE. The range of values of maximum carboxylation rate (V_{cmo}) was selected according to previous literature (Duffour et al., 2016; Prikaziuk & van der Tol, 2019; Verrelst et al., 2015). The theoretical formulation of the stomatal conductance utilized in SPARSE differs from that applied in SCOPE (i.e., Jarvis type (Jarvis, 1976) vs Ball-Berry based (Ball, Woodrow, & Berry, 1987) conductance models). As such, the minimum stomatal resistances were selected to realistically correspond to the SCOPE Vcmo values, i.e. high V_{cmo} for low stomatal resistance, and vice versa. The reference surface albedo was calculated as the ratio between SCOPE radiance output and the incoming solar radiation input. The variation of the leaf area indices (LAI) and water status conditions applied in this study is tabulated in Table 6.

Table 6: input dataset: the range of biophysical and water stress parameters / variables as applied in the current study.

variable / parameter [unit]	Value range
Maximum rate of carboxylation -Vcmo $[\mu\mathrm{mol\ m^{-2}\ s^{-1}}]$	25, 75, 125, 180
Soil resistance - Rss $[\mathrm{s\ m^{-1}}]$	1, 200, 500, 1000, 2000, 3000
Leaf area index - LAI $[\mathrm{m^2\ m^{-2}}]$	1, 2, 3, 5, 7
Wind speed - Ua $[\mathrm{m\ s^{-1}}]$	0.5*, 1, 2*, 3, 5
Surface albedo [-]	from SCOPE output

* *only for the nadir-based experiments*

Incoming radiation and meteorological conditions

The synthetic experiments were performed using data collected from an in-situ meteorological station located in Aurade, south-west of France (as in Duffour et al. (2016)). The dataset included incoming solar radiation, relative humidity, air temperature. Three clear sky days were selected with disparate atmospheric conditions (that is, during spring, summer and winter; day of year 79, 173 and 354, respectively). Figure 30 plots some of the radiation and atmospheric variables from the study site. As part of the synthetic experiments, the wind speed was varied according to Table 6. The observed radiant fluxes and meteorological variables were henceforth used to drive all model (both SCOPE and SPARSE/SPARSE4) scenarios. As mentioned earlier, the surface exchange components (e.g., turbulent fluxes, surface temperatures, etc.) simulated by SCOPE were taken as the 'observations'.

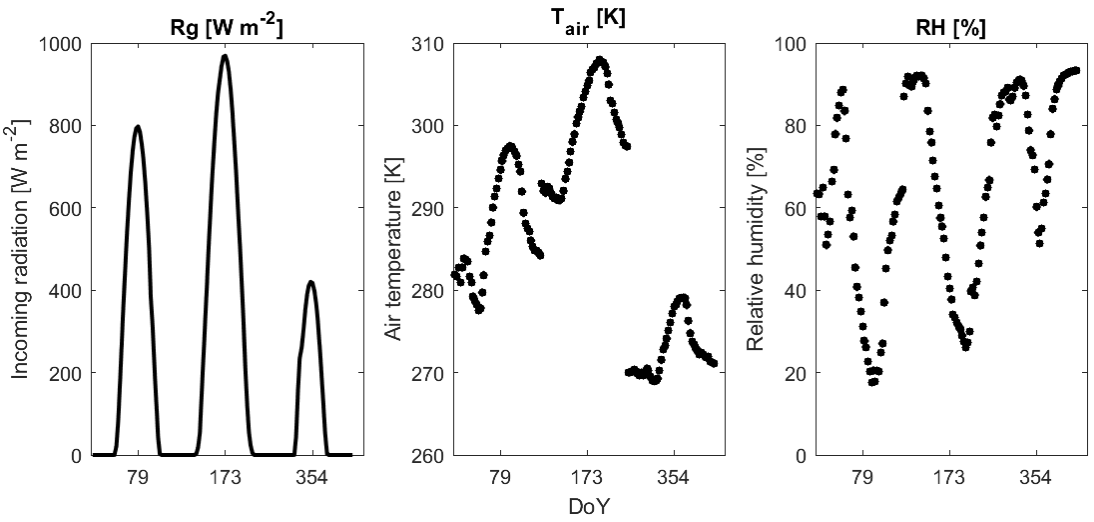

Figure 30: Incoming solar radiation, air temperature and the atmosphere relative humidity as measured at the experimental site over the three clear-sky days (DoYs: 79, 173 and 354). The wind speed was varied according to Table 6

6.1.3. Results

6.1.3.1. SCOPE comparisons

Recent modifications and updates in Yang et al. (2021) were aimed at, *inter alia*, reducing the computational demand of the energy and radiative balance modules. In addition to making modifications to the full SCOPE scheme, they introduced a lite version (an effective sunlit leaf class per layer by aggregating over all leaf angles, i.e., weighted average of the 13x36 inclination x azimuth leaf angles), and a big leaf method (which considers only two sources by lumping the shaded and sunlit

soil/vegetation components). To aid justify the use of the time-efficient version in the synthetic experiments (in this section as well as the next section), a comparison of simulations (for a couple of surface conditions) from the full SCOPE version versus the SCOPE lite model is first presented.

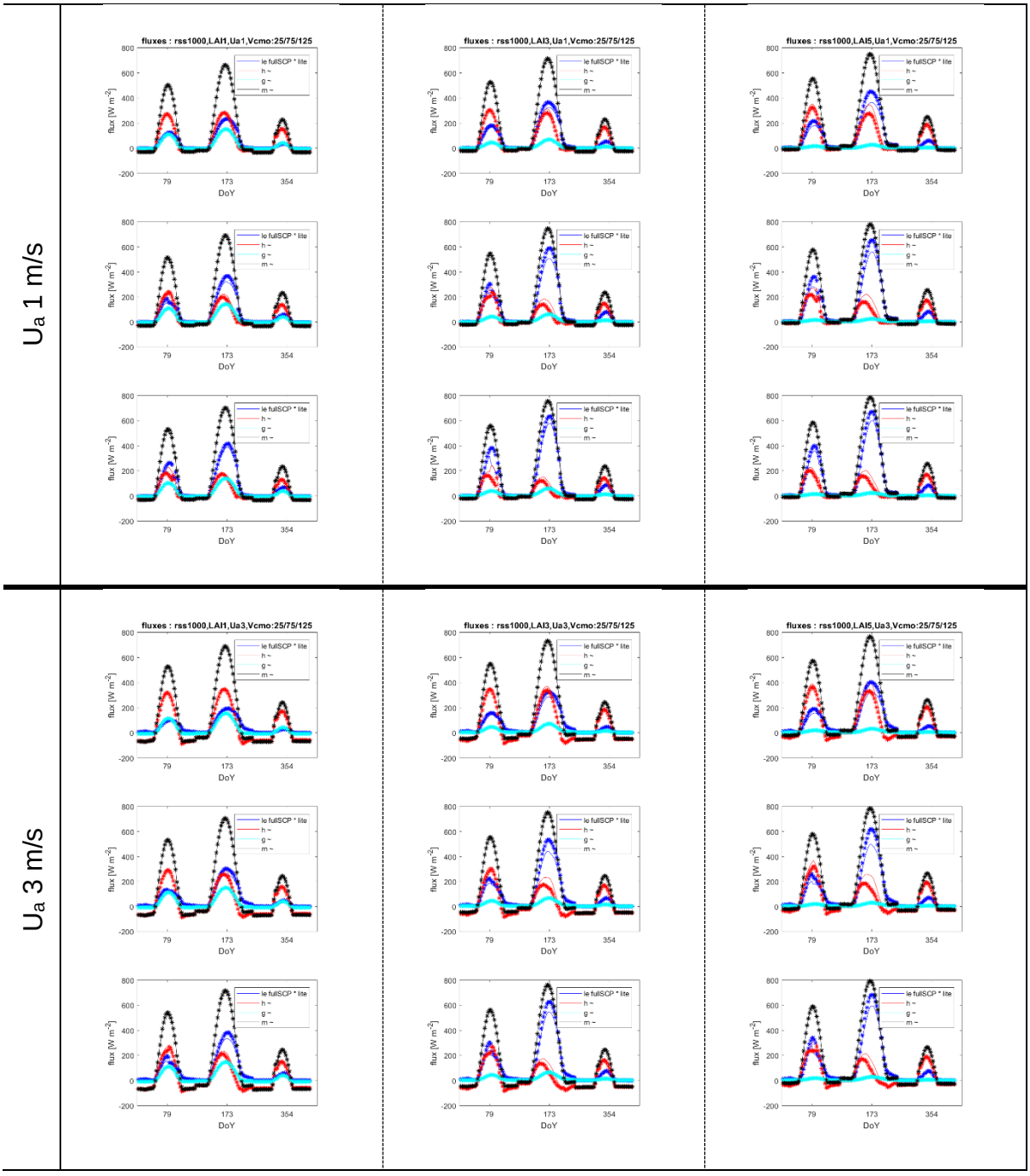

Figure 31: comparison of overall fluxes simulated by the full (-) and lite (*) SCOPE versions for several surface and meteorological characteristics

The overall fluxes as well as the directional brightness temperatures (directional anisotropies) simulated by the different SCOPE versions are illustrated in Figure 31, Figure 32 and Figure 34. Note that the comparison results mainly relate to SCOPE

version 2.0, which has since been updated to version 2.1 where the congruence between full and lite is even much better.

There are some differences between the overall fluxes and the subsequent directional brightness temperatures simulated by the two SCOPE versions. When presenting SCOPE lite, Yang et al. (2021) provided information showing that this simplified version of SCOPE was simulating slightly higher brightness temperatures and photosynthetic fluxes. Our results show an opposite trend as SCOPE lite brightness temperatures were systematically lower than SCOPE temperatures. However, the difference in temperature seems to decrease while water stress increases (lower Vcmo). In theory, increase in temperature should translate in increase of the sensible heat flux. The positive correlation between the temperature differences and sensible heat flux differences is thus expected. While the surface differences are generally somewhat small, the differences in the subsequently simulated fluxes can be quite large, averaging at ~25 $\mathrm{W\,m^{-2}}$ [30 $\mathrm{W\,m^{-2}}$] for sensible [latent] heat fluxes. The vegetation fraction cover (as described by the LAI) – and to some extent the wind speed – appear to be the main drivers of the variations. In sparsely vegetated surfaces (low LAI) a larger surface temperature difference results in a relatively lower sensible heat flux variation, while in denser canopies, a smaller temperature difference translates to a much higher difference in simulated fluxes. As such, the relationship between sensible heat flux and temperature for 'lite' and 'full' (Figure 32), shows better agreement at lower LAIs while degrading with increasing LAI. The differences also show some sensitivity to the vegetation water stress descriptor. The flux aggregation refinements made in SCOPE version 2.1 appear to have improved the 'lite' and 'full' agreement of the H versus T relation, especially for lower wind speed simulations.

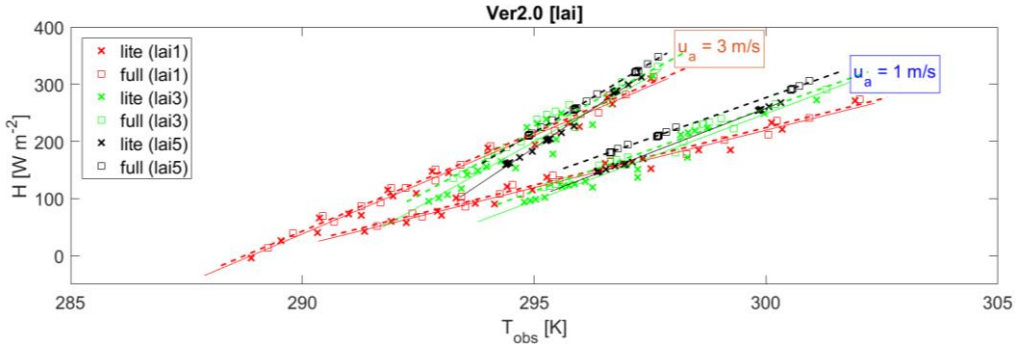

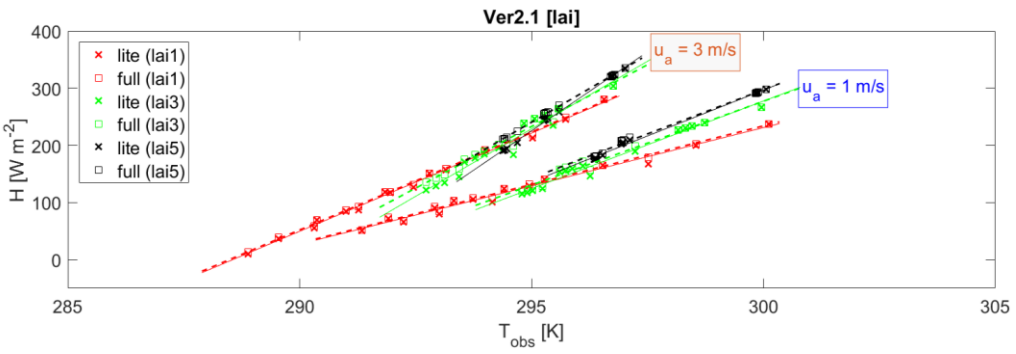

Figure 32: daytime flux differences versus surface temperature differences (SCOPE full – SCOPE lite) with differentiation between the separate varied variables (wind speed, leaf area index, Vcmo and soil resistance)

In terms of directional anisotropy, the SCOPE lite model generally reproduces simulations by the full SCOPE (as visualized in the polar plots - Figure 33, Figure 49). Nonetheless, there are still some differences in the simulated DAs, which follow a similar trend as the TB, but with a much lesser magnitude (Figure 34). Given the relatively similar DAs simulated, the lite version could be used to provide computationally efficient estimates where aspects related to directional anisotropy and not accuracy of the energy balance components are of interest.

directional anisotropy (LAI 1, 5)

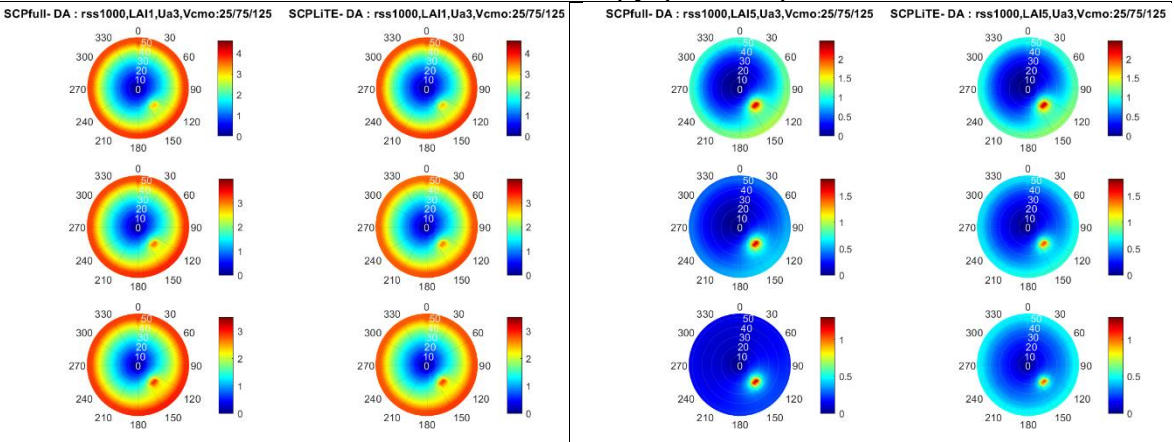

Figure 33: comparison of noon DA simulated by the full and lite SCOPE (Ver2.0)

and next, polar plots of the differences

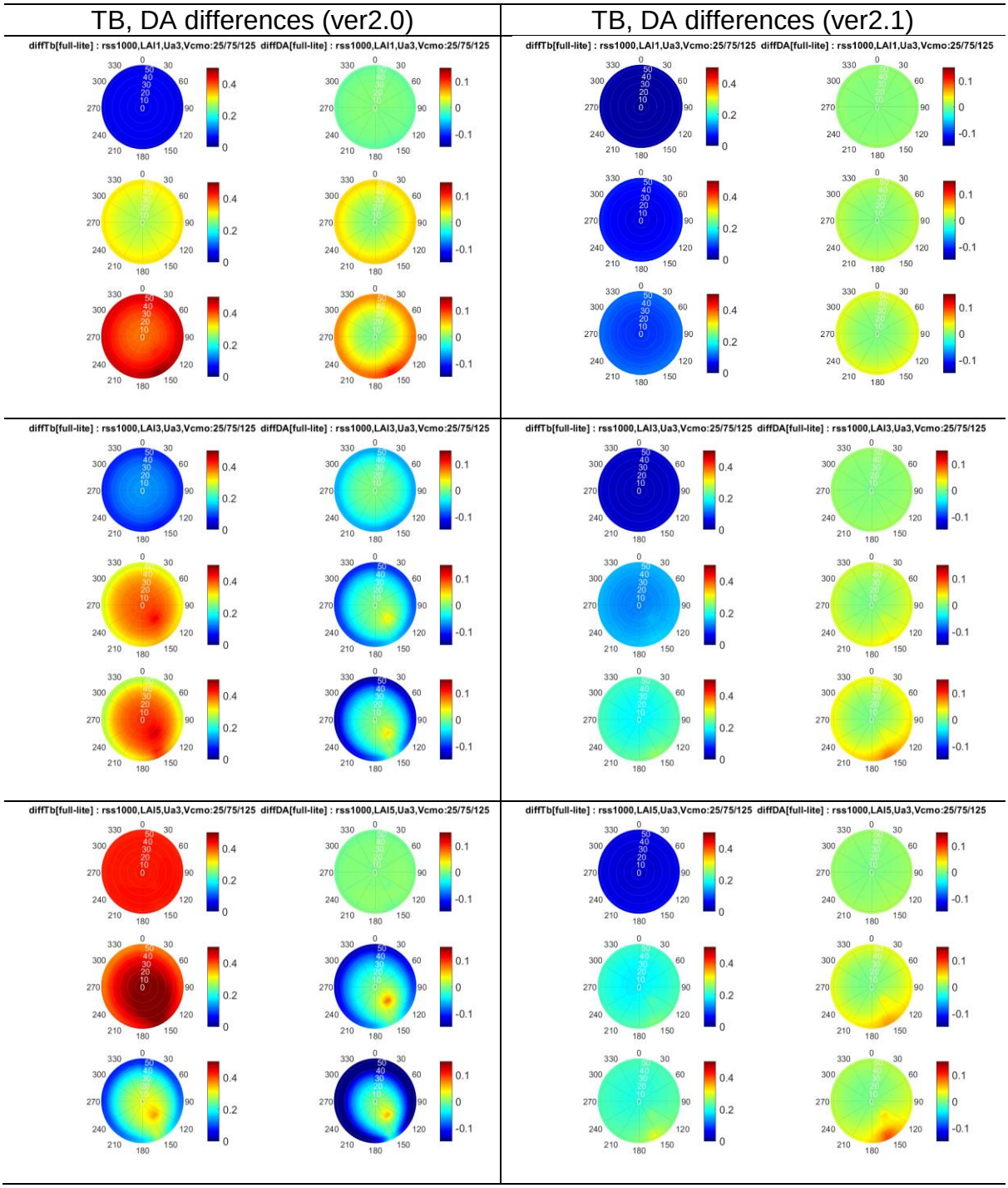

Figure 34: comparison of differences noon directional brightness temperatures (and directional anisotropy) simulated by the full and lite SCOPE versions

Overall, the two models provide coherent anisotropy and relations between fluxes and brightness temperatures. SCOPE lite simulates slightly different results due to the differences in calculation and aggregation methods. However, no elements can indicate which model performs optimally, even if the original SCOPE model is more detailed and better accounts for non-linearity in the calculation of fluxes and temperature and could be assumed as more accurate (Yang et al., 2021).

6.1.3.2. Turbulent fluxes

In this section, we summarize results that compare the SPARSE and SPARSE4 model simulations of energy fluxes against the 'observation truths' (the 'references' estimates). The SPARSE / SPARSE4 estimates used here were those simulated using nadir surface brightness temperatures retrieved from SCOPE. The total fluxes simulated over the range of surface characteristics (*viz.*, vegetation fraction cover, vegetation and soil water statuses, etc. as summarized in Table 6) show overall good agreement with the references (see Figure 35, Figure 50). This is expected since both methods are subjected to similar atmospheric demands described by the meteorological conditions (in Figure 30) for each time step of the model. There are however observable deviations in the model estimates, for all simulation exercises irrespective of soil resistance. That is, at low stomatal conductances, vegetation covers (LAIs), and higher wind speeds, For instance, as the vegetation cover increases (from LAI = 1 $\mathrm{m}^2\ \mathrm{m}^{-2}$ through LAI = 7 $\mathrm{m}^2\ \mathrm{m}^{-2}$), the 1:1 deviations between the reference (SCOPE) and SPARSE/SPARSE4 turbulent flux simulations can be seen to be enhanced. Similar observations are also made at higher wind speeds (1 $\mathrm{m/s}$ to 5 $\mathrm{m/s}$) and higher stomatal resistances (50 $\mathrm{s/m}$ to 200 $\mathrm{s/m}$) are simulated. This can perhaps be attributed to the inherent differences between the mass transfer and momentum / heat transport theories used in, and the parameterization of, the different modelling methods. One example is the aforementioned differences in the employed stomatal conductance formulations. Both SPARSE and SCOPE nonetheless utilize aerodynamic properties founded on SW or Shuttleworth and Wallace (1985) theory, which allows for interactions between different surface components. However, a key difference between the applied resistance schemes is the turbulent mixing in the roughness sublayer, which is not considered in earlier SW-based methods. The SPARSE and SCOPE models apply different SW flavours based on extensions that are – respectively - described in Shuttleworth and Gurney (1990), and by Wallace and Verhoef (2000) who modified Wallace's (1997) ERIN model to allow for turbulence enhancement in the roughness sublayer.

The net radiation was also somewhat underestimated (relative to the reference) at high canopy leaf areas again pointing to differences in the respective model structures, and consequently resulting in variation in the simulated variables such as turbulent fluxes, source temperatures, etc. This was even more apparent in SPARSE

simulations where the net radiation fluxes (at high LAIs) were systematically lower than those simulated by SCOPE. While SPARSE4 retrievals of the sensible heat flux were consistently better than those from SPARSE, the latent flux simulations show mixed performance. At low wind speeds the performance is better with SPARSE4. The same is observed at higher wind speeds except at intermediate canopy cover fractions. Nonetheless, the inter-comparison results demonstrate the utility of 0-D surface energy balance methods in the estimation of surface fluxes but also point to the need for improvements in simplified methods that would allow better replication of reality. Indeed, the observed differences between the two SCOPE versions described in the previous section (and illustrated in Figure 32, Figure 34) showing the non-exact nature of replication even in methods that should more or less be equivalent aid to emphasize this view.

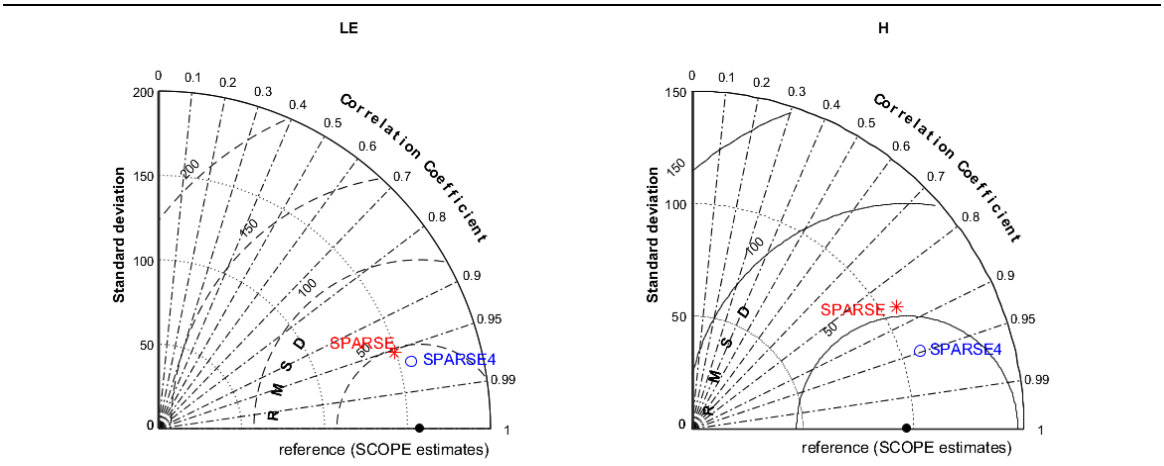

Figure 35: Taylor diagrams of the estimated fluxes (SPARSE and SPARSE4) against the 'reference' SCOPE flux estimates (latent heat, left; sensible heat energy, right) for the combined [varied] biophysical parameters and surface characteristics, i.e. soil resistance leaf area indices, stomatal conductance, wind speed

6.1.3.3. Directionality

In addition to nadir brightness temperatures (as applied in the previous section), SCOPE can simulate thermal emission signals in off-nadir (oblique) directions, as is often the case with remotely sensed (space-borne or airborne) acquisitions. This is achieved by simulating the observed thermal radiance stream using an extended 4SAIL, a thermal infrared radiative transfer method that is integrated/coupled within the model. In this section, we used the aforementioned directional brightness temperature simulations to re-run the SPARSE surface energy budget methods. Given that evapotranspiration estimation is the main end goal in surface energy balance

modelling, the section mainly focuses on the latent heat fluxes. The objective here was to check the consistency of the resulting simulated fluxes. Ideally, the prevailing surface fluxes should remain the same irrespective of the direction of the outgoing thermal emission as described by the temperature forcing (i.e., the observed surface emission or temperature is a consequence of near-land surface interactions and not vice versa). There should therefore be congruence between the oblique- and nadir-based component retrievals. This observed reality is however rarely achieved in surface energy balance inversion modelling where directional surface temperature is used.

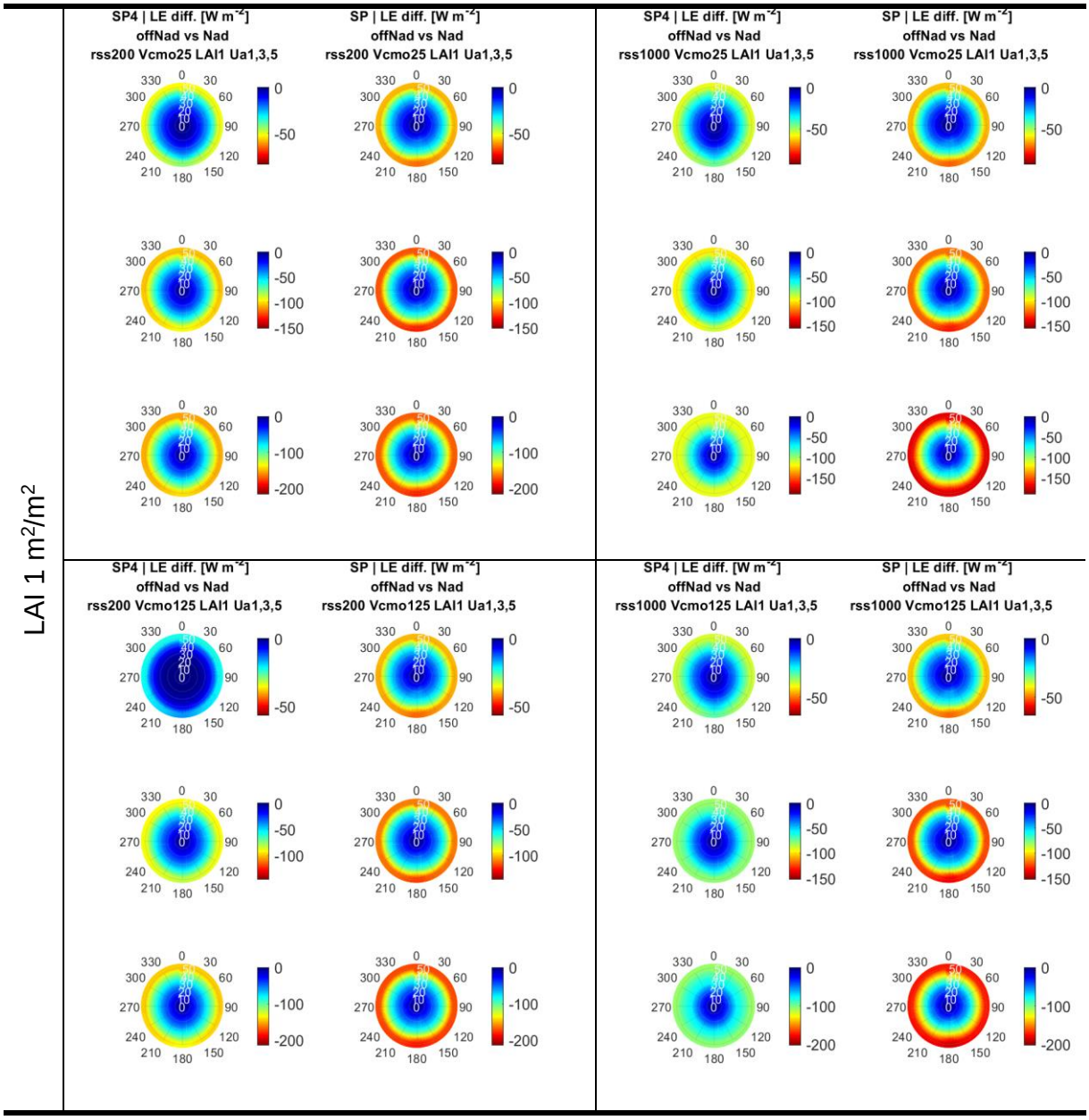

LAI 3 $m^2.m^2$	SP4 | LE diff. [W m^{-2}] offNad vs Nad rss200 Vcmo25 LAI3 Ua1,3,5	SP | LE diff. [W m^{-2}] offNad vs Nad rss200 Vcmo25 LAI3 Ua1,3,5	SP4 | LE diff. [W m^{-2}] offNad vs Nad rss1000 Vcmo25 LAI3 Ua1,3,5	SP | LE diff. [W m^{-2}] offNad vs Nad rss1000 Vcmo25 LAI3 Ua1,3,5
	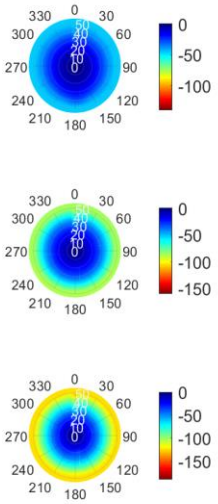	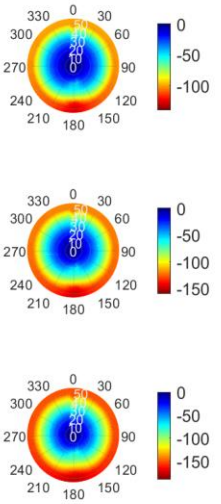	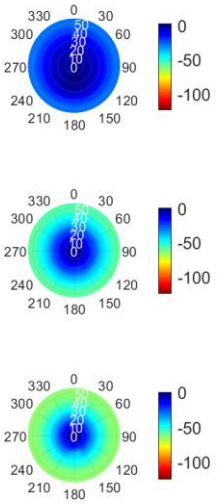	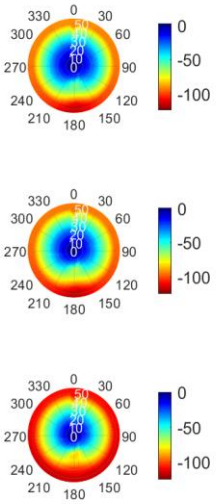
	SP4 | LE diff. [W m^{-2}] offNad vs Nad rss200 Vcmo125 LAI3 Ua1,3,5	SP | LE diff. [W m^{-2}] offNad vs Nad rss200 Vcmo125 LAI3 Ua1,3,5	SP4 | LE diff. [W m^{-2}] offNad vs Nad rss1000 Vcmo125 LAI3 Ua1,3,5	SP | LE diff. [W m^{-2}] offNad vs Nad rss1000 Vcmo125 LAI3 Ua1,3,5
	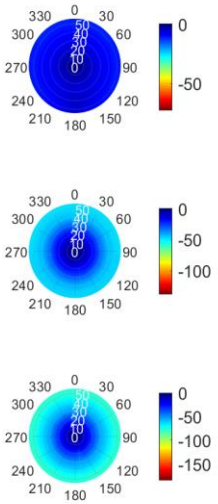	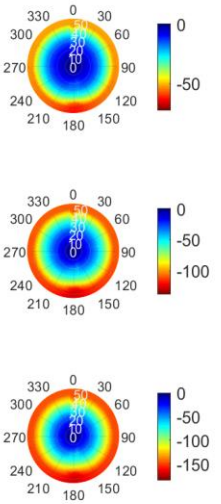	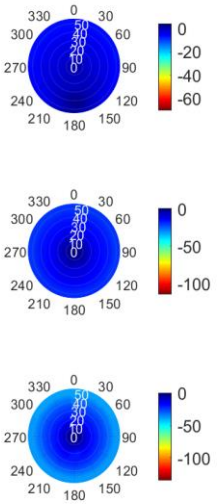	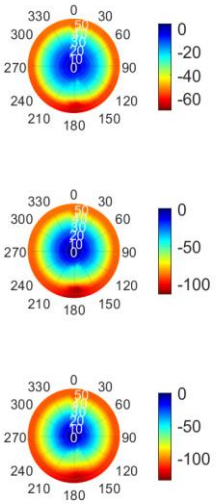
5 m^2/m^2	SP4 | LE diff. [W m^{-2}] offNad vs Nad rss200 Vcmo25 LAI5 Ua1,3,5	SP | LE diff. [W m^{-2}] offNad vs Nad rss200 Vcmo25 LAI5 Ua1,3,5	SP4 | LE diff. [W m^{-2}] offNad vs Nad rss1000 Vcmo25 LAI5 Ua1,3,5	SP | LE diff. [W m^{-2}] offNad vs Nad rss1000 Vcmo25 LAI5 Ua1,3,5
	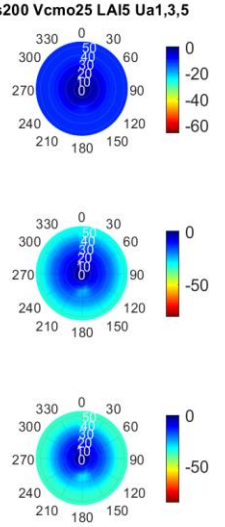	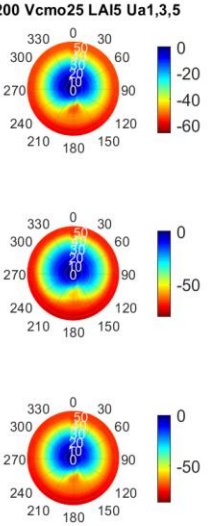	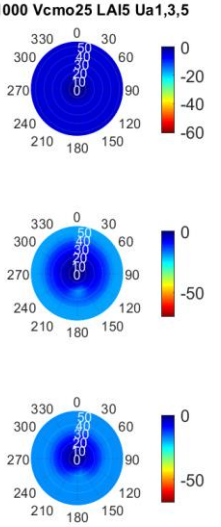	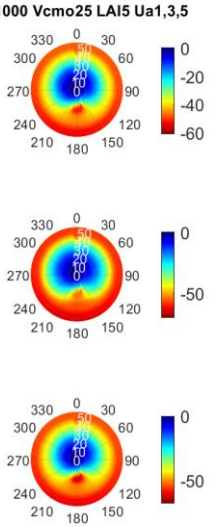

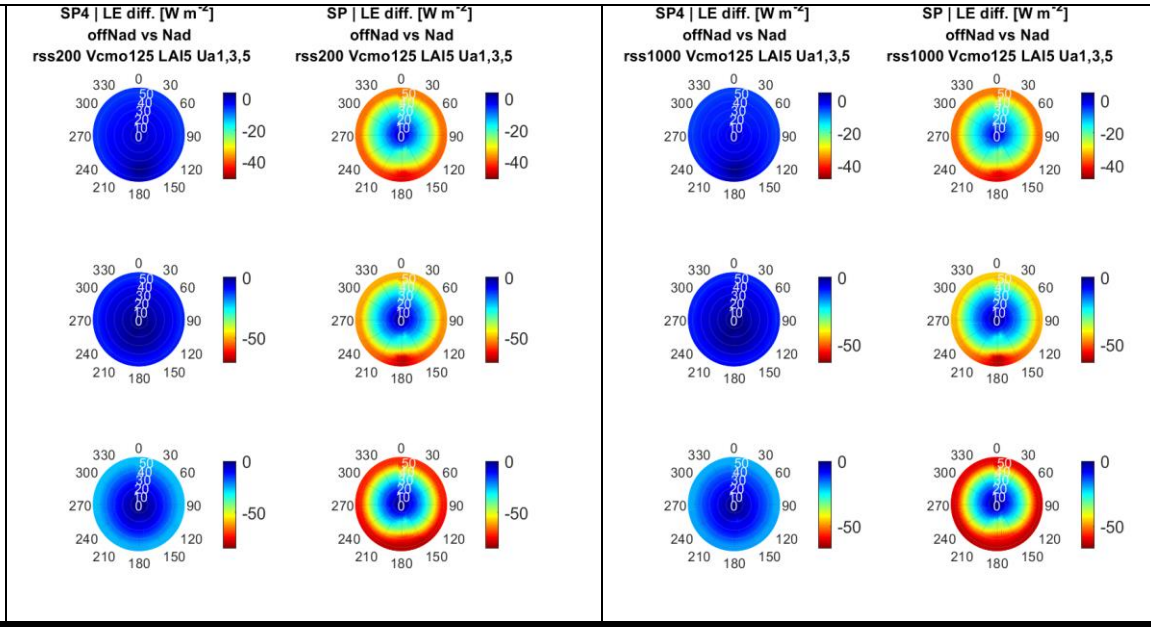

Figure 36: Directional sensitivity of latent heat flux retrieval (Off-nadir-based less nadir-based] biases for selected wind speed and surface characteristics (water stress and vegetation cover). Biases calculated over all days but for midday estimates

Here, we use the *[off-nadir-based – nadir-based retrievals]* biases to quantify the directional retrieval inconsistencies of the SPARSE and SPARSE4 energy budget schemes. The apparent influences of angular anisotropy on the simulations as described by the oblique-nadir estimate biases can be visualized through the polar plots. For instance, the [negative] latent heat biases generally increase further off-nadir. These directional inconsistencies occur with varying degrees depending on the surface or meteorological variables (as listed or illustrated in Table 6 and Figure 30). Separately, the directional retrieval inconsistencies relative to viewing angle are illustrated in Figure 37 below.

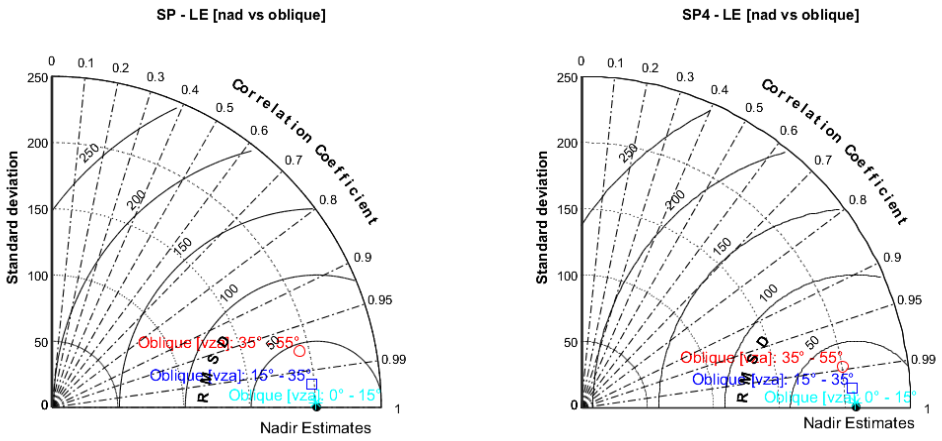

Figure 37: Taylor Diagrams quantifying the directional retrieval inconsistencies of the latent heat energy flux at midday for varying viewing angles (i.e., near-nadir to higher view zenith angles)

Separately, Taylor diagrams (Taylor, 2001) that quantify other nadir versus hotspot/anti-hotspot metrics are displayed in Figure 38 below.

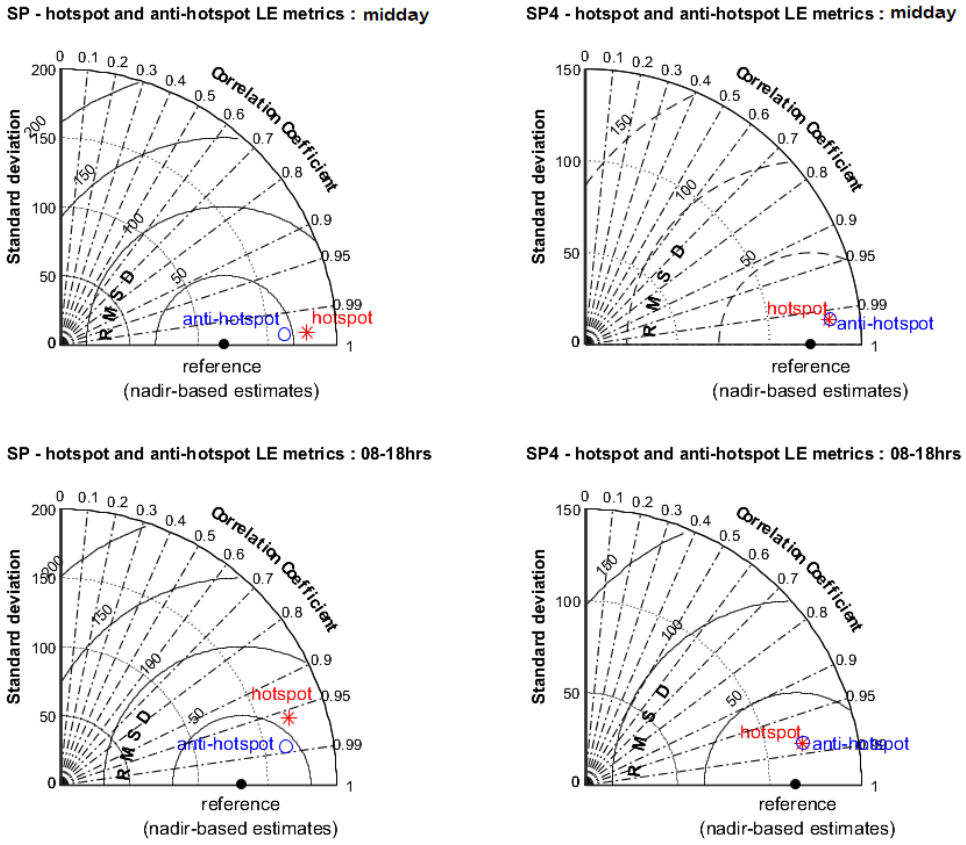

Figure 38: Taylor diagrams quantifying the directional inconsistencies in the hotspot and anti-hotspot directions relative to the nadir-based retrievals (plotted for: LAI 3, rss 1000, Vcmo75 & Ua1 over the entire experiment period). top: midday and bottom: daytime metrics

In the following, we summarize the observations according to each varied factor (i.e., the incoming radiation and atmospheric conditions, and the surface characteristics (water status and vegetation fraction cover)).

Incoming solar radiation

Incoming solar radiation plays an important role in thermal radiation directionality since it by and large defines the net radiation and thus the available energy required for the turbulent processes at the near land surface. Indeed, it has previously been ranked by Duffour et al. (2016) as the factor with the most or significant influence on angular anisotropy. Here, we observed an overall influence of the short-wave irradiance on inconsistencies in retrievals (in absolute terms) where higher radiation generally translated to higher inconsistencies, and vice versa. During periods with lower radiations (in winter, for example, where there is also low atmospheric moisture demand due to the relatively high humidity), the angular anisotropy in the directional

surface temperatures is also minimal, meaning that the surface energy balance retrieval inconsistencies over the retrieval polar grid are also reduced. Conversely, the higher radiation during summer results in higher available energy (for partitioning into the turbulent fluxes) as well as increased directional anisotropies. This in turn leads to larger oblique- versus nadir-based retrieval inconsistencies, which are further magnified by the angular anisotropy in the directional thermal data. Similarly, larger influences of the directional anisotropy are - as expected - observed during the day. Evidently, the daytime incoming radiation (especially around noon as discussed later and illustrated in Figure 39) will tend to contribute to the larger diurnal anisotropy and thus more inconsistencies, with nocturnal variations being negligible. While these effects were observed in both schemes, they are more muted in the case of SPARSE4, which shows a much better nadir versus oblique retrieval consistency.

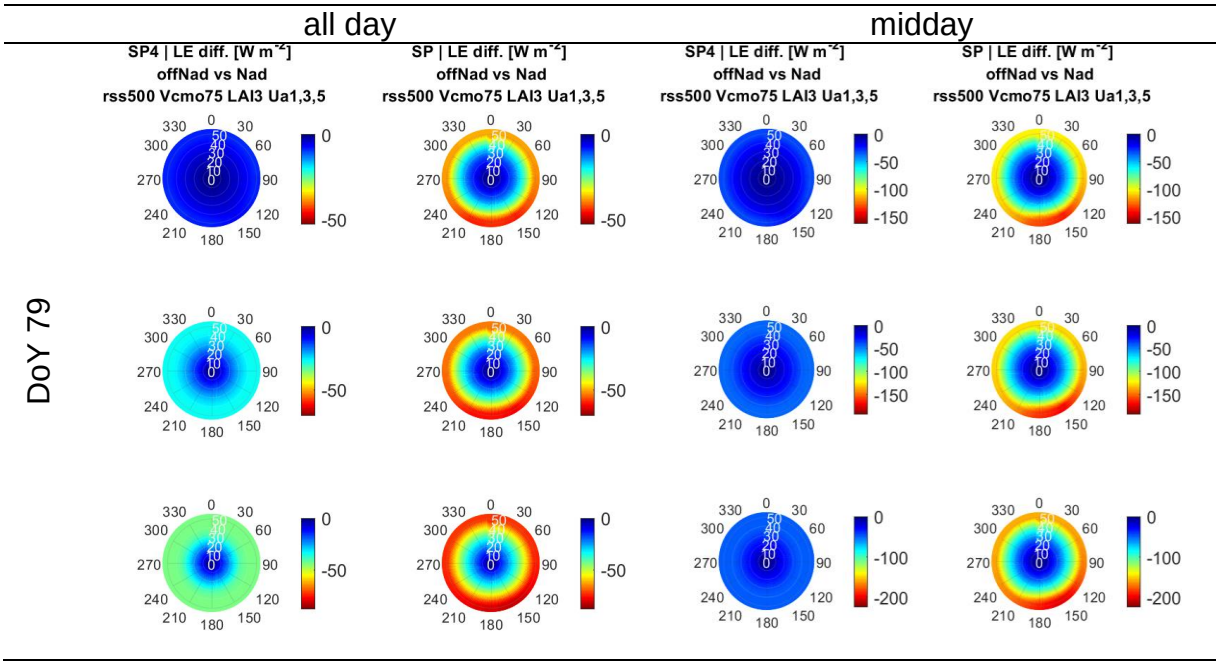

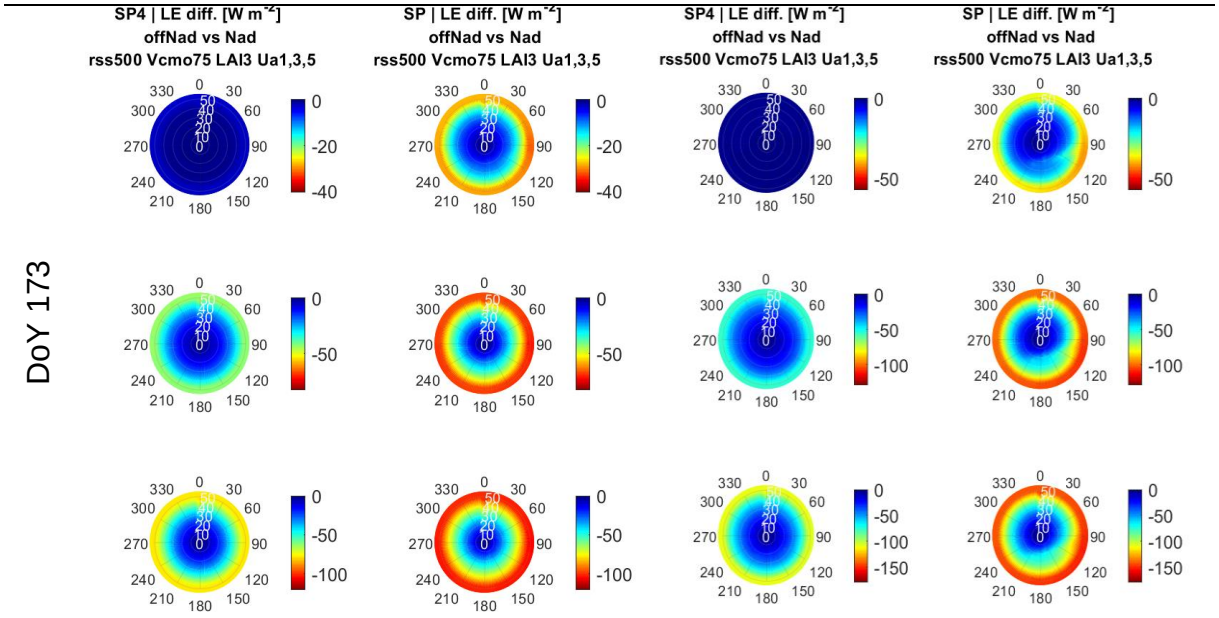

Figure 39: Polar plots depicting the directional retrieval [in]consistencies for an intermediate LAI and soil resistance over the two spring and summer days with the high radiations; left: all day (relatively low averaged radiation) versus right: midday off-nadir - nadir differences

Wind speed

The horizontal wind profile drives turbulent mixing at the atmospheric surface (boundary) layer through forced convection, and can therefore be understood as being an indirect influencing factor of thermal radiation directionality. Indeed, Duffour et al. (2016) reported that angular anisotropy tends to decrease with increase in wind speed (since winds contribute to eddies heat transport thus enhancing surface cooling – with the resulting lower component temperatures generally translating to low anisotropies). However, the directionality impacts due to wind speed were observed to be low when compared to the other influencing factors (Duffour, Lagouarde, Olioso, et al., 2016; Duffour, Lagouarde, & Roujean, 2016). The current experiments therefore sought to understand how the anisotropy in the temperature forcing coupled with wind variations affected the nadir-oblique consistency in the SEB models. The flux retrieval inconsistencies resulting from the TRD of the thermal inputs were here observed to increase with increase in wind speed (this was the case in both SPARSE and SPARSE4), i.e., there was a better correspondence between nadir-based and oblique-based estimates at lower wind speeds, which degraded when higher wind speeds were used in the simulations (Figure 40). This was observed in the entire simulation set but with varying degrees relative to the vegetation fraction cover (see Figure 36, Figure 39, and also Figure 40). Since there is relatively low anisotropy variation due

to change in wind speed, the observed inconsistencies could likely be attributed to the model structures of the energy balance schemes. This shows the need for a better and more realistic representation of turbulence (in terms of heat and momentum transport dynamics at the surface boundary layer) to ensure directionality issues that may arise are alleviated. Again, as observed with other anisotropy driving factors, the extended SPARSE4 model, which offers a more direct discrimination of illumination of surface sources, appears to reduce the enhanced retrieval inconsistencies with increasing wind speed (as illustrated in Figure 40).

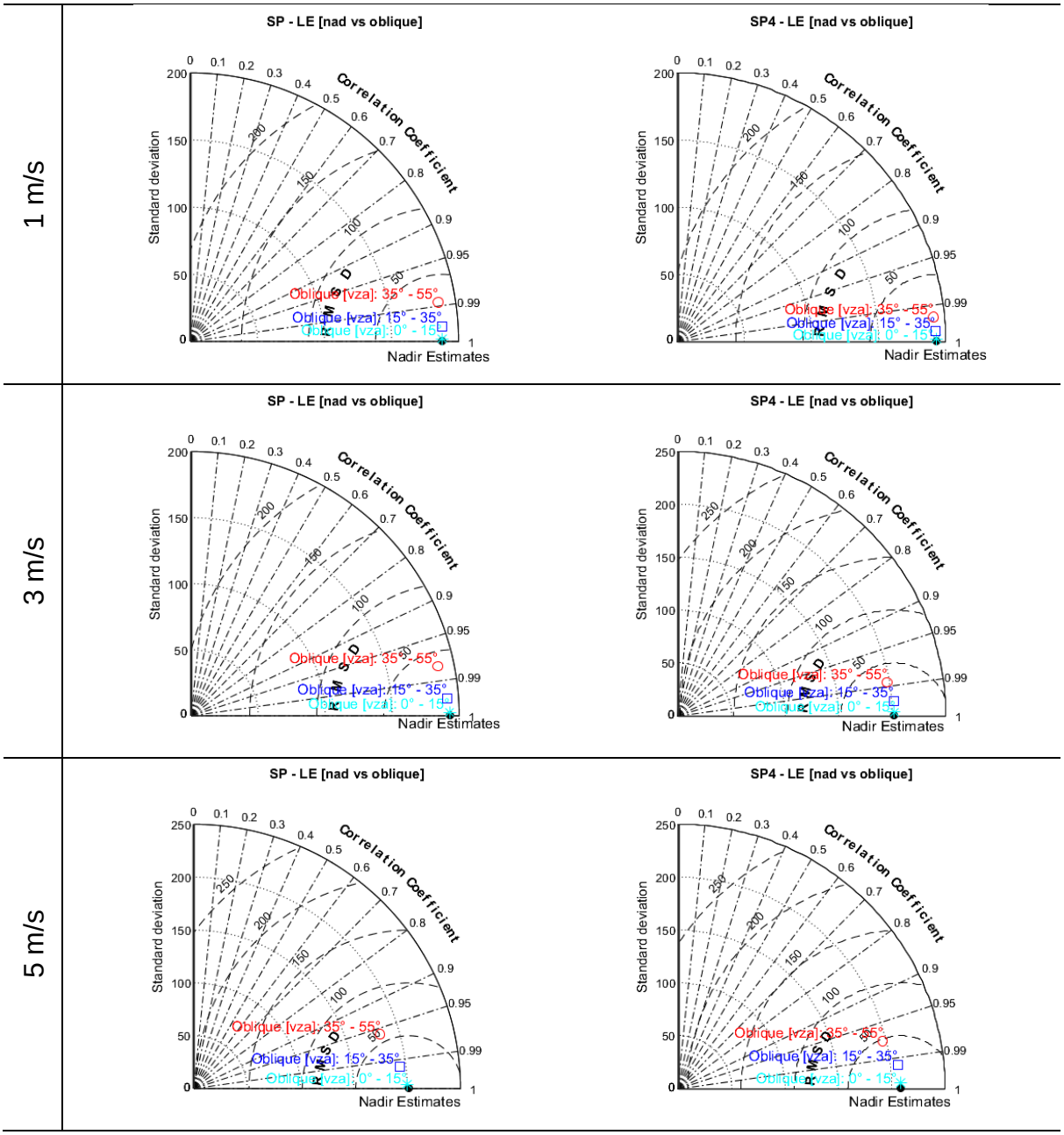

Figure 40: Taylor diagrams illustrating the directional retrieval inconsistencies relative to change in wind speed

Fraction of vegetation cover

Directional anisotropy will generally vary depending on characteristics that describe surface roughness. Ideally, bare surfaces will usually lead to little angular anisotropy that is mainly driven by topsoil components such as clogs, rocks, among others; such bare soil characteristics are rarely modelled in most SVAT schemes, including SCOPE. Farmlands are nonetheless often vegetated. The vegetation cover (as described by the canopy leaf area) introduces surface roughness characteristics that in turn result in directional anisotropy in outgoing spectral signals. Evidently, the retrieval inconsistencies are herein shown to be somewhat reduced, both at low canopy leaf areas (LAIs) and at high LAIs, since in such scenarios, the surface or canopy exhibits relatively moderate roughness homogeneity translating to low angular anisotropies. However, relatively higher retrieval inconsistencies of the oblique- vs nadir-based estimates are observed at intermediate vegetation canopy coverage. In all, the SPARSE4 scheme achieves a better nadir versus oblique retrieval consistency, particularly at higher viewing angles.

Surface water status

The surface water conditions simulated in these modelling exercises were separately comprised of a range of vegetation and soil water conditions (i.e., stomatal conductance and soil resistance, respectively). Generally, terrestrial water availability allows for homeostatic surface cooling in form of latent heat exchanges. This regulates the component temperatures and, consequently, the resulting thermal directionality effects. As such, surfaces/canopies under water stress will have higher temperatures, which subsequently enhances the angular anisotropy. With respect to the nadir- and oblique-based flux retrievals, we observe that the consistency particularly diminishes with increase in vegetation water stress. Because the observed vegetation cover fraction increases with view zenith angle, the upward tuning of the vegetation temperatures (for convergence of the modelled off-nadir thermal emission to the water-stressed reference) results in the increased inconsistencies. The influence of soil water availability on the retrieval inconsistencies is however muted at relatively high LAIs since the contribution of the soil to the top of canopy radiances is minimal in dense canopies. Furthermore, the soil's contribution is generally reduced under oblique viewing.

6.1.4. Discussion

Inter-comparison of the SEB methods

In most of the simulated scenarios, the retrievals by SPARSE4 showed overall better angular consistency compared to those from SPARSE. A similar observation was made in Mwangi et al. (2022) as presented in section 4.5, where nadir- and oblique-based (i.e., thermoradiometer installed at 45° zenith, south facing) surface components were modelled. The relative consistency improvement between the two energy balance methods is also influenced by the various surface characteristics. At low vegetation cover, for instance, both methods perform similarly since there is generally little to no directional anisotropy. As the vegetation cover fraction increases, however, SPARSE4's angular-based retrievals exhibit low inconsistency when compared to those by SPARSE. The discrimination of vegetation temperature into its sunlit and shaded components appears to aid in ensuring a better representation of the thermal radiation directionality without influencing the prevailing surface fluxes especially at the higher canopy leaf areas. While the nadir- vs oblique-based mismatches are not entirely eliminated, the overall reduction in retrieval inconsistencies shows that accounting only for the fractions in the field of view of the observer is perhaps not sufficient and there is also need for consideration of thermal infrared directionality effects when inverting remotely sensed emission signals for characterization of surface exchanges.

Ordinarily, space-borne thermal radiometers are designed to pass above any local point on Earth at a particular or known moment. The common overpass time for many Sun synchronous satellites is around 1000 – 1400 hrs local time. Further, the incoming solar radiation (thus available energy) is highest around noon with the lowest irradiances observed at night, evenings and early mornings. Consequently, the largest thermal radiation directionality effects are expected at about midday. Further analyses on the retrieval mismatches that arise due to directional anisotropy during this period are thus presented. As mentioned previously, the season-dependency of the incident radiation (as depicted in Figure 35) also plays an important role on the observed [in-]consistencies, and mostly impacts the around noontime components. As expected, the aforementioned impacts are thus highest in summer and lowest during the colder season. In fact, in some cases (for example when simulating water stressed scenarios)

the retrieval inconsistencies relative to the standard nadir-based estimates (expressed in terms of bias) are quite large, rendering the estimates based off of high-oblique temperatures meaningless.

Unlike in-situ and airborne installed radiometers, thermal polar-orbiters have a global coverage with established and known design criteria. For example, an established orbit geometry (ascending and/or descending orbit inclinations and the maximum scan angles, among others). These limit the viewing angles that can be achieved for any geographical location. Assuming an inclination of 98.7 and scan angle of 55°, for example, a polar orbiter can ideally only provide a range of: 90±8.7° to -90±8.7° in viewing azimuth and less than ~55° in viewing zenith. Many directionality phenomena (such as the hotspot) do not therefore influence remote sensing acquisitions in global regions beyond the sub-tropics with the influences in the tropics and sub-tropics also limited to countable occurrences throughout the year (mostly during summer). Remotely sensed signals over the Aurade site, which is located in the northern tropics, are therefore less likely to present directional anisotropy influences. It is also clear that directional retrieval in-consistencies are more pronounced in higher view zenith angles (see polar plots and Taylor diagrams, e.g. Figure 36, Figure 37, Figure 40). At these higher zeniths, the extended SPARSE4 is nevertheless shown to reduce the sensitivity of flux retrieval to the direction of input thermal data.

6.1.5. Summary and Conclusions

Land surface temperature can help in the monitoring of terrestrial water status and thus enable the timely detection of plant water stress in critical agro ecosystems. The spatial scales needed in agro-hydrological applications can often only be attained through remote sensing (e.g. via space-borne sensors), which can in-turn introduce signal interpretation issues due to angular anisotropy. In this study, we analysed how thermal radiation directionality (which is directional anisotropy in the thermal infrared domain) coupled with surface and atmospheric factors influence modelled energy exchanges and their retrieval consistency (i.e., oblique- versus nadir-based estimates). To this end, the SCOPE tool (a comprehensive soil vegetation atmosphere transfer model) was used to provide ‘observations’ (i.e., directional temperatures and other energy balance components) that were then used to drive and assess the SPARSE and SPARE4 surface energy budget schemes. The variables used in the

data generation consisted of meteorological and radiation information for three clear-sky days with varying incoming solar radiations (during winter, spring and summer). Some of the surface and atmospheric characteristics required as model inputs (i.e., wind speed, leaf area indices, soil resistance and canopy conductance) were varied to allow SCOPE simulations that could mimic a broad range of terrestrial conditions/statuses that are likely to exist.

First, the model (SPARSE/SPARSE4) estimates as retrieved using surface temperature from a standard (i.e. nadir) direction were compared to those from SCOPE. The turbulent fluxes from the SEB methods showed a generally good agreement with the 'references'. Nevertheless, there were some observed differences depending on factors or variables being simulated. For instance with increasing wind speed and canopy coverage, which could perhaps be attributed to use of inexact parameterizations that might have arose due to differences in the modelling structures. The effect of directionality on the retrieved fluxes was then analysed. That is, in terms of nadir- versus oblique-based surface state components estimated using the directional brightness temperatures. Generally, the angular anisotropy is expected to low when the surface coverage is uniform, i.e., when there is hardly any surface roughness. As such, low directional anisotropy and thus little retrieval inconsistencies due to such anisotropy could be observed when the surface was sparsely vegetated and at very high vegetation cover fractions. Overall, however, the nadir versus off-nadir retrieval inconsistencies (hence weak model performance) were mostly observed to have a major influence at low elevation angles (larger zenith angles), with minimal effects on near-nadir based retrievals (as would be the case with current and proposed TIR RS missions) – see Figure 37. When using close-to-nadir directional temperatures, current formulations of the surface energy balance (i.e., two sources with proper accounting of fractions) could therefore be reasonably applied, with a better representation of the out-of-canopy radiation needed when dealing with earth observation products with wider scan angles.

6.2. Influence of TRD on surface flux retrieval: T-fc Space as used in Contextual evapotranspiration estimation: synthetic experiments

Summary

Contextual models, specifically the surface temperature versus vegetation cover ($T - f_c$) relationship, have been very helpful in estimating latent fluxes over large spatial extents without requiring a lot of ground based input variables. Remotely sensed data applied in such estimation methods are however susceptible to directionality effects that arise from the sun-earth-view geometry. For example, the presence of thermal radiation directionality effects will generally be expected to have a direct influence on the $T - f_c$ feature space and would therefore require correction/normalization to ensure consistency of flux estimates. The current work analyzes the effect of viewing geometry on surface temperature observations and consequently, how such angular aspects influence the dry/cold edges as applied in contextual evapotranspiration modelling. A synthetic experiment utilizing the SMEX02 data was carried out where we simulated nadir and off-nadir directional temperatures (as would be observed by a polar orbiter) using the SCOPE model. The $T - f_c$ feature spaces resulting from the 'viewed' directional temperatures were compared to those derived using nadir temperatures (that are generally considered standard for contextual evapotranspiration). From the preliminary results, we observe insignificant effects when the area of interest (AOI) is close to the satellite's sub-track as well as in small image scenes given that the viewing angle differences for pixels within such images are minimal. For cases where the AOI is located further off the sub-track, there is a likelihood of influence on the cold / dry edges with this influence being more pronounced when the AOI is viewed in the solar direction. While the edge shifts can counteract and thus balance out - especially for non-hotspot acquisitions - there is need for a standardized way to allow normalization of directional observations. Simple positioning tools (such as; sun path diagrams and specifications of viewing geometry) can also help identify this angular anisotropy exposure.

Keywords: Contextual ET, $T - f_c$ space, thermal radiation directionality, temperature normalization

Résumé

Les modèles contextuels, en particulier la relation entre la température de surface et la couverture végétale ($T - f_c$), ont été très utiles pour estimer les flux latents sur de grandes étendues spatiales sans nécessiter beaucoup de variables d'entrée au sol. Les données de télédétection appliquées à ces méthodes d'estimation sont toutefois sensibles aux effets de directionnalité qui découlent de la géométrie de la vue soleil-terre. Par exemple, on s'attend généralement à ce que la présence d'effets de directionnalité du rayonnement thermique ait une influence directe sur l'espace caractéristique $T - f_c$ et nécessite donc une correction/normalisation pour assurer la cohérence des estimations de flux. Le travail

actuel analyse l'effet de la géométrie d'observation sur les observations de la température de surface et, par conséquent, la façon dont ces aspects angulaires influencent les bords secs/froids tels qu'ils sont appliqués dans la modélisation contextuelle de l'évapotranspiration. Une expérience synthétique utilisant les données SMEX02 a été réalisée où nous avons simulé les températures directionnelles au nadir et hors nadir (telles qu'elles seraient observées par un orbiteur polaire) en utilisant le modèle SCOPE. Les espaces caractéristiques $T - f_c$ résultant des températures directionnelles "vues" ont été comparés à ceux dérivés des températures au nadir (qui sont généralement considérées comme standard pour l'évapotranspiration contextuelle). D'après les résultats préliminaires, nous observons des effets insignifiants lorsque la zone d'intérêt (AOI) est proche de la sous-piste du satellite ainsi que dans les petites scènes d'image, étant donné que les différences d'angle de vue pour les pixels de ces images sont minimes. Dans les cas où la zone d'intérêt est située plus loin de la sous-piste, il y a une probabilité d'influence sur les bords froids/secs, cette influence étant plus prononcée lorsque la zone d'intérêt est vue dans la direction du soleil. Bien que les décalages des bords puissent se contrebalancer et donc s'équilibrer - en particulier pour les acquisitions sans points chauds - il est nécessaire de trouver une méthode standardisée pour permettre la normalisation des observations directionnelles. Des outils de positionnement simples (tels que des diagrammes de la course du soleil et des spécifications de la géométrie d'observation) peuvent également aider à identifier cette exposition à l'anisotropie angulaire.

Mots clés : ET contextuelle, espace $T - f_c$, directionnalité du rayonnement thermique, normalisation de la température.

6.2.1. Introduction

Previous sections have dealt with single-pixel surface energy balance modelling. This section therefore presents initial analyses that were carried out in relation to contextual ET. The estimation of evapotranspiration at catchment scale has become important as it aids in the monitoring of water usage and thus identify water deficiencies that may lead to regional food insecurity. To monitor water fluxes at such spatial scales, contextual-based evapotranspiration models, which exploit the physically meaningful relationship between surface temperature and biophysical variables at the land surface to describe the terrestrial water statuses, have been developed. As introduced in section 2.2.2, these approaches are based on the land surface temperature – vegetation index (T_S versus VI) triangle or trapezoidal method introduced for evapotranspiration estimation by Price (1990); this was after Goward et al. (1985) observed that latent heat exchange from plants (presenting in form of ‘greenness’) was a key factor controlling surface temperature. In addition to the T-VI space, other

contextual methods utilizing the relationship between surface temperature and either vegetation fraction cover or surface albedo have been proposed (Menenti et al., 1989). The common variable, i.e. the land surface temperature (LST), helps to characterize the terrestrial water status or stress level. The theoretical presumption is that, within a remotely acquired LST image, pixels with maximum water stress (inherently equivalent to minimum evapotranspiration) and minimum water stress (maximum evapotranspiration) will be present allowing the conceptualization of a feature space bounded by dry and cold edges, i.e. radiation controlled and evaporation controlled bounds, respectively, which help in the partitioning of available energy.

The prevailing surface temperatures utilized in contextual methods are generally observed from space-borne thermal infra-red (TIR) sensors that orbit the Earth from relatively high altitudes thus allowing retrieval of thermal data covering large swaths. The view geometry as defined by the field of view of space-borne sensors adds angular effects that can lead to directional temperature variations depending on an area of interest (AOI's) location relative to the sun and the satellite's sub-track. Analysis of the effects of thermal radiation directionality on the temperature-vegetation fraction cover $(T - f_c)$ contextual relationship as applied in the estimation of evapotranspiration is therefore important. Previous studies have considered how anisotropy affects emissivity as well as reflectance (albedo) in S-SEBI modeling experiments (Mattar et al., 2014).

This study seeks to analyze the influence of thermal directionality on the $(T - f_c)$ contextual space. For this, the SMACEX dataset is used in synthetic experiments wherein the soil canopy observation of photochemistry and energy fluxes (SCOPE) model is applied to derive directional (nadir and off-nadir) temperatures as would be observed by a polar orbiter. The resulting dry and cold edges are then analyzed for a better interpretation of the TRD effects. The next section describes the dataset used followed by a summary of the methods used. Finally the results are presented and conclusions drawn.

6.2.2. Materials and methods

Data description

The dataset from the Soil Moisture EXperiment 2002 (SMEX02) of the Walnut Creek catchment, Iowa, USA, was used in these experiments. It extends a vertical-horizontal

grid tile of about 10 km by 30 km, respectively (Long & Singh, 2012), The dataset has been used in several hydrological studies, with particular emphasis in contextual evapotranspiration estimation (e.g., Anderson et al., 2004; Long & Singh, 2012; Yuting Yang & Shang, 2013). It contains a broad range of hydrological information collected in-situ (as well as remotely) during the period from DoY 166 through 189 (data source: https://nsidc.org/data/amsr_validation/soil_moisture/smex02/index.html). In this work, data preparation/processing focused on variables that allows initializing / running the SCOPE soil vegetation atmosphere transfer model, these include: radiation and meteorological data – incoming radiation, air temperature and humidity, wind speed, etc.; biophysical variables according to the land classes within the area of interest (AOI).

In the land cover classification report (provided as part of the dataset), only soybean and maize were classified with reasonable accuracy. According to the confusion matrix therein, user (producer) accuracies [%] of 96.85 (98.61) and 98.0 (96.1) were achieved for corn and soybean, respectively while those for other classes (e.g., built-up, trees, water, etc.) were generally less than 55% (Anderson et al., 2004). Only pixels classified as either soybean or corn were thus utilized and analyzed hereafter. Leaf Area Indices (LAIs) and vegetation heights for each pixel were estimated using empirical NDWI (normalized difference water index) regressions for the dataset and site given in Anderson et al. (2004), i.e.:

$$\mathrm{y} = (\mathrm{a} \times \mathrm{NDWI} + \mathrm{b}) \times \left(1 + \mathrm{c} \times \mathrm{e}^{\mathrm{d} \times \mathrm{NDWI}}\right) \tag{6.1}$$

where y is either LAI or vegetation height. $\mathrm{a}, \mathrm{b}, \mathrm{c}\ \mathrm{and}\ \mathrm{d}$ are regression coefficients, i.e. for $\mathrm{y} = \mathrm{LAI}$: 2.88, 1.14, 1.04e-1 & 4.1 for both corn and soybean; and for $\mathrm{y} = \mathrm{vegetation\ height}$: 1.20, 0.60, 4.00e-2, 5.30 and 0.50, 0.26, 5.00e-3, 4.50 for corn and soybean, respectively. NDWI of the vegetation was calculated from 30 m resolution Landsat data as (Gao, 1996):

$$\mathrm{NDWI} = \frac{\rho_{\mathrm{NIR}} - \rho_{\mathrm{SWIR}}}{\rho_{\mathrm{NIR}} + \rho_{\mathrm{SWIR}}} \tag{6.2}$$

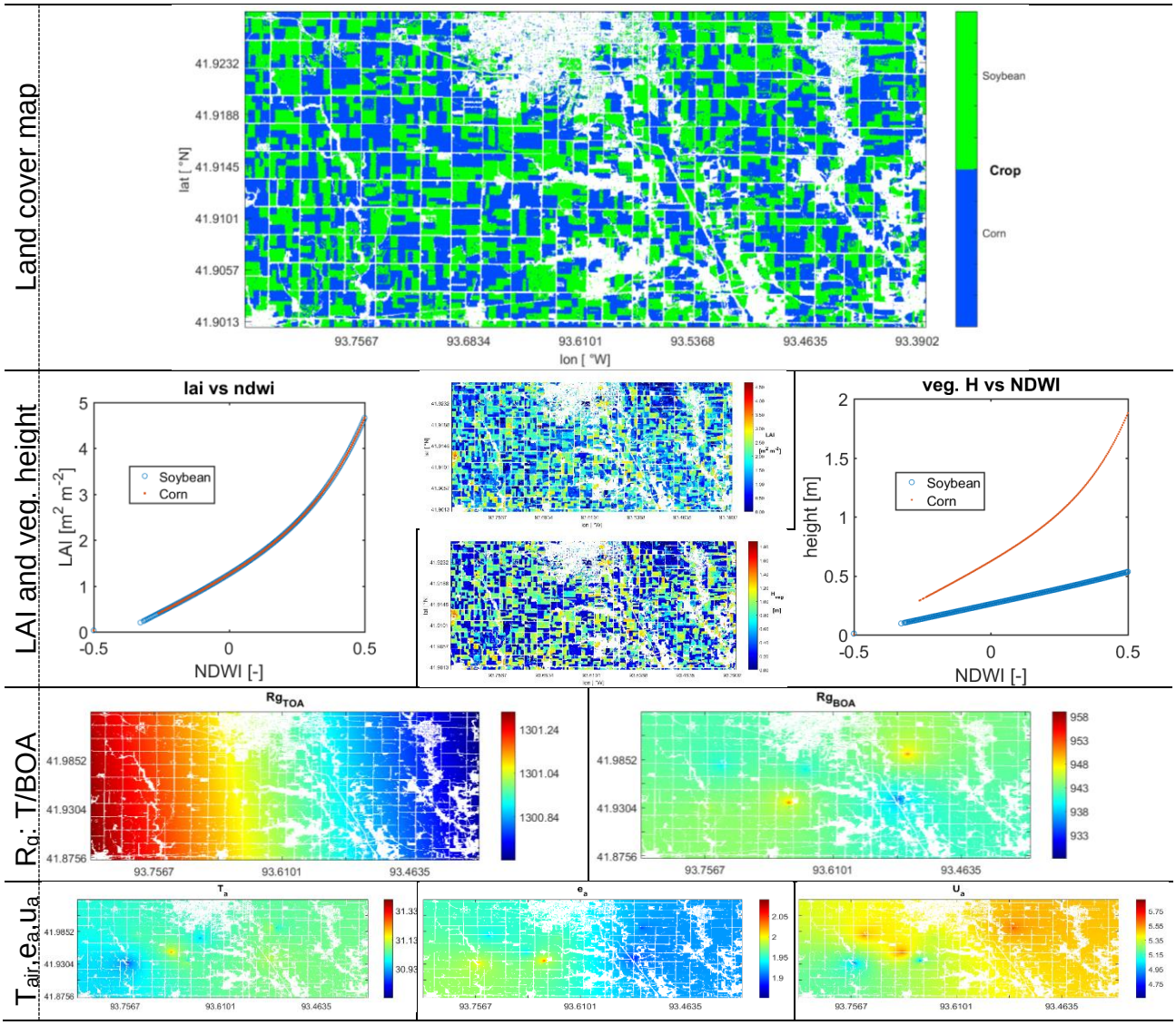

Figure 41: Site details and data: The land cover map of the Walnut creek watershed (only soybean and corn/maize used). The leaf area index and vegetation height maps and their respective relationships with the NDWI. Radiation (TOA and BOA) and meteorological (air temperature, atmospheric pressure and wind speed) data

Meteorological variables (wind speed, air temperature, air pressure, etc.) measured at in-situ observation stations within the watershed were numerically extended to other pixels using a nearest-neighbor approach for use in the soil vegetation atmosphere transfer modelling exercises. The Top of Atmosphere (TOA) solar radiation at each pixel (Iqbal, 1983; Parodi, 2000) were used together with those observed in-situ (i.e., Bottom of Atmosphere short wave radiation) to estimate the atmosphere's transmittance. These transmittances were subsequently similarly extended to other pixels using a nearest-neighbor method. The BOA solar radiation was finally derived as a product of the atmospheric transmittance and the extraterrestrial TOA radiance. The sun angles were calculated according to Iqbal (1983).

View angles of a polar orbiter: zenith and azimuth (VZA, θ_v and VAA, , ϕ_v)

Sun-synchronous orbiters (or space-borne satellites in general) will often have set design criteria that defines various mission technical specifications, such as satellite altitude, scan angles, among others. Figure 42 illustrates some of these geometrical specifications that describe the position of a remote sensor relative to the Earth.

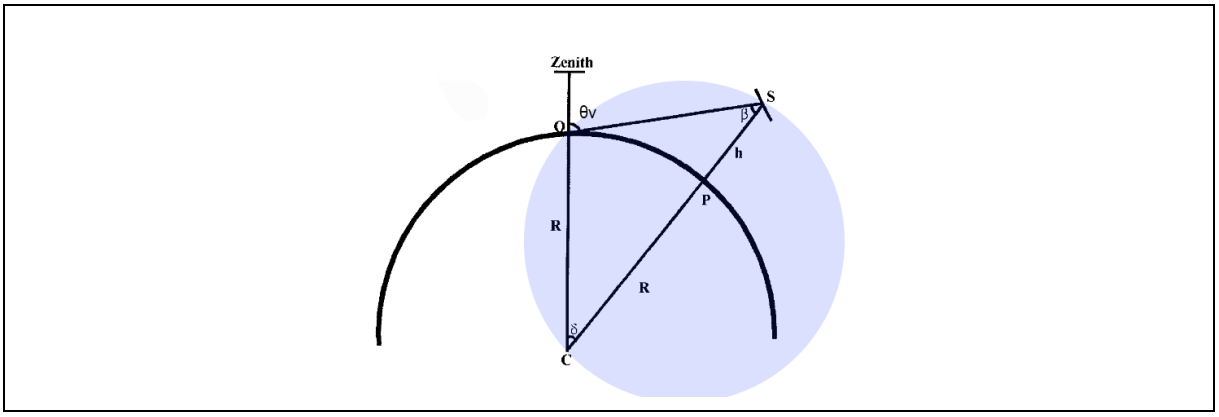

Figure 42: satellite-earth view geometry (adapted from Niu et al. (2001))

For polar orbiters, viewing angles for pixels within an image can be estimated using Niu et al.'s (2001) method. They validated their approach using viewing angles of the Advanced Very High Resolution Radiometer (AVHRR) polar orbiter, giving good accuracy. Assuming a satellite altitude of h (e.g., TRISHNA $\sim 761\ \mathrm{Km}$) and an orbit inclination of i, the viewing zenith angle (θ_v) for a pixel (point 'O') in the swath can be retrieved by rewriting the sine rule $\frac{R+h}{\sin(\pi-\theta_v)} = \frac{R}{\sin\beta} = \frac{R}{\sin(\theta_v-\delta)}$ as:

$$\theta_v = \tan^{-1}\left(\frac{\sin\delta}{\cos\delta - R/(R+h)}\right) \tag{6.3}$$

where R is the radius of the earth. $\beta = \theta_v - \delta$ is the sensor's scan angle for point *'O'*, $\delta = \sin^{-1}(\sin[\pi - i]\sin\overline{OP})$ is the length of arc '$\overline{OP}$' in Figure 42, which can be calculated from the nadir (*'P'*) and pixel-of-interest (*'O'*) coordinates.

The viewing azimuth angle is formulated thusly,

$$\varphi_v = \begin{cases} \cos^{-1}\left(\frac{-\cos i}{\cos\delta}\right), & \lambda_O < \lambda_P \\ \pi + \cos^{-1}\left(\frac{-\cos i}{\cos\delta}\right), & \lambda_O > \lambda_P \end{cases} \tag{6.4}$$

Here, the longitude (λ) is taken to be negative / positive to the west / east. By assuming

an orbit inclination of $\sim 98.7\,^{\circ}$ or $\sim 81.3\,^{\circ}$, the azimuth equation above will generally result in $\sim 81.3\,^{\circ}$ or $\sim 98.7\,^{\circ}$ when the pixel of interest is to the left of the satellite's subtrack and $\sim 261.3\,^{\circ}$ or $\sim 278.7\,^{\circ}$ when the pixel is to the right of the subtrack. The exact variations in the reference or 'real'/'actual' azimuths – as depicted in the histogram (Figure 43) below - are however not precisely reproduced. This is perhaps due to the fact that - unlike the reference, which uses a possibly more realistic geoid representation of the Earth - Niu et al.'s (2001) method uses a simplified Earth surface model. Note that the satellite geometries used in the calculations were computed using CNES software *(Gamet Ph., Personal Communication, 2022)*.

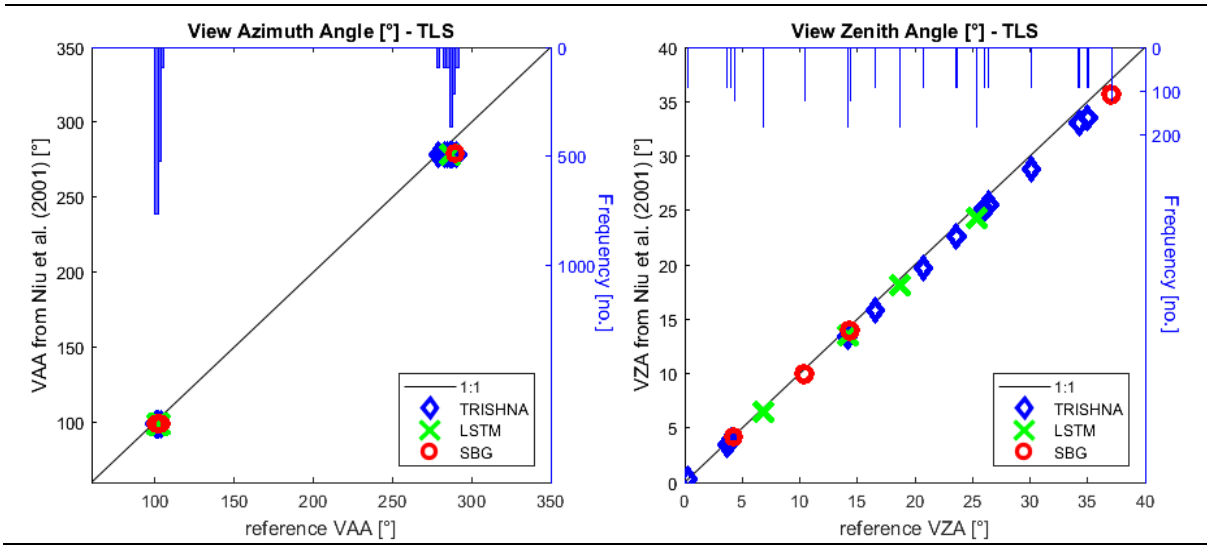

Figure 43: Viewing angles as calculated using Niu et al.'s (2001) method versus the reference angles for the TRISHNA, LSTM and SBG (abbreviated TLS) overpasses over the three combined sites (i.e. Wankama, Niger; Grosseto, Italy; Lonzée, Belgium). See introduction in Chapter 1 for a brief description of the dataset. Satellite altitudes: TRISHNA, ~761 Km; LSTM, ~639.5 Km; SBG, ~666 Km. Right axis: histograms of reference dataset

Figure 43 scatters the view angles (azimuth and zenith) calculated using Niu et al.'s (2001) method versus reference angles calculated using proprietary algorithms used by the TRISHNA, LSTM and SBG missions. This comparison was performed over a combined three sites (Niger; Grosseto, Italy, Lonzée, Belgium) that have already been briefly described in Chapter 1. Given the illustrated accuracy, the simple, relatively easy to implement tool could help in remote sensing analyses involving polar orbiters especially where viewing angle data is not readily available.

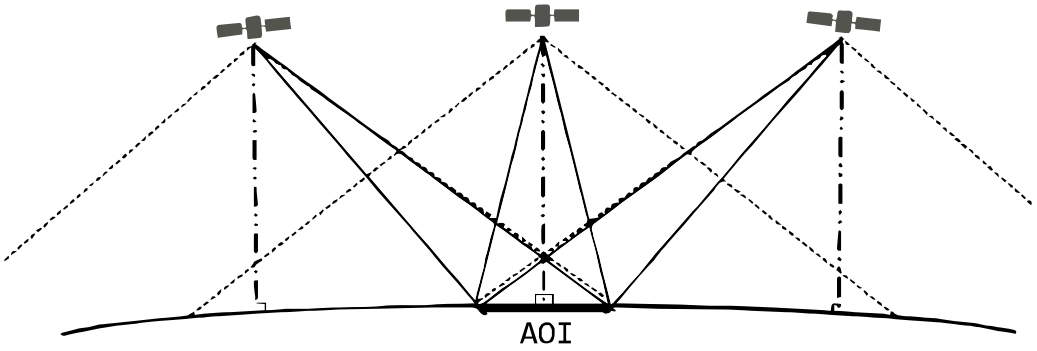

[a] AOI to the right of the subtrack	[b] AOI ~on subtrack	[c] AOI to the left of the subtrack
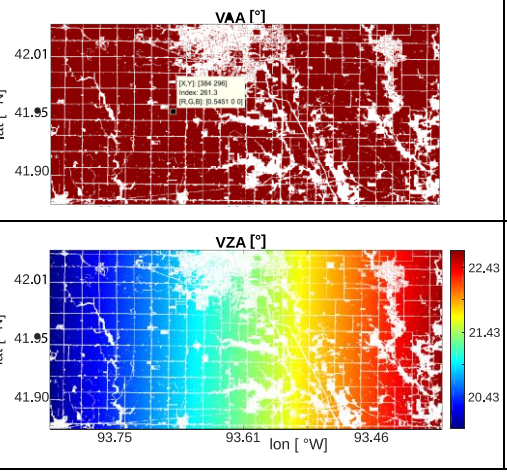	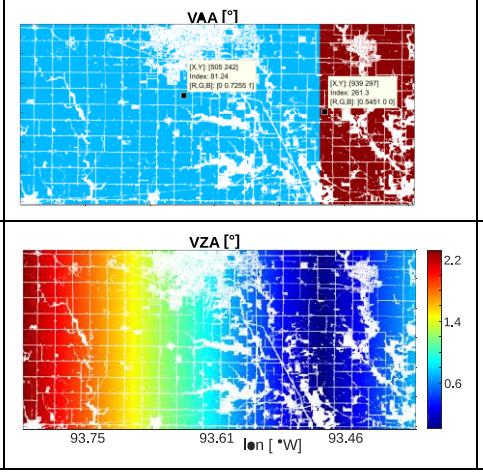	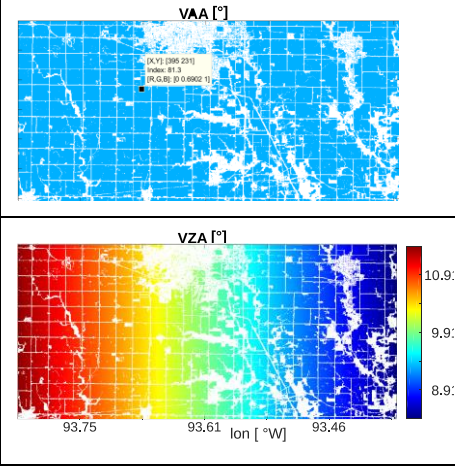

Figure 44: view angles (azimuth and zenith) as calculated using Niu et al.'s (2001) method for three viewing scenarios, i.e.: left - AOI to the right of the satellite's subtrack; centre – AOI on the satellite's subtrack and; right – AOI to the left of the sensor's subtrack.

Additionally, to allow capturing of the hotspot region, the scene was shifted downwards/southwards (i.e., from ~42 °N to ~25 °N) while also moving the sensor's sub-track such that some (or majority) of the pixels could eventually be simulated to be viewed in the Sun's direction. The input dataset were subsequently used to simulate directional temperature 'observations' throughout the tile.

SCOPE Model

We utilize the SCOPE sun-shade model (van der Tol et al., 2009; Yang et al., 2021), which has already been described in earlier sections. To recall, SCOPE is a comprehensive soil vegetation atmosphere transfer (SVAT) model that combines several physically-based models that describe radiative, turbulent and biochemistry processes within canopy systems. Herein, SCOPE was thus used to model out of canopy directional (nadir and off-nadir) surface brightness temperatures for the different pixels with varying conditions, i.e. meteorological, biophysical, soil water/resistance (uniformly randomized between 200-2500 s/m to ensure a broad range of water stress conditions). Synthetic thermal infrared (TIR) images as would be observed by a sun-synchronous polar orbiter (in view angles as computed using Niu et al.'s (2001) method above) were generated from the estimated directional temperature.

6.2.3. Results Summary and Discussion

Figure 45 illustrates the feature spaces and histograms plotted for different scenarios from the initial analyses. That is, temperature-vs-vegetation fraction using temperatures as would be observed from [panel labels – also see Figure 44]: [a] in the direction of the sun (satellite's subtrack to the left here), [b] temperatures observed from close-to-nadir, and [c] in the direction away from the sun (subtrack to the right of the AOI here). Also displayed is the $(T - f_c)$ space depicting the distribution close to hotspot region. Apart from panel [c], the T-fc spaces using off-nadir data are in red with the nadir feature spaces in blue. For the histograms, the off-nadir temperatures are in red with the nadir surface temperatures in blue. Similar to the biophysical input variables, directional temperature estimates also portray a bimodal trend.

The simulations done with the AOI northwards (hence different viewing and sun angles, i.e. SAA ~210 °, VAA ~270 °) illustrate that the oblique temperatures simulated in panels [a], [b] and [c] are very close to the nadir-simulated surface temperatures. As displayed in the bottommost row, however, directionality issues clearly begin to manifest in resulting temperature-vegetation ccover space when the tile is located southwards in the tropics (such that $\mathrm{VAA} \approx \mathrm{SAA};\ \mathrm{VZA} \approx \mathrm{SZA}$)

For SAA ~210 ° ; SZA ~20 ° :

[a] vza ~7 °-10 ° vaa ~270 °	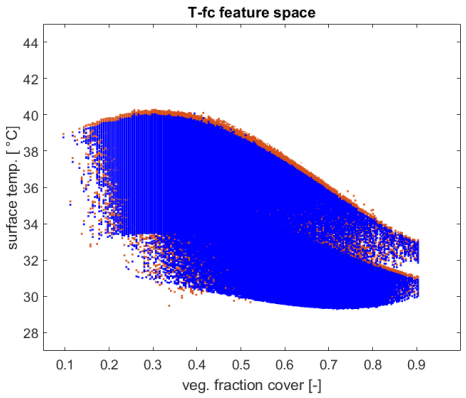	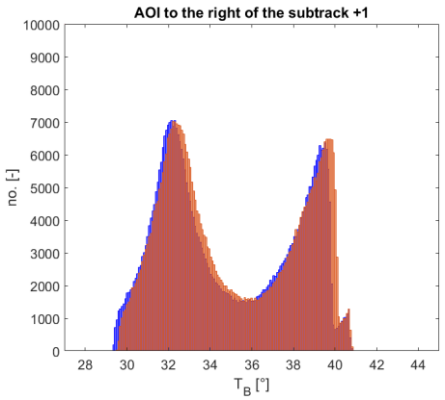
[a] vza ~19 °-23 ° vaa ~270 °	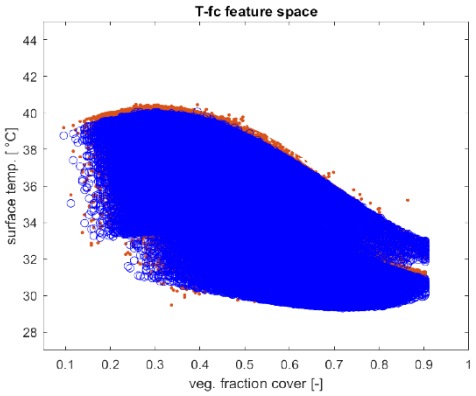	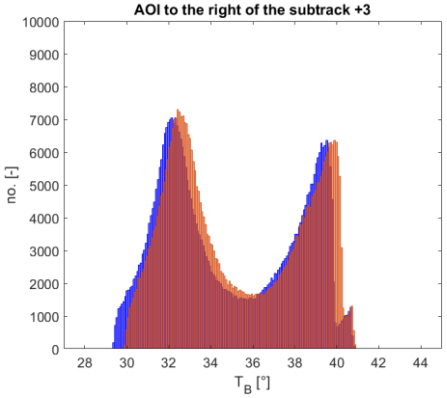
[b] vza ~0 °-3 ° vaa ~90 ° & ~270 °	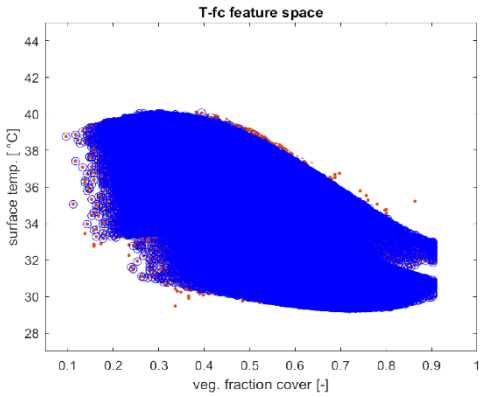	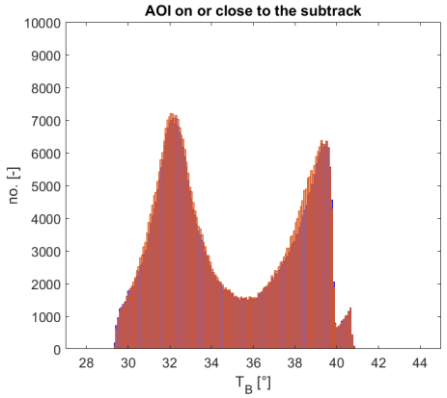
[c] vza ~7 °-10 ° vaa ~90 °	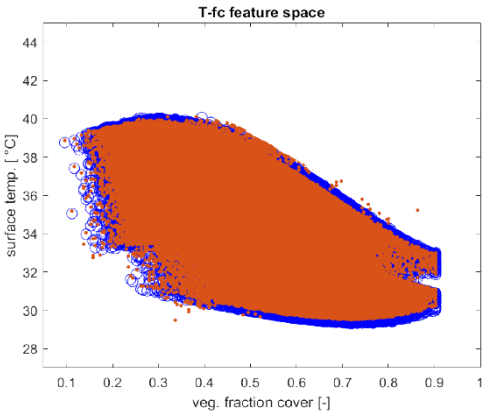	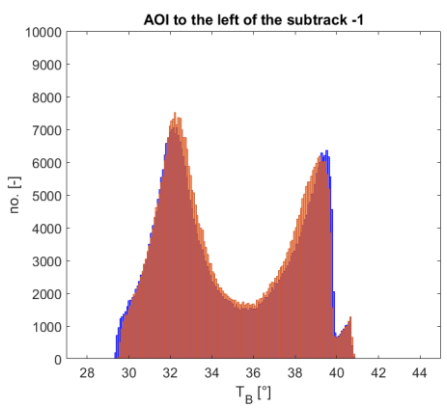

For SAA ~270 ° ; SZA ~10 °:		
[a] vza ~8 °-11 ° vaa ~270 °	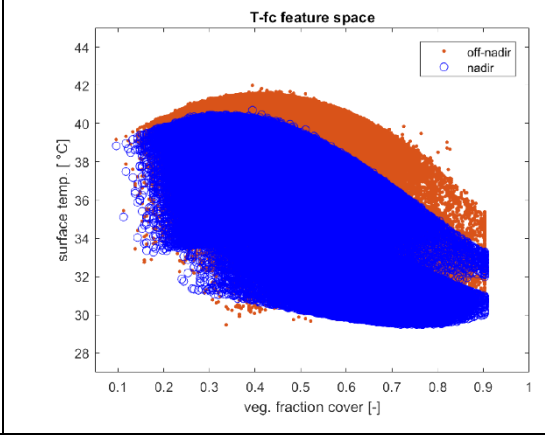	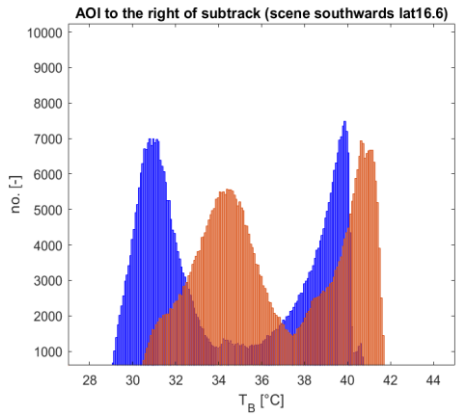

Figure 45: surface temperature versus vegetation cover fraction scatter diagrams and the respective histograms in the nadir and oblique directions for different sun-target-view configurations (AOI = area of interest).

View direction relative to sun angles and likelihood of viewing the hotspot

By providing scan angles of ~40 °, space-borne polar orbiters can observe large swaths of the Earth surface but only at a narrow azimuth window that is limited by the specific orbit inclination. These sun-synchronous satellites are also designed to allow day-time capturing of terrestrial variables at any location on earth from mid-morning to early afternoon (typically around 10:00 – 14:00). For example, the MODerate resolution Imaging Spectroradiometer (MODIS) sensor aboard the Terra and Aqua satellites provides surface temperature acquisitions at 10:30 am and 13:30 pm, respectively, while the anticipated TRISHNA mission is also expected to achieve similar acquisition times (see details in Chapter 1, Figure 2).

Figure 46 shows sun path diagrams for five latitudes: 45 °N, 23.43 °N (Tropic of Cancer), 0° (Equator), 23.43 °S (Tropic of Capricorn) and 45 °S. Also displayed in the diagrams is the likely scanning range of a polar orbiter (90° ± ~8.3° orbit inclination), which qualitatively illustrates the likelihood of viewing within the solar region throughout the year. Recalling from previous descriptions (section 3.1.4), date lines are depicted as either: solid lines from bottom to top representing January to June, or; dotted lines running from top to bottom, i.e., from July to December. Highlighted in red are sun paths during possible overpass times, i.e., left to right – 10:00 am to 02:00 pm).

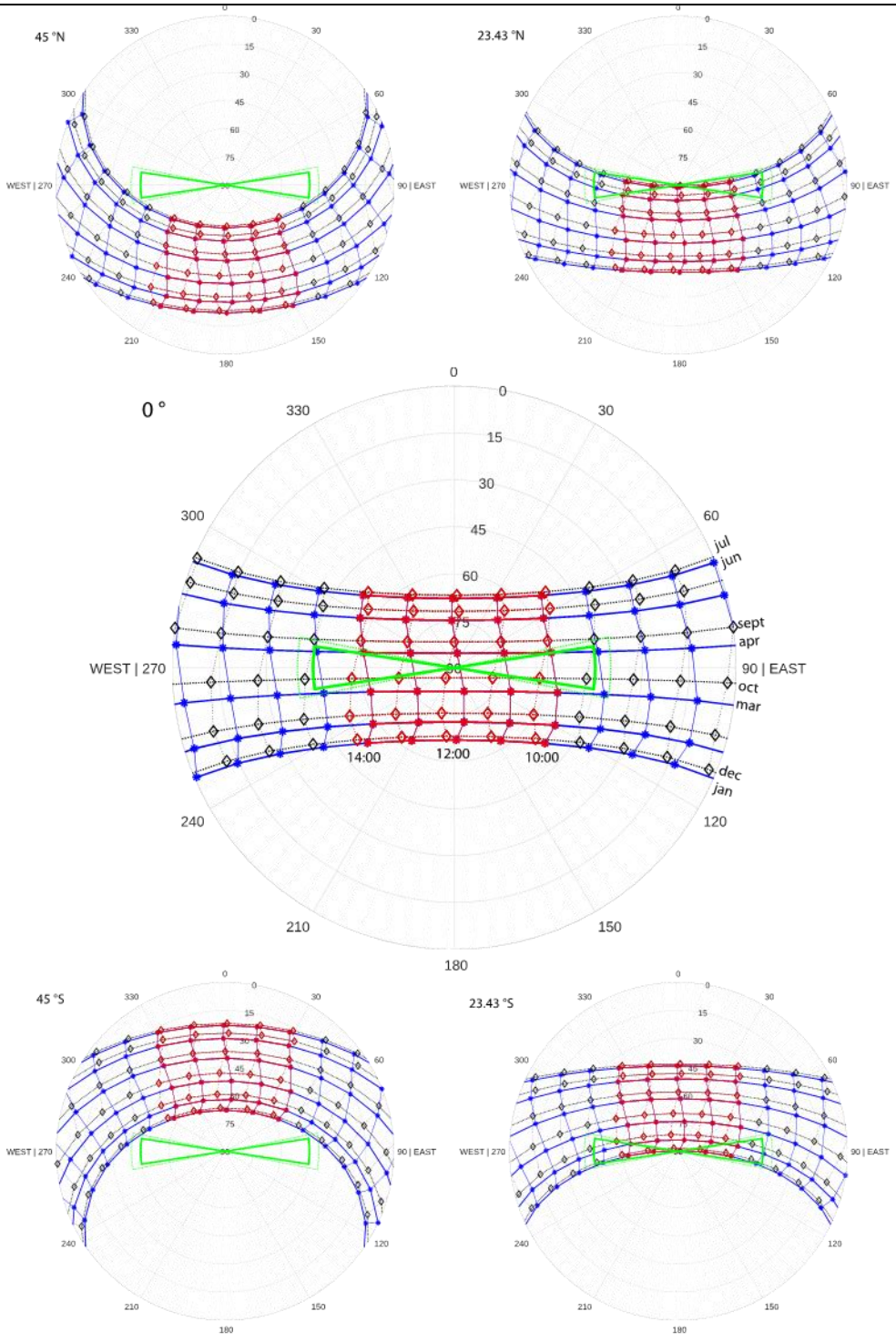

Figure 46: Sun path diagrams depicting the sun angles (azimuth and altitude/elevation) for five latitudes - northern hemisphere (45° N, 23.5° N), equator, and southern hemisphere (45° S, 23.5° S). Blue date/hour [solid] lines: January to June; grey date/hour [dotted] lines: July to December; Red hour lines: 1000 hrs – 1400 hrs

From the diagrams, it is evident that beyond the Southern and Northern tropics, observing the hotspot is highly unlikely even for hours outside the overpass time range. This has also been shown in the earlier exercise illustrated within Figure 2. At

the Southern tropic (23.43 °S), the possibility of hotspot viewing at overpass time is higher in January, February and December, and to a smaller extent in November. Similarly, the possibility is higher during summer (i.e., in June, July, August - and possibly May) at the Northern tropic (23.43 °N). The same can be observed at the Equator, where view and sun angles are likely to coincide during the period between March to April and September to October. Overall, and as illustrated in the $(T - f_c)$ feature spaces, the likelihood of acquiring images in the hotspot direction are limited to a maximum of four months and constrained to the Tropics.

View direction

While some differences can be observed in the feature spaces derived using off-nadir surface temperatures versus those from nadir temperatures, the effects are generally insignificant especially in relatively small image scenes (the Walnut Creek gridded image measured around 10 km by 30 km, relatively smaller than the 100 km by 100km tiles that will be provided within TRISHNA). This is because differences in viewing angles between the various pixels within the image are minimal. For example, in the differences of viewing zenith angles throughout our AOI range from 0°-2.5°, meaning anisotropy effects do not vary too much from one end of the scene to the other. This is particularly true when the AOI is located on or close to the sub-track, meaning the directional temperatures will be quite similar to those that would otherwise be observed from nadir.

This, however, would probably not hold for thermal imagery with very large areal coverage, e.g., half of the swath coverage where the differences in view zenith angles for pixels within the image can approach the sensor's scan angle. Nonetheless, images covering such big regions are typically not used for contextual ET modelling, as there will likely be considerable variations in the meteorological conditions.

If the AOI is located further off the sub-track, there is higher likelihood of an influence on the dry/cold edges in the $(T - f_c)$ space (and consequently on ET retrieval) relative to the ones retrieved from the nadir thermal data. This is even more pronounced when the area of interest is viewed in the principal plane from the sun's direction. The viewing azimuth angles for polar orbiting satellites are close to either ~90° or ~270° depending on the location of a pixel relative to the sensor's subtrack with zenith angles of up to ~40°. Viewing the entire AOI in the hotspot direction is therefore more likely to occur in the tropics since the sun angles for such regions can reach those values

at daytime overpasses.

Angular/directionality effects will be less pronounced in very sparsely vegetated scenes and overall non-existent over bare (and relatively flat) ground. This infers that the Y-intercept of the dry edge will generally show minimal change irrespective of direction of view and may thus mask the shift in other contextual temperatures within the space, especially when the AOI is mostly viewed from the solar direction.

Concluding remarks

Chapters 4, 5, 6 summarize evaluations and analyses of the surface energy balance methods described in Chapter 3 over a variety of canopies. The original and extended soil plant atmosphere remote sensing of evapotranspiration (SPARSE and SPARSE4) methods (presented in Chapter 3) are assessed using data collected from several experimental sites. These evaluations are undertaken over diverse canopies (heterogeneous and heterogeneous landscapes) as well as on synthetic data. The sites and datasets, which include meteorological (wind speed, air temperature and humidity) and surface flux (radiation and turbulent) data, are described within the pertinent chapters/sections. Data-preparation and processing procedures that were undertaken are also summarized therein.

Summary of model analyses:

With regard to the first study (Chapter 4), the regression slopes and correlation of the energy balance were deemed reasonably closed in the datasets collected over the four diverse canopies. On the vineyard (Chapter 5), energy imbalance corrections on scale-attributed biases in the available energy (instead of the standard turbulent flux corrections) allowed better agreement with the observed turbulent fluxes.

While evaluating the surface energy balance algorithms (SPARSE and SPARSE4) using observed data (from the Orchards, wheat and soybean sites, as well as using data from the Vineyard), we observed that both schemes showed no noticeable differences in their estimation of overall fluxes when run using nadir-based thermal data. Incorporating the solar direction and discriminating between sunlit and shaded elements was however observed to improve the partitioning of the total fluxes between the surface sources (soil and vegetation), especially in water-stressed environments. Separately, the sensitivity of flux and component temperature estimates to the viewing direction of the sensor was tested by using two - simultaneously observed - sets of thermal data (nadir and oblique) to force the models where it was illustrated that sensitivity to viewing direction was reduced thus ensuring better nadir-oblique based retrieval consistency. The sensitivity of flux and component temperature estimates to the viewing direction of the sensor was also tested over the heterogeneous Vineyard site. Reconstructed sets of thermal data (nadir and oblique) were used to force the models. Over the row canopy, degraded flux retrieval in the cross-row was observed

with better consistency along rows. Overall, it was nevertheless shown that by using the extended method, the sensitivity to viewing direction can significantly be reduced.

Summary of synthetic analyses (point- [Section 6.1] and initial contextual [section 6.2] experiments):

A synthetic study was separately performed in a homogeneous canopy setup comparing model retrievals with those from the SCOPE model, which is able to provide 'references' of flux estimates and directional temperatures. Here, SPARSE4 was observed to improve directional consistency of the flux retrievals over wide-ranging simulation conditions. As with directional anisotropy, different conditions were observed to influence the directional retrieval consistency, with the main driver observed to be the incoming radiation. Wind speed and vegetation fraction cover (as described by the leaf area index) also influence the directional retrievals. Nonetheless, the retrieval inconsistencies (hence weak model performance) were mostly observed to have a major influence at higher zeniths, with minimal effects on near-nadir based (as would be the case with current TIR RS missions) retrievals.

Preliminary contextual analyses carried out using simulated directional temperature 'observations' showed that the effects of thermal radiation directionality on the temperature-fraction cover space are low when the 'observations' of thermal emission are viewed in directions away from the sun. in hotspot viewing, however, directionality effects manifest. Simple sun positioning tools (sun path diagrams combined with known sensor positions in space) can help identify such exposures. The contextual experiments on sparsely vegetated surfaces were based on the assumption that the non-vegetated surface is relatively smooth, which in many cases may not hold. Since the SCOPE model does not simulate anisotropy resulting from uneven soil surfaces, the effects of surface roughness were not considered and were therefore a limitation to the these experiments. Surface roughness can indeed influence the slope of the dry- (and possibly cold-) edges, subsequently affecting the surface flux retrievals/estimations from resulting contextual spaces derived from directional surface temperatures.

Chapter 7: General conclusion and perspectives

7.1. Summary

As global warming develops into an increasingly worrisome concern that is likely to threaten food security, land surface temperature (LST) becomes an important variable that can aid in the characterization of the water status of critical eco-agro systems. Indirectly, it can aid in signaling when plants are experiencing water stress, which will generally translate to suboptimal biomass production (and - in extreme cases - permanent crop failure). The need for monitoring LST has consequently inspired space agencies around the globe to initiate earth observation programmes focused on the thermal infrared spectral domain. Space-borne (remote sensing) thermal missions therefore aim at interpreting the observed thermal emissions for the characteristic brightness (and subsequently radiative) temperature. The monitoring of evapotranspiration at field scale with the aim of optimizing irrigation scheduling has warranted the use of thermal data at relatively high spatial and temporal resolution. This means that acquisitions have to be available at a higher revisit frequency, which then implies the likelihood of angular anisotropy. The directional or angular anisotropy phenomenon can be described as the directional variability that often manifests in remotely sensed radiation signals. This is illustrated using orbit simulation datasets from three proposed thermal infrared missions (TRISHNA, LSTM and SBG), over three sites located at different latitudes (Figure 2). This satellite combination achieves near-daily overpasses with hotspot directional anisotropy effects mostly expected in the tropics.

In the current study, we sought to analyze how directional anisotropy in thermal acquisitions influences surface energy balance inversion and thus water flux (in form of evapotranspiration) estimation. The work begins by extending the dual source soil plant atmosphere remote sensing of evapotranspiration (SPARSE) model, where the two vegetation and soil components or sources were discriminated into their respective illuminated and shaded elements. This was effected by first partitioning the

incoming solar radiation into its diffuse and direct components using the Erbs et al. (1982) method, thus allowing conceptualization of separate energy balance schemes for the different components. The unified François model was then applied for weighting between sunlit and shaded elements and linking the elemental emissions to the out-of-canopy radiation, as would be observed by a remote sensor. An initial intercomparison analysis between the UFR97 model, 4SAIL and the 'reference' DART simulations – performed using data from a heterogeneous row site – showed the UFR97 simulations to be more consistent with the DART 'truths' particularly in terms of temperature distribution over the polar space.

The performance of the SPARSE and extended SPARSE model (SPARSE4) were then assessed using available data collected from diverse environments, i.e., orchards, vineyard, soybean and wheat fields. Initial evaluations were thus focused on retrieval of surface fluxes using nadir temperatures. Separately, directional brightness temperatures were used to drive the models so as to assess directional consistency of flux retrievals. With respect to nadir-based overall estimates, both methods perform similarly with generally no observable differences. The inclusion of the Sun direction and thus partitioning the incoming radiation into its direct and diffuse components (and distinguishing sunlit/shaded elements) does appear to improve the partitioning of fluxes between the soil and the vegetation especially with regard to the latent heat energy (i.e., evapotranspiration into evaporation and transpiration).

Directional consistency analyses of the flux retrievals followed. This involved use of synchronous nadir and oblique surface brightness temperatures to drive the surface energy balance schemes with the aim of checking sensitivity of estimated fluxes to directional thermal data. Ideally, since surface emissions (thus fluxes) do not depend on the outward TIR observed by a remote sensor but vice versa, the retrieved energy balance components should be consistent from one viewing angle to the other (whether nadir or oblique). Consistency in this case therefore referred to agreement between nadir-retrieved fluxes to oblique-retrieved estimates; which should ideally be equivalent. Directional temperature data was only available from one experimental site. Accordingly, we also used reconstructed surface temperature data from a heterogeneous (vineyard) site as well as synthetic data from the SCOPE soil vegetation atmosphere transfer model for homogeneous experiments.

In the case of the heterogeneous vineyard experiments, two sets of reconstructed

temperatures were applied: *1)* directional temperatures reconstructed using the UFR97 radiative transfer scheme, and *2)* as already pointed out above, surface temperatures simulated using the 3D DART model over a select clear-sky days. Generally, we observed a more consistent retrieval of the surface fluxes when using directional temperatures of the surface in the direction along the vine row, with degraded performance at high zenith angles in the cross-row direction. In the latter case however (where dissymmetry of the directional temperatures simulated by DART was present, i.e., in the directions in and away from the Sun), directional inconsistencies of flux retrievals close to the row especially in the direction of minimal solar illumination were observed. While SPARSE4 outperformed SPARSE in terms of directional retrieval consistency, it was still unable to simulate the dissymmetry modelled by DART since it uses the relatively simple UFR97 scheme. This shows that, while the use of turbid canopy models could be sufficient, there may be need for better and realistic representation of the canopy structures and surface geometries.

In the synthetic experiments that involved the use of the SCOPE model as the source of 'reference' data, the effects of different input factors on the retrieval consistency of the SEB estimation were analyzed. These particular experiments involved running the 'reference' and energy balance methods in homogeneous canopy landscapes with varying atmospheric and surface water status conditions. While estimating the surface energy balance components, the incoming radiation was observed to be the main driver of the retrieval inconsistencies. Wind speed and the vegetation fraction cover (as described by the leaf area index) also contributed to the directional inconsistencies. Overall, however, directional inconsistency issues were observed to be more prevalent when using thermal infrared inputs observed at relatively higher view angles, typically at the potential scan edges of current remote sensors. Separately, the contextual evapotranspiration experiments showed that the temperature versus vegetation index feature space will generally exhibit little variability especially when the remotely-sensed signals are not observed within the extremes (e.g. hotspot region). As such (and comparably to the point-SEB analyses), feature spaces derived using close-to-nadir (within the satellite's sub-track) acquisitions will tend to exhibit little directionality influences, with such effects increasing with increasing view/scan angles. Accordingly, simple positioning tools (such as. Sun path diagrams and specifications of view geometry) can qualitatively help identify thermal

radiation directionality exposure on contextual methods.

7.2. Outlook

Further refinement of the extended SPARSE scheme is prospected. That is, by revisiting the radiative transfer, and conductance schemes applied when discriminating between the different elements in the surface vegetation and soil sources. Regarding the radiative transfer scheme, this would entail addressing the multiple reflection scheme and better accounting of multispectral data. The asymmetry in directional data from the more realistic 3D DART model showed that there was need for a better representation of the turbid models used in the radiative scheme. This could possibly involve: *i)* considering other leaf distributions (inclinations and orientations) that also occur in natural terrestrial systems, such as planophile / erectophile leaf distributions; *ii)* representing the vertical vegetation column (especially of tree canopies) with better realism (for instance, considering the upper whorl and lower trunk separately for realistic directional gap frequency estimations). The current method used to estimate or invert the soil reflectance (given the surface and vegetation characteristics) also requires further analysis/evaluation to allow a better representation of the extremes/limits where the reflectance curve - as currently conceptualized and implemented - appears to provide spurious estimates.

Given that there was limited availability of directional thermal data over different kinds of canopies, we propose carrying out field campaigns that would allow collection of such data. Observation of elemental sunlit / shaded soil and vegetation temperatures while simultaneously acquiring the aggregated directional surface temperatures should aid in further evaluation and refinement of the radiative transfer methods that are coupled within the surface energy balance schemes. Comprehensive radiative transfer methods like DART - that are meant to simulate observation-like signals - would benefit as well. On the satellite data product level, these data should also help to evaluate the simple normalizing methods that are proposed for use when processing raw (BOA) emission radiances from TIR earth observation missions (e.g. TRISHNA).

The influence of [horizontal] turbulence has become an important contributing aspect to thermal radiation directionality, needing further investigation. Generally, forced convection, which is instituted by the near-surface wind profile, will result in spatially

varying turbulence that is expected to influence the temporal variation of directional anisotropy. Given that remote thermal infrared remote sensors provide instantaneous acquisitions, methods that are capable of properly representing this momentum transfer could perhaps help alleviate any directionality issues introduced through turbulence. However, this is rarely the case as schemes that are often applied to simulate the dynamics at the aerodynamic level do not always model the interactions accurately. We therefore propose to compare and evaluate how well these interactions are represented in the current schemes and thus check the feasibility of implementing a more complete and realistic turbulence mixing scheme of the surface boundary layer.

Separately, a more careful look at how directionality affects contextual evapotranspiration methods is also necessary, where an analysis of how the directionality-influenced T-VI (surface temperature versus vegetation index feature space) affects the retrieved actual evapotranspiration. Addressing the effects of surface roughness, especially at very low vegetation cover is many times not incorporated in soil vegetation atmosphere transfer (SVAT) methods (SCOPE, for example). Directional anisotropy and effects resulting from such surface roughness should therefore be considered to allow a better representation of the surface temperature versus surface characteristic (e.g. temperature – vegetation fraction cover) feature space, especially in relation to the dry-edge. This should help alleviate dryness/wetness bias issues on the edges that could manifest during contextual evapotranspiration estimation when using directional thermal data. This will also be a likely issue that will need to be considered when normalizing remotely surface temperatures, that are to be applied in contextual surface flux tools such as EVASPA.

7.1. Résumé

Alors que le réchauffement climatique devient de plus en plus préoccupant et risque de menacer la sécurité alimentaire, la température de surface devient une variable importante qui peut aider à caractériser l'état hydrique des agro- éco-systèmes et les enjeux qui leur sont associés (sécheresse, risque d'incendie, optimisation de la ressource etc). Indirectement, elle peut aider à signaler le moment où les plantes subissent un stress hydrique, ce qui se traduit généralement par une production sous-optimale de biomasse (et, dans les cas extrêmes, par une perte permanente de récolte). La nécessité de surveiller les TCL a donc incité les agences spatiales du monde entier à lancer des programmes d'observation de la Terre axés sur le domaine spectral de l'infrarouge thermique. Les missions spatiales de télédétection thermique visent donc à interpréter les émissions thermiques observées pour la température caractéristique de brillance (et par la suite radiative). Le suivi de l'évapotranspiration à l'échelle du champ dans le but d'optimiser la programmation de l'irrigation a justifié l'utilisation de données thermiques à relativement haute résolution spatiale et temporelle. Cela signifie que les acquisitions doivent être disponibles à une fréquence de revisite plus élevée, ce qui implique alors la probabilité d'une anisotropie angulaire. Le phénomène d'anisotropie directionnelle ou angulaire peut être décrit comme la variabilité directionnelle qui se manifeste souvent dans les signaux de rayonnement télédétectés. Ceci est illustré à l'aide de jeux de données de simulation d'orbite de trois missions infrarouges thermiques proposées (TRISHNA, LSTM et SBG) sur trois sites situés à des latitudes différentes (Figure 2). Cette combinaison de satellites permet d'obtenir des passages quasi-quotidiens avec des effets d'anisotropie directionnelle de points chauds principalement attendus dans les tropiques.

Dans l'étude actuelle, nous avons cherché à analyser comment l'anisotropie directionnelle des acquisitions thermiques influence l'inversion du bilan énergétique de surface et donc l'estimation du flux d'eau (sous forme d'évapotranspiration). Le travail commence par l'extension de la télédétection sol-plante-atmosphère à double source de l'évapotranspiration (SPARSE), où les deux composantes ou sources de végétation et de sol ont été discriminées dans leurs éléments éclairés et ombragés respectifs. Pour ce faire, le rayonnement solaire entrant a d'abord été divisé en composantes directe et diffuse à l'aide du modèle d'Erbs, ce qui a permis de conceptualiser des bilans énergétiques distincts pour les différentes composantes. Le

modèle unifié de François a ensuite été appliqué pour pondérer les éléments éclairés et ombragés et relier les émissions élémentaires au rayonnement hors canopée tel qu'il serait observé par un capteur à distance. Une première analyse d'intercomparaison entre le modèle UFR97, 4SAIL et les simulations DART "de référence" - réalisée à l'aide de données provenant d'un site de rangées hétérogènes - a montré que les simulations UFR97 étaient plus cohérentes avec les "vérités" DART, notamment en termes de distribution de la température dans l'espace polaire.

Le modèle SPARSE étendu a ensuite été évalué à l'aide de données recueillies dans divers environnements, à savoir des vergers, des vignobles, des champs de soja et de blé. Les premières évaluations ont donc porté sur l'extraction des flux de surface à l'aide des températures au nadir. Ensuite, les températures de luminosité directionnelle ont été utilisées pour piloter les modèles afin d'évaluer la cohérence directionnelle des récupérations de flux. En ce qui concerne les estimations globales basées sur le nadir, les deux méthodes donnent des résultats assez similaires, sans différences observables. L'inclusion de la direction du soleil et donc la partition du rayonnement entrant en ses composantes directes et diffuses semble améliorer la partition des flux entre le sol et la végétation, en particulier en ce qui concerne l'énergie thermique latente (c'est-à-dire l'évapotranspiration en évaporation et transpiration).

Des analyses de cohérence directionnelle des récupérations de flux ont suivi. Cela impliquait l'utilisation de températures de brillance de surface obliques pour piloter les schémas de bilan énergétique de surface dans le but de vérifier la sensibilité des flux estimés aux données thermiques directionnelles. Idéalement, étant donné que les émissions de surface (et donc les flux) ne dépendent pas de la direction du capteur IRT, mais plutît l’inverse, les composantes issues de l'inversion du bilan énergétique devraient être cohérentes d'un angle de vue à l'autre (qu'il s'agisse d'un angle nadir ou oblique). Dans ce cas, la cohérence se réfère donc à l'accord entre les flux récupérés au nadir et les estimations récupérées en oblique de manière synchrone, qui devraient idéalement être équivalentes. Les données de température directionnelle n'étaient disponibles que pour un seul site expérimental. Par conséquent, nous avons également utilisé des données de température de surface reconstituées provenant d'un site hétérogène (vignoble) ainsi que des données synthétiques provenant du modèle SCOPE SVAT pour les expériences homogènes.

Dans le cas des expériences sur les vignobles hétérogènes, deux ensembles de

températures reconstruites ont été appliqués : 1) les températures directionnelles reconstruites à l'aide du schéma de transfert radiatif UFR97 et 2) comme nous l'avons déjà souligné ci-dessus, les températures de surface simulées à l'aide du modèle 3D DART sur une sélection de jours de ciel clair. En général, nous avons observé une récupération plus cohérente des flux de surface en utilisant les températures directionnelles de la surface dans la direction du rang de vigne, avec une performance dégradée à des angles zénithaux élevés dans la direction transversale du rang. Dans ce dernier cas cependant (où une dissymétrie des températures directionnelles simulées par le DART était présente, c'est-à-dire dans les directions vers le Soleil et à l'opposé de celui-ci), des incohérences directionnelles des récupérations de flux près de la ligne, en particulier dans la direction de l'illumination solaire minimale, ont été observées. Bien que SPARSE4 ait surpassé SPARSE en termes de cohérence de l'extraction directionnelle, il n'a toujours pas été en mesure de simuler la dissymétrie modélisée par DART puisqu'il utilise le schéma relativement simple de l'UFR97. Cela montre que, bien que l'utilisation de modèles de canopée turbide puisse être suffisante, il peut être nécessaire d'avoir une représentation meilleure et réaliste des structures de la canopée et des géométries de surface.

Dans les expériences synthétiques qui impliquaient l'utilisation du modèle SCOPE comme source de données de "référence", les effets de différents facteurs d'entrée sur la cohérence de l’inversion des différents termes du Bilan Energétique des Surfaces (BES) ont été analysés. Ces expériences ont consisté à générer des températures directionnels et les flux de surface avec SCOPE pour des canopées homogènes avec des conditions atmosphériques et d'état de l'eau de surface variables. Pour ces simulations le rayonnement solaire incident s’est révélé être le facteur prédominant. La vitesse du vent et la fraction de couverture végétale (décrite par l'indice de surface foliaire) ont également contribué aux incohérences directionnelles. Dans l'ensemble, cependant, les problèmes d'incohérence directionnelle ont été observés comme étant plus fréquents lors de l'utilisation d'entrées infrarouges thermiques observées à des angles de vue relativement élevés, généralement au niveau des bords de balayage potentiels des capteurs actuels. Par ailleurs, les expériences de simulation avec les méthodes contextuelles ont montré que l'espace caractéristique de la température par rapport à l'indice de végétation présente généralement une faible variabilité, en particulier lorsque les signaux

télédétectés ne sont pas observés dans les extrêmes (par exemple, la région des points chauds). En tant que tels (et de manière comparable aux analyses par points), les espaces caractéristiques dérivés d'acquisitions proches du nadir (à l'intérieur de la sous-piste du satellite) auront tendance à présenter peu d'influences de directionnalité, ces effets augmentant avec l'augmentation des angles de vue/balayage. Par conséquent, des outils de positionnement simples (tels que des diagrammes de la course du soleil et des spécifications de la géométrie de la vue) peuvent aider qualitativement à identifier l'exposition à la directionnalité du rayonnement thermique par des méthodes contextuelles.

7.2. Perspectives

La revisite du schéma SPARSE étendu est envisagée. Il s'agira notamment de revoir les schémas de transfert radiatif, et de conductance appliqués lors de la discrimination entre les différents éléments de la végétation de surface et les sources du sol. Concernant le schéma de transfert radiatif, il s'agit d'abandonner le schéma de réflexion multiple en faveur d'une approche semblable à SCOPE à 2 nœuds, et de mieux prendre en compte les données multispectrales. L'asymétrie des données directionnelles mise en évidence avec le modèle DART 3D a montré qu'il était nécessaire d'avoir une meilleure représentation des modèles turbides utilisés dans le schéma radiatif. Cela pourrait peut-être impliquer : i) de considérer d'autres inclinaisons/orientations foliaires qui se produisent également dans les systèmes terrestres naturels, telles que les distributions de feuilles planophiles/érectophiles ; ii) représenter la colonne de végétation verticale (en particulier des arbres) avec un meilleur réalisme (par exemple, en considérant séparément le verticille supérieur et le tronc inférieur pour des estimations réalistes de la fréquence des écarts directionnels). La méthode actuelle utilisée pour estimer ou inverser l'estimation de la réflectance du sol (compte tenu des caractéristiques de la surface et de la végétation) nécessite également une analyse/évaluation plus approfondie pour permettre une meilleure représentation des extrêmes/limites où la courbe de réflectance - tel qu'actuellement conceptualisé et mis en œuvre - semble fournir de fausses estimations.

Étant donné que la disponibilité de données thermiques directionnelles sur différents types de canopées était limitée, nous proposons de mener des campagnes de terrain qui permettraient de collecter de telles données. La collecte des températures élémentaires du sol et de la végétation ensoleillées / ombragées tout en acquérant

simultanément les températures de surface directionnelles agrégées devrait contribuer à une évaluation plus approfondie et à l'affinement des méthodes de transfert radiatif qui sont couplées dans les schémas de bilan énergétique de surface. Des méthodes complètes de transfert radiatif telles que DART, destinées à simuler des signaux de type observation, en bénéficieraient également. Au niveau des produits de données satellitaires, ces données devraient également aider à évaluer les méthodes de normalisation simples qui sont proposées pour être utilisées lors du traitement des luminances d'émission brutes (BOA) des missions d'observation de la Terre TIR telles que TRISHNA.

L'influence de la turbulence [horizontale] est devenue un aspect important de la directionnalité du rayonnement thermique, qui nécessite une étude plus approfondie. Étant donné que les capteurs infrarouges thermiques à distance fournissent des acquisitions instantanées, les méthodes capables de représenter correctement ce transfert de quantité de mouvement pourraient peut-être aider à atténuer les problèmes de directionnalité introduits par la turbulence. Cependant, c'est rarement le cas car les schémas qui sont souvent appliqués pour simuler la dynamique au niveau aérodynamique ne modélisent pas toujours les interactions avec précision. Nous proposons donc de comparer et d'évaluer dans quelle mesure ces interactions sont représentées dans les schémas actuels et de vérifier ainsi la faisabilité de la mise en œuvre d'un schéma de mélange de turbulences plus complet et réaliste de la couche limite de surface.

Un examen plus attentif de la façon dont la directionnalité affecte les méthodes d'évapotranspiration contextuelle est également nécessaire, où une analyse de la façon dont la T-VI (température de surface par rapport à l'espace caractéristique de l'indice de végétation) influencée par la directionnalité affecte l'évapotranspiration réelle récupérée. La prise en compte des effets de la rugosité de la surface, en particulier lorsque la couverture végétale est très faible, n'est souvent pas intégrée dans les méthodes SVAT (par exemple SCOPE). L'anisotropie directionnelle et les effets résultant de cette rugosité de surface doivent donc être pris en compte pour permettre une meilleure représentation de l'espace des caractéristiques de la température de surface par rapport au couvert végétal, en particulier en ce qui concerne le bord sec. Cela devrait permettre d'atténuer les problèmes de biais de sécheresse/humidité sur les bords qui pourraient se manifester lors de l'estimation

contextuelle de l'ET en utilisant des données thermiques directionnelles. Ce sera également un problème qui devra être pris en compte lors de la normalisation des températures de surface qui doit être appliquée dans les outils de flux de surface contextuels tels que EVASPA.

References

Agam, N., Kustas, W. P., Anderson, M. C., Norman, J. M., Colaizzi, P. D., Howell, T. A., … Wilson, T. B. (2010). Application of the priestley-taylor approach in a two-source surface energy balance model. *Journal of Hydrometeorology*, *11*(1), 185–198. https://doi.org/10.1175/2009JHM1124.1

Allen, R. G., Pereira, L. S., Raes, D., Smith, M., & Ab, W. (1998). Fao,1998. *Crop Evapotranspiration - Guidelines for Computing Crop Water Requirements - FAO Irrigation and Drainage Paper 56*, 300. Retrieved from http://www.kimberly.uidaho.edu/water/fao56/fao56.pdf

Allen, R. G., Tasumi, M., & Trezza, R. (2007). Satellite-based energy balance for mapping evapotranspiration with internalized calibration (METRIC) - Model. *Journal of Irrigation and Drainage Engineering*, *133*(4), 380–394. https://doi.org/10.1061/(ASCE)0733-9437(2007)133:4(380)

Anderson, M. C., Neale, C. M. U., Li, F., Norman, J. M., Kustas, W. P., Jayanthi, H., & Chavez, J. (2004). Upscaling ground observations of vegetation water content, canopy height, and leaf area index during SMEX02 using aircraft and Landsat imagery. *Remote Sensing of Environment*, *92*(4), 447–464. https://doi.org/10.1016/j.rse.2004.03.019

Annear, R. L., & Wells, S. A. (2007). A comparison of five models for estimating clear-sky solar radiation. *Water Resources Research*, *43*(10). https://doi.org/10.1029/2006WR005055

Ball, J. T., Woodrow, I. E., & Berry, J. A. (1987). A Model Predicting Stomatal Conductance and its Contribution to the Control of Photosynthesis under Different Environmental Conditions. In *Progress in Photosynthesis Research* (Vol. IV, pp. 221–224). Dordrecht: Springer Netherlands. https://doi.org/10.1007/978-94-017-0519-6_48

Bastiaanssen, W. G. M. G. M., Menenti, M., Feddes, R. A., Holtslag, A. A. M., Pelgrum, H., Wang, J., … Van Der Wal, T. (1998). A remote sensing surface energy balance algorithm for land (SEBAL): 2. Validation. *Journal of Hydrology*, *212–213*(1–4), 213–229. https://doi.org/10.1016/S0022-1694(98)00254-6

Bastiaanssen, W. G. M., Menenti, M., Feddes, R. A., & Holtslag, A. A. M. (1998). A remote sensing surface energy balance algorithm for land (SEBAL). 1. Formulation. *Journal of Hydrology*, *212–213*(1–4), 198–212. https://doi.org/10.1016/S0022-1694(98)00253-4

Bastiaanssen, W. G. M., Noordman, E. J. M., Pelgrum, H., Davids, G., Thoreson, B. P., & Allen, R. G. (2005). SEBAL model with remotely sensed data to improve water-resources management under actual field conditions. *Journal of Irrigation and Drainage Engineering*, *131*(1), 85–93. https://doi.org/10.1061/(ASCE)0733-9437(2005)131:1(85)

Bian, Z., Cao, B., Li, H., Du, Y., Lagouarde, J. P., Xiao, Q., & Liu, Q. (2018). An analytical four-component directional brightness temperature model for crop and forest canopies. *Remote Sensing of Environment*, *209*(March), 731–746. https://doi.org/10.1016/j.rse.2018.03.010

Bian, Z., Du, Y., Li, H., Cao, B., Huang, H., Xiao, Q., & Liu, Q. (2017). Modeling the Temporal Variability of Thermal Emissions from Row-Planted Scenes Using a Radiosity and Energy Budget Method. *IEEE Transactions on Geoscience and Remote Sensing*, *55*(10), 6010–6026. https://doi.org/10.1109/TGRS.2017.2719098

Bian, Z., Roujean, J. L., Lagouarde, J. P., Cao, B., Li, H., Du, Y., … Liu, Q. (2020). A semi-empirical approach for modeling the vegetation thermal infrared directional anisotropy of canopies based on using vegetation indices. *ISPRS Journal of Photogrammetry and Remote Sensing*, *160*(March 2019), 136–148. https://doi.org/10.1016/j.isprsjprs.2019.12.004

Bian, Z., Xiao, Q., Cao, B., Du, Y., Li, H., Wang, H., … Liu, Q. Q. (2016). Retrieval of Leaf, Sunlit Soil, and Shaded Soil Component Temperatures Using Airborne Thermal Infrared Multiangle Observations. *IEEE Transactions on Geoscience and Remote Sensing*, *54*(8), 4660–4671. https://doi.org/10.1109/TGRS.2016.2547961

Bird, R. E., & Hulstrom, R. L. (1981). A Simplified Clear Sky Model for Direct and Diffuse Insolation on Horizontal Surfaces. *National Renewable Energy Laboratory*.

Boulet, G., Mougenot, B., Lhomme, J. P., Fanise, P., Lili-Chabaane, Z., Olioso, A., … Lagouarde, J. P. (2015). The SPARSE model for the prediction of water stress and evapotranspiration components from thermal infra-red data and its evaluation over irrigated and rainfed wheat. *Hydrology and Earth System Sciences*, *19*(11), 4653–4672. https://doi.org/10.5194/hess-19-4653-2015

Boulet, G., Olioso, A., Ceschia, E., Marloie, O., Coudert, B., Rivalland, V., … Chehbouni, G. (2012). An empirical expression to relate aerodynamic and surface temperatures for use within single-source energy balance models. *Agricultural and Forest Meteorology*, *161*, 148–155. https://doi.org/10.1016/j.agrformet.2012.03.008

Boulet, Gilles, Delogu, E., Saadi, S., Chebbi, W., Olioso, A., Mougenot, B., … Lagouarde, J. P. (2018). Evapotranspiration and evaporation/transpiration partitioning with dual source energy balance models in agricultural lands. In *Proceedings of the International Association of Hydrological Sciences* (Vol. 380, pp. 17–22). https://doi.org/10.5194/piahs-380-17-2018

Boulet, Gilles, Mwangi, S., Olioso, A., Dantec, V. Le, Merlin, O., Malick, K., … Rafi, Z. (2022). Advantages and opportunities in using multisensor remote sensing data for evapotranspiration retrieval as well as better partitioning between evaporation and transpiration. In *IAHS-AISH Scientific Assembly 2022* (p. 194). Montpellier, France. https://doi.org/10.5194/iahs2022-194

Bowen, I. S. (1926). The Ratio of Heat Losses by Conduction and by Evaporation from any Water Surface. *Phys. Rev.*, *27*(6), 779–787. https://doi.org/10.1103/PhysRev.27.779

Braud, I., Dantas-Antonino, A. C. C., Vauclin, M., Thony, J. L. L., & Ruelle, P. (1995). A simple soil-plant-atmosphere transfer model (SiSPAT) development and field verification. *Journal of Hydrology*, *166*(3–4), 213–250. https://doi.org/10.1016/0022-1694(94)05085-C

Brutsaert, W. (1975). On a derivable formula for long-wave radiation from clear skies. *Water Resources Research*, *11*(5), 742–744. https://doi.org/10.1029/WR011i005p00742

Brutsaert, W. (1982). *Evaporation into the Atmosphere*. *Environmental Fluid Mechanics*. Dordrecht: Springer Netherlands. https://doi.org/10.1007/978-94-017-1497-6

Brutsaert, W. (1999). Aspects of Bulk Atmosph Eric Bou N Dary Layer Free-Convective. *Reviews of Geophysics*, *37*(4), 439–451.

Businger, J. A., Wyngaard, J. C., Izumi, Y., & Bradley, E. F. (1971). Flux-Profile Relationships in the Atmospheric Surface Layer. *Journal of the Atmospheric Sciences*, *28*(2), 181–189. https://doi.org/10.1175/1520-0469(1971)028<0181:FPRITA>2.0.CO;2

Campbell, G. S., & Norman, J. M. (1998a). Radiation Fluxes in Natural Environments. In *An Introduction to Environmental Biophysics* (pp. 167–184). New York, NY: Springer New York. https://doi.org/10.1007/978-1-4612-1626-1_11

Campbell, G. S., & Norman, J. M. (1998b). The Light Environment of Plant Canopies. In *An Introduction to Environmental Biophysics* (pp. 247–278). New York, NY: Springer New York. https://doi.org/10.1007/978-1-4612-1626-1_15

Cao, B., Guo, M., Fan, W., Xu, X., Peng, J., Ren, H., … Liu, Q. (2018). A new directional canopy emissivity model based on spectral invariants. *IEEE Transactions on Geoscience and Remote Sensing*, *56*(12), 6911–6926. https://doi.org/10.1109/TGRS.2018.2845678

Cao, B., Liu, Q., Du, Y., Roujean, J. L., Gastellu-Etchegorry, J. P., Trigo, I. F., … Xiao, Q. (2019). A review of earth surface thermal radiation directionality observing and modeling: Historical development, current status and perspectives. *Remote Sensing of Environment*, *232*(October 2018), 111304. https://doi.org/10.1016/j.rse.2019.111304

Carlson, T. (2007). An Overview of the "Triangle Method" for Estimating Surface Evapotranspiration and Soil Moisture from Satellite Imagery. *Sensors*, *7*(8), 1612–1629. https://doi.org/10.3390/s7081612

Carlson, T. N., Taconet, O., Vidal, A., Gillies, R. R., Olioso, A., & Humes, K. (1995). An overview of the workshop on thermal remote sensing held at La Londe les Maures, France, September 20–24, 1993. *Remote Sensing Reviews*, *12*(3–4), 147–158. https://doi.org/10.1080/02757259509532283

Carrer, D., Geiger, B., Roujean, J. L., Hautecoeur, O., Meurey, C., & Franchistéguy, L. (2008). Land surface albedo and down-welling short-wave radiation retrievals using high frequency observations from msg geostationary satellite. *International Geoscience and Remote Sensing Symposium (IGARSS)*, *5*(1), 487–490. https://doi.org/10.1109/IGARSS.2008.4780135

Carrer, D., Roujean, J. L., Lafont, S., Calvet, J. C., Boone, A., Decharme, B., … Gastellu-Etchegorry, J. P. (2013). A canopy radiative transfer scheme with explicit FAPAR for the interactive vegetation model ISBA-A-gs: Impact on carbon fluxes. *Journal of Geophysical Research: Biogeosciences*, *118*(2), 888–903. https://doi.org/10.1002/jgrg.20070

Cellier, P., & Olioso, A. (1993). A simple system for automated long-term Bowen ratio measurement. *Agricultural and Forest Meteorology*, *66*(1–2), 81–92. https://doi.org/10.1016/0168-1923(93)90083-T

Chebbi, W., Boulet, G., Le Dantec, V., Lili Chabaane, Z., Fanise, P., Mougenot, B., & Ayari, H. (2018). Analysis of evapotranspiration components of a rainfed olive orchard during three contrasting years in a semi-arid climate. *Agricultural and Forest Meteorology*, *256–257*(January), 159–178. https://doi.org/10.1016/j.agrformet.2018.02.020

Chen, J. M., & Black, T. A. (1991). Measuring leaf area index on plant canopies with brach arquitecture. *Agricultural and Forest Meteorology*, *57*(1–3), 1–12. https://doi.org/10.1016/0168-1923(91)90074-Z

Chen, J. M., Menges, C. H., & Leblanc, S. G. (2005). Global mapping of foliage clumping index using multi-angular satellite data. *Remote Sensing of Environment*, *97*(4), 447–457. https://doi.org/10.1016/j.rse.2005.05.003

Chen, Jing M. (1996). Optically-based methods for measuring seasonal variation of leaf area index in boreal conifer stands. *Agricultural and Forest Meteorology*, *80*(2–4), 135–163. https://doi.org/10.1016/0168-1923(95)02291-0

Chen, Jing M., & Liu, J. (2020). Evolution of evapotranspiration models using thermal and shortwave remote sensing data. *Remote Sensing of Environment*, *237*(November 2019), 111594. https://doi.org/10.1016/j.rse.2019.111594

Chen, Y., Zhan, W., Quan, J., Zhou, J., Zhu, X., & Sun, H. (2014). Disaggregation of Remotely Sensed Land Surface Temperature: A Generalized Paradigm. *IEEE Transactions on Geoscience and Remote Sensing*, *52*(9), 5952–5965. https://doi.org/10.1109/TGRS.2013.2294031

Colaizzi, P. D., Evett, S. R., Agam, N., Schwartz, R. C., & Kustas, W. P. (2016). Soil heat flux calculation for sunlit and shaded surfaces under row crops: 1. Model development and sensitivity analysis. *Agricultural and Forest Meteorology*, *216*, 115–128. https://doi.org/10.1016/j.agrformet.2015.10.010

Colaizzi, P. D., Kustas, W. P., Anderson, M. C., Agam, N., Tolk, J. A., Evett, S. R., … O'Shaughnessy, S. A. (2012). Two-source energy balance model estimates of evapotranspiration using component and composite surface temperatures. *Advances in Water Resources*, *50*, 134–151. https://doi.org/10.1016/j.advwatres.2012.06.004

Collatz, G. J., Ball, J. T., Grivet, C., & Berry, J. A. (1991). Physiological and environmental regulation of stomatal conductance, photosynthesis and transpiration: a model that includes a laminar boundary layer. *Agricultural and Forest Meteorology*, *54*(2–4), 107–136. https://doi.org/10.1016/0168-1923(91)90002-8

de Vries, D. A. (1963). Thermal Properties of Soils. *Physics of Plant Environment*, 210–235.

Delogu, E, Boulet, G., Olioso, A., Coudert, B., Chirouze, J., Ceschia, E., … Lagouarde, J. P. (2012). Reconstruction of temporal variations of evapotranspiration using instantaneous estimates at the time of satellite overpass. *Hydrology and Earth System Sciences*, *16*(8), 2995–3010. https://doi.org/10.5194/hess-16-2995-2012

Delogu, Emilie, Boulet, G., Olioso, A., Garrigues, S., Brut, A., Tallec, T., … Lagouarde, J. P. (2018). Evaluation of the SPARSE dual-source model for predictingwater stress and evapotranspiration from thermal infrared data over multiple crops and climates. *Remote Sensing*, *10*(11). https://doi.org/10.3390/rs10111806

Delogu, Emilie, Olioso, A., Alliès, A., Demarty, J., & Boulet, G. (2021). Evaluation of Multiple Methods for the Production of Continuous Evapotranspiration Estimates from TIR Remote Sensing. *Remote Sensing*, *13*(6), 1086. https://doi.org/10.3390/rs13061086

Dong, Y., McCartney, J. S., & Lu, N. (2015). Critical Review of Thermal Conductivity Models for Unsaturated Soils. *Geotechnical and Geological Engineering*, *33*(2), 207–221. https://doi.org/10.1007/s10706-015-9843-2

Duchemin, B., Hadria, R., Erraki, S., Boulet, G., Maisongrande, P., Chehbouni, A., … Simonneaux, V. (2006). Monitoring wheat phenology and irrigation in Central Morocco: On the use of relationships between evapotranspiration, crops coefficients, leaf area index and remotely-sensed vegetation indices. *Agricultural Water Management*, *79*(1), 1–27. https://doi.org/10.1016/j.agwat.2005.02.013

Duffour, C., Lagouarde, J. P., Olioso, A., Demarty, J., & Roujean, J. L. (2016). Driving factors of the directional variability of thermal infrared signal in temperate regions. *Remote Sensing of Environment*, *177*, 248–264. https://doi.org/10.1016/j.rse.2016.02.024

Duffour, C., Lagouarde, J. P., & Roujean, J. L. (2016). A two parameter model to simulate thermal infrared directional effects for remote sensing applications. *Remote Sensing of Environment*, *186*, 250–261. https://doi.org/10.1016/j.rse.2016.08.012

Duffour, C., Olioso, A., Demarty, J., Van der Tol, C., & Lagouarde, J. P. (2015). An evaluation of SCOPE: A tool to simulate the directional anisotropy of satellite-measured surface temperatures. *Remote Sensing of Environment*, *158*, 362–375. https://doi.org/10.1016/j.rse.2014.10.019

Dufresne, J.-L. (2008). The measurement of the solar constant by Claude Pouillet. *La Meteorologie*, (60), 36–43. Retrieved from https://hal.archives-ouvertes.fr/hal-00423480/document

Duursma, R. A., & Medlyn, B. E. (2012). MAESPA: a model to study interactions between water limitation, environmental drivers and vegetation function at tree and stand levels, with an example application to [CO₂] × drought interactions. *Geoscientific Model Development*, *5*(4), 919–940. https://doi.org/10.5194/gmd-5-919-2012

Er-Raki, S., Chehbouni, A., Ezzahar, J., Khabba, S., Boulet, G., Hanich, L., & Williams, D. (2009). Evapotranspiration partitioning from sap flow and eddy covariance techniques for olive orchards in semi-arid region. *Acta Horticulturae*, *846*, 201–208. https://doi.org/10.17660/ActaHortic.2009.846.21

Erbs, D. G., Klein, S. A., & Duffie, J. A. (1982). Estimation of the diffuse radiation fraction for hourly, daily and monthly-average global radiation. *Solar Energy*, *28*(4), 293–302. https://doi.org/10.1016/0038-092X(82)90302-4

Fernández, J., Escayo, J., Hu, Z., Camacho, A. G., Samsonov, S. V., Prieto, J. F., … Ancochea, E. (2021). Detection of volcanic unrest onset in La Palma, Canary Islands, evolution and implications. *Scientific Reports*, *11*(1), 1–15. https://doi.org/10.1038/s41598-021-82292-3

Foken, T. (2006, June 20). 50 years of the Monin-Obukhov similarity theory. *Boundary-Layer Meteorology*. https://doi.org/10.1007/s10546-006-9048-6

Foken, T. (2008). THE ENERGY BALANCE CLOSURE PROBLEM: AN OVERVIEW. *Ecological Applications*, *18*(6), 1351–1367. https://doi.org/10.1890/06-0922.1

François, C. (2002). The potential of directional radiometric temperatures for monitoring soil and leaf temperature and soil moisture status. *Remote Sensing of Environment*, *80*(1), 122–133. https://doi.org/10.1016/S0034-4257(01)00293-0

Francois, C., Ottle, C., & Prevot, L. (1997). Analytical parameterization of canopy directional emissivity and directional radiance in the thermal infrared. Application on the retrieval of soil and foliage temperatures using two directional measurements. *International Journal of Remote Sensing*, *18*(12), 2587–2621. https://doi.org/10.1080/014311697217495

Friedl, M. A. (2002). Forward and inverse modeling of land surface energy balance using surface temperature measurements. *Remote Sensing of Environment*, *79*(2–3), 344–354. https://doi.org/10.1016/S0034-4257(01)00284-X

Gallego-Elvira, B., Olioso, A., Mira, M., Castillo, S. R.-, Boulet, G., Marloie, O., … Boutron, O. (2013). EVASPA (EVapotranspiration Assessment from SPAce) Tool: An overview. *Procedia Environmental Sciences*, *19*, 303–310. https://doi.org/10.1016/j.proenv.2013.06.035

Gao, B. (1996). NDWI—A normalized difference water index for remote sensing of vegetation

liquid water from space. *Remote Sensing of Environment*, *58*(3), 257–266. https://doi.org/10.1016/S0034-4257(96)00067-3

Gastellu-Etchegorry, J. (1996). Modeling radiative transfer in heterogeneous 3-D vegetation canopies. *Remote Sensing of Environment*, *58*(2), 131–156. https://doi.org/10.1016/0034-4257(95)00253-7

Geiger, B., Meurey, C., Lajas, D., Franchistéguy, L., Carrer, D., & Roujean, J.-L. (2008). Near real-time provision of downwelling shortwave radiation estimates derived from satellite observations. *Meteorological Applications*, *15*(3), 411–420. https://doi.org/10.1002/met.84

Goward, S. N., Cruickshanks, G. D., & Hope, A. S. (1985). Observed relation between thermal emission and reflected spectral radiance of a complex vegetated landscape. *Remote Sensing of Environment*, *18*(2), 137–146. https://doi.org/10.1016/0034-4257(85)90044-6

Guillevic, P. C., Bork-Unkelbach, A., Gottsche, F. M., Hulley, G., Gastellu-Etchegorry, J.-P., Olesen, F. S., & Privette, J. L. (2013). Directional Viewing Effects on Satellite Land Surface Temperature Products Over Sparse Vegetation Canopies—A Multisensor Analysis. *IEEE Geoscience and Remote Sensing Letters*, *10*(6), 1464–1468. https://doi.org/10.1109/LGRS.2013.2260319

Hapke, B. (1981). Bidirectional reflectance spectroscopy. *Icarus*, *195*(2), 918–926. https://doi.org/10.1016/j.icarus.2008.01.003

Herrero, J., & Polo, M. J. (2012). Parameterization of atmospheric longwave emissivity in a mountainous site for all sky conditions. *Hydrology and Earth System Sciences*, *16*(9), 3139–3147. https://doi.org/10.5194/hess-16-3139-2012

Hoedjes, J. C.B., Chehbouni, A., Jacob, F., Ezzahar, J., & Boulet, G. (2008). Deriving daily evapotranspiration from remotely sensed instantaneous evaporative fraction over olive orchard in semi-arid Morocco. *Journal of Hydrology*, *354*(1–4), 53–64. https://doi.org/10.1016/j.jhydrol.2008.02.016

Hoedjes, Joost C.B., Chehbouni, A., Ezzahar, J., Escadafal, R., & De Bruin, H. A. R. (2007). Comparison of large aperture scintillometer and eddy covariance measurements: Can thermal infrared data be used to capture footprint-induced differences? *Journal of Hydrometeorology*, *8*(2), 144–159. https://doi.org/10.1175/JHM561.1

Huxman, T. E., Wilcox, B. P., Breshears, D. D., Scott, R. L., Snyder, K. A., Small, E. E., … Jackson, R. B. (2005). Ecohydrological implications of woody plant encroachment. *Ecology*, *86*(2), 308–319. https://doi.org/10.1890/03-0583

Idso, S. B. (1981). A set of equations for full spectrum and 8- to 14-μm and 10.5- to 12.5-μm thermal radiation from cloudless skies. *Water Resources Research*, *17*(2), 295–304. https://doi.org/10.1029/WR017i002p00295

Iqbal, M. (1983). *An Introduction to Solar Radiation*. New York: Academic Press.

Jacquemoud, S., & Baret, F. (1990). PROSPECT : A Model of Leaf Optical Properties Spectra, *91*, 75–91.

Jammer, M. (1989). The History of Modern Physics. In *The Conceptual Development of Quantum Mechanics* (2nd ed., p. 13). American Institute of Physics / Tomash Publishers.

Jarvis, P. G. (1976). The interpretation of the variations in leaf water potential and stomatal conductance found in canopies in the field. *Philosophical Transactions of the Royal Society of London. B, Biological Sciences*, *273*(927), 593–610. https://doi.org/10.1098/rstb.1976.0035

Jiang, Y., Tang, R., & Li, Z.-L. (2022). A framework of correcting the angular effect of land surface temperature on evapotranspiration estimation in single-source energy balance models. *Remote Sensing of Environment*, *283*, 113306. https://doi.org/https://doi.org/10.1016/j.rse.2022.113306

Kerr, Y. H., Waldteufel, P., Wigneron, J. P., Martinuzzi, J. M., Font, J., & Berger, M. (2001). Soil moisture retrieval from space: The Soil Moisture and Ocean Salinity (SMOS) mission. *IEEE Transactions on Geoscience and Remote Sensing*, *39*(8), 1729–1735. https://doi.org/10.1109/36.942551

Kimes, D. S., & Kirchner, J. A. (1983). Directional radiometric measurements of row-crop temperatures. *International Journal of Remote Sensing*, *4*(2), 299–311. https://doi.org/10.1080/01431168308948548

Kustas, W. P., & Norman, J. M. (1996). Use of remote sensing for evapotranspiration monitoring over land surfaces. *Hydrological Sciences Journal*, *41*(4), 495–516. https://doi.org/10.1080/02626669609491522

Kuusk, A. (1991). The Hot Spot Effect in Plant Canopy Reflectance. In *Photon-Vegetation Interactions* (pp. 139–159). Berlin, Heidelberg: Springer Berlin Heidelberg. https://doi.org/10.1007/978-3-642-75389-3_5

Kuusk, Andres. (1985). The hot-spot effect of a uniform vegetative cover. *Soviet Journal of Remote Sensing*, (January). Retrieved from http://refhub.elsevier.com/S0034-4257(18)30103-2/rf0115

Lagouarde, J.-P., Bhattacharya, B. K., Crébassol, P., Gamet, P., Adlakha, D., Murthy, C. S., … Sarkar, S. S. (2019). Indo-French High-Resolution Thermal Infrared Space Mission for Earth Natural Resources Assessment and Monitoring – Concept and Definition of Trishna. *ISPRS - International Archives of the Photogrammetry, Remote Sensing and Spatial Information Sciences*, *XLII-3/W6*(February), 403–407. https://doi.org/10.5194/isprs-archives-xlii-3-w6-403-2019

Lagouarde, J., & Bhattacharya, B. K. (2018). TRISHNA : a new high spatio-temporal resolution Indian-French mission in the thermal infrared. In *Remote Sensing and Hydrology Symposium (ICRS-IAHS)* (p. 2024).

Lagouarde, J. P., & Irvine, M. (2008). Directional anisotropy in thermal infrared measurements over Toulouse city centre during the CAPITOUL measurement campaigns: First results. *Meteorology and Atmospheric Physics*, *102*(3–4), 173–185. https://doi.org/10.1007/s00703-008-0325-4

Lagouarde, Jean Pierre, Bach, M., Sobrino, J. A., Boulet, G., Briottet, X., Cherchali, S., … Fargant, G. (2013). The MISTIGRI thermal infrared project: Scientific objectives and mission specifications. *International Journal of Remote Sensing*, *34*(9–10), 3437–3466. https://doi.org/10.1080/01431161.2012.716921

Lagouarde, Jean Pierre, & Boulet, G. (2016). Energy balance of continental surfaces and the use of surface temperature. In *Land Surface Remote Sensing in Continental Hydrology* (pp. 323–361). https://doi.org/10.1016/B978-1-78548-104-8.50010-3

Lagouarde, Jean Pierre, Dayau, S., Moreau, P., & Guyon, D. (2014). Directional anisotropy of brightness surface temperature over vineyards: Case study over the Medoc Region (SW France). *IEEE Geoscience and Remote Sensing Letters*, *11*(2), 574–578. https://doi.org/10.1109/LGRS.2013.2282492

Li, J., Fan, W., Liu, Y., Zhu, G., Peng, J., & Xu, X. (2017). Estimating savanna clumping index using hemispherical photographs integrated with high resolution remote sensing images.

Remote Sensing, *9*(1). https://doi.org/10.3390/rs9010052

Liebethal, C., Huwe, B., & Foken, T. (2005). Sensitivity analysis for two ground heat flux calculation approaches. *Agricultural and Forest Meteorology*, *132*(3–4), 253–262. https://doi.org/10.1016/j.agrformet.2005.08.001

Long, D., & Singh, V. P. (2012). A Two-source Trapezoid Model for Evapotranspiration (TTME) from satellite imagery. *Remote Sensing of Environment*, *121*, 370–388. https://doi.org/10.1016/j.rse.2012.02.015

Luquet, D., Bégué, A., Vidal, A., Clouvel, P., Dauzat, J., Olioso, A., … Tao, Y. (2003). Using multidirectional thermography to characterize water status of cotton. *Remote Sensing of Environment*, *84*(3), 411–421. https://doi.org/10.1016/S0034-4257(02)00131-1

Luquet, D., Vidal, A., Dauzat, J., Bégué, A., Olioso, A., & Clouvel, P. (2004). Using directional TIR measurements and 3D simulations to assess the limitations and opportunities of water stress indices. *Remote Sensing of Environment*, *90*(1), 53–62. https://doi.org/10.1016/j.rse.2003.09.008

Lv, S., Simmer, C., Zeng, Y., Wen, J., & Su, Z. (2022). The Simulation of L-Band Microwave Emission of Frozen Soil during the Thawing Period with the Community Microwave Emission Model (CMEM). *Journal of Remote Sensing*, *2022*, 9754341. https://doi.org/10.34133/2022/9754341

Mallick, K., Jarvis, A. J., Boegh, E., Fisher, J. B., Drewry, D. T., Tu, K. P., … Niyogi, D. (2014). A Surface Temperature Initiated Closure (STIC) for surface energy balance fluxes. *Remote Sensing of Environment*, *141*, 243–261. https://doi.org/10.1016/j.rse.2013.10.022

Mallick, K., Trebs, I., Boegh, E., Giustarini, L., Schlerf, M., Drewry, D. T., … Wofsy, S. C. (2016). Canopy-scale biophysical controls of transpiration and evaporation in the Amazon Basin. *Hydrology and Earth System Sciences*, *20*(10), 4237–4264. https://doi.org/10.5194/hess-20-4237-2016

Masson, V., Champeaux, J. L., Chauvin, F., Meriguet, C., & Lacaze, R. (2003). A global database of land surface parameters at 1-km resolution in meteorological and climate models. *Journal of Climate*, *16*(9), 1261–1282. https://doi.org/10.1175/1520-0442-16.9.1261

Matsushima, D. (2005). Relations between aerodynamic parameters of heat transfer and thermal-infrared thermometry in the bulk surface formulation. *Journal of the Meteorological Society of Japan*, *83*(3), 373–389. https://doi.org/10.2151/jmsj.83.373

Mattar, C., Franch, B., Sobrino, J. A. A., Corbari, C., Jiménez-Muñoz, J. C. C., Olivera-Guerra, L., … Mancini, M. (2014). Impacts of the broadband albedo on actual evapotranspiration estimated by S-SEBI model over an agricultural area. *Remote Sensing of Environment*, *147*, 23–42. https://doi.org/10.1016/j.rse.2014.02.011

McElrone, A. J., Shapland, T. M., Calderon, A., Fitzmaurice, L., Paw U, K. T., & Snyder, R. L. (2013). Surface Renewal: An Advanced Micrometeorological Method for Measuring and Processing Field-Scale Energy Flux Density Data. *Journal of Visualized Experiments*, (82). https://doi.org/10.3791/50666

McFeeters, S. K. (1996). The use of the Normalized Difference Water Index (NDWI) in the delineation of open water features. *International Journal of Remote Sensing*, *17*(7), 1425–1432. https://doi.org/10.1080/01431169608948714

Medlyn, B. E., Duursma, R. A., Eamus, D., Ellsworth, D. S., Prentice, I. C., Barton, C. V. M.,

… Wingate, L. (2011). Reconciling the optimal and empirical approaches to modelling stomatal conductance. *Global Change Biology*, *17*(6), 2134–2144. https://doi.org/10.1111/j.1365-2486.2010.02375.x

Menenti, M., Bastiaanssen, W., van Eick, D., & Abd el Karim, M. A. (1989). Linear relationships between surface reflectance and temperature and their application to map actual evaporation of groundwater. *Advances in Space Research*, *9*(1), 165–176. https://doi.org/10.1016/0273-1177(89)90482-1

Merlin, O., Al Bitar, A., Rivalland, V., Béziat, P., Ceschia, E., & Dedieu, G. (2011). An analytical model of evaporation efficiency for unsaturated soil surfaces with an arbitrary thickness. *Journal of Applied Meteorology and Climatology*, *50*(2), 457–471. https://doi.org/10.1175/2010JAMC2418.1

Moran, M. S., Clarke, T. R., Inoue, Y., & Vidal, A. (1994). Estimating crop water deficit using the relation between surface-air temperature and spectral vegetation index. *Remote Sensing of Environment*, *49*(3), 246–263. https://doi.org/10.1016/0034-4257(94)90020-5

Mwangi, S., Boulet, G., & Olioso, A. (2022). Assessment of an extended SPARSE model for estimating evapotranspiration from directional thermal infrared data. *Agricultural and Forest Meteorology*, *317*(February), 108882. https://doi.org/10.1016/j.agrformet.2022.108882

Nicodemus, F. E., Richmond, J. C., Hsia, J. J., Ginsberg, I. W., & Limperis, T. (1977). Geometrical Considerations and Nomenclature for Reflectance. *Natl Bur Stand (US) Monogr*, *11*(160), 1–52. Retrieved from https://graphics.stanford.edu/courses/cs448-05-winter/papers/nicodemus-brdf-nist.pdf

Nieto, H., Guzinsk, R., Sandholt, I., Karamitilios, G., Olander Rasmusse, M., Bellver, J., … Koetz, B. (2020). *USER MANUAL FOR SEN-ET SNAP PLUGIN*. Retrieved from https://web.archive.org/web/20220615173735/https://www.esa-sen4et.org/static/media/sen-et-user-manual-v1.1.0.5d1ac526.pdf

Nilson, T. (1971). A theoretical analysis of the frequency of gaps in plant stands. *Agricultural Meteorology*, *8*(1966), 25–38. https://doi.org/10.1016/0002-1571(71)90092-6

Niu, Z., Wang, C., Wang, W., Zhang, Q., & Young, S. S. (2001). Estimating bidirectional angles in NOAA AVHRR images. *International Journal of Remote Sensing*, *22*(8), 1609–1615. https://doi.org/10.1080/01431160119571

Njoku, E. G., & Entekhabi, D. (1996). Passive microwave remote sensing of soil moisture. *Journal of Hydrology*, *184*(1–2), 101–129. https://doi.org/10.1016/0022-1694(95)02970-2

Noilhan, J., & Planton, S. (1989). A Simple Parameterization of Land Surface Processes for Meteorological Models. *Monthly Weather Review*, *117*(3), 536–549. https://doi.org/10.1175/1520-0493(1989)117<0536:ASPOLS>2.0.CO;2

Norman, J. M., Kustas, W. P., & Humes, K. S. (1995). Source approach for estimating soil and vegetation energy fluxes in observations of directional radiometric surface temperature. *Agricultural and Forest Meteorology*, *77*(3–4), 263–293. https://doi.org/10.1016/0168-1923(95)02265-Y

Norman, John M., & Becker, F. (1995). Terminology in thermal infrared remote sensing of natural surfaces. *Agricultural and Forest Meteorology*, *77*(3–4), 153–166. https://doi.org/10.1016/0168-1923(95)02259-Z

Olioso, A, Carrière, S., Allies, A., Sobrino, J., Skokovic, D., Demarty, J., … Weiss, M. (2022).

Evapotranspiration mapping from remote sensing data: uncertainties and ensemble estimates based on multimodel-multidata simulations. In *INTERNATIONAL SYMPOSIUM: RECENT ADVANCES IN QUANTITATIVE REMOTE SENSING (RAQRS VI)* (pp. 78–79). Torrent (Valencia) SPAIN.

Olioso, Albert. (1995). Estimating the difference between brightness and surface temperatures for a vegetal canopy. *Agricultural and Forest Meteorology*, *72*(3–4), 237–242. https://doi.org/10.1016/0168-1923(94)02163-E

Olioso, Albert, Braud, I., Chanzy, A., Courault, D., Demarty, J., Kergoat, L., … Wigneron, J. P. (2002). SVAT modeling over the Alpilles-ReSeDA experiment: Comparing SVAT models over wheat fields. *Agronomie*, *22*(6), 651–668. https://doi.org/10.1051/agro:2002054

Olioso, Albert, Carlson, T. N., & Brisson, N. (1996). Simulation of diurnal transpiration and photosynthesis of a water stressed soybean crop. *Agricultural and Forest Meteorology*, *81*(1–2), 41–59. https://doi.org/10.1016/0168-1923(95)02297-X

Olioso, Albert, Carrière, S., Gamet, P., Delogu, E., Weiss, M., Guillevic, P., & Boulet, G. (2022). Improving continuous monitoring of evapotranspiration with future thermal infrared missions. In *IAHS-AISH Scientific Assembly 2022* (p. 324). Montpellier, France. https://doi.org/10.5194/iahs2022-354

Olioso, Albert, Taconet, O., Mehrez, B., Nivoit, D., Promayon, F., & Rahmoune, L. (1995). Estimation of evapotranspiration using SVAT models and surface IR temperature. In *1995 International Geoscience and Remote Sensing Symposium, IGARSS '95. Quantitative Remote Sensing for Science and Applications* (Vol. 1, pp. 516–518). IEEE. https://doi.org/10.1109/IGARSS.1995.520324

Parodi, G. N. (2000). AVHRR Hydrological Analysis System. *Wres-Itc: 1, 77*.

Price, J. C. (1990). Using spatial context in satellite data to infer regional scale evapotranspiration. *IEEE Transactions on Geoscience and Remote Sensing*, *28*(5), 940–948. https://doi.org/10.1109/36.58983

Prikaziuk, E., & van der Tol, C. (2019). Global Sensitivity Analysis of the SCOPE Model in Sentinel-3 Bands: Thermal Domain Focus. *Remote Sensing*, *11*(20), 2424. https://doi.org/10.3390/rs11202424

Rautiainen, K., Lemmetyinen, J., Schwank, M., Kontu, A., Ménard, C. B., Mätzler, C., … Pulliainen, J. (2014). Detection of soil freezing from L-band passive microwave observations. *Remote Sensing of Environment*, *147*, 206–218. https://doi.org/10.1016/j.rse.2014.03.007

Roerink, G. J., Su, Z., & Menenti, M. (2000). S-SEBI: A simple remote sensing algorithm to estimate the surface energy balance. *Physics and Chemistry of the Earth, Part B: Hydrology, Oceans and Atmosphere*, *25*(2), 147–157. https://doi.org/10.1016/S1464-1909(99)00128-8

Rosa, R., & Tanny, J. (2015). Surface renewal and eddy covariance measurements of sensible and latent heat fluxes of cotton during two growing seasons. *Biosystems Engineering*, *136*, 149–161. https://doi.org/10.1016/j.biosystemseng.2015.05.012

Roujean, J.-L. (1996). A tractable physical model of shortwave radiation interception by vegetative canopies. *Journal of Geophysical Research: Atmospheres*, *101*(D5), 9523–9532. https://doi.org/10.1029/96JD00343

Roujean, J. L. (2000). A parametric hot spot model for optical remote sensing applications.

Remote Sensing of Environment, *71*(2), 197–206. https://doi.org/10.1016/S0034-4257(99)00080-2

Rouse, J. W., Haas, R. H., Schell, J. A., & Deering, D. W. (1973). Monitoring vegetation systems in the great plains with ERTS.

Santanello, J. A., & Friedl, M. A. (2003). Diurnal covariation in soil heat flux and net radiation. *Journal of Applied Meteorology*, *42*(6), 851–862. https://doi.org/10.1175/1520-0450(2003)042<0851:DCISHF>2.0.CO;2

Sauer, T. J., & Horton, R. (2015). Soil heat flux. *Micrometeorology in Agricultural Systems*, (47), 131–154. https://doi.org/10.2134/agronmonogr47.c7

Savitzky, A., & Golay, M. J. E. (1964). Smoothing and Differentiation of Data by Simplified Least Squares Procedures. *Analytical Chemistry*, *36*(8), 1627–1639. https://doi.org/10.1021/ac60214a047

Scanlon, T. M., & Kustas, W. P. (2010). Partitioning carbon dioxide and water vapor fluxes using correlation analysis. *Agricultural and Forest Meteorology*, *150*(1), 89–99. https://doi.org/10.1016/j.agrformet.2009.09.005

Scanlon, T. M., & Sahu, P. (2008). On the correlation structure of water vapor and carbon dioxide in the atmospheric surface layer: A basis for flux partitioning. *Water Resources Research*, *44*(10), 1–15. https://doi.org/10.1029/2008WR006932

Schaepman-Strub, G., Schaepman, M. E., Painter, T. H., Dangel, S., & Martonchik, J. V. (2006). Reflectance quantities in optical remote sensing-definitions and case studies. *Remote Sensing of Environment*, *103*(1), 27–42. https://doi.org/10.1016/j.rse.2006.03.002

Shuttleworth, W. J., & Gurney, R. J. (1990). The theoretical relationship between foliage temperature and canopy resistance in sparse crops. *Quarterly Journal of the Royal Meteorological Society*, *116*(492), 497–519. https://doi.org/10.1002/qj.49711649213

Shuttleworth, W. J., & Wallace, J. S. (1985). Evaporation from sparse crops-an energy combination theory. *The Quarterly Journal of the Royal Meteorological Society*, *111*(465), 839–855. https://doi.org/10.1002/qj.49711146510

Sinclair, T. R., Murphy, C. E., & Knoerr, K. R. (1976). Development and Evaluation of Simplified Models for Simulating Canopy Photosynthesis and Transpiration. *The Journal of Applied Ecology*, *13*(3), 813. https://doi.org/10.2307/2402257

Spencer, J. W. (1971). Fourier series representation of the position of the sun. *Search*, *2*(5), 172. Retrieved from http://www.mail-archive.com/sundial@uni-koeln.de/msg01050.html

Street, L. E., Shaver, G. R., Williams, M., & Van Wijk, M. T. (2007). What is the relationship between changes in canopy leaf area and changes in photosynthetic CO2 flux in arctic ecosystems? *Journal of Ecology*, *95*(1), 139–150. https://doi.org/10.1111/j.1365-2745.2006.01187.x

Su, Z. (2002). The Surface Energy Balance System (SEBS) for estimation of turbulent heat fluxes. *Hydrology and Earth System Sciences*, *6*(1), 85–100. https://doi.org/10.5194/hess-6-85-2002

Su, Zhongbo. (2005). Estimation of the Surface Energy Balance. In *Encyclopedia of Hydrological Sciences*. Chichester, UK: John Wiley & Sons, Ltd. https://doi.org/10.1002/0470848944.hsa068

Suits, G. H. (1971). The calculation of the directional reflectance of a vegetative canopy. *Remote Sensing of Environment*, *2*(C), 117–125. https://doi.org/10.1016/0034-

4257(71)90085-X

Taconet, O., Bernard, R., & Vidal-Madjar, D. (1986). Evapotranspiration over an Agricultural Region Using a Surface Flux/Temperature Model Based on NOAA-AVHRR Data. *Journal of Climate and Applied Meteorology*, *25*(3), 284–307. https://doi.org/10.1175/1520-0450(1986)025<0284:EOAARU>2.0.CO;2

Tang, R., Li, Z. L., & Tang, B. (2010). An application of the Ts-VI triangle method with enhanced edges determination for evapotranspiration estimation from MODIS data in arid and semi-arid regions: Implementation and validation. *Remote Sensing of Environment*, *114*(3), 540–551. https://doi.org/10.1016/j.rse.2009.10.012

Taylor, K. E. (2001). Summarizing multiple aspects of model performance in a single diagram. *Journal of Geophysical Research*, *106*(D7), 7183–7192. https://doi.org/10.1029/2000JD900719

Teixeira, A. H. de C., Bastiaanssen, W. G. M., & Bassoi, L. H. (2007). Crop water parameters of irrigated wine and table grapes to support water productivity analysis in the São Francisco river basin, Brazil. *Agricultural Water Management*, *94*(1–3), 31–42. https://doi.org/10.1016/j.agwat.2007.08.001

Tolpekin, V., & Stein, A. (2012). Pysics. In *The core of GIScience: a process-based approach* (ITC Educat, pp. 71–92). Enschede: University of Twente, Faculty of Geo-Information Science and Earth Observation (ITC).

Trigo, I. F., Monteiro, I. T., Olesen, F., & Kabsch, E. (2008a). An assessment of remotely sensed land surface temperature. *Journal of Geophysical Research*, *113*(D17), D17108. https://doi.org/10.1029/2008JD010035

Trigo, I. F., Monteiro, I. T., Olesen, F., & Kabsch, E. (2008b). An assessment of remotely sensed land surface temperature. *Journal of Geophysical Research*, *113*(D17), D17108. https://doi.org/10.1029/2008JD010035

van der Tol, C., Verhoef, W., Timmermans, J., Verhoef, A., & Su, Z. (2009). An integrated model of soil-canopy spectral radiances, photosynthesis, fluorescence, temperature and energy balance. *Biogeosciences*, *6*(12), 3109–3129. https://doi.org/10.5194/bg-6-3109-2009

Verhoef, W. (1984). Light scattering by leaf layers with application to canopy reflectance modeling: The SAIL model. *Remote Sensing of Environment*, *16*(2), 125–141. https://doi.org/10.1016/0034-4257(84)90057-9

Verhoef, W., Jia, L., Xiao, Q., & Su, Z. (2007). Unified optical-thermal four-stream radiative transfer theory for homogeneous vegetation canopies. *IEEE Transactions on Geoscience and Remote Sensing*, *45*(6), 1808–1822. https://doi.org/10.1109/TGRS.2007.895844

Verrelst, J., Rivera, J. P., van der Tol, C., Magnani, F., Mohammed, G., & Moreno, J. (2015a). Global sensitivity analysis of the SCOPE model: What drives simulated canopy-leaving sun-induced fluorescence? *Remote Sensing of Environment*, *166*, 8–21. https://doi.org/10.1016/j.rse.2015.06.002

Verrelst, J., Rivera, J. P., van der Tol, C., Magnani, F., Mohammed, G., & Moreno, J. (2015b). Global sensitivity analysis of the SCOPE model: What drives simulated canopy-leaving sun-induced fluorescence? *Remote Sensing of Environment*, *166*, 8–21. https://doi.org/10.1016/j.rse.2015.06.002

Vezy, R., Christina, M., Roupsard, O., Nouvellon, Y., Duursma, R., Medlyn, B., … le Maire, G. (2018). Measuring and modelling energy partitioning in canopies of varying

complexity using MAESPA model. *Agricultural and Forest Meteorology*, *253–254*(August 2017), 203–217. https://doi.org/10.1016/j.agrformet.2018.02.005

Vinnikov, K. Y., Yu, Y., Goldberg, M. D., Tarpley, D., Romanov, P., Laszlo, I., & Chen, M. (2012). Angular anisotropy of satellite observations of land surface temperature. *Geophysical Research Letters*, *39*(23), n/a-n/a. https://doi.org/10.1029/2012GL054059

Wallace, J. (1997). Evaporation and radiation interception by neighbouring plants. *Quarterly Journal of the Royal Meteorological Society*, *123*(543), 1885–1905. https://doi.org/10.1256/smsqj.54305

Wallace, J., & Verhoef, A. (2000). Modelling interactions in mixed-plant communties: light, water and carbon dioxide. In B. Marshall & J. A. Roberts (Eds.), *Leaf Development and Canopy Growth* (pp. 204–250). Sheffield Academic Press, UK.

Wang, Y., Kallel, A., Yang, X., Regaieg, O., Lauret, N., Guilleux, J., … Gastellu-Etchegorry, J.-P. (2022). DART-Lux: An unbiased and rapid Monte Carlo radiative transfer method for simulating remote sensing images. *Remote Sensing of Environment*, *274*, 112973. https://doi.org/10.1016/j.rse.2022.112973

Wigneron, J. P., Olioso, A., Calvet, J. C., & Bertuzzi, P. (1999). Estimating root zone soil moisture from surface soil moisture data and soil-vegetation-atmosphere transfer modeling. *Water Resources Research*, *35*(12), 3735–3745. https://doi.org/10.1029/1999WR900258

Williams, D. G., Cable, W., Hultine, K., Hoedjes, J. C. B., Yepez, E. A., Simonneaux, V., … Timouk, F. (2004). Evapotranspiration components determined by stable isotope, sap flow and eddy covariance techniques. *Agricultural and Forest Meteorology*, *125*(3–4), 241–258. https://doi.org/10.1016/j.agrformet.2004.04.008

Wilson, K., Goldstein, A., Falge, E., Aubinet, M., Baldocchi, D., Berbigier, P., … Verma, S. (2002). Energy balance closure at FLUXNET sites. *Agricultural and Forest Meteorology*, *113*(1–4), 223–243. https://doi.org/10.1016/S0168-1923(02)00109-0

Wohlfahrt, G., & Widmoser, P. (2013). Can an energy balance model provide additional constraints on how to close the energy imbalance? *Agricultural and Forest Meteorology*, *169*, 85–91. https://doi.org/10.1016/j.agrformet.2012.10.006

Yan, B. Y., Xu, X. R., & Fan, W. J. (2012). A unified canopy bidirectional reflectance (BRDF) model for row crops. *Science China Earth Sciences*, *55*(5), 824–836. https://doi.org/10.1007/s11430-012-4380-9

Yang, P., Prikaziuk, E., Verhoef, W., & van der Tol, C. (2021). SCOPE 2.0: a model to simulate vegetated land surface fluxes and satellite signals. *Geoscientific Model Development*, *14*(7), 4697–4712. https://doi.org/10.5194/gmd-14-4697-2021

Yang, Yongmin, Su, H., Zhang, R., Tian, J., & Li, L. (2015). An enhanced two-source evapotranspiration model for land (ETEML): Algorithm and evaluation. *Remote Sensing of Environment*, *168*, 54–65. https://doi.org/10.1016/j.rse.2015.06.020

Yang, Yuting, & Shang, S. (2013). A hybrid dual-source scheme and trapezoid framework-based evapotranspiration model (HTEM) using satellite images: Algorithm and model test. *Journal of Geophysical Research Atmospheres*, *118*(5), 2284–2300. https://doi.org/10.1002/jgrd.50259

Zhao, X., Liu, Y., Tanaka, H., & Hiyama, T. (2010). A Comparison of Flux Variance and Surface Renewal Methods With Eddy Covariance. *IEEE Journal of Selected Topics in Applied Earth Observations and Remote Sensing*, *3*(3), 345–350.

https://doi.org/10.1109/JSTARS.2010.2060473

Zheng, D., Van Der Velde, R., Su, Z., Booij, M. J., & Hoekstra, A. Y. (2014). Assessment of roughness length schemes implemented within the noah land surface model for high-altitude regions. *Journal of Hydrometeorology*, *15*(3), 921–937. https://doi.org/10.1175/JHM-D-13-0102.1

Zreda, M., Desilets, D., Ferré, T. P. A., & Scott, R. L. (2008). Measuring soil moisture content non-invasively at intermediate spatial scale using cosmic-ray neutrons. *Geophysical Research Letters*, *35*(21), 1–5. https://doi.org/10.1029/2008GL035655

Annexure

A1. Comparison with Sentinel for evapotranspiration (SenET)

The SenET programme (Nieto et al., 2020) has already been described earlier (section 2.2.2.2). Here, a brief comparison between SenET (pyTSEB) and SPARSE estimates was performed. First, the inputs and estimates for Verdu co-ordinates were extracted from the SenET data (see Figure 23 for the SenET meteorological input variables at the site). The evapotranspiration estimates were then compared to the SPARSE estimates over the experimental period. Other than select deviations, the average trend is similar between the in-situ driven and the SenET estimates. This is expected given the relative equivalence of the meteorological [and other variable] inputs as depicted in Figure 23. The SEB algorithms were also separately run using the extracted SenET input data where relatively similar magnitudes of the models' evapotranspiration estimates are observed (Figure 26 c). In this case, the comparable trends can be attributed to similar modeling framework between the TSEB and SPARSE schemes.

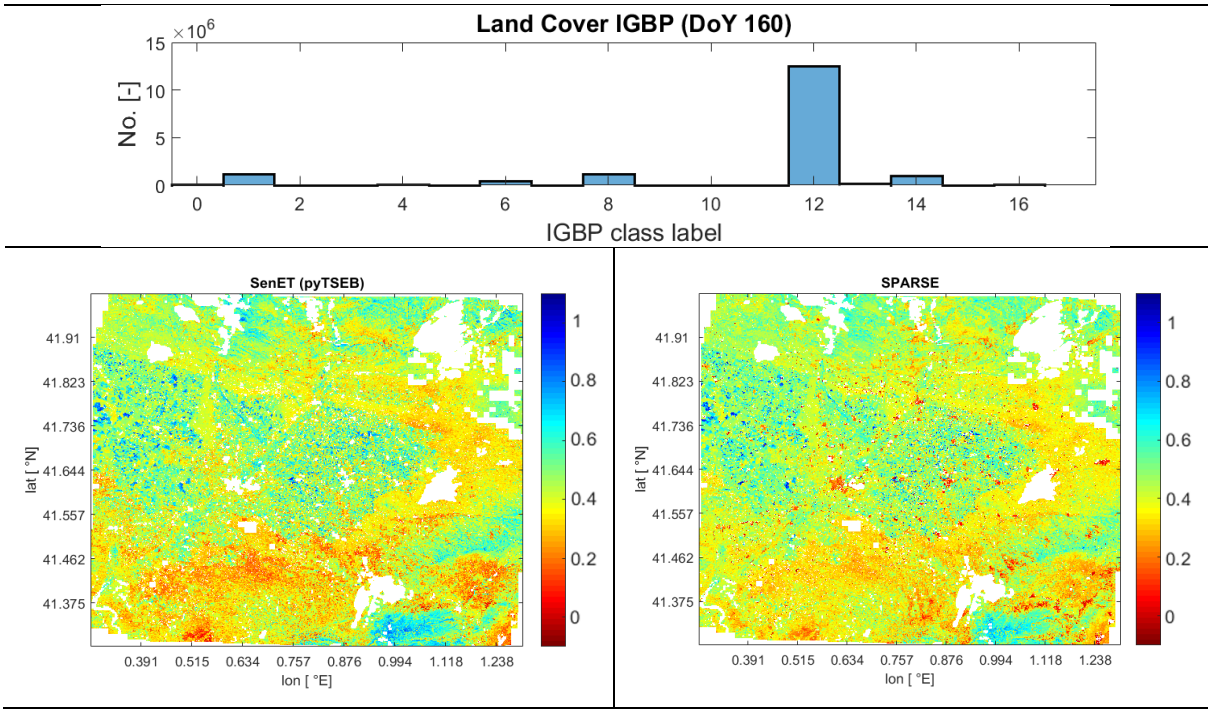

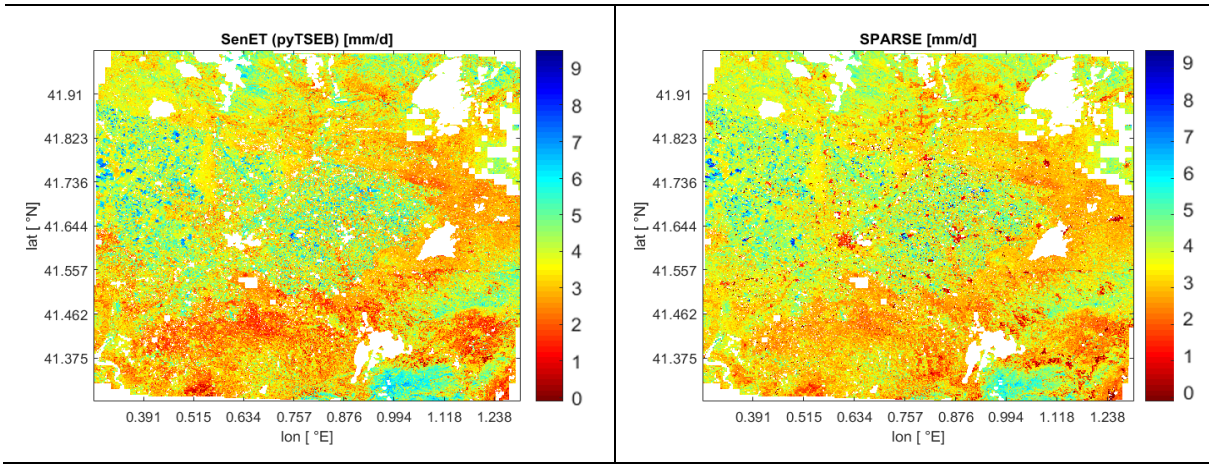

Figure 47: left) SenET (pyTSEB) and right) SPARSE; top) instantaneous [mm/hr] and bottom) daily [mm/d] evapotranspiration maps for DoY 160

Since the SenET extent is quite large, we also select a few days where input data is available for most of the pixels. The pixel-wise IGBP (International Geosphere Biosphere Programme) land-cover classes were used as reference when assigning the required minimum stomatal resistance input (look-up table realistically compiled according to the literature (e.g., Masson et al., 2003). For instance: IGBP Class "4" – "Deciduous broadleaf forests" is assigned a minimum stomatal resistance of 200 s/m; pixels with IGBP Class "12" – "Croplands" - assigned 100 s/m). The input data were then applied to the classic SPARSE to allow simulation of the spatial distribution of evapotranspiration. The instantaneous as well as the daily (assuming a daily self-preservation of latent-to-incoming solar radiation, i.e., $\lambda E_{inst}/S^{\downarrow}_{inst} \approx \lambda E_{day}/S^{\downarrow}_{day}$, according to the SenET methodology) evapotranspiration.

B1. Comparison of SCOPE versions

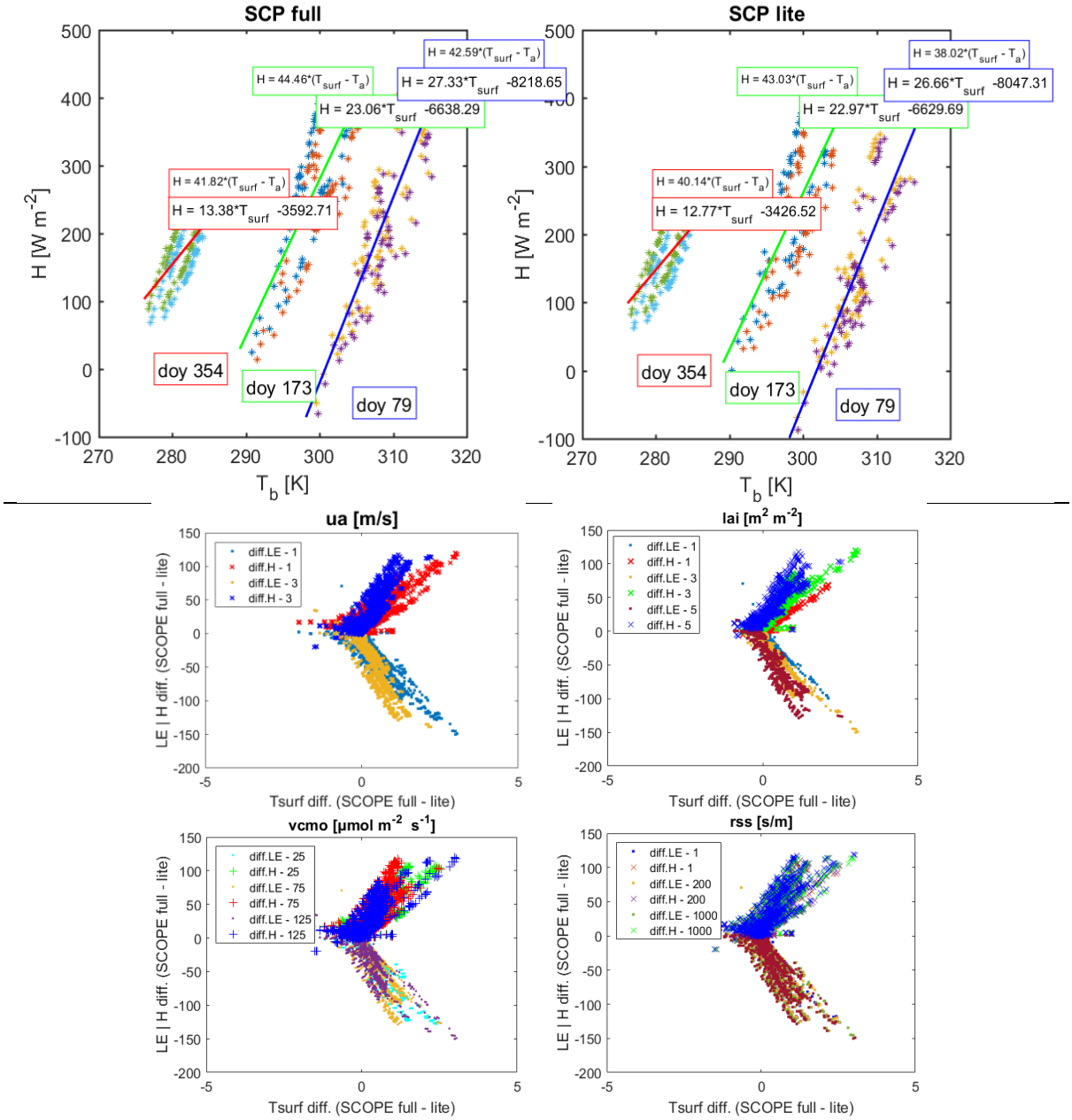

Figure 48: daytime flux differences versus surface temperature differences (SCOPE full – SCOPE lite) with differentiation between the separate varied variables (wind speed, leaf area index, Vcmo and soil resistance)

simulated brightness temperatures		directional anisotropy	
SCPfull- T_B : rss1000,LAI1,Ua1,Vcmo:25/75/125	SCPLiTE- T_B : rss1000,LAI1,Ua1,Vcmo:25/75/125	SCPfull- DA : rss1000,LAI1,Ua1,Vcmo:25/75/125	SCPLiTE- DA : rss1000,LAI1,Ua1,Vcmo:25/75/125
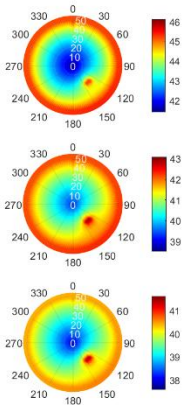	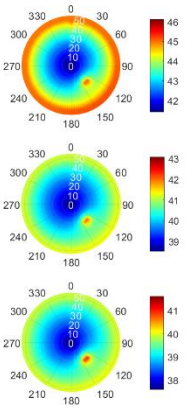	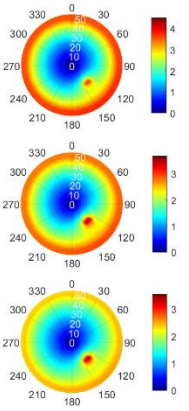	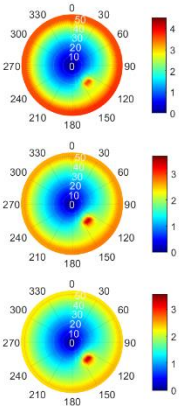
SCPfull- T_B : rss1000,LAI1,Ua3,Vcmo:25/75/125	SCPLiTE- T_B : rss1000,LAI1,Ua3,Vcmo:25/75/125	SCPfull- DA : rss1000,LAI1,Ua3,Vcmo:25/75/125	SCPLiTE- DA : rss1000,LAI1,Ua3,Vcmo:25/75/125
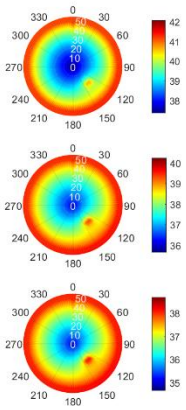	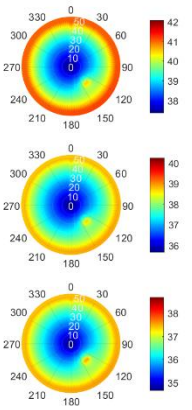	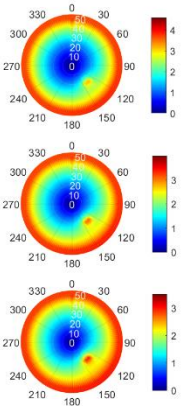	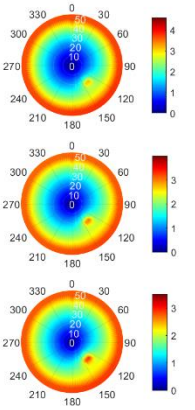
SCPfull- T_B : rss1000,LAI3,Ua1,Vcmo:25/75/125	SCPLiTE- T_B : rss1000,LAI3,Ua1,Vcmo:25/75/125	SCPfull- DA : rss1000,LAI3,Ua1,Vcmo:25/75/125	SCPLiTE- DA : rss1000,LAI3,Ua1,Vcmo:25/75/125
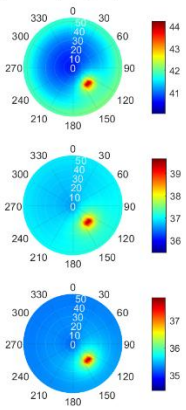	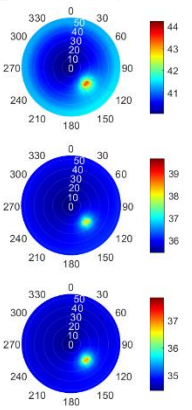	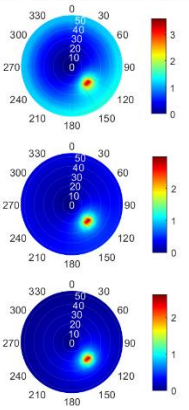	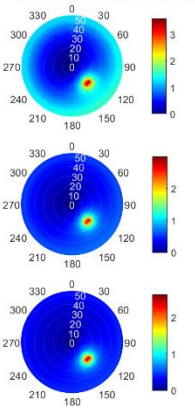

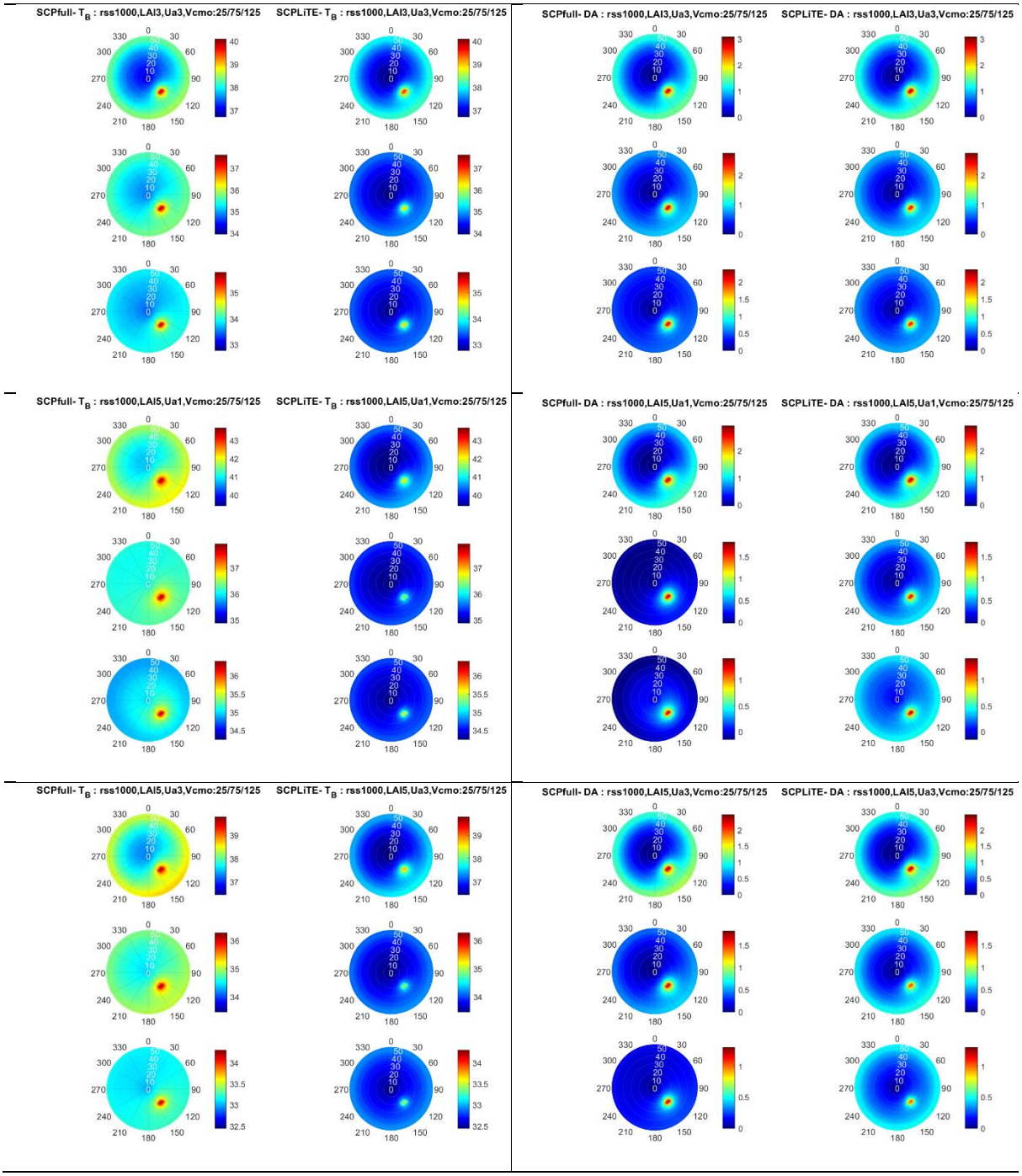

Figure 49: comparison of noon directional brightness temperatures (and directional anisotropy) simulated by the full and lite SCOPE versions

B2. SPARSE, SPARSE4 vs SCOPE comparisons – retrievals using nadir brightness temperatures

LAI [1 m^2m^{-2}]

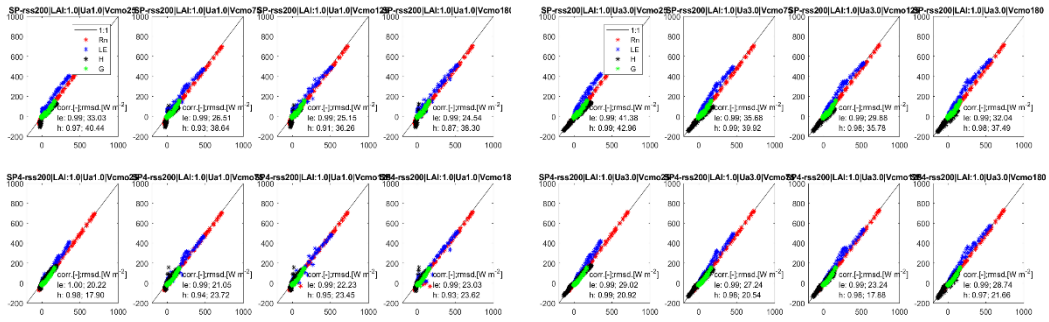

LAI [3 m^2m^{-2}]

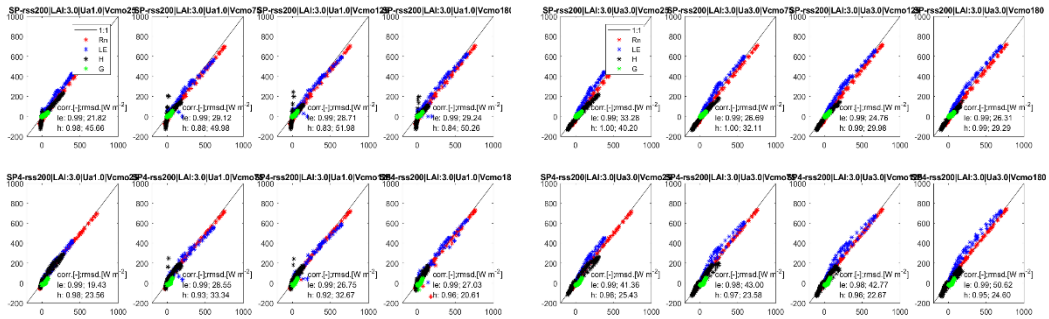

LAI [5 m^2m^{-2}]

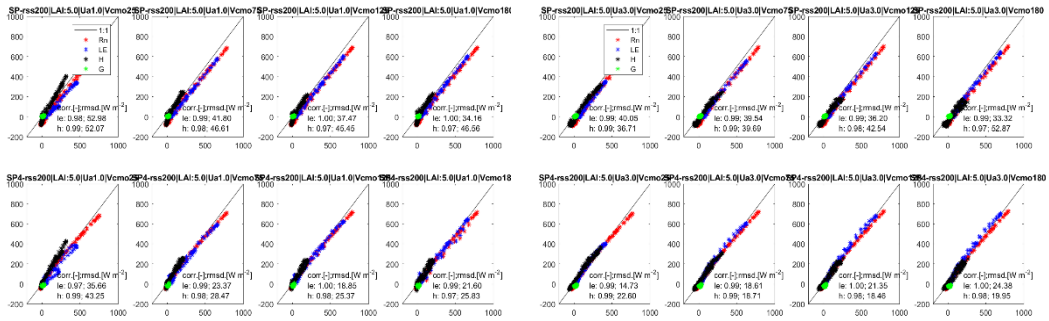

LAI [1 m^2m^{-2}]

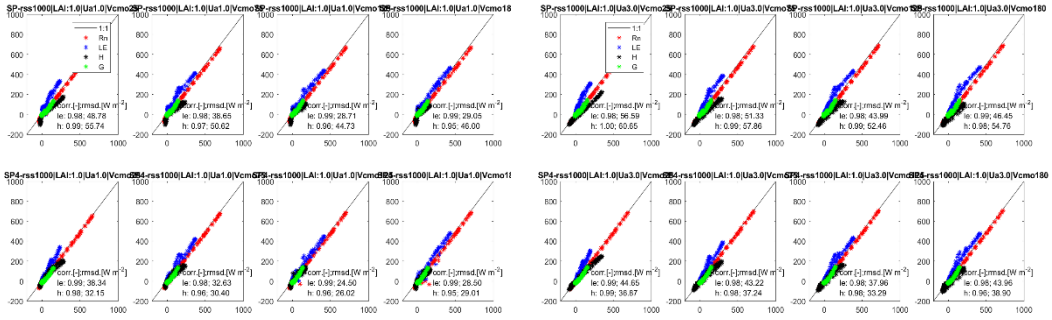

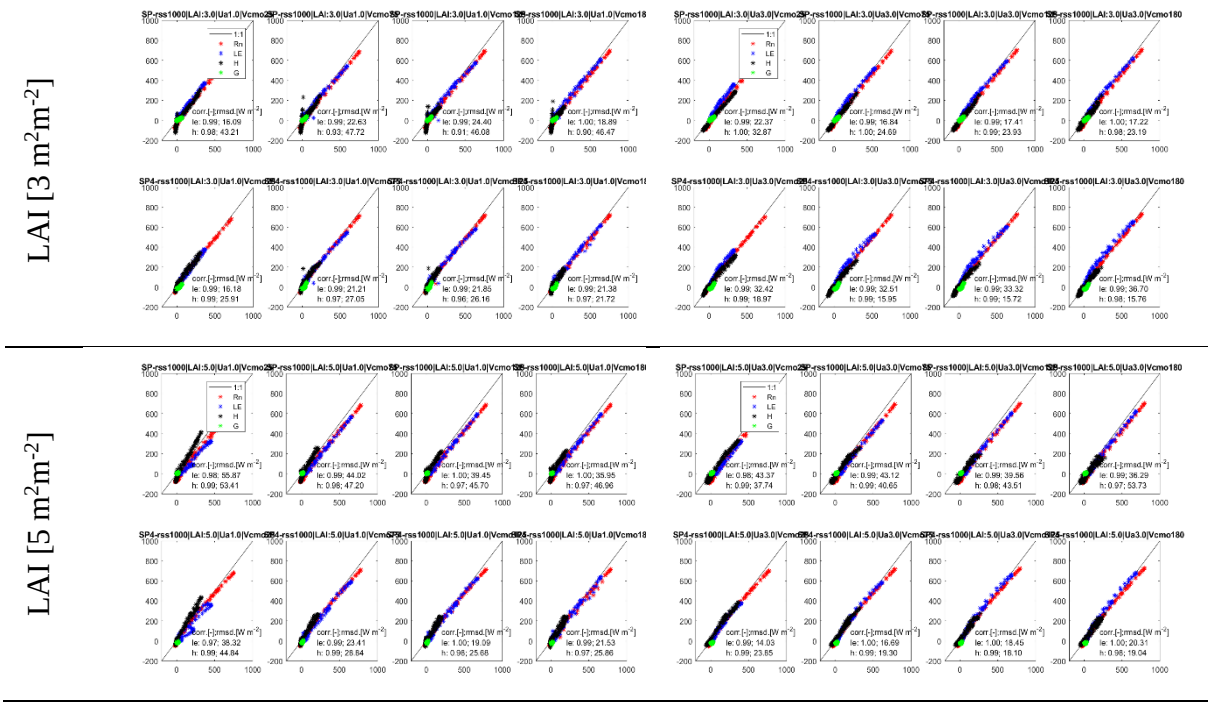

Figure 50: The estimated fluxes (SPARSE and SPARSE4) against the 'reference' SCOPE flux estimates for varying biophysical parameters and surface characteristics, i.e. leaf area indices, stomatal conductance, wind speed.

B3. Directionality consistency evaluations

1 m²/m²

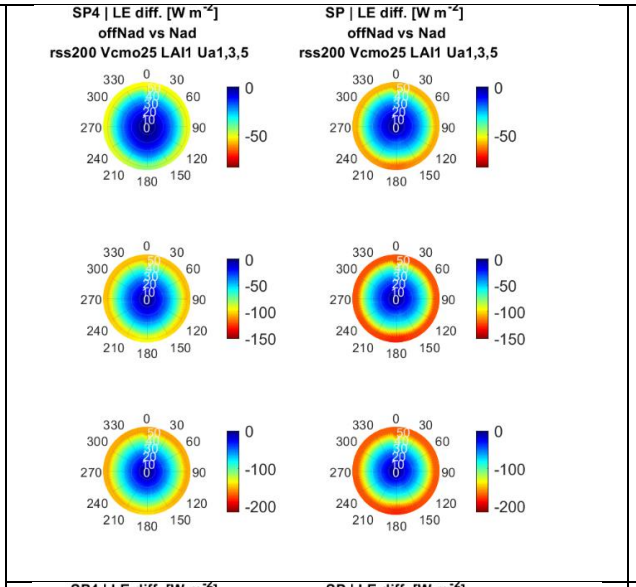

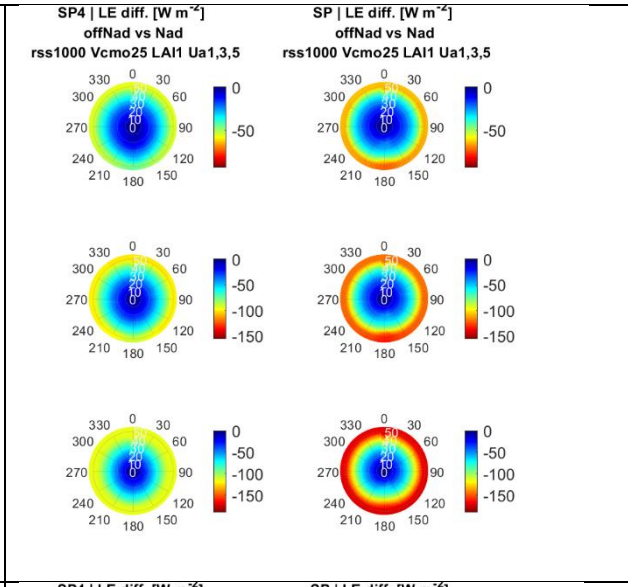

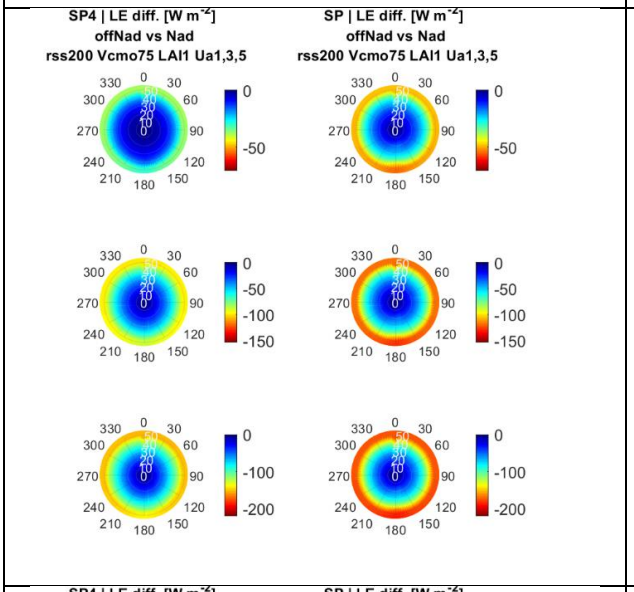

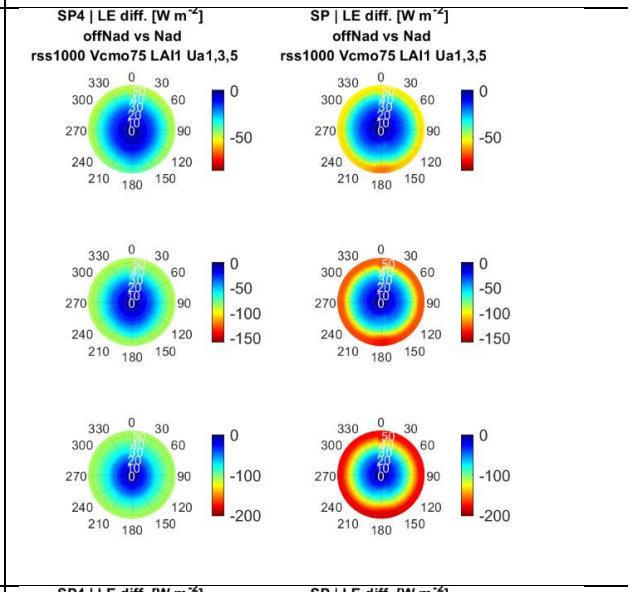

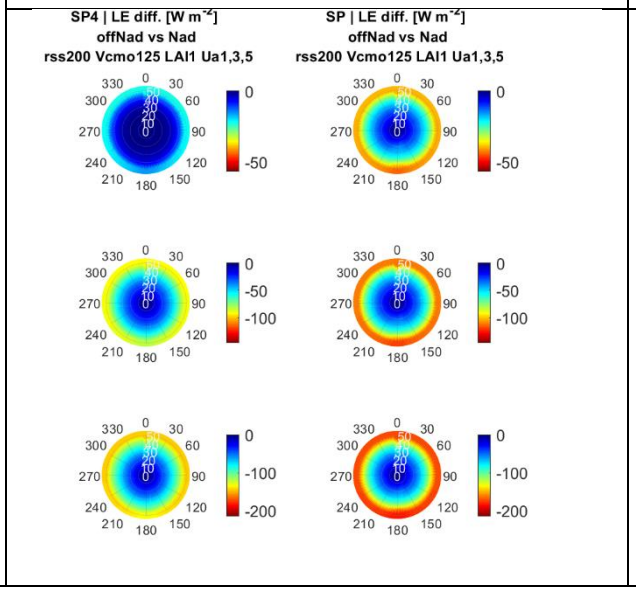

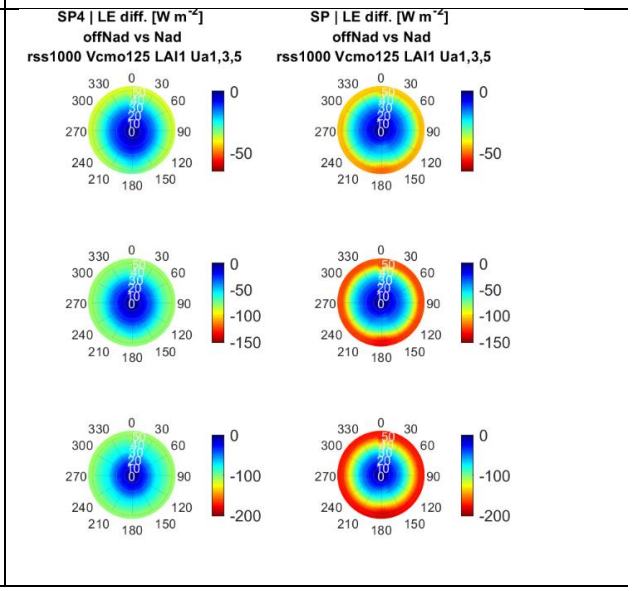

LAI 3 m^2/m^2

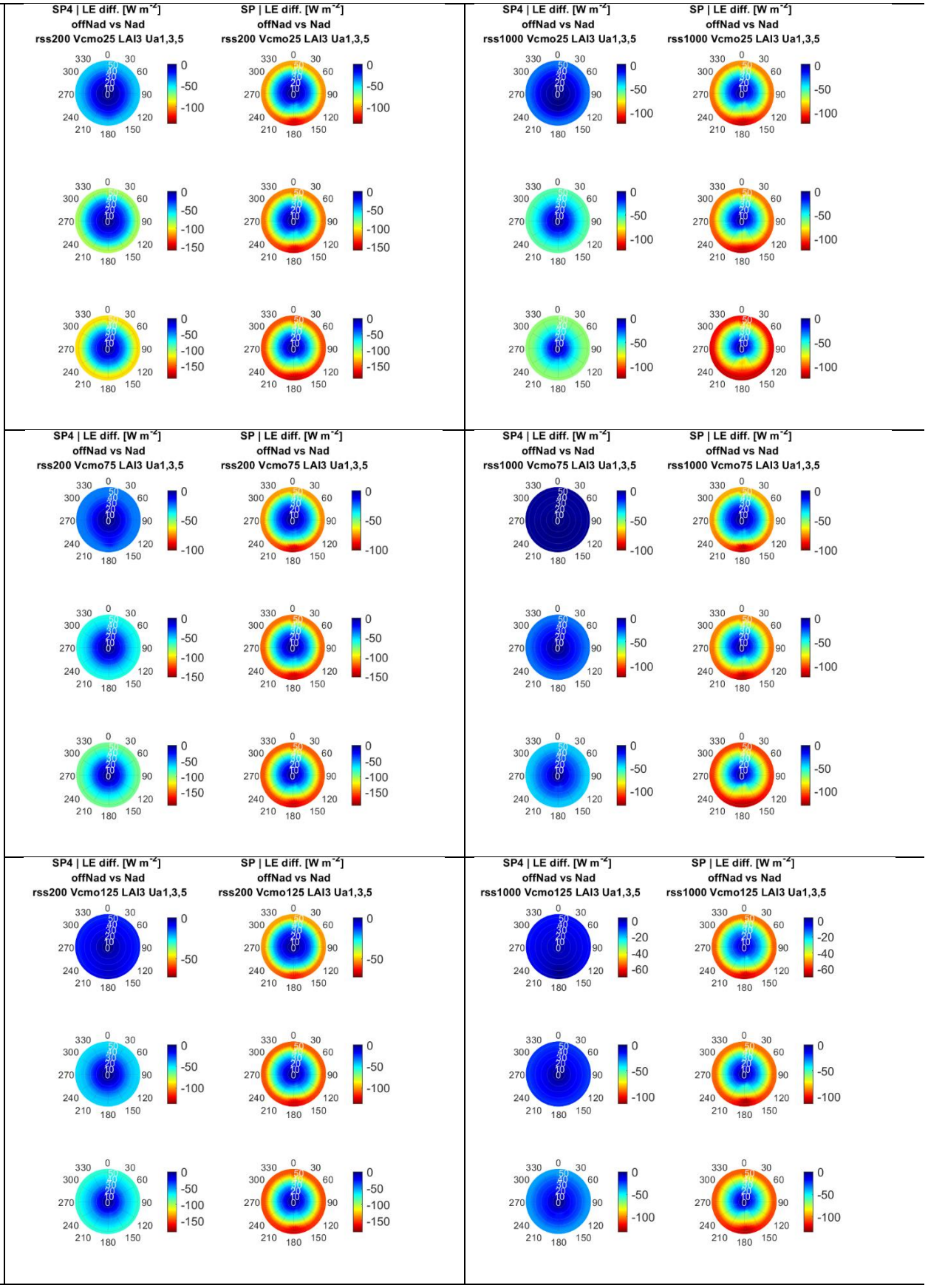
SP4 | LE diff. [W m-2]
offNad vs Nad
rss200 Vcmo25 LAI3 Ua1,3,5
SP | LE diff. [W m-2]
offNad vs Nad
rss200 Vcmo25 LAI3 Ua1,3,5
SP4 | LE diff. [W m-2]
offNad vs Nad
rss1000 Vcmo25 LAI3 Ua1,3,5
SP | LE diff. [W m-2]
offNad vs Nad
rss1000 Vcmo25 LAI3 Ua1,3,5
SP4 | LE diff. [W m-2]
offNad vs Nad
rss200 Vcmo75 LAI3 Ua1,3,5
SP | LE diff. [W m-2]
offNad vs Nad
rss200 Vcmo75 LAI3 Ua1,3,5
SP4 | LE diff. [W m-2]
offNad vs Nad
rss1000 Vcmo75 LAI3 Ua1,3,5
SP | LE diff. [W m-2]
offNad vs Nad
rss1000 Vcmo75 LAI3 Ua1,3,5
SP4 | LE diff. [W m-2]
offNad vs Nad
rss200 Vcmo125 LAI3 Ua1,3,5
SP | LE diff. [W m-2]
offNad vs Nad
rss200 Vcmo125 LAI3 Ua1,3,5
SP4 | LE diff. [W m-2]
offNad vs Nad
rss1000 Vcmo125 LAI3 Ua1,3,5
SP | LE diff. [W m-2]
offNad vs Nad
rss1000 Vcmo125 LAI3 Ua1,3,5

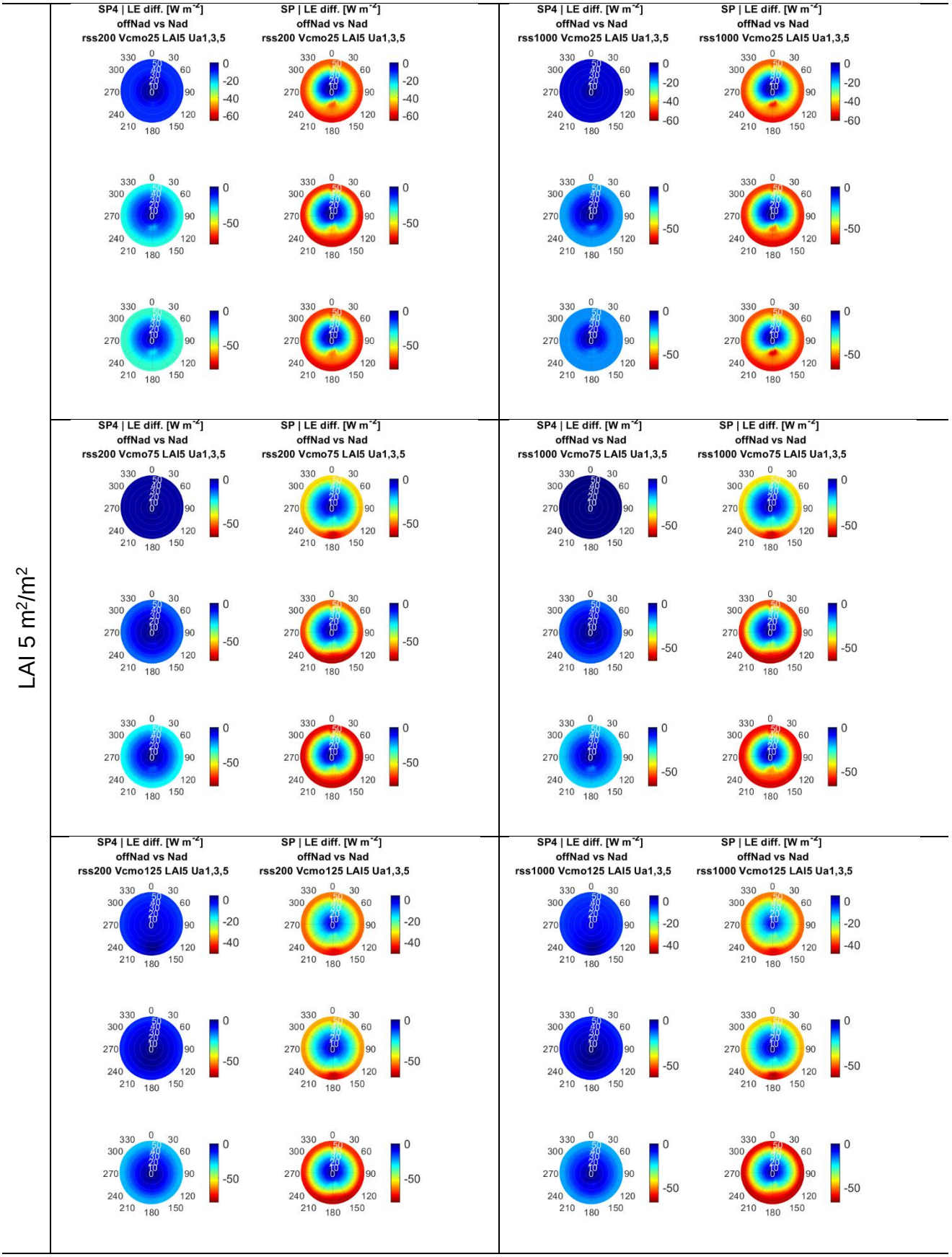

Figure 51: Directional sensitivity of latent heat flux retrieval (Off-nadir-based less nadir-based] biases for selected wind speed and surface characteristics (water stress and vegetation cover). Biases calculated over all days but for midday estimates

1 m^2/m^2

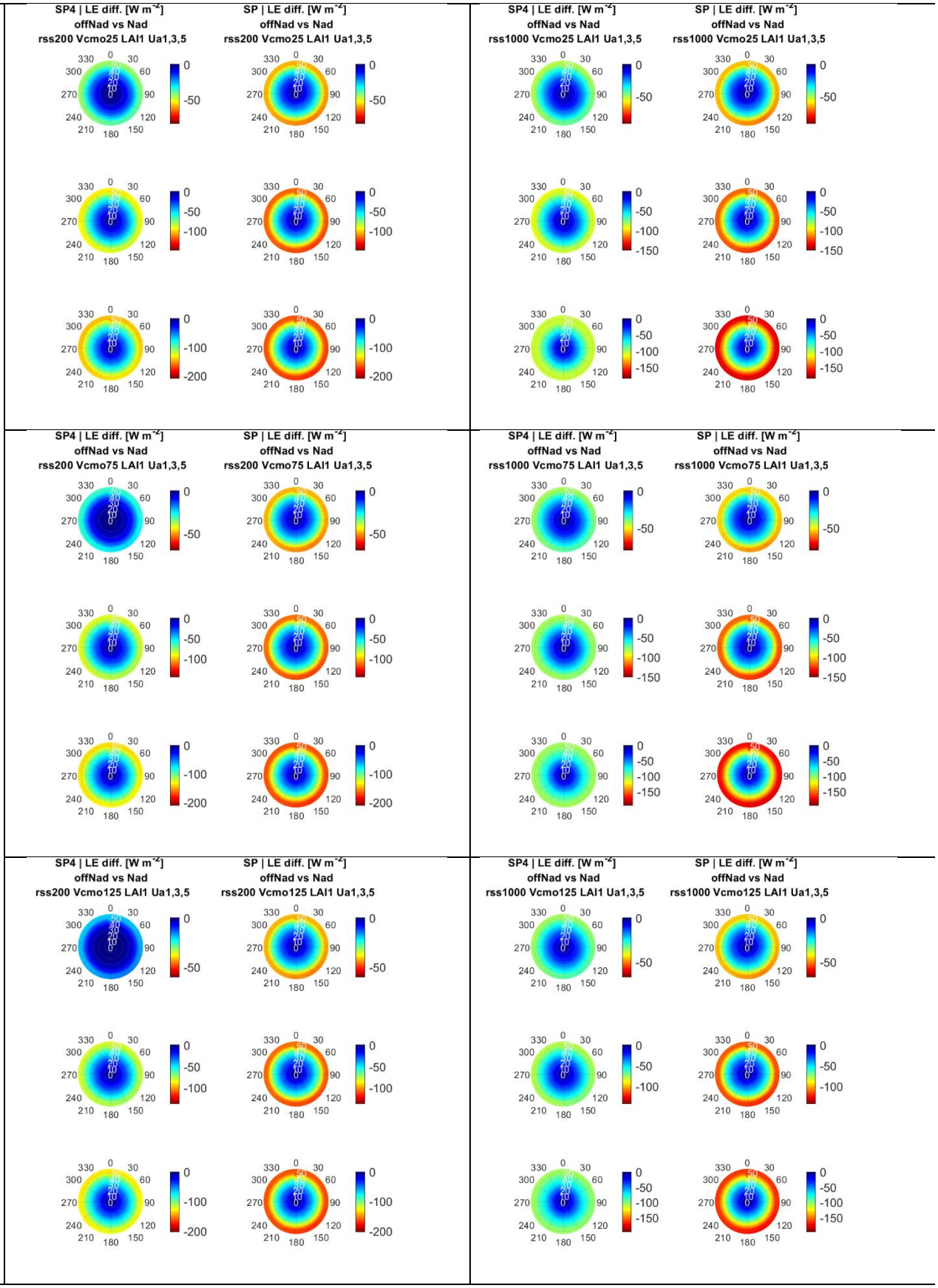
SP4 | LE diff. [W m-2]
offNad vs Nad
rss200 Vcmo25 LAI1 Ua1,3,5
SP | LE diff. [W m-2]
offNad vs Nad
rss200 Vcmo25 LAI1 Ua1,3,5
SP4 | LE diff. [W m-2]
offNad vs Nad
rss1000 Vcmo25 LAI1 Ua1,3,5
SP | LE diff. [W m-2]
offNad vs Nad
rss1000 Vcmo25 LAI1 Ua1,3,5
SP4 | LE diff. [W m-2]
offNad vs Nad
rss200 Vcmo75 LAI1 Ua1,3,5
SP | LE diff. [W m-2]
offNad vs Nad
rss200 Vcmo75 LAI1 Ua1,3,5
SP4 | LE diff. [W m-2]
offNad vs Nad
rss1000 Vcmo75 LAI1 Ua1,3,5
SP | LE diff. [W m-2]
offNad vs Nad
rss1000 Vcmo75 LAI1 Ua1,3,5
SP4 | LE diff. [W m-2]
offNad vs Nad
rss200 Vcmo125 LAI1 Ua1,3,5
SP | LE diff. [W m-2]
offNad vs Nad
rss200 Vcmo125 LAI1 Ua1,3,5
SP4 | LE diff. [W m-2]
offNad vs Nad
rss1000 Vcmo125 LAI1 Ua1,3,5
SP | LE diff. [W m-2]
offNad vs Nad
rss1000 Vcmo125 LAI1 Ua1,3,5

LAI 3m²/m²

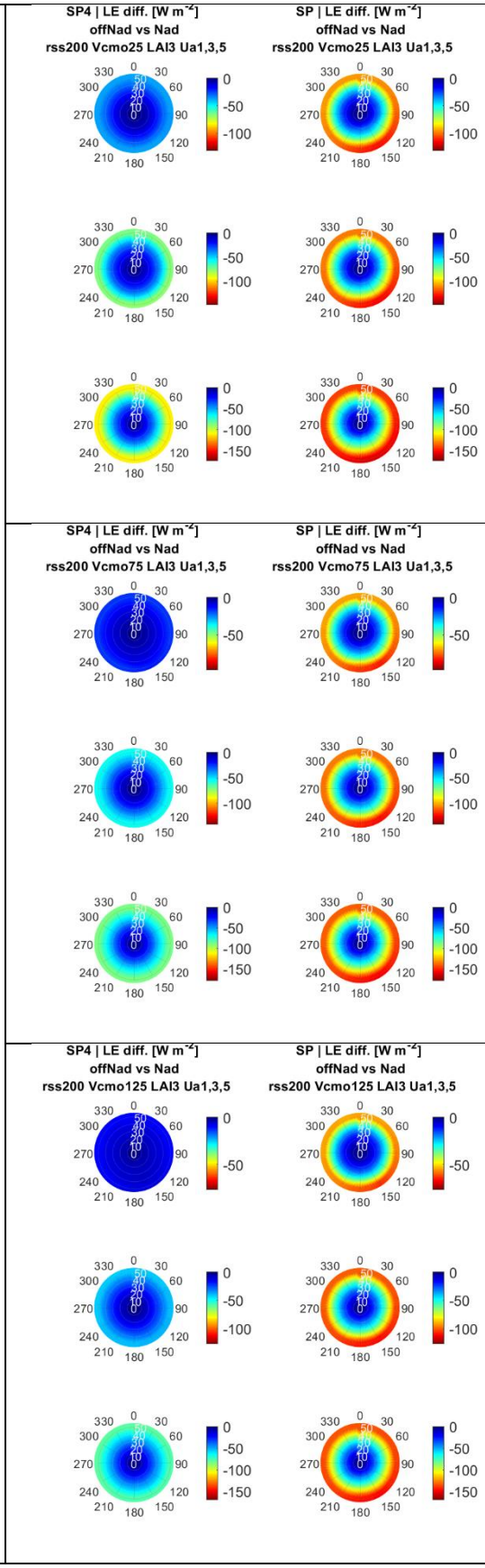
SP4 | LE diff. [W m⁻²]
offNad vs Nad
rss200 Vcmo25 LAI3 Ua1,3,5
SP | LE diff. [W m⁻²]
offNad vs Nad
rss200 Vcmo25 LAI3 Ua1,3,5
SP4 | LE diff. [W m⁻²]
offNad vs Nad
rss200 Vcmo75 LAI3 Ua1,3,5
SP | LE diff. [W m⁻²]
offNad vs Nad
rss200 Vcmo75 LAI3 Ua1,3,5
SP4 | LE diff. [W m⁻²]
offNad vs Nad
rss200 Vcmo125 LAI3 Ua1,3,5
SP | LE diff. [W m⁻²]
offNad vs Nad
rss200 Vcmo125 LAI3 Ua1,3,5

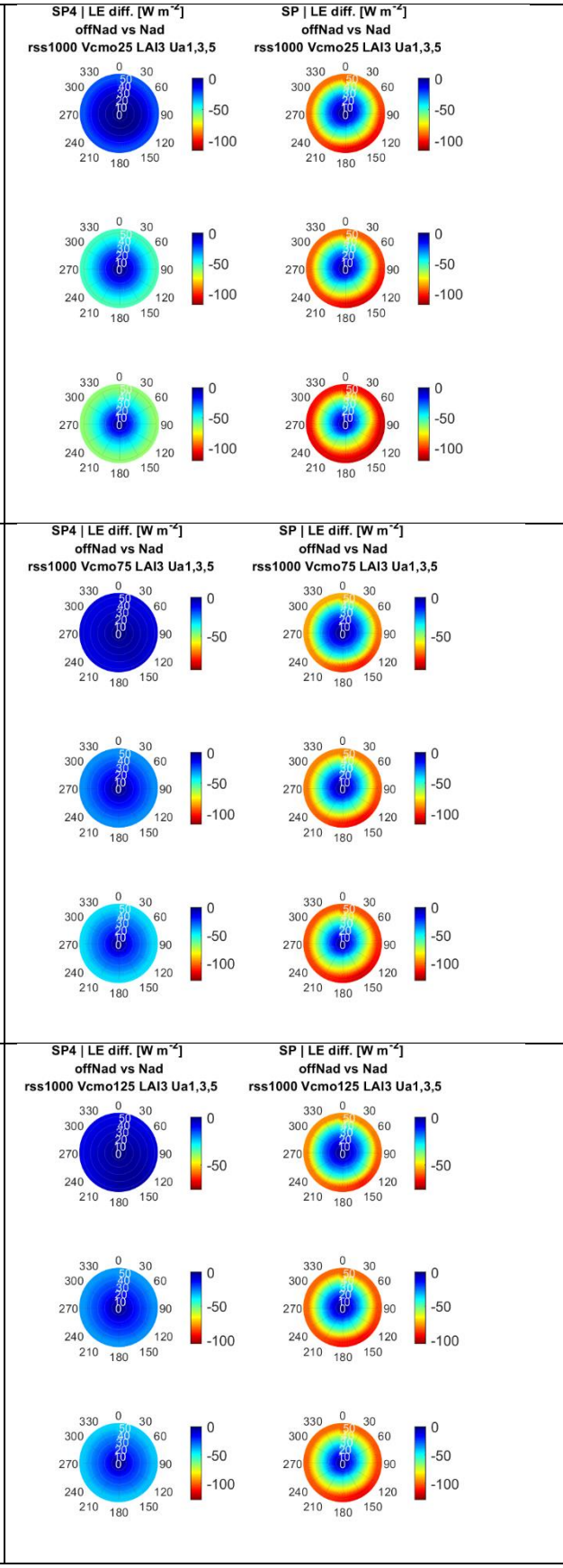
SP4 | LE diff. [W m⁻²]
offNad vs Nad
rss1000 Vcmo25 LAI3 Ua1,3,5
SP | LE diff. [W m⁻²]
offNad vs Nad
rss1000 Vcmo25 LAI3 Ua1,3,5
SP4 | LE diff. [W m⁻²]
offNad vs Nad
rss1000 Vcmo75 LAI3 Ua1,3,5
SP | LE diff. [W m⁻²]
offNad vs Nad
rss1000 Vcmo75 LAI3 Ua1,3,5
SP4 | LE diff. [W m⁻²]
offNad vs Nad
rss1000 Vcmo125 LAI3 Ua1,3,5
SP | LE diff. [W m⁻²]
offNad vs Nad
rss1000 Vcmo125 LAI3 Ua1,3,5

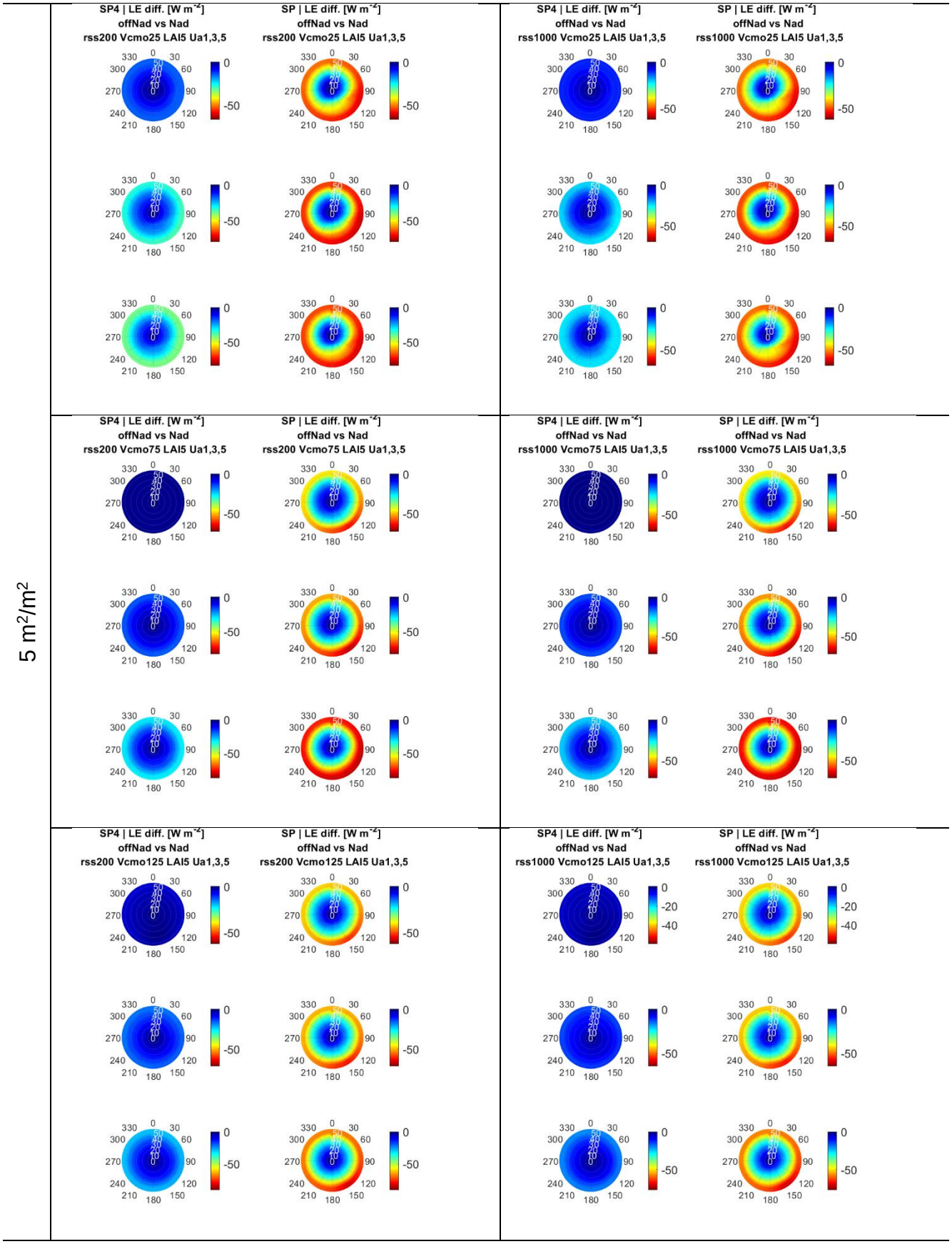

Figure 52: Same as Figure 51 but for 10-14 average estimates